Understanding the reactivity and defect chemistry of ceria based materials using synchrotron and neutron radiation techniques

Huw Rhys Marchbank

University College London

A thesis presented in partial fulfilment of the
requirements for the degree of Doctor of Philosophy

2017

Declaration

I, Huw Rhys Marchbank, confirm that the work presented in this thesis is my own. Where information has been derived from other sources, I confirm that this has been indicated in the thesis.

Signed____________________

Abstract

The work, that has formed the basis of this project, has looked at the developing the understanding of ceria and related ceria materials through the investigation of the short-, medium- and long-range structure.

The structure of four samples of ceria was investigated using neutron and X-ray total scattering, and X-ray absorption spectroscopy (XAS). Detailed analysis of the total pair distribution functions (PDFs) revealed that in all the samples the occupancy of both Ce^{4+} and O^{2-} are very close to the ideal stoichiometry. The main differences observed in the pair correlations from various diffraction techniques were attributed to the particle size of the CeO_2. Detailed analysis of the Ce L_3- and K-edge EXAFS data support this finding; the decrease in higher shell coordination numbers with respect to the NIST standard, can also be attributed to differences in particle size.

A combination of both x-ray and neutron *in situ* PDF, Ce L_3- and K-edge, Pd K-edge and Pt L_3-edge XAS were performed on high surface area ceria, 5wt% Pd and 5wt% Pt loaded high surface area ceria samples under reducing conditions. This allowed for a thorough and in depth study of how pure ceria behaves and whether the loading of PGMs onto the support effects its behaviour under reducing conditions. Detailed analysis of PDF and XAS data for the pure ceria support show a reduction under heating in H_2:N_2 whilst under cooling it 'reoxidises' to its original stoichiometry. In contrast both the addition of Pd and Pt to the ceria support shows enhanced reduction of the ceria upon heating and no reoxidation upon cooling under a reducing atmosphere.

The effect of Pd loading on ceria was examined by using combined *in situ* XAS/high resolution x-ray diffraction (HRXRD) as well as *in situ* PDF studies. This investigated a high surface area ceria support and 1, 2.5 and 5wt% Pd loaded ceria samples respectively. All methods showed that an increase in the Pd loading decreased the reduction temperature for both the Ceria support and PdO to Pd metal formation. Both XAS and HRXRD show the reduction of all samples upon heating, whereas on cooling there is no reoxidation for the Pd loaded samples in comparison to the pure support. The method in which the Pd is incorporated onto ceria is also important, as the reoxidation is seen with a physical mixture of PdO and ceria.

The reduction and oxidation of Ceria-Zirconia kappa and fluorite materials was studied using X-ray diffraction and PDF, and how the introduction of Pd into these systems influences the reduction behaviour. The Fluorite based materials show no phase change under heating in either oxidising or reducing atmospheres there are no phase changes observed. In contrast, the heating of the Kappa based materials under reducing conditions show the loss of oxygen from the lattice and the conversion to the pyrochlore structure. Upon cooling and treating with air, these are converted back to the Kappa structure.

Table of Contents

List of Figures

List of Tables

Acknowledgements

I would initially like to thank those who I have met, talked with or collaborated with throughout the course of my studies, in particular those at UCL, Johnson Matthey, and the synchrotron and neutron sources I have worked at.

I would like to pay thanks to Professor Sankar, for taking a risk in handing me the opportunity to pursue my career in chemistry, motivation and assistance throughout my research. His ideas, experience and suggestions have been invaluable to my research and studies.

I would like to thank Johnson Matthey for their financial support and Timothy Hyde for his supervision throughout my PhD. I thank Janet Fisher and Amy Kolpin for the provision of samples and advice, and those who aided me in beamtimes. I’d like to acknowledge Hoi Jobson and Edd Bilbé, their words of advice have been of great help. Working with Johnson Matthey has given me an important insight in industrial-academic collaborations.

Huge gratitude is owed to those beamline scientists who I have worked with and been helped by. At ESRF, I would like to thank Simon Kimber, Alessandro Longo and Manual Monte for their help during the collection of data and advice on analysis. At APS, I would like to thank Karena Chapman and Kevin Beyer for their help in the collection of data and advice on analysis. At ISIS, I owe an immense thanks and praise for Matthew Tucker and Helen Playford. Not only have they been extremely helpful in the collection of data they have helped guide me through complicated analysis and given useful suggestions for my work as a whole. Their help has allowed me to probe further and deeper into my studies which, I hope, is evident in my work.

I would like to thank to former and present Sankar group members. Their help at beamtimes ensured that working was fun but also constructive (especially the night shifts). Thanks Adam, Zarrin, Anastasia, Ian, Glen, Tom and Husna.

Further thanks are owed EPSRC and Johnson Matthey for their financial support, without which this work would not have happened.

Special thanks are given to those of my close friends who have supported me since the start of thesis. Without their never ending support, this worked would have not have been as enjoyable. Those in particular are Banuka, Cessie, Ieuan, Jesse, Vince, Mailis and Lucy. Though they gave me blank looks when I discussed my work, their encouragement and distraction was grateful.

Finally, I thank my family for their support throughout the last 4 years. Their belief in me has been instrumental in my university career and my further studies.

Chapter 1: Introduction

1.1 Heterogeneous Catalysis

Catalysis is where there is an increase in the rate of reaction in the presence and contribution of a supplementary material, a catalyst.[1] These catalysts do not interfere with the equilibrium of the reaction but aids in accelerating it. This is achieved by the formation of a transition state between the reactants and catalyst, and in the case of heterogeneous catalysts can separate and recycle the catalyst.[2] The lower activation energy for the reaction results in an increased rate of reaction compared to the same reaction performed without a catalyst present, though the energy released from the reaction is the same for either reaction pathway. The effectiveness of the catalyst used is dependent on inhibitors ("poisons") being present or (in the case of heterogeneous catalysis) the rate of diffusion for the reactants onto the catalyst.

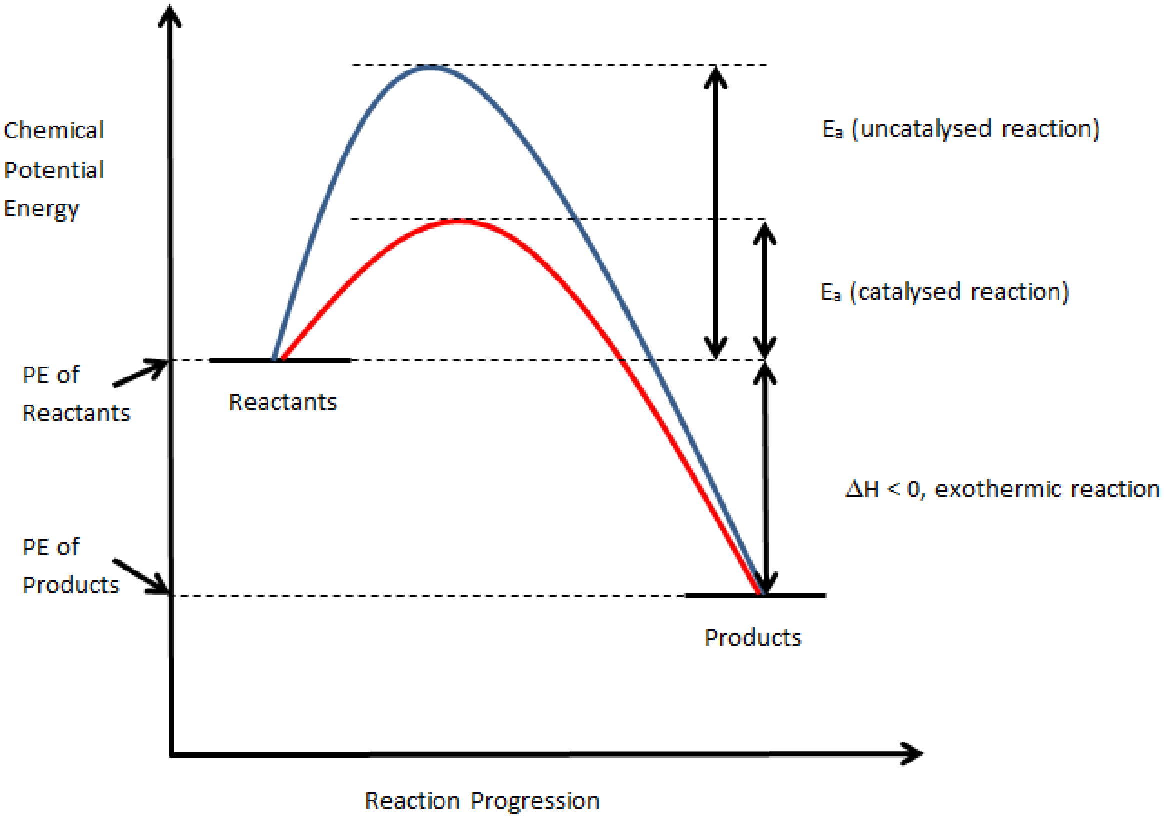

Figure 1-1: A typical reaction energy diagram for the conversion of reactants to products. Catalysed reaction pathway (Red) Uncatalysed Reaction Pathway (Blue)

The catalysts form intermediates, which are short lived species as the reaction proceeds, between the catalyst and the reactant(s), which then goes on to form the product, as seen in the equation below where A and B are the reactants, C is the product and **Cat** is the catalyst c.f. a transition state is the formation of a new molecule between the reactants and products.

$$A + \boldsymbol{Cat} \rightarrow A\boldsymbol{Cat}$$

$$B + A\boldsymbol{Cat} \rightarrow AB\boldsymbol{Cat}$$

$$AB\boldsymbol{Cat} \rightarrow C\boldsymbol{Cat}$$

$$C\boldsymbol{Cat} \rightarrow C + \boldsymbol{Cat}$$

The catalysts used can either be homogeneous or heterogeneous. Homogeneous catalysts are present in the same state of matter as the reactants whereas heterogeneous catalysts exist in a different state in comparison to the reactants. The main benefit in using heterogeneous catalysis is that they are in the different phase in comparison to the reactants, normally a solid catalyst and reactants in the liquid or gas phase. This ensures that the separation of catalysis from the products is more straightforward.[3,4] The active sites, where the formation of the transition states occur, can occur on the surface of the catalyst therefore is dependent on the surface activity and types of surface present. Furthermore these active sites could be located at crystal edge where mixed valent metal ions are present, or other defects are present.

There are many areas in which heterogeneous catalysis plays an important role in both scientific research and industrial applications.[5] These can be as different as uses in organic chemistry, electrochemical processes, the manufacture of plastics or medicines, in the area of energy[6,7] and catalytic control in the automotive industry,[8–12] In addition, the most relevant with respect to this thesis, is the use of heterogeneous catalysts in the conversion of automatic exhaust pollutants to ‘safer’ by-products and pollution abatement e.g. conversion of carbon monoxide and nitrogen oxides. These are of such importance that this family of catalysts make up 35% of global GDP[13] and that more than 1 trillion US $ are spent on these with Johnson Matthey being a leader in emission control catalysis.[14–16]

Some of the most important e.g. most selective and active are Platinum Group metals[17] (PGMs).[4] These are either used as a single metal only, or as a bimetallic system, though these are expensive, their long life makes them cost effective.[18] Moreover transition metals can be used in catalysis.[19] As these PGMs are expensive, they are typically supported on another material e.g. silica, titania, alumina, ceria etc. and form a sizeable set of systems that can be utilised in numerous areas. Furthermore loading PGMs onto a support increases efficiency because of the increased surface area to volume ratio.[20] The work presented here focusses on Pd and Pt supported on a ceria support.

An example of the catalysis in which this family of materials are in catalytic converters and three-way catalysis.[21] Due to the relative harm caused by automotive pollutants, being able to convert these to 'less' harmful products is an important. Three way catalysis relates to three simultaneous reactions that occur on the catalysts:

$$2CO + O_2 \rightarrow 2CO_2$$

$$2NO_x \rightarrow N_2 + xO_2$$

$$C_yH_{2y+2} + \left(\frac{3y+1}{2}\right)O_2 \rightarrow yCO_2 + (y+1)H_2O$$

These reactions show that CO is oxidised to CO_2, NO_x decomposes to N_2 and O_2, and any unburnt hydrocarbons are oxidised to CO_2 and water. The abatement of the pollutants is so important that nearly all road going vehicles[22] are equipped with an auto catalyst. Furthermore these are of such important that more than half of the world's platinum production goes into the manufacture of autocatalysts.[23] Metals in particular platinum, rhodium and palladium are normally used in three way catalysts. Palladium catalyses oxidation, Rhodium catalyses reduction whereas platinum has activity for both reactions. These can be then used to form bimetallic systems which improve the catalytic conversion of reduction and oxidation reactions in exhaust catalysis.[24] Furthermore, the addition of other elements has been investigated to improve the catalytic conversion of certain reactions.[21] Typically, between 0.1 – 0.2 % of the catalyst mass is noble metal. This are dispersed onto a support to both maximise surface area/efficiency but help minimise particle sintering. These supports are typically ceria, ceria-zirconia, alumina etc. Ceria and ceria based catalyst supports have been found to influence the catalyst by stabilising Pd-only systems but also due to its redox properties and OSC.[25]

Furthermore, PGM based catalysts have been found to have uses in Water-gas shift (WGS) reactions.[26] This allows for the production of hydrogen and carbon dioxide from water and carbon monoxide[27] or vice versa. This is achieved through a series of reactions between the reactants, a support and active sites on the metallic catalyst (σ).[28]

$$CO + H_2O \rightleftarrows H_2 + CO_2$$

This reaction is a source of hydrogen and providing a method for purification,[29] removing any water vapour in a hydrogen stream and converting it to hydrogen. The WGS reaction is an important process in the production of methanol[30] through the use of CO, CO_2 and H_2

though WGS reaction affects this process as the reaction proceeds faster than that for methanol synthesis.[31] The WGS reaction normally consists of high temperature shift (HTS) and low temperature shift (LTS) reactions, which are performed between 300-400°C and 200-300°C respectively. The HTS reaction has high rates of reaction but is limited thermodynamically, leading to some CO not being oxidised. The development of new LTS catalysts is important due to poisoning of copper based catalysts by sulphur. The use of PGMs in LTS has been shown to avoid problems with self-heating whilst having high activity.[32] In the WGS reaction, the water is adsorbed onto the catalyst support, where upon it is dissociated into hydrogen and the support is oxidised. Hydrogen will then desorb from the surface and adsorbed oxygen will migrate to the PGM. The migrated oxygen will then react with CO present resulting in CO_2. Therefore 2 separate sites are required for the reaction to proceed.

Ceria has been found to be an important support for PGMs in LTS reactions because of its OSC[33] and the ability of the Ce ions present to undergo redox reactions i.e. leading to vacancy formation.[34] In the case of Pt/ceria systems, the reaction proceeds as:

$$CO + Pt \longrightarrow CO_{adsorbed}$$

$$CeO_2 + CO_{adsorbed} \longrightarrow Ce_2O_3 + CO_2$$

$$Ce_2O_3 + H_2O \longrightarrow CeO_2 + H_2$$

As seen in the above equations, reduction of CeO_2 is important in the formation of CO_2. The ceria support is reduced and Ce (IV) ions are reduced to Ce (III) ions. Though due to the properties of the Ce (III) ion, it can easily be oxidised, resulting in both the formation of H_2 and the oxidation of Ce_2O_3 to its original CeO_2 starting material. In addition oxygen vacancies formed during CO adsorption process provide suitable sites for the dissociation of H_2O and formation of H_2.[35] Not only has Pt been found to be useful in WGS reactions but numerous other PGMs have been shown to be of use.[36] This is further complicated by the support and how different syntheses can influence the support structure and the effect it might have on the WGS reaction, as the OSC is dependent on the microstructure.[35]

1.2 Ceria and its structural properties

Cerium is a rare earth element, with an atomic number of 58, and part of the lanthanide series. The electronic configuration is [Xe] $4f^1 5d^1 6s^2$. This electronic structure allows cerium atoms present in materials such as cerium dioxide (Ceria), to undergo redox reactions, so it can easily switch between Ce (III) and Ce (IV). Having both these oxidations states ensures that cerium oxides can be between Ce_2O_3 and CeO_2, and can be easily synthesised purely by the reaction of cerium with oxygen. Interestingly, we can influence what oxide is formed by this reaction by varying the pressure of the oxygen gas or temperature used.

In this thesis, the main phase of ceria present is the ceria fluorite phase, space group $Fm\bar{3}m$, *a* = 5.411651 Å (for Ceria NIST diffraction standard). This structure has a face centred cubic (FCC) unit cell where each cerium ion has 8 nearest neighbour (NN) oxygen atoms, whereas each oxygen ion has 4 NN cerium atoms i.e. oxygen can be seen as tetrahedral coordinated by cerium.

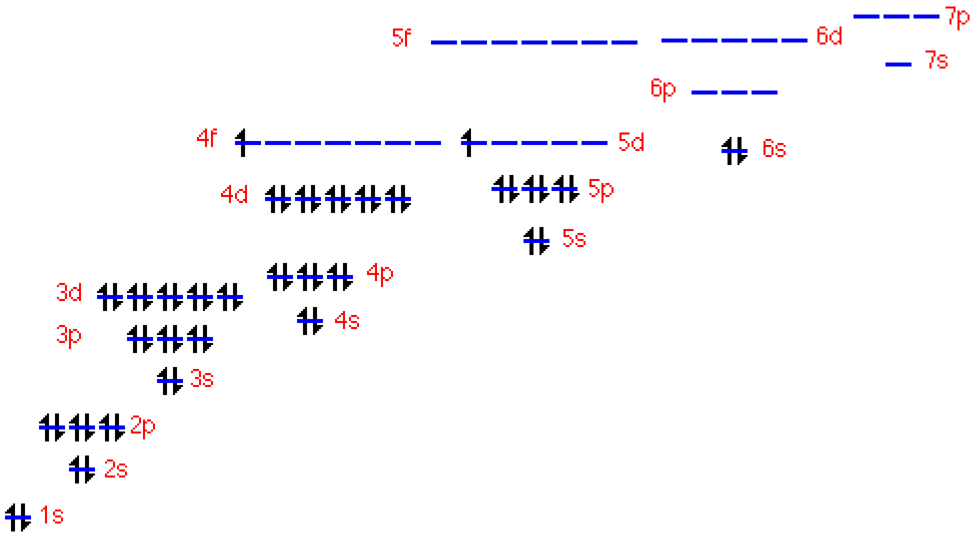

Figure 1-2: Comparison of respective energies of the atomic orbitals in cerium. This shows the close proximity of the energies for the 4f, 5d and 6s orbitals.[117]

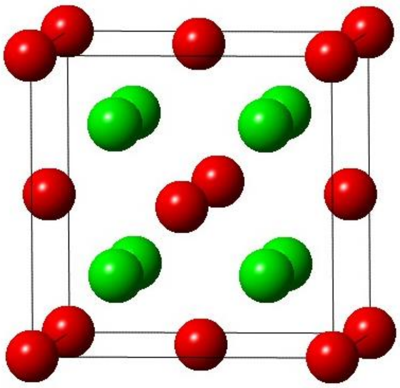

Figure 1-3: Ceria has the fluorite structure (space group: $Fm\bar{3}m$), Ce (Red): 4a, 0, 0, 0 and O (green): 8c, ¼, ¼, ¼

$$CeO_2 \rightleftharpoons CeO_{2-x} + \frac{x}{2}O_2$$

$$O_o \rightleftharpoons \frac{1}{2}O_2 + V_o^{\cdot\cdot} + 2e'$$

$$2Ce^{4+} + 2e' \rightleftharpoons 2Ce^{3+}$$

With cerium's ability to undergo reduction and oxidation, we are able to remove and introduce oxygen into the ceria fluorite structure e.g. reducing with hydrogen gas or oxidising by air. When Ce (IV) is reduced to Ce (III), oxygen atoms are removed, introducing vacant sites within the structure (Intrinsic defects). This creates non stoichiometric cerium oxides with oxygen missing but on cooling can produce related fluorite superstructures. These non-stoichiometric materials are stable enough that an alpha ceria fluorite phase occurs for CeO_{2-x}, where x can vary between 0 and 0.3. XRD patterns show that no super structures are formed for this phase. Furthermore the unit cell size increases with the increase of oxygen vacancies within the structure.[37,38] This is due to the radius of Ce (III) ions being larger than that for Ce (IV), with values of 1.14 Å vs 0.97 Å respectively.[39]

Figure 1-4 shows the comparison of the unit cell size vs reduction temperature for CeO_2. This shows that as the sample is heated to 1100 K that an intermediate CeO_{2-x} phase is formed. The increase in lattice parameter will be due to a combination of both thermal expansion and the increase in cation size. As the samples are heated further the unit cell size starts to contract. This is due to the formation of the hexagonal Ce_2O_3 phase.

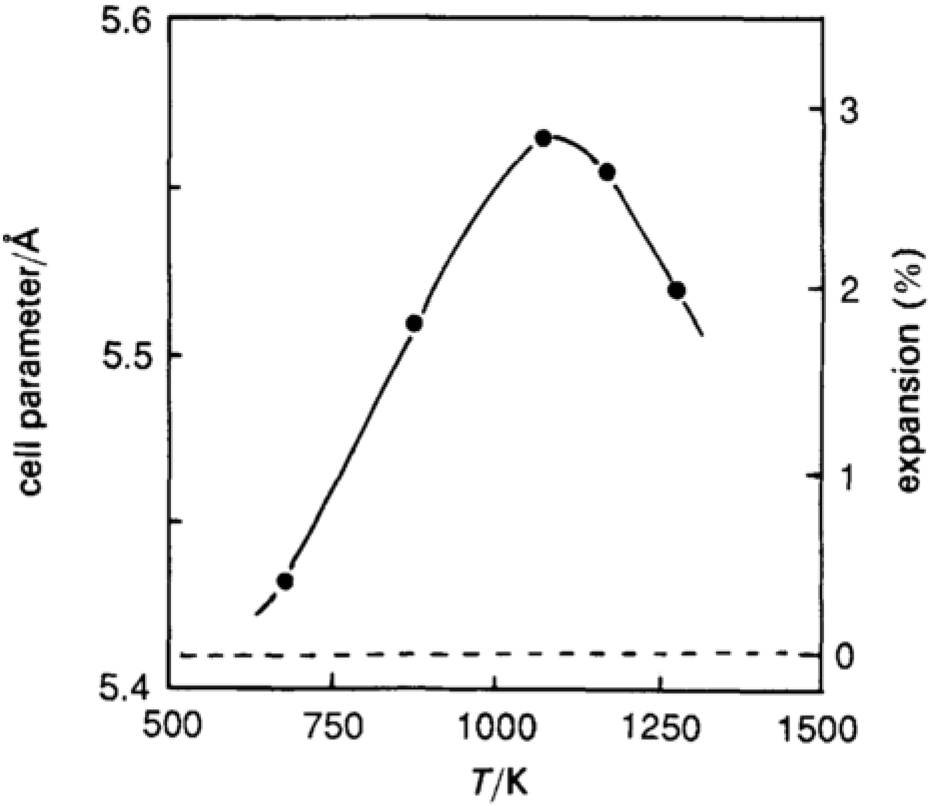

Figure 1-4: Comparison of the reduction temperature and lattice parameter for ceria.[40] This shows as the temperature increases, there is an increase in the unit cell size up to ~1100 K.

The alpha phase is observed at high temperatures, as oxygen is removed from the lattice, but on cooling to lower temperatures it forms ordered fluorite based phases, Ce_nO_{2n-2m}, by a disorder-order process. This results in ceria materials varying from CeO_2 through to $CeO_{1.714}$,[41–43] though this is misleading as the resulting material is a combination of 2 ceria phases with varying stoichiometry for oxygen. However, understanding the oxygen deficient ceria structures is relatively difficult, this is due to the problems obtaining a single crystal of ceria and requiring the use of neutron based radiation for diffraction studies due to the manners in which this radiation interacts with both cerium and oxygen ions. Once oxygen is removed from the structure, the FCC symmetry is lost but cerium and oxygen atoms still sit on their ideal positions, therefore the observed peaks in the diffraction pattern relate to the ceria fluorite structure. The ceria superstructures do show complex diffraction patterns which are related to the ceria fluorite diffraction pattern but have peak splitting due to the loss of oxygen causing a loss of symmetry. This indicates that cerium atoms do not migrate and change their positions with respect to each other cation, and any changes in the material are explained by the loss of oxygen from the lattice and/or the migration of oxygen through the fluorite structure.

There are 2 types of defects that can be introduced by disorder through thermal means. These are Schottky and Frenkel defects. Schottky defects are a vacancy defect and are caused by the removal of ion pairs from the structure and can be represented using Kröger-Vink notation.[44]

$$CeO_2 \rightarrow V_{Ce}'''' + 2V_O^{\cdot\cdot}$$

Frenkel defects relate to the migration of an ion from its respective site in the structure to an interstitial site and the creation of a vacancy on that original site. In the case of ceria, this type of defect relates to the migration of oxygen throughout the lattice and/or removal of oxygen from the lattice, and the creation of a vacancy on that oxygen site. Similarly the energetics of this process supports this suggestion.[45]

$$O_O \rightarrow O_i^{\cdot\cdot} + V_O$$

As previously discussed, oxygen defects can be produced by the reduction of ceria using hydrogen and/or elevated temperatures. This either ensures oxygen migration and/or the removal of oxygen from the lattice entirely, either way this creates vacancies. If oxygen ions are removed from the lattice by reduction, then this means that the unit cell should have a net positive charge. Net charge neutrality is maintained by the reduction of 2 Ce (IV) ions by 2 e^- to Ce (III).

$$CeO_{2-x} \leftrightarrow xV_O^{\cdot\cdot} + (2-x)O_O + 0.5xO_2(g) + 2xCe'_{Ce} + (1-2x)Ce_{Ce}$$

There has been extensive research into the understanding of defects due to the importance of defect sites in the catalytic behaviour of ceria. Models that use interstitial cerium ions[46] and vacant oxygens,[47] based on conductivity data, have been created to understand their properties. Whereas others have reported more direct observations of the defects within ceria, in comparison to interfering defects from other measurements such as the measurement of diffusion data in ceria,[48] neutron diffraction,[49] and x-ray diffraction.[50] Although discussing defects in ceria as purely point defects is misleading as this suggests that these species are restricted to a set site or sites. In reality, the oxygen sub lattice as a whole, is the root of the non-stoichiometric behaviour and in turn the defect structures. So much so, that at low temperatures, there is the ordering of oxygen vacancies forming ordered fluorite based phases, Ce_nO_{2n-2m}. This is of such importance that two main approaches have been developed.[51,52]

A simple way in which we can represent how defects can be modelled in ceria is locating oxygen ions within a tetrahedral coordination of cerium ions whereas cerium cations are FCC. When looking at the tetrahedral coordinated oxygen sites, there is a sub formula of $Ce_{0.5}O$, therefore if oxygen is removed from the lattice, it creates a $Ce_{0.5}V^{\cdot\cdot}$ subunit, with a positive charge, where $V^{\cdot\cdot}$ is a defect. This causes the ions to adjust[52,53] their position within the unit cell e.g. oxygen anions contract by 0.3 Å in the vicinity of a vacancy though cerium cations will expand by 0.15 Å around the oxygen vacancy. Still, this is a simplistic viewpoint as this is under the assumption of a point defect at one site, whereas this is extended the NN oxygen ions, i.e. a $Ce_{0.5}V^{\cdot\cdot}$ sub unit is surrounded by 6 $Ce_{0.5}O$ sub units which would result in an overall formula of $Ce_{3.5}O_6V^{\cdot\cdot}$ i.e. $CeO_{1.714}$. Stoichiometric ceria would consist of 7 sub units put together giving Ce_4O_8 i.e. CeO_2. Hence we can describe Ce_nO_{2n-2m} by combining Ce_4O_8 and $Ce_{3.5}O_6V^{\cdot\cdot}$.[54–56] The structures formed following these principles:

1. Cation sub lattice will relax, and stabilises intermediate structures
2. All cerium oxides can be explained by a fluorite structure even is oxygen anions are removed from the lattice and the symmetry is broken.
3. No $Ce_{0.5}V^{\cdot\cdot}$ vacancy subunit can be adjacent to another vacant oxygen site.
4. The CeO_2 system is an ionic compound, so interaction between ions is much greater than that of any covalent nature within the structure.

So far, this has only discussed intrinsic defects, those created by the removal of oxygen from the lattice. This is only one area from which we can approach these materials. In addition to this, extrinsic defects can be incorporated into the fluorite structure by the aliovalent dopants or impurities. The fluorite structure is relatively open and can allow a relatively large level of disorder such as those introduced by intrinsic and extrinsic defects. This creates a high amount of electronic contribution to such properties as conductivity because of the electrons and vacancies created. If an aliovalent ion is doped into the ceria fluorite structure then the following can occur to balance the charges:

1. A vacancy has to be formed
2. The dopant can sit in an interstitial site
3. Cerium cation sits on an interstitial site

Calculations indicate that creating a vacancy within the structure is the most favourable route to balance the charges where the dopant as a ionic radii > 0.8Å.[45]

$$(1-x)CeO_2 + xMO_{1.5} \rightarrow 0.5xV_O^{\cdot\cdot} + (2-0.5x)O_O + xM'_{Ce} + (1-x)Ce_{Ce}$$

For cations < 0.8Å, they can be doped into the structure by their placement on interstitial sites in the fluorite structure.

$$(1-x)CeO_2 + MO \rightarrow xV_O^{\cdot\cdot} + (2-x)O_O + xM''_{Ce} + (1-x)Ce_{Ce}$$

This indicate that if *x* moles of dopant oxide are introduced into the fluorite structure, then *x* moles of Ce (IV) have dopant ions on those sites, hence (1-*x*) moles of Ce (IV) sites are filled by Ce (IV).

Further to this, these vacancies created by the addition of dopants into ceria are associated with the cations within the structure. This is due to the coulombic interaction of the defects due to their respective charges.

$$M''_{Ce} + V_O^{\cdot\cdot} \rightarrow [M''_{Ce}V_O^{\cdot\cdot}]$$

In addition to the inclusion of ionic species into the ceria lattice, ceria has wide industrial applications as a support for Platinum Group metals (PGMs). This is due to ceria, as a pure support, having weaknesses such as activity at low temperatures and issues with thermal resistance.[57] Hence developing ceria based catalysts is of great importance so the important OSC characteristics are maintained but providing more stable catalysts. This is normally performed by:

1. Dispersion of PGM or transition metals on the surface.[58]
2. Doping ceria with transition or lanthanide metals.[59–61]
3. Creating mixed metal oxide supports.[62,63]

These types of material can be produced through a number of synthetic methods:

1. Flame Spray Pyrolysis[64]
2. Incipient wetness impregnation[65]
3. Deposition
4. Co-precipitation[66]

Mixed metal oxides at stable at higher temperatures compared to pure ceria whereas the inclusion of dopants into the fluorite structure promotes ceria reduction at lower temperatures. These properties can be enhanced further by the dispersion of transition and PGM on the metal oxide surface. Though this is complicated by numerous factors:[67]

1. Amount of metal present
2. Metal Particle size[68,69]
3. Degree of dispersion[70]
4. Strength of metal-support interaction[71]
5. Surface morphology[72]

The transition metals or PGMs that have been loaded onto ceria normally form a highly dispersed metallic phase (PGM/CeO_2) or metal oxide phase on the surface of the support (PGM-Oxide/CeO_2).[73] These types of systems are well documented and have found to be affected by strong metal support interaction (SMSI) which describes the chemical interactions between the catalyst support and dispersed metal/metal oxide on the surface. This is dependent on both the type of support used and the metal present. This effect was first reported by Tauser *et al.* investigating the reduction of metals supported on titania. This showed that CO and H_2 chemisorption was inhibited though not explicable by poisoning, sintering of metal particles and the encapsulation of metals.[74] This is not only seen for titania, CO adsorption on Pd/CeO_2 has been observed, showing that the presence of Pd favours CO adsorption in comparison to pure ceria support,[75] where the initial PdO phase is reduced to Pd as CO is adsorped onto the PGM oxide. Furthermore, the inclusion of Pd onto ceria creates larger amounts of oxygen defects and Ce (III) ions. These sites interact with Pd surface atoms, causes a stronger Pd-CO bond, indicative of electron transfer from the ceria support to palladium if the samples are treated under hydrogen. This effect is not only observed for Pd, it has been documented to occur for both dispersed Rh and Pt on ceria samples.[76] The effect is, furthermore, dependent on the support on which the PGM is deposited. Typically, these supports can be CeO_2, Al_2O_3, SiO_2, TiO_2 etc. e.g. the conversion temperatures for HC, NO and CO are lower on Pd or Pt on Al_2O_3 in comparison to CeO_2.[77] The turnover frequencies for Pt/CeO_2 are less than those calculated for Pd/CeO_2. Bera *et al.* have calculated that if there is a solid solution of PGM and ceria, that PGM ions substitute

1% of Ce (IV) ions. The Ce (IV) ions are bonded to neighbouring oxide ions, therefore the inclusion of PGM into the lattice, and substitution of Ce (IV) ions, reduces the ceria itself. These experiments show that CO will be adsorbed onto the ceria support at lower temperatures when Pd and Pt ions are present in comparison to a bare support. This effect is enhanced further by dispersing the PGM more thoroughly across the surface of the support.[78] As there is a reduction in the amount of Pt loaded onto the support, the Pt is dispersed to a greater extent. Moreover this effect is less prevalent in either SiO_2 or Al_2O_3 in comparison to CeO_2, showing the importance of both metal and support in their respective interaction. Lower Pt loading results in smaller Pt particle sizes leading to a higher surface area of Pt, enhancing the metal-support interface. If the PGM is oxidised, the interface is via an oxygen bond from the surface oxide layer and the support.[79]

Further to this, the interactions of the reactants and the metal catalyst needs to be taken into account. This describes the best scenario in which a reaction can take place in the presence of a catalysts. The interactions must be of the right strength; it should neither be too strong where the product will not dissociate or too weak where the reactants will not adsorb onto the surface of the catalyst.[80] This is known as the Sabatier principle.

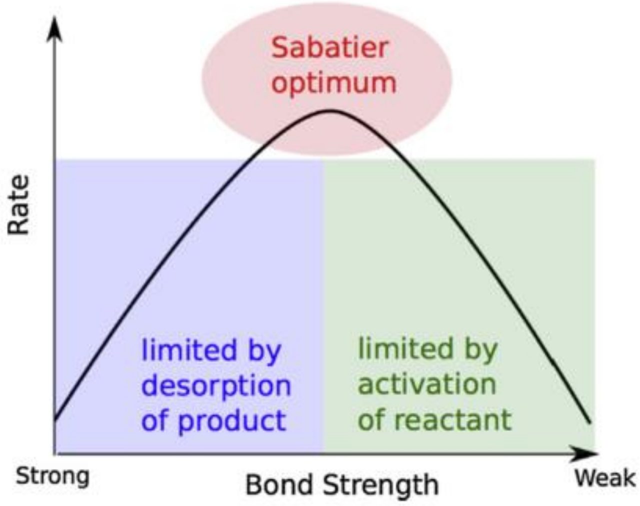

Figure 5: Comparison of bond strength between substrate/catalyst and the rate of reaction. This highlights the optimum area between desorption and adsorption. Adapted from Medford *et al.*[81]

In the case of the interaction of formic acid with metal catalysts, PGMs have the optimum desorbing and adsorption rate leading to the highest rate of reaction in contrast to Au which has the strongest interaction between metal or W where the activation of the reactant is the limiting step.[82]

1.3 Ceria-Zirconia and its structural properties

The understanding of zirconia and zirconia based materials is of importance due to numerous uses in areas such as catalysis,[21,83–85] inert matrix,[86] highly mobile oxygen storage materials,[87–89] chlorine production[90] etc. To understand fully the phase transformation of these materials are of importance as they can be developed to avert unwanted chemical or mechanical transformations when used in 'real world' or 'industrially relevant' applications.[91]

The phase transformation diagram for pure zirconia (at ambient pressure) shows that it can phase change from Cubic to tetragonal at 2640 K and Tetragonal to Monoclinic at 1400 K (Melting at 2979 K).[92]

$$\frac{Cubic}{Fm\bar{3}m} \leftrightarrow \frac{Tetragonal}{P4_2/nmc} \leftrightarrow \frac{Monoclinic}{P2_1c}$$

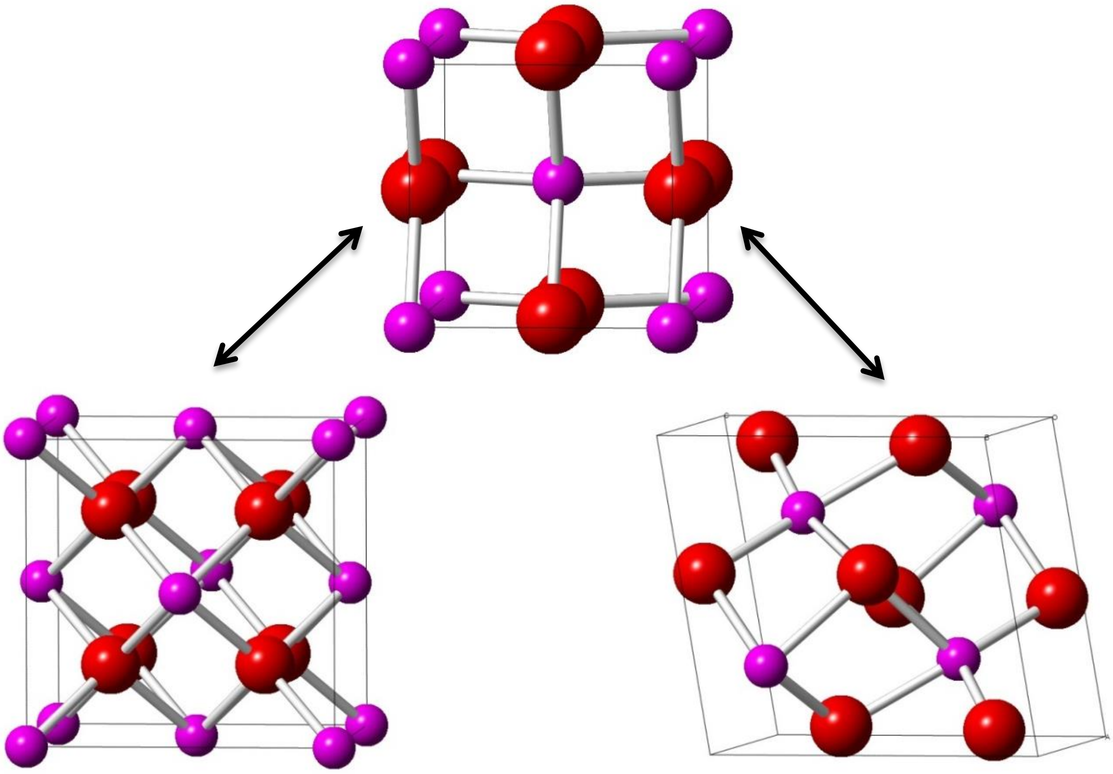

Figure 1-6: Comparison of the varying phases of zirconia Cubic (Left), Tetragonal (Centre) and Monoclinic (Right). (Magenta) Zirconium (Red) Oxygen

As observable from Figure 1-6, for both tetragonal and cubic the Zr atoms present are 8-coorindated whereas for the monoclinic Zr atoms are 7-coordinated. The 7 coordinated Zr atoms are favoured by the ionic radius (0.84 Å)[93] and the covalent nature of Zr-O.[94] The 8-fold coordination of both cubic and tetragonal phase is unfavourable so doping with various valent cations can relieve any stress in the lattice by the formation of oxygen defects/vacancies.[95]

$$xMO_2 + (1-x)ZrO_2 \rightarrow xM_{Zr}^{x} + (1-x)Zr_{Zr}^{x} + 2O_O^{x}$$

$$xMO_{1.5} + (1-x)ZrO_2 \rightarrow xM'_{Zr} + 0.5xV_O^{\cdot\cdot} + (1-x)Zr_{Zr}^{x} + (2-0.5x)O_O^{x}$$

$$xMO + (1-x)ZrO_2 \rightarrow xM''_{Zr} + xV_O^{\cdot\cdot} + (1-x)Zr_{Zr}^{x} + (2-x)O_O^{x}$$

Though in the case of ceria-zirconia systems this is further complicated by the presence of 3 tetragonal phases, t, t' and t'' respectively.[96]

Table 1-1: Comparison of the Ce amount in Ceria-Zirconia, Space group and phase

Composition (% mol Ce in CeO_2-ZrO_2)	**Space Group**	**Phase**
100-80	$\boldsymbol{Fm\bar{3}m}$	**Cubic**
80-65	$\boldsymbol{P4_2/nmc}$	**Tetragonal (t")**
65-30	$\boldsymbol{P4_2/nmc}$	**Tetragonal (t')**
30-10	$\boldsymbol{P4_2/nmc}$	**Tetragonal (t)**
10-0	$\boldsymbol{P2_1c}$	**Monoclinic**

Though this is not an exact rule and materials with phases that do not relate to their respective composition have been observed.[97] As observed in Table 1-1 the structure of the Ceria-Zirconia relates to the parent metal oxide such as a ceria rich material has the cubic or tetragonal structure e.g. the cations occupy the cation sites in the fluorite structure for t".

Redox treatments on CeO_2-ZrO_2 have been investigated widely due to their use in OSC, though due to their metastable structures it can be difficult to rationalise the redox treatments. This is further complicated by any phase segregation during the chemical treatment e.g. oxidising in high tempateratures.[98] The solid solutions formed are also helped by the reduction of some Ce (IV) ions to Ce (III) which aid in ion mobility throughout the lattice and the creating of vacancies.[37] This highlights the fact that the calcination temperature and time must be optimised accordingly, as both variables might influence the final structure of the catalytic material. Vergard's rule would indicate that as less CeO_2 is present within the ceria-zirconia, then the lattice contraction is observed. This is complicated whether the material is high surface area i.e. smaller crystallite size or sintered upon heating. This assumes that the samples are homogeneous throughout, whereas in reality local domains of either Ce- or Zr-rich phases.[99] This has been shown in the calcination of various $CeZrO_4$ materials which have been synthesised via different methods. They show that dependent on synthesis routine, even after calcination full phase segregation does not occur.[100]

In contrast to calcination (under an oxidising environment), heating in a reducing atmosphere does not favour phase separation which has been studied extensively for $Ce_{0.5}Zr_{0.5}O_2$.[101–103] The pyrochlore structure, $Ce_2Zr_2O_7$, has been by a reduction method.[104] This structure has oxygen atoms occupying 7 of the 8 tetrahedral sites whereas the Ce (III) and Zr (IV) ions occupy the 16c and 16d sites, where the space group is Fd3m. Furthermore a mild reoxidation of the pyrochlore can form an oxygen intercalated, $Ce_2Zr_2O_{7.36}$. [105] High temperature reduction can be viewed as a pyrochlore-type formation with ordered Ce (III) and Zr (IV) ions.

1.4 Disorder and Defects

Disorder can be described as the offset or difference from that of a perfect crystal. Ideally each atom has a set site within a unit cell of a material but in real world applications this is a simplification and the story is different. The main cause of disorder that will be discussed in this thesis, is disorder caused by thermal vibrations and oxygen loss. With the input of thermal energy into the system, atoms will move off their ideal site in the structure. This is a well characterised structural property and a refinable parameter in numerous types of analytical techniques, even if a material is described as crystalline.

A crystalline material is a material where the atoms are positioned in a periodic and ordered 3D arrangement. The periodic arrangement of the atoms within the crystal is at the heart of the study. The unit cell which forms the basis of a crystal is a descriptor for the atoms present and how they are arranged. These unit cells belong to one of 7 lattice types which is then further refined to one of 230 space groups. Therefore for the arrangement of a crystal, only need 4 basic elements:

1. The space group
2. The dimensions of the unit cell i.e. a, b, c and α, β, γ
3. The locations of the atoms in the asymmetric unit cell
4. The types of atoms present

In the case of ceria, the space group is $Fm\overline{3}m$, a = 5.411561 Å, cerium and oxygen atoms are present and the atoms are located at 0, 0, 0 and 0.25, 0.25, 0.25 respectively.

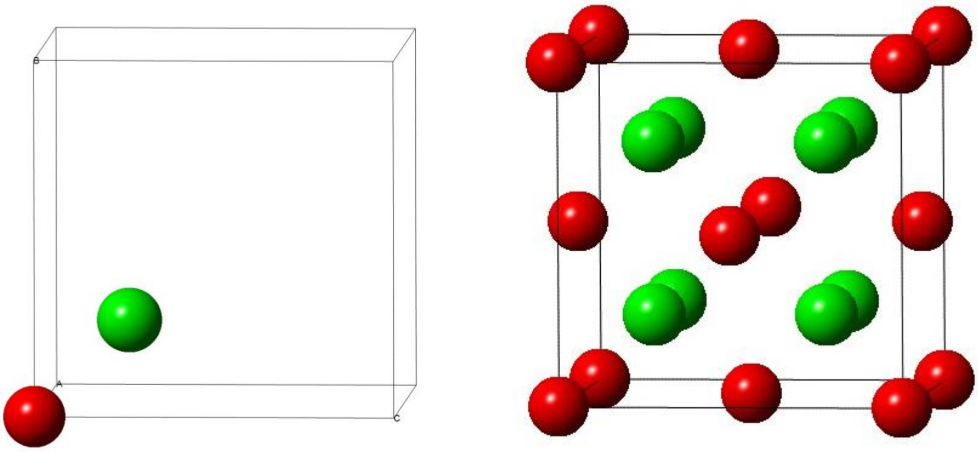

Figure 1-7: Cerium (Red) Oxygen (Green) (Left) Cerium and Oxygen atoms placed at 0, 0, 0 and 0.25, 0.25, 0.25 respectively (Right) The ceria fluorite structure unit cell after the appropriate space group has been applied to the basic structure

These regular arrangement of atoms make crystalline materials perfect structures that can be characterised using diffraction based analysis with either x-rays or neutrons (as described later in this thesis).

In an ideal system all atoms would be fixed to their optimum sites within the crystal and all structures would be relatively well understood. In the real world this is not the case and disorder might arise within the crystal structure. Understanding the disorder present is important as materials that are disordered might have differing characteristics that make them useful in real world applications.

The most ‘basic’ form of disordering that can occur within crystalline materials is those caused by thermal energy and resulting thermal vibrations. This describes how the atoms present in the crystal might be offset from their ideal positions within the unit cell, though on average would be seen to occupy their ideal positions. This can be described in a basic fashion as an isotropic offset i.e. offset by the same amount in all axes, or an anisotropic offset where the offset from the ideal site is dependent on the axis. Either of these are parameters that can be modelled by diffraction based methods i.e. atoms offset from their ideal position leads to the loss of intensity in the Bragg peaks (as the concentration of atoms in the specific Miller plane is reduced)

After thermal motion in a crystal, the next form of disorder present in the materials described in this thesis would be partial occupancy of certain atom types and positions within the unit cell. This can be described as Point defects which are 0 dimension defects, which related to single site and relate to the atom. The main point defect that might occur is those caused by the reduction of cerium and the loss of oxygen from the lattice creating a vacant oxygen site.

$$O_o \rightleftharpoons O_i'' + V_o^{\cdot\cdot}$$

Kröger-Vink notation[44] gives a useful description of what defects are being formed and where these defects are placed and what interstitial ions are created. In the case of ceria, oxygen moves from its ideal position (the tetrahedral site in the fluorite structure) into an interstitial position[106] creating a vacant oxygen site with a net charge.

Disorder in crystalline materials can further be made more complex by 1 and 2 dimension defects where 1-dimension defects can be e.g. dislocations, or 2-dimension defects can be e.g. grain boundaries, antiphase domains etc.

This is further complicated as crystals might not repeat themselves *ad infinitum* and the bulk properties of the probed material might not represent how the crystal and the respective disorder occurs over different structural lengths i.e. the short-, medium- and long-range structure. For example in the case of Ceria-Yttria systems it has been found that the local structure i.e. first co-ordination shells does not give consistent results with results to analysis of the bulk structure (through reciprocal space analysis).[107]

In addition disorder can be obscured further by the creation of nanocrystal or nanocrystalline systems. These are made up of crystals with nano-sized domains or nanoparticles i.e. particulates in the nano-sized region (< 100 nm in one dimension or more) which can be demonstrated by electron microscopy (resulting in images of the nano particles or nano-sized domains) or via Bragg diffraction. This is due to a significant deviation from the Bragg angle, leading to peak broadening and can be measured using the Scherrer Equation (though this is approximate and relies on other factors).[108]

1.5 Characterisation of Ceria

Within materials chemistry there are numerous techniques that can be applied to the materials in order to investigate how these work. Within the lab there are numerous techniques that can be used:

- X-ray diffraction (XRD)
- Neutron Diffraction (ND)
- X-ray Absorption Spectroscopy (XAS) split into X-ray absorption near edges spectroscopy (XANES) and Extended x-ray absorption fine structure (EXAFS)
- X-ray and neutron total scattering

6.5.1 XAS and Defect structures

Both XANES and EXAFS are important techniques for the investigation of defects present in metal oxides. XANES can be used to investigate electronic configuration and coordination number of the probed atom present in the samples whereas EXAFS allows us to computationally model the coordination environment of the metal present in the metal oxide (or look at any dopants that have been added and how these influence defects within the material).

The cerium L_3-edge is an absorption edge that is probed. This looks at the excitation of 2p level electrons. The XANES features relate to the electronic transitions to empty bound states (below the vacuum level) and to the continuum. The former are not seen for ceria but the latter are responsible for the peaks and shoulders observed at the absorption energy. The dipole selection rules dictate which excitations are allowed, in this case, there is a transition from $2p_{3/2}$ to $5d_{5/2,3/2}$.[109] The EXAFS region extends beyond the XANES region, probing the continuum with higher energies, although the case of cerium L_3-edge is hindered by the close Ce L_2-edge, truncating the region that can be used in the analysis.

A great example of how EXAFS and XANES can be used to successfully model defects within a doped ceria is “Defect structures in doped CeO_2 studied by using X-ray absorption spectrometry” by S. Yamazaki *et al.*[110] This looks at the doping of ceria with numerous transition metals and Lanthanides.

$$\mathrm{Ce_{1-x}Ln_xO_{2-}}{}^{x}\!/_{2} \text{ where } \mathrm{Ln} = \mathrm{Sc, Y, Nd, Sm, Gd} \text{ and } \mathrm{Yb} \text{ where } \mathrm{x} = 0 \rightarrow 0.3$$

The doping of ceria is important since at low concentrations, an increase in dopant will increase the ionic conductivity[111,112] which is important when e.g. used within solid electrolytes. When the dopants are added to the ceria, a trivalent dopant ion substitutes a tetravalent cerium ion which introduces an oxide vacancy for every second dopant ion that is added. With these free oxygen vacancies accounting for the increase of the electrical conductivity though at high dopant levels these O-vacancies become ordered and there are associations between these vacancies and the dopants.

At this stage this is where EXAFS is an important tool in studying how these dopants affect defects within the host material. EXAFS has the ability to look at the distance between different coordination shells and show whether the amplitude of these peaks change i.e. whether coordination number is affected by the introduction of dopants and whether these create vacancies.

An example of how EXAFS can be used to look at disorder caused by the introduction of Yttrium into ceria. The EXAFS shows a decreasing in interatomic distances for Ce-(Ce,Y) as dopant levels increase which is similarly seen for Y-(Y,Ce) interatomic distances. This is due to the disorder of the cation sub lattice by substitution. Further use of EXAFS shows that Y-O interatomic distances decrease as dopant levels increase which would suggest oxide ions in the vicinity of oxygen vacancies are relaxed thus shortening both Ce-O and Y-O interatomic distances. This EXAFS data in conjunction with a defect cluster model also allows a visual representation of the defects present within these doped materials (Figure 1-8).

The analysis indicates that the dopant cations and oxygen vacancies are in positions that are differing to the ideal lattice sites as well as the oxygen vacancies being favoured near the trivalent dopant cations.

XANES on the other hand helps determine the oxidation state of the metals present within the material, presenting more evidence on what is happening within the material. In the case of Yamazaki *et al*[110] the Ce-L$_3$ data of the doped samples was compared to those of pure ceria and cerium phosphate (CePO$_4$) shows that the cerium present in the system is Ce (IV).

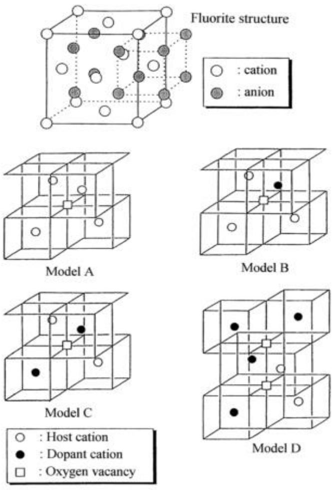

Figure 1-8: A visual representation of defects found within doped ceria. (Adapted from Yamazaki *et al*[110]

This is similarly seen in “X-ray absorption studies of ceria with trivalent dopants” by Li *et al*.[113] EXAFS was used to investigate the influence that scandium doping would have on ceria and gadolinium doped ceria respectively. For example, the EXAFS for scandia doped ceria shows that Sc (III) ions replace Ce (IV) ions, these are randomly distributed throughout the crystal structure forming a solid solution whereas when scandium was introduced into gadolinium doped ceria, there was the formation of Sc-O clusters since Gd (III) ions form oxygen vacancies which Sc (III) have a strong scavenging effect on these vacancies.

Similarly the XANES data shows that the coordination environment for Sc (III) has changed in comparison to known standards.

Furthermore, the inclusion of Pd into ceria has been investigated by Walton *et al*.[114]This probed the inclusion of Pd into the ceria fluorite structure by hydrothermal synthesis sand the relative stability of these materials using XRD and EXAFS. Analysis of the Pd K-edge EXAFS showed that the Pd (II) ions are located in an interstitial site with a square planar geometry, centred between four oxygen atoms. This was supported by TEM and theoretical studies. Additionally the insertion of more Pd into the lattice, decreases the reduction temperature though after prolonged heating Pd is leached from the ceria lattice forming dispersed metallic Pd.

1.5.2 Pair Distribution Function

Both XAFS and PDF show the distance and coordination number for different shells but using different methods. Where XAFS uses the interaction of X-rays of different energies to find an absorption edge in order to see the changes in absorption co-efficient, the PDF uses a Fourier transform of the total scattering diffraction pattern. This is of note as the diffraction pattern gives the average, periodic structure for the material but once it has been analysed gives both short and long range structural correlations.[115]

In the same manner in which EXAFS has been used to look at the defects that are introduced by dopants, PDF has been successfully utilised (both x-ray and neutron diffraction) to investigate how the doping of ceria with yttria. “Local disorder in Yttrium doped ceria ($Ce_{1-x}Y_xO_{2-x/2}$) probed by joint x-ray and neutron powder diffraction” by Coduri *et al*[107] investigates how doping with yttria affects vacancies within ceria and how it influences interatomic distances. This shows that when ceria is doped with yttria certain interatomic distances shorten. There are other coordination environments that increase in distance which suggests that, when doped, the disorder is spread over a long range which cannot be seen using only EXAFS. An interesting observation is with neutron diffraction which be used to calculate O-O interatomic distances whereas EXAFS is unable to ‘see’ the oxygen atoms.

This ability to see oxygen is important within neutron diffraction experiments since this allows the observation of interstitial oxygen within the metal oxide material. In “Structural defects in a nano-scale powder of CeO_2 studied by pulsed neutron diffraction” by Mamontov and Egami,[106] the use of Rietveld refinement of the neutron diffraction data and PDF analysis shows that there are interstitial oxygen defects within the fluorite structure of ceria and these oxide ions provide the mobility that allows ceria to act as an oxygen store for catalysis.

Even though PDF is a very important and useful technique in the studying of both short range and long range ordering in materials, it is not element sensitive in comparison to EXAFS. Therefore if the material contains ions with similar sized ionic radii e.g. Ce (IV) and Gd (III) then it is difficult to separate the influences of Ce (IV) and Gd (III) ions respectively. In "Differential Pair Distribution Function applied to $Ce_{1-x}Gd_xO_{2-x/2}$ system" by Allieta *et al*[116] discusses the use of the application of anomalous X-ray diffraction technique to total scattering thus giving the Differential Pair Distribution Function (DPDF). A comparison of the DPDF data against the PDF data for gadolinia and ceria shows that there is no Gd-Gd peak present in the materials tested (and for comparison the ceria sample) therefore Gd(III) ions must contribute to the to the G(r) function.

1.6 Aims and Objectives

The main aim of this work is to develop the understanding of ceria and related materials through the investigation of the short-, medium- and long-range structure employing suite of X-ray and neutron based techniques.

The initial work was to investigate pure ceria systems and how the variation in synthetic procedure may influence the structure from the short to long range and how using different radiation sources i.e. x-ray or neutrons might show any differences caused by the synthetic procedure. This formed a solid basis of understanding of both the techniques and the ceria systems themselves before allowing more complicated investigation into ceria based catalysts.

Secondly, the incorporation of PGMs onto a ceria support was investigated, and how the use of PGMs can influence the catalytic behaviour of these materials. This was carried out using a suite of *in-situ* x-ray and neutron characterisation techniques to probe both the overall structure and the migration of oxide ions through the fluorite structure under reducing conditions.

Finally, the phase transformation of ceria-zirconia pyrochlore and fluorite structures was investigated using x-ray *in-situ* XRD to investigate the structure of the materials under real world conditions.

1.7 Bibliography

1 R. Schlögl, *Angew. Chemie - Int. Ed.*, 2015, **54**, 3465–3520.

2 J. Hagen, *Industrial Catalysis: An integrated Approach*, Wiley-VCH, 2006.

3 B. A. Averill, J. A. Moulijn, R. A. van Santen and P. W. N. M. van Leeuwen,

Catalysis: An Integrated Approach, Elsevier, 2nd edn., 2000.

4 J. J. McKetta Jr, *Chemical Processing Handbook*, CRC Press, 1993.

5 J. N. Armor, *Catal. Today*, 2011, **163**, 3–9.

6 F. Zaera, *Chem. Soc. Rev.*, 2013, **42**, 2746–2762.

7 P. B. Weisz, *Annu. Rev. Phys. Chem.*, 1970, **21**, 175–196.

8 R. J. Farrauto and R. M. Heck, *Catal. Today*, 1999, **51**, 351–360.

9 J. Kašpar, P. Fornasiero and N. Hickey, *Catal. Today*, 2003, **77**, 419–449.

10 A. Trovarelli, Ed., *Catalysis by Ceria and Related Materials*, Imperial College Press, London, 2002.

11 A. Trovarelli, C. De Leitenburg, M. Boaro and G. Dolcetti, *Catal. Today*, 1999, **50**, 353–367.

12 V. A. M. Selvan, R. B. Anand and M. Udayakumar, *ARPN J. Eng. Appl. Sci.*, 2009, **4**, 1–6.

13 Z. Ma and F. Zaera, in *Encyclopedia of Inorganic Chemistry*, John Wiley & Sons, Ltd, 2006.

14 T. Johnson, *Platin. Met. Rev.*, 2008, **52**, 23–37.

15 M. V Twigg, *Platin. Met. Rev.*, 2003, **47**, 157–162.

16 M. V Twigg, *Platin. Met. Rev.*, 2003, **47**, 15–19.

17 H. Renner, G. Schlamp, I. Kleinwächter, E. Drost, H. M. Lüschow, P. Tews, P. Panster, M. Diehl, J. Lang, T. Kreuzer, A. Knödler, K. A. Starz, K. Dermann, J. Rothaut, R. Drieselmann, C. Peter and R. Schiele, in *Ullmann's Encyclopedia of Industrial Chemistry*, Wiley-VCH Verlag GmbH & Co. KGaA, 2000.

18 J. A. Rabo, *Catal. Today*, 1994, **22**, 201–234.

19 D. Astruc, in *Nanoparticles and Catalysis*, Wiley-VCH Verlag GmbH & Co. KGaA, 2008, pp. 1–48.

20 M. E. Dry, *Catal. Today*, 2002, **71**, 227–241.

21 H. Shinjoh, *J. Alloys Compd.*, 2006, **408–412**, 1061–1064.

22 H. S. Gandhi, G. W. Graham and R. W. McCabe, *J. Catal.*, 2003, **216**, 433–442.

23 U. Bardi and S. Caporali, *Minerals*, 2014, **4**, 388–398.

24 R, *Handb. Heterog. Catal.*, 1997, 1569–1595.

25 R. Di Monte, P. Fornasiero, J. Kašpar, P. Rumori, G. Gubitosa and M. Graziani, *Appl. Catal. B Environ.*, 2000, **24**, 157–167.

26 J. Sun, J. Desjardins, J. Buglass and K. Liu, *Int. J. Hydrogen Energy*, 2005, **30**, 1259–1264.

27 N. Schumacher, A. Boisen, S. Dahl, A. Gokhale, S. Kandoi, L. Grabow, J. Dumesic, M. Mavrikakis and I. Chorkendorff, *J. Catal.*, 2005, **229**, 265–275.

28 S. Hilaire, X. Wang, T. Luo, R. J. Gorte and J. Wagner, *Appl. Catal., A*, 2001, **215**, 271–276.

29 A. F. Ghenciu, *Curr. Opin. Solid State Mater. Sci.*, 2002, **6**, 389–399.

30 P. B. Rasmussen, P. M. Holmblad, T. Askgaard, C. V Ovesen, P. Stoltze, J. K. Norskov and I. Chorkendorff, *Catal. Lett.*, 1994, **26**, 373–381.

31 M. Maack, H. Friis-jensen, S. Sckerl, J. H. Larsen and I. Chorkendorff, *Top. Catal.*, 2003, **22**, 151–160.

32 Q. Fu, H. Saltsburg and M. Flytzani-Stephanopoulos, *Science (80-.).*, 2003, **301**, 935–938.

33 F. Garin and O. Maire, 1997, **149**, 245–256.

34 T. R. Reina, W. Xu, S. Ivanova, M. Á. Centeno, J. Hanson, J. A. Rodriguez and J. A. Odriozola, *Catal. Today*, 2013, **205**, 41–48.

35 R. Jain, A. S. Poyraz, D. P. Gamliel, J. Valla, S. L. Suib and R. Maric, *Appl. Catal. A Gen.*, 2015, **507**, 1–13.

36 Ç. Odabaşı, M. E. Günay and R. Yildirim, *Int. J. Hydrogen Energy*, 2014, **39**, 5733–5746.

37 H. Chiang, R. Blumenthal and R. Fournelle, *Solid State Ionics*, 1993, **66**, 85–95.

38 G. Brauer and K. A. Gingerich, *J. Inorg. Nucl. Chem.*, 1960, **16**, 87–99.

39 R. D. Shannon, *Acta Crystallogr. Sect. A*, 1976, **32**, 751–767.

40 A. Laachir, V. Perrichon, A. Badri, J. Lamotte, E. Catherine, J. C. Lavalley, J. El Fallah, L. Hilaire, F. Le Normand, E. Quemere, G. N. Sauvion and O. Touret, *J. Chem. Soc. Faraday Trans.*, 1991, **87**, 1601–1609.

41 M. A. Panhans and R. N. Blumenthal, *Solid State Ionics*, 1993, **60**, 279–298.

42 D. J. M. Bevan and J. Kordis, *J. Inorg. Nucl. Chem.*, 1964, **26**, 1509–1523.

43 J. Campserveux and P. Gerdanian, *J. Solid State Chem.*, 1978, **23**, 73–92.

44 F. A. Kröger and H. J. Vink, *Solid State Phys.*, 1956, **3**, 307–435.

45 L. Minervini, *Solid State Ionics*, 1999, **116**, 339–349.

46 R. N. Blumenthal, P. W. Lee and R. J. Panlener, *J. Electrochem. Soc.*, 1971, **118**, 123–129.

47 H. L. Tuller and A. S. Nowick, *J. Electrochem. Soc.*, 1979, **126**, 209–217.

48 B. C. H. Steele and J. M. Floyd, *Proc. Brit. Ceram. Soc.*, 1971, **19**, 55–76.

49 J. Faber, A. Seitz and M. H. Mueller, *J. Phys. Chem. Solids*, 1976, **37**, 909–915.

50 J. Faber, M. A. Seitz and M. H. Mueller, *J. Phys. Chem. Solids*, 1976, **37**, 903–907.

51 B. F. Hoskins and R. L. Martin, *Aust. J. Chem.*, 1995, **48**, 709–739.

52 Z. C. Kang, J. Zhang and L. Eyring, *Z. Anorg. Allgem. Chem.*, 1996, **622**, 465–472.

53 S. P. Ray and D. E. Cox, *J. Solid State Chem.*, 1975, **15**, 333–343.

54 Z. C. Kang and L. Eyring, *Aust. J. Chem*, 1996, **49**, 981–996.

55 Z. C. Kang and L. Eyring, *J. Alloy. Compd.*, 1997, **249**, 206–212.

56 Z. C. Kang and L. Eyring, *J. Alloy. Compd.*, 1998, **277**, 30–36.

57 S. J. Schmieg and D. N. Belton, *Appl. Catal. B Environ.*, 1995, **6**, 127–144.

58 K. R. Priolkar, P. Bera, P. R. Sarode, M. S. Hegde, S. Emura, R. Kumashiro and N. P. Lalla, *Chem. Mater.*, 2002, **14**, 2120–2128.

59 D. A. B. and T. H. G. M. D. Salazar-Villalpando, *Int. J. Hydrogen Energy*, 2008, **33**, 2695–2703.

60 G. G. and M. G. P. Vidmar, P. Fornasiero, J. Kaspar, *J. Catal.*, 1997, **171**, 160–168.

61 V. A. Sadykov, N. N. Sazonova, A. S. Bobin, V. S. Muzykantov, E. L. Gubanova, G. M. Alikina, A. I. Lukashevich, V. A. Rogov, E. M. S. E. N. Ermakova, N. V. Mezentseva, S. A. V. E. G. Zevak, M. Muhler, C. Mirodatos, Y. Schuurman and A. C. V. Veen, *Catal. Today*, 2011, **169**, 125–137.

62 E. G. and M. P. C. Bozo, N. Guilhaume, *Catal. Today*, 2000, **59**, 33–45.

63 S. E. D. and O. T. H. W. Jen, G. W. Graham, W. Chun, R. W. McCabe, J. P. Cuif, *Catal. Today*, 1999, **50**, 309–328.

64 H. Oh and S. Kim, *J. Aerosol Sci.*, 2007, **38**, 1185–1196.

65 R. V. Gulyaev, A. I. Stadnichenko, E. M. Slavinskaya, A. S. Ivanova, S. V. Koscheev and A. I. Boronin, *Appl. Catal. A Gen.*, 2012, **439–440**, 41–50.

66 L. Qiu, F. Liu, L. Zhao, Y. Ma and J. Yao, *Appl. Surf. Sci.*, 2006, **252**, 4931–4935.

67 M. Valden, X. Lai and D. W. Goodman, *Science (80-.).*, 1998, **281**, 1647–1650.

68 Y. Zhang, M. L. Toebes, A. van der Eerden, W. E. O'Grady, K. P. de Jong, D. C. Koningsberger and W. E. O'Grady, *J. Phys. Chem. B*, 2004, **108**, 18509–18519.

69 J. H. Holles, R. J. Davis, T. M. Murray and J. M. Howe, *J. Catal.*, 2000, **195**, 193–206.

70 X. Chen, J. Chen, Y. Zhao, M. Chen and H. Wan, *Chinese J. Catal.*, 2012, **33**, 1901–1905.

71 J. Fan, X. Wu, R. Ran and D. Weng, *Appl. Surf. Sci.*, 2005, **245**, 162–171.

72 S. Damyanova and J. M. . Bueno, *Appl. Catal. A Gen.*, 2003, **253**, 135–150.

73 R. K. B. and H. S. G. J. Z. Shyu, K. Otto, W. L. H. Watkins, G. W. Graham, *J. Catal.*, 1988, **114**, 23–33.

74 S. J. Tauster, S. C. Fung and R. L. Garten, *J. Am. Chem. Soc.*, 1978, **100**, 170–175.

75 D. T. and F. B.-V. A. Bensalem, J.-C. Muller, *J. Chem. Soc., Faraday Trans.*, 1996, **92**, 3233–3237.

76 S. R. and M. S. Hegde, *Catal. Commun.*, 2008, **9**, 811–815.

77 G. N. S. and M. S. H. P. Bera, K. C. Patil, V. Jayaram, *J. Catal.*, 2000, **196**, 293–301.

78 M. S. C. and H. L. W. X. N. Chen, J. Y. Chen, Y. Zhao, *Chinese J. Catal.*, 2012, **33**,

1901–1905.

79 S. A. and D. W. G. M. S. Chen, Y. Cai, Z. Yan, K. K. Gath, *Surf. Sci.*, 2007, **601**, 5326–5331.

80 A. A. Balandin, *Adv. Catal.*, 1969, **19**, 1–210.

81 A. J. Medford, A. Vojvodic, J. S. Hummelshøj, J. Voss, F. Abild-Pedersen, F. Studt, T. Bligaard, A. Nilsson and J. K. Nørskov, *J. Catal.*, 2015, **328**, 36–42.

82 W. J. M. Rootsaert and W. M. H. Sachtler, *Zeitschrift für Phys. Chemie*, 1960, **26**, 16–26.

83 T. Masui, T. Ozaki, K. Machida and G. Adachi, *J. Alloys Compd.*, 2000, **303–304**, 49–55.

84 M. Ozawa, *J. Alloys Compd.*, 1998, **275277**, 886–890.

85 D. Terribile, *Catal. Today*, 1998, **43**, 79–88.

86 K. Ferguson, *Trans. Am. Nucl. Soc.*, 1996, **75**, 75.

87 B. J. Wuensch, K. W. Eberman, C. Heremans, E. M. Ku, P. Onnerud, E. M. E. Yeo, S. M. Haile, J. K. Stalick and J. D. Jorgensen, *Solid State Ionics*, 2000, **129**, 111–133.

88 M. Pirzada, R. W. Grimes, L. Minervini, J. F. Maguire and K. E. Sickafus, *Solid State Ionics*, 2001, **140**, 201–208.

89 P. J. Wilde and C. R. A. Catlow, *Solid State Ionics*, 1998, **112**, 173–183.

90 M. Moser, C. Mondelli, T. Schmidt, F. Girgsdies, M. E. Schuster, R. Farra, L. Szentmiklósi, D. Teschner and J. Pérez-Ramírez, *Appl. Catal. B Environ.*, 2013, **132–133**, 123–131.

91 M. Yashima, M. Kakihana and M. Yoshimura, *Solid State Ionics*, 1996, **86–88**, 1131–1149.

92 M. Yashima, T. Hirose, M. Kakihana, Y. Suzuki and M. Yoshimura, *J. Am. Ceram. Soc.*, 1997, **80**, 171–175.

93 R. D. Shannon, *Acta Crystallogr. Sect. A*, 1976, **32**, 751–767.

94 S.-M. Ho, *Mater. Sci. Eng.*, 1982, **54**, 23–29.

95 P. Li, I.-W. Chen and J. E. Penner-Hahn, *J. Am. Ceram. Soc.*, 1994, **77**, 118–128.

96 M. Yashima, K. Morimoto, N. Ishizawa and M. Yoshimura, *J. Am. Ceram. Soc.*, 1993, **76**, 1745–1750.

97 P. Fornasiero, G. Balducci, R. Di Monte, J. Kašpar, V. Sergo, G. Gubitosa, A. Ferrero and M. Graziani, *J. Catal.*, 1996, **164**, 173–183.

98 G. Colón, F. Valdivieso, M. Pijolat, R. . Baker, J. . Calvino and S. Bernal, *Catal. Today*, 1999, **50**, 271–284.

99 E. Mamontov, R. Brezny, M. Koranne and T. Egami, *J. Phys. Chem. B*, 2003, **107**, 13007–13014.

100 P. Fornasiero, R. Di Monte, T. Montini, J. Kašpar and M. Graziani, in *12th International Congress on Catalysis Proceedings of the 12th ICC*, eds. S. M. Avelino Corma Francisco V. Melo and J. L. G. Fierro, Elsevier, 2000, vol. 130, pp. 1355–1360.

101 T. Omata, H. Kishimoto, S. Otsuka-Yao-Matsuo, N. Ohtori and N. Umesaki, *J. Solid State Chem.*, 1999, **147**, 573–583.

102 G. Balducci, P. Fornasiero, R. Di Monte, J. Kaspar, S. Meriani and M. Graziani, *Catal. Letters*, 1995, **33**, 193–200.

103 S. Otsuka-Yao-Matsuo, N. Izu, T. Omata and K. Ikeda, *J. Electrochem. Soc.*, 1998, **145**, 1406–1413.

104 J. B. Thomson, A. Robert Armstrong and P. G. Bruce, *J. Am. Chem. Soc.*, 1996, **118**, 11129–11133.

105 J. B. Thomson, A. Robert Armstrong and P. G. Bruce, *J. Solid State Chem.*, 1999, **148**, 56–62.

106 E. Mamontov and T. Egami, *J. Phys. Chem. Solids*, 2000, **61**, 1345–1356.

107 M. Coduri, M. Scavini, M. Allieta, M. Brunelli and C. Ferrero, *J. Phys. Conf. Ser.*, 2012, **340**, 12056.

108 A. L. Patterson, *Phys. Rev.*, 1939, **56**, 978–982.

109 A. V. Soldatov, T. S. Ivanchenko, S. Della Longa, A. Kotani, Y. Iwamoto and A. Bianconi, *Phys. Rev. B*, 1994, **50**, 5074–5080.

110 S. Yamazaki, T. Matsui, T. Ohashi and Y. Arita, *Solid State Ionics*, 2000, **136–137**,

913–920.

111 H. Inaba and H. Tagawa, *Solid State Ionics*, 1996, **83**, 1–16.

112 T. Kudo and H. Obayashi, *J. Electrochem. Soc.*, 1976, **123**, 415–419.

113 P. Li, I.-W. Chen, J. E. Penner-Hahn and T.-Y. Tien, *J. Am. Ceram. Soc.*, 1991, **74**, 958–967.

114 C. I. Hiley, J. M. Fisher, D. Thompsett, R. J. Kashtiban, J. Sloan and R. I. Walton, *J. Mater. Chem. A*, 2015, **3**, 13072–13079.

115 C. A. Young and A. L. Goodwin, *J. Mater. Chem.*, 2011, **21**, 6464–6476.

116 M. Allieta, M. Brunelli, M. Coduri, M. Scavini and C. Ferrero, *Z. Krist. Proc.*, 2011, **2011**, 15–20.

117 https://www.webelements.com/cerium/atoms.html Date Accessed: 06/04/2017

Chapter 2: Experimental methods

2.1 Summary

The main aim and title of this thesis is to understand the defect chemistry of binary and ternary oxides using neutron and synchrotron radiation. Therefore, is necessary to discuss the history and theory behind both synchrotron and neutron radiation and how these can be utilised in the understanding of disorder in materials. Bragg scattering, Total scattering and x-ray absorption spectroscopy (XAS) are all discussed in detail as well as mentioning beamlines utilised throughout this work namely POLARIS at ISIS, ID-11-B at APS, SNBL at ESRF, Dubble at ESRF, BM23 at ESRF and ID15, ESRF.

Historically, Bragg diffraction has been used to investigate materials and how the structure of the crystal present themselves whereas diffuse scattering from the materials has been either ignored and fitted even though this contains a lot of important and relevant information. Similarly, XAS is an important tool in the investigation of the short range structural ordering (or disorder) of materials. These are both powerful techniques, if we have the ability to characterise the short-, medium- and long-range structure simultaneously, we can understand more thoroughly how these materials behave. This leads to the use of total scattering techniques in order to produce a Pair distribution function, allowing the characterisation of the medium range structural characterisation, which cannot be observed through XAS or standard Bragg diffraction techniques. Further to this, if there were to be a methodology by which all these techniques can be incorporated together in the analysis, it would be very formidable in comprehending these materials, allowing each technique to contribute their positive aspects to the characterisation of industrially relevant materials.

2.2 Introduction

The main characterisation techniques used in this project are X-ray absorption spectroscopy, X-ray total scattering technique and Neutron scattering in order to carry out X-ray absorption spectroscopy, it is necessary to have tuneable X-ray source. Similarly, for total X-ray scattering methods, a short wavelength of ca 0.2 Å is required; although scattering experiments can be done at longer wavelength, the usable Q-range will not provide sufficient resolution in the R-space to extract useful structural information. In addition to the above, 'tuneability' and short wavelength, intensity of the X-ray is an important factor to obtain high quality data and also to perform time-resolved measurements. Therefore, it is ideal to use Synchrotron Radiation source as they meet these requirements.

2.3 Overview of Synchrotron radiation

In 1895, Wilhelm Röntgen discovered the X-ray[1] through a series of experiments using modified cathode ray tubes. After this discovery it took until 1947 for Elder *et al* to report an observation of synchrotron radiation (SR)[2] though it had been known since the late 19th century that any charged particle subjected to acceleration will emit electromagnetic radiation (EM radiation).[3,4] The discovery and observation in 1947 of SR was performed on a 70 MeV synchrotron source at General Electric Laboratories.[5] This 'very bright spot of light' was observed by Langmuir[6] after having seen some sparks emitted. At the time, this SR was thought to be more of a scientific novelty[7] rather than the radiation that is utilised daily in the understanding of materials.

Synchrotron sources offer a high powered radiation source which can be used for fast data collection on *insitu* samples using relatively small amounts of sample.[3] It took until the 1950s for synchrotron radiation to go from scientific curio to useful tool. This was performed by Tomboulian and Hartman who used the Cornell Synchrotron in the UV-Region.[8,9]

The initial synchrotron sources (first generation sources) utilised were not purpose built for use in the characterisation of materials. These were normally built for use in high energy physics. They were modified in a manner that they allowed for experiments with EM radiation *e.g.* UV-radiation.[10,11] These initial sources did not have a storage rings. With time, the area of SR, became very useful due to the wavelengths of EM-radiation created. The ability to add a storage ring to the accelerator would be beneficial for studies as this allows the accessibility of numerous types of the EM-radiation. The first purpose built storage ring for SR was Tantalus[12] based at the University of Wisconsin. These synchrotron sources were still undergoing parasitic operation so there were limitations. This lead to the development of the second generation of synchrotron sources, with the Synchrotron Radiation Source at Daresbury Laboratory being the first in the second generation. This clamour for new purpose built facilities lead to the improvement in the techniques used at these facilities such as extended x-ray absorption fine-structure spectroscopy, protein crystallography etc. With the advent of undulators and wigglers whilst also needing to adjust synchrotrons for improved brightness lead to the establishment of third generation synchrotrons. These would be designed to increase the brightness of the beam whilst allowing greater number of undulators.[3] The first of these hard x-ray third generation sources being the European Synchrotron Radiation Facility, opening in 1994. With both the Advanced Photon Source (APS), USA[13] and SPring-8, Japan[14]- coming online a few years later. These synchrotron sources are also complimented by smaller, less expensive, facilities with shorter straight sections and fewer undulators in comparison; an example being Diamond, UK.[15]

Even though, the content of this thesis will relate to the use of SR in the area of catalysis, this is not the only area where SR can be utilised. It can be used in a wide variety of areas such as catalysis, geology, medicine, biology etc.[16–20]

2.3.1 How synchrotron radiation is produced

As previously stated, it had been known since the late 19th century that any charged particle subjected to acceleration will emit electromagnetic radiation (EM radiation).[3,4] Though this took until the 1950s until this could be utilised. The charged particle that is used to create SR is an electron. This travels along a circular path whilst passing through a magnetic field. As this stream of electron passes through the magnetic field it will emit EM radiation (i.e. synchrotron radiation) tangentially to their circular path. The passing through of a magnetic field and emission of radiation leads to a loss of energy therefore the electron energy must be ‘topped up’. This is ensured by the use of a radio frequency cavity (and/or cavities) within the storage ring.

The whole process of creating SR is initiated with the production of electrons from an electron gun. This stream of electrons is then accelerated to higher energies by passing through a linear accelerator (LINAC). For example, the LINAC used at APS will accelerate the electrons to 450 MeV. At this energy it relates to a speed greater than 99.999% of the speed of light, *c*. After this has occurred, the electrons are injected into the booster ring. Within the booster ring they are accelerated to greater speeds (ultra relatavistic speeds). This further accelerated electrons are then injected into the storage ring where they travel in ‘bunches’.

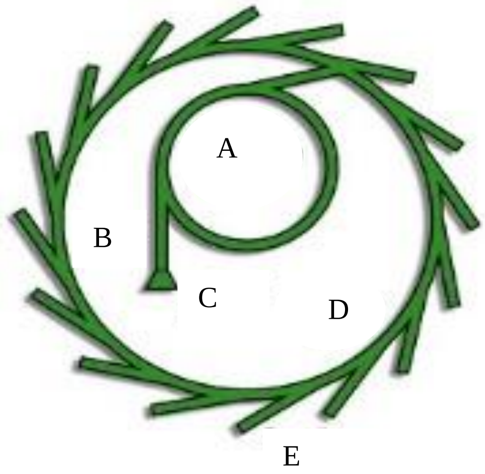

Figure 2-9: A basic schematic diagram of Diamond Light Source.[21] (A) Booster Synchrotron (B) LINAC (C) Electron gun (D) Storage Ring (E) Beamline

This ring is a pipe which is under vacuum where the electrons travel through. In order to ensure that the electrons move in a ring made up of straight sections and bending points, they are restrained in their path by the use of powerful magnets such as a series of quadrupole, hexapole and dipole (bending) magnets. This is being developed further in the case of 4th generation synchrotron light sources. The dipole magnets curve the orbit of the electrons whereas the other magnets keep the path of the beam stable.

The electrons will travel in a straight path unless they come under the influence of an external force. This external force can be split into two categories in which the x-ray is inserted into the beamline either a bending magnet or insertion device. Bending magnets produce a broad spectrum of x-ray wavelengths which is very stable.

These electrons are forced to move in an arc and then make their way down another straight section of storage ring though this bending of the electrons radiates energy in the form of x-ray radiation where it is emitted as the electrons pass along a sweeping trajectory. The radiation is emitted as a cone which has an angular width (in radians) of γ^{-1} where $\gamma=E/mc^2$ with mc^2 the energy of the electron at rest and E being the electron energy.

Insertion devices are further broken down into two sub categories of a wiggler and an undulator. The wiggler produces a cone of radiation where the angular width is greater than γ^{-1} due to the electrons. As the tuning of the magnetic field is dissimilar to that of the frequency of the synchrotron radiation. This ensures that every electron present radiates individually leading to a broad radiation cone. Whereas undulators produce a cone of radiation which is narrower than either a bending magnet or wiggler with an angular width of γ^{-1}. A complex arrangement of magnets induces a transverse oscillation of the electrons.

This ensures a constructive interference between the oscillating electrons and other electrons, narrowing the radiation cone.

The creation of radiation continues throughout the storage ring and these electrons can be circulated, though this time is dependent on the synchrotron and operating mode. Due to the loss of energy through synchrotron radiation at bending magnets and insertion devices, an RF cavity is used to replenish the energy and maintain the bunch coherency. Furthermore, more electrons are injected into the ring to top up their respective number either at a set period of time or in a constant process.

2.4 X-ray Absorption Spectroscopy (XAS)

De Broglie[22] reported the initial observation of an x-ray absorption edge in 1913 and Fricke noted, in 1920,[23] the first measurement of X-ray absorption fine structure in a spectrum. Over the last 100 years, the theory describing XAS has been developed further in order to understand how observations in x-ray absorption spectrums relate to real changes in materials. Kronig[24] put forward the first theory to explain the origins of features relating to the fine structure. The understanding, reported by Kronig, was based on using a bulk crystal structure to justify the presence of oscillations. A disadvantage of this theory is that this is based on the short range structure is similar to that of the long range/bulk material thus leading to short range models being developed.[25] Lyle, Sayers and Stern used the Fourier transform as a tool for analysis showing how the explanation of the fine structure oscillations were due to the short range structure of the material and not the long range structure as first discussed by Kronig. This formed the basis of for the use of EXAFS in routine characterisation of materials using synchrotron radiation, as this radiation source is required to produce high resolution x-rays needed to reveal the weak features in the XANES region and small oscillations in the absorption spectra.

XAS can be used on a variety of materials such as amorphous/highly disordered, crystalline solids and solutions. Since XAS is tuned to specific energies this technique can be used to find trace amounts of an element within a sample and if in sufficient concentration it is possible to extract electronic and structural information. In the work presented, XAFS has been performed where the x-rays are tuned with a monochromator in order to use x-ray energies near or above the core binding energies; this means that the use of synchrotrons is needed. Synchrotrons also have different beam lines that allow different experimental setups to be used *e.g. insitu* XAFS testing with different gas flows and ramping temperatures, allowing us to probe further into how the local environments within a crystal structure influence catalytic performance.

2.4.1 What are XANES and EXAFS

XAS is split up into 2 different areas: Extended x-ray absorption fine structure spectroscopy (EXAFS) and X-ray Absorption Near edge spectroscopy (XANES) (Figure 2-10). Both of these are used to (a) determine oxidation state and (b) coordination environment around a given central absorption atom in any given system, irrespective of its state of matter and concentration. XANES is defined as the region about 10 eV below and ca. 50 eV above the absorption edge of the element. EXAFS data is interpreted above ca. 50 eV above the absorption edge and all the way to ca between 500 and 10000 eV above the edge.

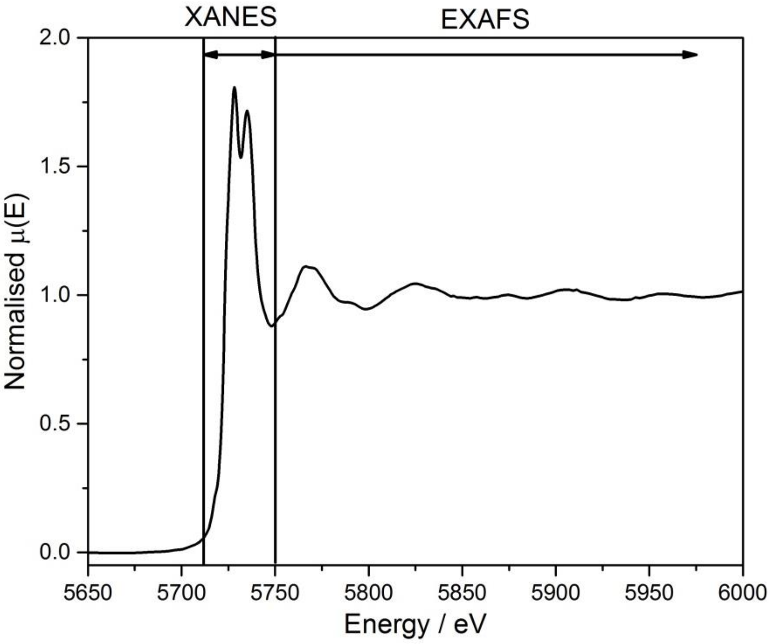

Figure 2-10: XAS spectra are, by convention, split into 2 sections, XANES and EXAFS respectively.

Both EXAFS and XANES work due to the photoelectric effect and the absorption of a photon by a core level electron *e.g.* 1s, 2s or 2p level. For this absorption to take place the energy of the X-ray photon must be greater than the binding energy of the core level electron. When this X-ray photon is absorbed, the electron from the core-level is excited to move to a partially or totally empty higher electron level.

The absorption of X-rays obeys Beer's Law:

$$I = I_0 \exp(-\mu t)$$

where I is intensity transmitted through sample, I_0 is intensity measured before the sample, t is the sample thickness and μ is the absorption co-efficient. The absorption co-efficient is also related to other properties of the sample that is being tested:

$$\mu \approx \frac{\rho z^4}{AE^3}$$

where A is atomic mass, E is X-ray energy, ρ is the density of the sample and z is the atomic number.

This equation shows that in XAFS there is a strong dependence on z and E for the absorption co-efficient. When the X-rays have energy greater than that of the binding energy of the core level electrons the absorption will rise, this edge will correspond to the promotion of the core level electrons to the continuum. These edges are named according to their respective principle quantum number, *n*, of the excited electron.

Table 2-1: Table showing what edge corresponds to which orbital

Edge	**Orbital**
K edge	***1s***
L edge	***2s 2p***

The transition of these excited electrons to higher states is determined by the dipole selection rule, $\Delta l = \pm 1$.

Table 2-2: Table relating the initial states and the states to which they are excited to

Initial State	**Final State**
s	**P**
p	**s,d**
d	**p,f**
f	**d,g**

These edges can further be broken down depending on the core level of the electronic state. For K-edge there is a promotion from 1s (core-level) to an unoccupied state whereas for L-edge there are three possible core-levels from which excited electrons can be promoted from (Table 2-3).

Table 2-3: A table showing how an edge can be further broken down into separate subcategories due to what state the excited electron is found in

L-edge	
L_1	**2s to an unoccupied state**
L_2	**$2p_{1/2}$ to an unoccupied state**
L_3	**$2p_{3/2}$ to an unoccupied state**

Though these selection rules do not always hold true and in some circumstances electrons may be excited to states where $\Delta l \neq \pm 1$ i.e. a 2p → 4f transition. The Laporte rule states that an electronic transition that preserves parity are forbidden in centrosymmetric molecules or atoms. These transitions can be observed if there is a disruption to the centre of symmetry *e.g.* tetrahedral symmetry and distortions in octahedral symmetry due to Jahn-Teller effect.

2.4.2 Fluorescence and Transmission

An excited state can decay by X-ray fluorescence where an electron with a higher energy will fill the hole of a promoted core electron producing an x-ray. These fluorescence energies are characteristic of an element so can be used to identify the elements within a sample and calculate their respective concentrations.

μ(E) is the value measured in XAS and this needs to be as accurate as possible. The XAS is monitored either in a transmittance or fluorescence mode where in transmittance:

$$\mu(E) = \ln \frac{I_0}{I}$$

and in fluorescence:

$$\mu \propto \frac{I_0}{I_f}$$

The XAS can further be monitored by more sophisticated techniques such as measuring drain current or auger electrons. This need to have precise tuning of energies in order to see the main absorption edge for a specific element means that the use of a synchrotron. The set up found within synchrotron facilities allow the choice of wavelength and most importantly a monochromator gives the choice of a specific energy.

For both transmittance and fluorescence, the intensities of the X-rays before and after the sample need to be measured accurately in order to calculate μ(E). For transmittance, ion chambers are used in order to measure the intensities. This is not a difficult process but in order to get accurate results the sample must be homogeneous, be packed properly in order to prevent any pin holes and the element being tested is the major component of the sample. For fluorescence on the other hand, this is the technique used when the element tested is not a major component of the sample being tested or working at relatively low X-ray energies. In comparison to the use of ion chambers for transmittance, in modern SR facilities, fluorescence measurements use a solid state Si or Ge detectors which have the advantage of measuring the whole fluorescence spectra by discriminating the photons from the scattering process.

2.4.3 EXAFS

When the X-rays have energy greater than that of the binding energy of the core level electrons the absorption will increase, this will only occur if there is a partially filled or empty state with appropriate energy and angular moment available for the photoelectron to be promoted. A simple view of this would there would be no sharp absorption edges if the energy of the X-ray is less than the binding energy of the core electrons. In theory this concept is simplistic, if the energy of the X-ray is less than that for 1s electrons, the electron will be promoted to a p orbital less than the binding energy of that electron. However, when sufficient energy is given the excitation process will take place to an electronic state.

This concept only accounts for an isolated atom which in reality is not found in real world conditions. In industrially relevant materials, there are neighbouring atoms around the atom that is being probed. In this model, the photoelectron will be scattered by the electrons in surround atoms and this will return to the atom that is being probed. This scattering will change the absorption co-efficient which is what is seen in XAFS.

The blue line shows how the XAFS would look on a lone atom whereas the red line shows how absorption co-efficient will change with neighbouring atoms scattering the photoelectron giving rise to EXAFS. This is defined by the EXAFS fine structure function:

$$X(E) = \frac{\mu(E) - \mu_0(E)}{\Delta\mu_0(E)}$$

Where $\mu(E)$ is the absorption co-efficient, $\mu_0(E)$ represents the absorption co-efficient of one atom with $\Delta\ \mu_0$ being the jump in $\mu(E)$ at E_0.

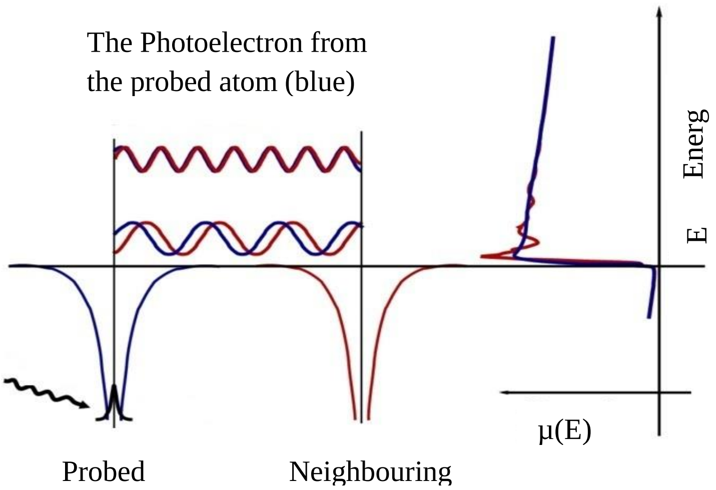

Figure 2-11: A diagram showing a change in the absorption co-efficient giving rise to XAFS.[26]

The varying frequencies, in $\chi(k)$, relates to the coordination environment of the probed element i.e. types and numbers of neighbouring atoms as $\chi(k)$ (Figure 2-11) contains all information from the interference patterns created by the interference of forward scattering waves from the central atom of interest and back scattering waves from the neighbouring atoms. The destructive and constructive interference caused by interaction of forward and back-scattering waves is influenced by the photoelectron energy, therefore modulating μ(E). This results different phase shifts for different atomic species neighbouring the probed atom present in various distances, allowing the characterisation of the local structure.

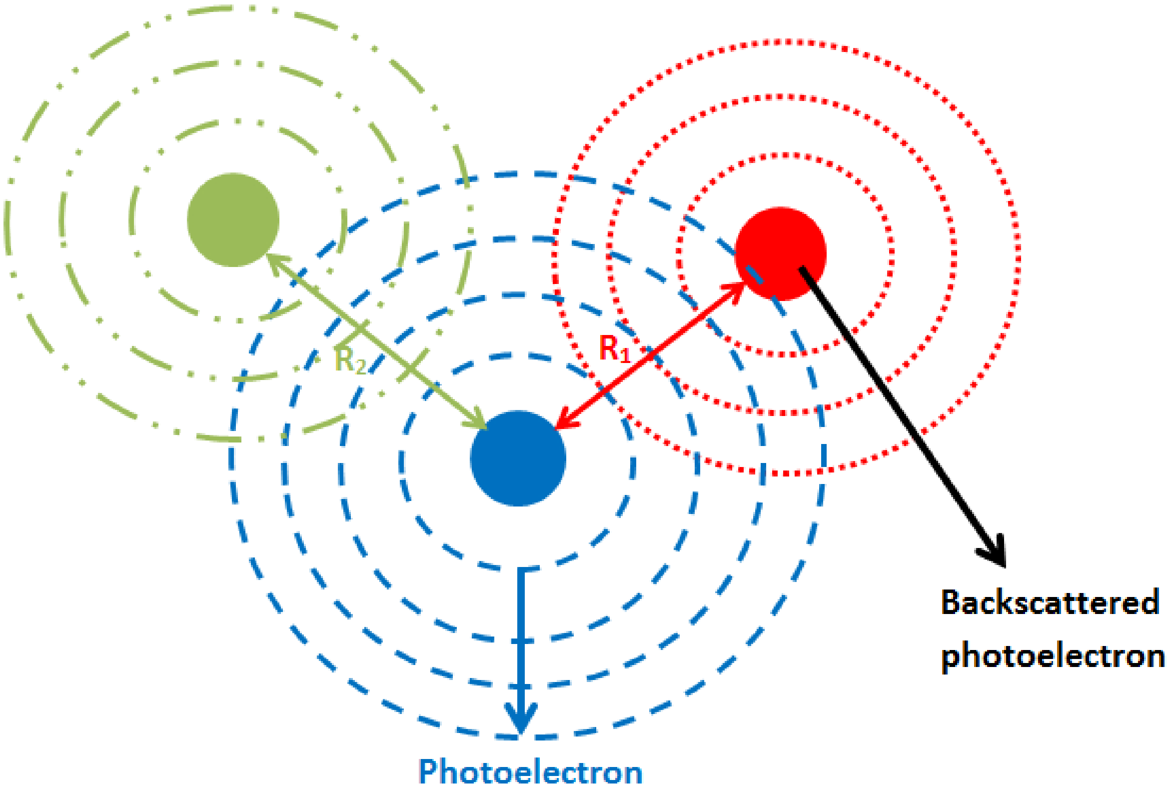

Figure 2-12: A graphical representation of the constructive and destructive interference of the Photoelectron by backscattering atoms (Red and Green respectively) from the central atom (Blue). The blue waves represent the forward scattering wave where the back scattered waves are in red and green, resultant from the neighbouring atoms electron clouds. R_1 and R_2 are the interatomic distances for each atom respectively which can be modelled from the EXAFS equation.

Lytle, Stern and Sayers formulated[27] the EXAFS equation:

$$\chi(k) = \sum_j \frac{N_j f_j(\mathrm{k}) \exp(-2k^2 \alpha_j^2)}{k R_j^2} \sin(2kR_j + \delta_j(k))$$

N is the number of neighbouring atoms with $f_j(k)$ and $\delta_j(k)$ being the back scattering amplitude and phase shift associated with the neighbouring atoms. R is the distance between the excited atom and its respective neighbouring atoms in the jth shell and σ^2 is the square of the mean disorder for R. As a photoelectron is created, this can be seen in terms of waves so the energy of the X-ray is commonly converted to a wave-number, K:

$$k = \sqrt{\frac{2m(E - E_0)}{\hbar^2}}$$

The EXAFS equation has a $1/R^2$ term which means that the amplitude of the higher neighbours decrease rapidly and therefore limited to the study of only few neighbouring shells, so that the local environment of a central absorbing atom can be accurately determined. In order to extract information such as distances for neighbouring shells, accurate values for the Backscattering amplitude factor, $f_j(k)$, and phase shift, $\delta_j(k)$, are needed for analysis. EXAFS is also limited by this being an x-ray based technique as it is influenced by mainly the heavy atoms i.e. the higher the atomic number the more strongly the x-rays are scattered which means that certain elements are difficult to detect *e.g.* hydrogen. This reliance on an interaction between the x-rays and electron density means that isoelectronic neighbouring atoms are difficult to distinguish, for example N and O.

In order to process and fit the EXAFS data both Athena and Artemis[28] data analysis suite of software were used, in this work were used. Athena is used to process the raw XAS data to remove both pre-edge (mass absorption) and post edge (single atom behaviour), Fourier transformations, deglitching etc. whereas Artemis is used to fit the EXAFS data using theoretical models and model the data allowing statistical analysis.

2.4.5 XANES

In comparison to EXAFS, it is difficult to describe XANES in a simplistic way using simple equations. XANES does give important information, nonetheless, on the valence state of the probed atoms and coordination environment.

EXAFS can be modelled theoretically in order to gain a perspective into the coordination environment of the sample; XANES is normally compared against standard materials with definitive oxidation state of the probed atom and coordination environment. This allows the valence of the probed atom to be found and with XANES allowing the use of lower concentrations in comparison to EXAFS; this allows the ability to find the ratio of mixed valent ions where samples have an element present in two valences. This can be further probed by performing calculations using *e.g.* FEFF.[29]

2.4.6 Advantages and Shortcomings of XAS

XAS is a powerful technique in the understanding of short range structural order allowing the understanding of the local coordination environment of the atom being ‘probed’. It allows, with XANES, the comprehension of the electronic structure whereas, with EXAFS, giving the local coordination environment. Due to the information that can be accessed from, XAS is a very effective technique for the understanding of reaction mechanisms in materials that would not be amenable to characterisation techniques such as X-ray diffraction as XAS does not require for the sample to be crystalline (Similarly to total scattering based methodologies). However this does not mean that XAS is the perfect technique for all situations.

- Element specific and therefore provides unique information on the absorbing atom
- Fourier Transform gives partial Radial Distribution Function which enables the determination of local structure specific to the absorbing atom.
- As derived from the XAFS equation there is R^{-2} dependence for the amplitude. This will constrain the distance at which the data can be analysed therefore higher coordination shells cannot be analysed *c.f.* PDF techniques.

2.5 Overview of Neutron radiation

The use of neutron radiation is also used is this work as a complimentary characterisation technique to that of both XAS, x-ray diffraction and total scattering techniques due to the manners in which each radiation source interacts with the atoms. James Chadwick reported the discovery of the neutron[30,31] showing that this radiation was made up of a neutral particle in 1932.

The use of neutron radiation is also used as a complimentary characterisation technique to that of synchrotron X-ray radiation due to its interacting, on average, with low-z scatterers stronger than x-rays. There is no definitive relationship between scattering length and atomic number. The de Broglie wavelength for a neutron is similar to that of the atomic spacing within materials allowing it to be used in diffraction experiments. Neutron radiation is penetrating since neutrons have no electric charge so don’t, in the case of neutron diffraction, interact with electrons *c.f.* X-ray radiation, though they can interact with unpaired electrons for use in magnetic studies. This means that neutron diffraction techniques can locate hydrogen atoms and distinguish isoelectronic atoms. Neutron diffraction techniques are also helpful by the scattering being constant with angle since this depends on a point object whereas x-rays scattering falls off as the angle increases since it is dependent on the volume of the electron density.

The neutron radiation can be produced either as a pulsed source or a neutron source. A pulsed neutron source is produced by the fusion of deuterium and tritium whereas a spallation neutron source is produced by the collision of protons into *e.g.* a tungsten source at ISIS. Generally, neutron diffraction utilises larger samples in comparison to synchrotron x-ray diffraction and for total scattering experiments need longer time than diffraction experiments, limiting *insitu* experimentation.

An example of a purpose built beamline is POLARIS at ISIS. This has the strength of rapid collection of time of flight neutron power diffraction due to the detectors being designed specifically for this purpose and having a high flux of epithermal (0.025 – 0.4 eV) neutrons. This bespoke design has also allowed POLARIS being a very useful beamline for non-ambient conditions such as changes in temperature, gas flow, pressure cells etc.

$$n\lambda = \frac{nh}{mv} = n\frac{h}{m}\frac{t}{L} = 2d\sin\theta$$

Where m is the neutron mass, v is velocity, t is total time of flight and L is the total flight path from the moderator through to the sample through to the detector. The total flight path is set by placing the sample in the sample position with fixed detector banks and t is the total time of flight.

Compared to other beamlines, POLARIS is “resolution focused” so each bank of detectors has the roughly the same resolution but neutrons arrive at these at different times.

This beam line also is optimised for PDF investigation is the use of a “Chopper”. This removes a portion of the neutron beam, the fastest neutrons that are unwanted for total scattering experiments.

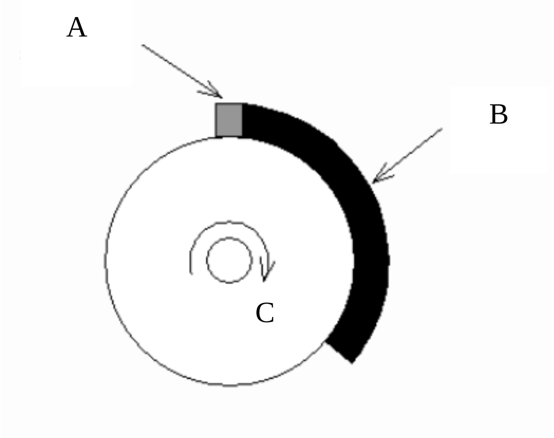

Figure 2-13: Schematic diagram of the Chopper[32] (A) Nimonic alloy block (B) B4C tail cutter (C) Direction of rotation

This chopper is made up of two parts: a nimonic alloy block with a B_4C tail cutter both having separate roles in the chopper setup. The alloy block cuts out the fastest neutrons from the neutron beam as these have very little usage for diffraction experiments but can still be slowed down enough that the can be scattered adding to the background of the experiment.

The tail cutter stops delayed neutrons, there are neutrons going through the moderator with velocities greater than the velocities calculated by arrival time to chopper, from travelling down the beamline to the sample position. The tail cutter also stops frame overlap. This is due to slow neutrons from the first pulse being overtaken by fast neutrons of the consecutive pulse.

Overall powder x-ray/neutron powder or single crystal diffraction are powerful techniques for investigation the long range structure of the materials but if both Bragg and diffuse scattering is corrected and is transformed properly this allows us to access short, medium and long range structural information that previously has only been accessible by the utilisation of numerous characterisation techniques such as XAFS and diffraction techniques.

2.6 Diffraction of X-rays and Neutrons by matter

The first diffraction of materials was performed by Max Von Laue on copper sulphate crystals. He had surmised that a material would diffract x-rays since the distance between atoms is similar to that of the wavelength of x-rays. The photographic plate showed numerous circles centred at the central beam showing the diffraction of the x-rays by the atoms.

The X-rays are scattered by the electron density of the atom (though there is not enough electron density in bonds to be observed) *c.f.* neutrons are scattered by the nucleus of an atom. When these X-rays are scattered there is a change in direction with no loss in energy. Either the atom as a whole (Rayleigh scattering) or a single electron (Thomson scattering) is excited by the X-ray and a vibration emits a photon with the same energy as that of the incident X-ray. As Thomson scattering is due to the scattering of an x-ray by an electron, there is a 1/mass^2 dependence which explains why a nucleus of an atom contributes a negligible amount to the overall scattering of the x-rays.

The work of Von Laue was developed further by William Lawrence and William Henry Bragg which then lead to the derivation of Bragg's law which shows the relationship between the scattering of radiation with the Miller planes within the crystal structure.

2.6.1 Bragg’s Law

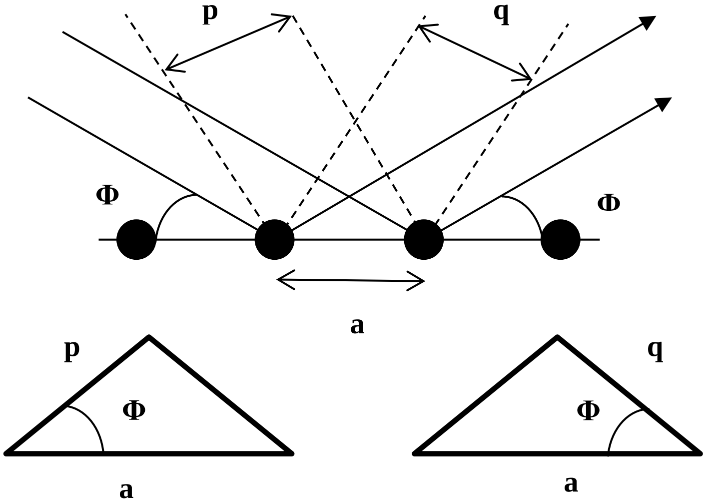

Figure 2-14: Diagram showing the scattering of X-rays by atoms present in a crystal

$$\text{Path difference} = \mathrm{p} - \mathrm{q} = \mathrm{a}\cos\varphi' - \mathrm{a}\cos\varphi$$

In order for constructive interference to occur there must be a whole number of wavelengths (nλ).

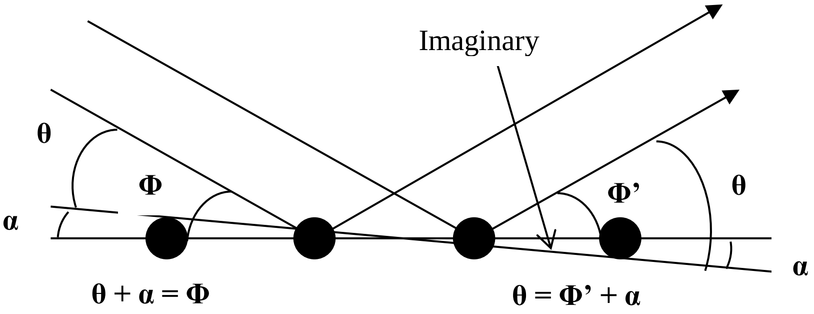

Figure 2-15: The measured angle is between that of the incident and scattered X-rays

The angle α can be related to the distance between these imaginary planes that are equivalent to miller planes within the crystal.

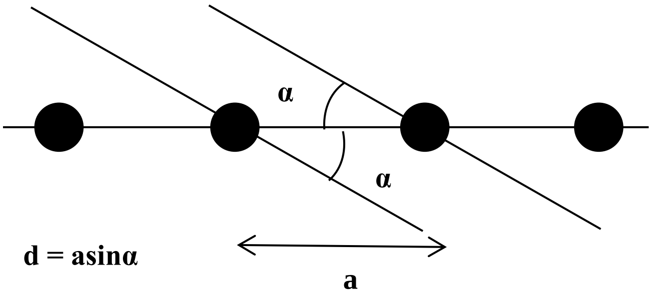

Figure 2-16: The distance between planes can be related to the angle α

$$\text{for constructive interference} = n\lambda = a\cos\varphi' - a\cos\varphi \ \text{ where } \varphi = \alpha + \theta \text{ and } \varphi' = \theta - \alpha$$

$$\therefore a\cos(\theta - \alpha) - a\cos(\theta + \alpha)$$

$$n\lambda = a\cos\theta\cos\alpha + a\sin\theta\sin\alpha - a\cos\theta\cos\alpha + a\sin\theta\sin\alpha = 2a\sin\theta\sin\alpha$$

$$\text{if } \sin\alpha = \frac{d}{a} \therefore 2d\sin\theta = n\lambda \text{ which is known as Braggs'law}$$

Sin θ is measured for each peak and 2θ is the angle found between that of the incident and scattered X-rays

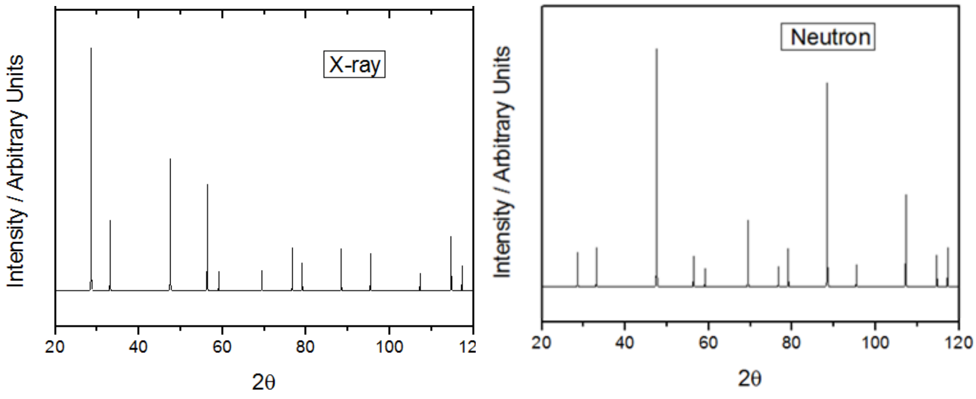

Figure 2-17: A comparison of simulated X-ray and Neutron diffraction patterns for ceria. Showing that different miller indices have different intensities dependent on the concentration, type of atoms present and that x-rays/neutrons interact differently with low-/high-z scatterers

Since the X-ray has a fixed wavelength throughout the experiment this allows the distance between Miller planes to be calculated. Each peak at different 2θ values corresponds to a different miller plane within the crystal structure. The different intensities observed for each peak is due to different concentrations of atoms present in each plane and heavier atoms scatter X-rays more than lighter atoms so contributing to different intensities. This also is affected by any nonspherical deformations of the valence electrons which interact with the x-rays, due to chemical bonding.

The intensities of the peaks can be determined by using the Structure factor. For example, in a centrosymmetric structure *e.g.* ceria:

$$F_{hkl} = \sum_{j=1}^{n} f_j \cos 2\pi(hx_j + ky_j + lz_j)$$

Where (x_j, y_j, z_j) are the coordinates of an atom in the miller plane, j is the number of atoms and f_j is the form factor which describes the scattering power of the atom.

$$\mathrm{I_{hkl}} \propto \mathrm{F_{hkl}^2}$$

$$\mathrm{I_{hkl}} = \mathrm{KL(\theta)p(\theta)A(\theta)m|F_{hkl}|^2}$$

Where *K* is a constant for the material, *L(θ)* is the Lorentz correction accounting for a geometric correction for all reflections, *p(θ)* is the polarisation correction, *A(θ)* is the absorption correction and *m* is the multiplicity correction.

As well as the structure factor having an influence on the intensity, there is an angular dependence on diffraction so at high values of 2θ there is weaker diffraction and symmetry within the crystal structure results in systematic absences.

The structure factor equation is:

$$F(\boldsymbol{S}) = \sum_n f_n \exp\{2\pi i(hx + ky + lz)\}$$

where f_n is the atomic structure factor. This equation can be broken down into a cosine and sine part:

$$F(\boldsymbol{S}) = \sum_n f_n \cos\{2\pi i(hx + ky + lz)\} + F(\boldsymbol{S}) = \sum_n f_n \sin\{2\pi i(hx + ky + lz)\}$$

$$where\ F_{hkl}^2 = (cosine\ part)^2 + (sine\ part)^2$$

Some Bragg peaks may have no intensity due to the symmetry of the unit cell. If there are planes of atoms present between Miller planes there may be some destructive interference of the scattered X-rays.

Neutron or x-ray diffraction can be used in either single crystal or powder modes. Single crystal uses one crystal and then measures the position and intensity of each Bragg peak either in the x, y or z axis allowing a solution to the crystal structure to be computed. In reality most samples are powdered and polycrystalline. The assumption made in powder x-ray diffraction is that there are thousands of crystals randomly orientated so when under an incident ray there every set of Miller planes are observed. Though this is hampered if the sample if amorphous (or nanocrystalline) or have some order of preferred orientation. In the x-ray work recently performed on nanocrystalline samples, this utilised a 2D detector that looks at the cones of diffraction and this is then converted from a 2D image to a graph of intensity vs 2θ (or Q) etc.

Powder diffraction can be utilised mainly as a way of phase identification of the material being tested. Powder diffraction also allows the calculation of the lattice parameter for the material which is a useful piece of information when looking at material *insitu e.g.* changing temperature or pressure to understand what is happening. The shape of the peaks gives useful information on the crystallinity of the material. If the material is highly crystalline then the peaks will be sharp whereas with nanocrystalline samples the peaks broaden, to the extent where these would not be useful in the characterisation of the sample.

A very important and useful use of powder diffraction is the refinement of the crystal structure using Rietveld refinement. A Rietveld refinement uses a least square method to minimise the difference between a calculated diffraction pattern and the experimentally obtained data. This is used as a standard technique to refine parameters such as unit cell size, thermal parameters etc. for crystalline materials but is difficult for amorphous or nanocrystalline materials. An issue with this is the attempt to refine a powder pattern to gain information about a 3D crystal structure. There are other refinements such as Le Bail and Pawley which can refine a theoretical model without a crystal structure giving the lattice parameter.

This is further complicated by peak broadening of the XRD. This can be due to instrumental broadening which depends on 2θ and the experimental set up though this can be resolved by a measurement of a reference. This can also be due to broadening by the sample itself. This can caused by size broadening where the periodic structure of the crystal is finite or by strain broadening caused by imperfections in the lattice such as dislocations, vacancies etc.

This broadening can be useful by allowing estimation in the lower limit of crystallite size using the Scherrer equation.

$$\tau = \frac{K\lambda}{\beta \cos\theta}$$

With K being the shape factor, λ is the wavelength of the X-ray, β is a measure of the line broadening at full width at half the maximum intensity (in radians), θ is the Bragg angle of the peak and τ is the crystallite size. Though as previously stated the peak broadening is influenced by numerous factors such as instrumental factors, strain broadening and defects present therefore this equation can only be used to give an estimate of the lower size of the crystallite present. It is possible to separate the strain and size influences using the Hall-Williamson method.

$$\mathrm{B}\cos(\theta) = \frac{\mathrm{k}\lambda}{\mathrm{D}} + \eta\sin(\theta)$$

Where D is the crystallite size and η is the strain within the crystal. Strain arises within a crystal structure from *e.g.* compression of the crystallite. If the sample is homogeneously strained then the crystal throughout is under the same forces *e.g.* compression. This leads to a shift in the 2θ value of the peaks since there is a change in d spacing. In reality the strain present within the crystal is inhomogeneous so is different throughout the crystal then the 2θ value for the same miller plane will be different therefore the peak will broaden.

Crystallography assumes periodicity within the crystal and that there is a perfect crystal structure i.e. the correct stoichiometry and all atoms are on their ideal positions within the unit cell. These atoms move from their ideal positions either due to zero-point energy or thermally induced vibrations. These displacements from the ideal positions (due to phonons) were derived by Debye and Waller therefore known as Debye-Waller factors (DW-factor).

$$R(t) = u(t) + \langle\langle R \rangle\rangle$$

$$where\ \langle\langle R \rangle\rangle\ is\ the\ deviation\ from\ the\ ideal\ lattice\ position\ and\ u\ is\ the\ deviation$$

$$from\ the\ lattice\ position$$

The vibrations present in the materials are dependent on time. This means that the scattering amplitude depends on time. This equation is further expanded to show how the DW-factor relates to the lattice displacement i.e. root mean square (r.m.s.) amplitude of lattice vibrations.

$$exp(-Q^2\langle\langle u^2 \rangle\rangle) = exp(-2Bs^2)\ where\ B = 8\pi^2\langle\langle u^2 \rangle\rangle\ and\ s = \frac{\sin\theta}{\lambda}$$

In general, $\langle\langle u^2 \rangle\rangle^{1/2}$ is less than 0.1Å when it is room temperature or less with an DW-factor above 0.1Å is due to disorder within the material. Though the Debye Waller approximation has limitations placed upon it which affect the values and their respective interpretation.

1. Correlated atomic displacements: This occurs when two atoms move in the same axis thus the change in distance between these atoms is smaller than the displacements for each. The DW-factor will the overestimate the displacement of these atoms but will underestimate these values if the motions are anticorrelated.
2. An uneven distribution of the r.m.s. displacements amplitudes. If a small percentage of the atoms are displaced by a different value compared to the majority of the remaining atoms then the DW-factor value will be skewed as one DW-factor is attempting to be fitted for one type of atoms whereas in reality there are two values.

3. Strong Anharmonicity: if the potential for an atom is in a double-well then there is bimodal distribution of the atoms. The DW-factor will then appear as a wide distribution of atom density in a soft potential instead of showing two explicit positions for the atoms.

Table 2-4: The advantages and disadvantages of different radiation sources

	Pros	Cons
Lab based X-ray	○ **Readily available** ○ **Can accurately measure the unit cell** ○ **Can perform PDF using a silver target**	○ **Poor Resolution** ○ **Peak areas are less defined** ○ **Can only reach up to Q = 15 Å^{-1}**
Synchrotron based X-ray	○ **Fast data collection** ○ ***In-situ* studies** ○ **High resolution** ○ **Small Samples** ○ **It can penetrate the sample container allowing high pressure studies** ○ **Can select λ in order to avoid any absorption or fluorescence issues**	○ **Limited time** ○ **Expensive** ○ **Interacts with heavier elements so might not see light elements** ○ **Can cause beam damage to certain types of chemical systems**
Neutron Diffraction	○ **Can distinguish neighbouring elements** ○ **No fall off of scattering with angle**	○ **Expensive** ○ **Limited time** ○ **Slow data collection** ○ **Relatively large samples needed**

DW-factor is Q-dependent: The DW-factor is dependent on what Q-range is chosen to calculate the DW-factor value as the drop off in measured intensity with increasing Q value is also similar to the effect DW-factor has, therefore in the refinement there needs to be a wide Q-range to differentiate between these two competing effects whilst also refining these independently of each other to remove any correlation effects.

2.6.2 Pair distribution function

2.6.2.1 Theory

At the same time as the development of Bragg's law and diffraction techniques, there was also interest in Pair distribution function. Peter Debye investigated the intensity of the scattering from materials.[33]

$$I(Q) = \sum_{\mu\nu} b_\mu b_\nu \exp(iQR_{\mu\nu})$$

$$R_{\mu\nu} = |R_{\mu\nu}| = |R_\nu - R_\mu|$$

Where b_μ and b_ν are the scattering lengths of the μ and ν atom respectively R_μ and R_ν are the positions of the μ and ν atom respectively.

$$\mathrm{Q} = |\mathbf{Q}| = \frac{4\pi \sin\theta}{\lambda}$$

Where Q is the magnitude of the diffraction vector or momentum transfer.

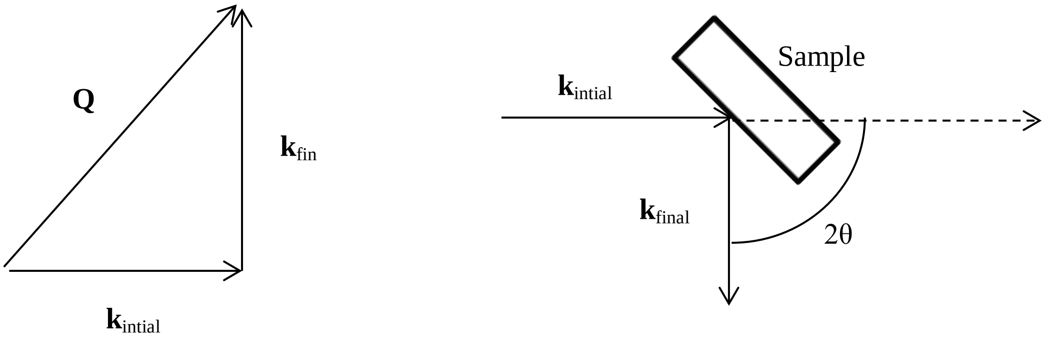

Figure 2-18: Diagram showing how Q is the magnitude of the scattering vectors

$$\boldsymbol{Q} = \boldsymbol{k}_{inital} - \boldsymbol{k}_{final}$$

$$|\boldsymbol{k}_{initial}| = \frac{2\pi}{\lambda_{initial}}\ and\ |\boldsymbol{k}_{final}| = \frac{2\pi}{\lambda_{final}} If\ the\ scattering\ is\ elastic\ \therefore \lambda_{initial} = \lambda_{final}\ so$$

$$k = |\boldsymbol{k}_{initial}| = |\boldsymbol{k}_{final}|$$

$$\mathrm{Q} = |\mathbf{Q}| = \frac{4\pi \sin\theta}{\lambda} = 2k \sin\theta$$

This was further developed to look at the scattering that would be for a powdered material.

$$I(Q) = \sum_{\mu\nu} b_\mu b_\nu \exp\left(\frac{\sin QR_{\mu\nu}}{QR_{\mu\nu}}\right)$$

Zernike and Prins showed that there is relationship between the scattering function and a 2 point atom pair correlation function.[34]

$$\mathrm{G(r)} = 4\pi\mathrm{r}[\rho(\mathrm{r}) - \rho_0] = \frac{2}{\pi}\int_{\mathrm{Q}=0}^{\mathrm{Q_{max}}} \mathrm{Q}[\mathrm{S(Q)} - 1]\sin(\mathrm{Qr})\,\mathrm{dQ}$$

The Fourier transformation of S(Q) can also be shown in different formalisms. They are used to show highlight different length scales. G(r) highlights the short range order, D(r) highlights the medium range order with T(r) highlights the longer range order.[35]

$$D(r) = 4\pi\rho_0 G(r)$$

$$T(r) = D(r) + T^0(r)\ where\ T^0(r) = 4\pi\rho_0\left(\sum_{i=1}^{n} c_i\overline{b_\iota}\right)^2$$

$$\frac{R(r)}{r} = \frac{2}{\pi}\int_{Q=0}^{Q_{max}} F(Q)\sin(Qr)\,dQ\ where\ R(r)\ is\ the\ radial\ distribution\ function$$

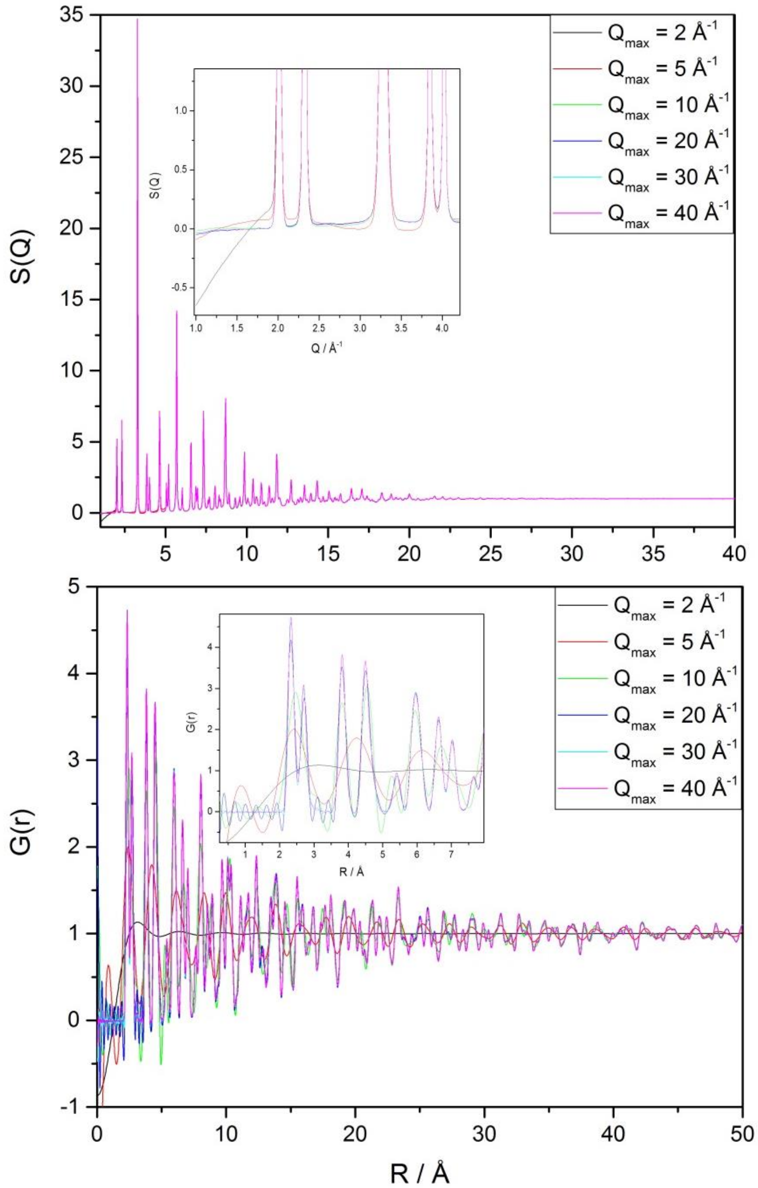

Figure 2-19: A graph showing how change in Q_{max} for the Fourier transformation gives more detail for higher values of Q for ceria for (top) S(Q) and (bottom) G(r)

Major work was initially performed by Bertram Warren,[36] Debye and Menke used this technique to investigate the local structure in liquid mercury,[37] Gingrich investigated other liquid elements[38] with the noted crystallographer, Rosalind Franklin using PDF to investigate non-graphitic carbons.[39] The problems encountered with this technique at the time was the Fourier transformation. At the time this was performed using Beevers-Lipson strips[40] which transformed the data from reciprocal to real space. This was a time intensive procedure compared to modern day computational based methods. This lead to the development of computational methods at the time to decrease the time taken to apply the Fourier transformation to the reciprocal space data allowing analysis of more samples.[41–45] These initial attempts are transformation reciprocal space data were plagued by termination ripples. The ripples and any artefacts caused by equipment were seen in the real space transformations and were even mistaken for atom pairs.[39] This can be overcome by measuring the data to a high value of Q. The figure below shows different PDF calculated using PDFgui[46] using 6 different values of Q max. This shows that any value of Q up to ~20 Å^{-1} does not give a useful PDF which has large termination ripples and very broad peaks. At 20 Å^{-1} and above we have sharpened peaks with little or no termination ripples. Though it must be noted that this simulation contains no artefacts from experimental set up which may cut off the Q_{max} to which the Fourier transformation can be applied. An empirical manner in which to calculate the cut off is to terminate the data at 3-fold the standard deviation of the Debye-Waller parameters gives very small if no termination ripples.

To gain G(r), S(Q) must be processed properly as this can either 'ruin' the transformation or make it into a powerful technique. S(Q), was produced by normalising the intensity and correcting instrumental backgrounds, multiple/inelastic scattering and absorption.

Table 5: Comparison of common targets used in lab based XRD experiments and their respective Q_{max} values

XRD Target	**Q_{max} / Å^{-1}**
Cu	**8.0**
Mo	**17.5**
Ag	**22.0**
W	**59.0**

Where ρ_0 is the atomic density of the probed system and the scattering vector, *Q*, is defined by:

$$S(Q) = 1 + \frac{[I_{coh}(Q) - \sum c_i |f_i(Q)|^2]}{|\sum c_i f_i(Q)|^2}$$

This transformation shows the probability of finding an atom at a distance r. Theoretically the upper limit for the integration should be infinite but in practice this value is limited by the probes wavelength.

This means that in practice there is a need to use pulsed neutrons and SR since these possess probes with short wavelengths. Though measuring Q above 50 $Å^{-1}$ is not normally required (dependent on the bond stiffness and temperature) since no more features are observed in S(Q).[47]

This technique can be very sensitive once these corrections are performed properly.

$$\mathrm{I_{total} = I_{coh} + I_{incoh} + I_{MS} + I_{bkg} + I_{flr}}$$

I_{coh} is the term for Thomson/coherent scattering. This occurs when an x-ray photon interacts with the atom such that there is no change to the energies of either the atom or photon. I_{coh} is needed for the calculation of S(Q) though this is not observed directly. Therefore the other terms need to be corrected for. Both I_{coh} and I_{incoh} are intrinsic to the sample and we need to account for Compton scattering whereas I_{MS}, I_{bkg} and I_{flr} need to be minimised experimentally.

The Oblique incidence corrects the skew in intensities for a finite thickness of the phosphor and the angle of incidence at high energies seen at a synchrotron source.

I_{incoh} is the Compton scattering term. This occurs when the photon is deflected by interacting with an electron. This electron then gains energy from the interaction and is moved from its orbital position whilst the photon also losing energy but continues to travel through the material. This photon has a longer wavelength than the incident radiation and is known as incoherent scattering since the energy change is not consistent and is angle dependent not material dependent. At different values of Q there are different amounts of Compton scattering. As Q increases the amount of Compton scattering increases and elastic scattering decreases and with the use of area detectors there is a measurement of both Compton and elastic scattering. This is very important since these detectors will be sensitive at different energies and these might be sensitive in Q regions where Compton scattering might be seen. As well as this at high values of Q there needs to be a larger correction.

I_{flr} is the fluorescence term. Fluorescence occurs when an atom is ionised after exposure to x-ray radiation. The ionisation process occurs when the energy of the x-ray is the same as and/or equivalent to the ionisation potential of a core level atom. This will eject the electron from the ionised atom. Due to the instability of the atom caused by this process, higher level electrons will ‘drop’ in the vacant core level orbital. This emits a photon of a different energy to the incident x-ray. This can be minimised or avoided by carefully selecting the energy of the incident x-ray beam in order to avoid any absorption energies of the atoms within the material.

There is a need to try and minimise I_{MS} (MS being multiple scattering) and I_{bkg}. This needs to be performed as any scattering seen from the background can be seen in the final G(r) after the FT leading to spurious peaks which may be interpreted as real bond lengths from the material.

2.6.2.2 Shortcomings of PDF

As with all characterisation techniques used in materials chemistry there are limitations that will affect how we use PDF, what systems we look at or what types of analytical methods should be used.

- *Q-range*: As seen previously, the upper limit for the Fourier transformation is the Q_{max} value. Firstly, this value will have an effect on the termination ripples which become greater as the value of Q_{max} decreases. Secondly, the resolution for the PDF is governed by the range of Q. Therefore, the larger the Q-range used the greater the resolution becomes. This is important as at high-r values the co-ordination shells get closer and closer to the point where they overlap.
- *Analysis of nanocrystalline materials*: The initial development of PDF was driven by the need to understand materials that could not be analysed by traditional crystallographic methods such as liquids or amorphous materials. Though the use of analytical methods, such as a Rietveld refinement, is a powerful technique to under the crystal structure of crystalline materials; this type of analysis is poor in the understanding of amorphous or nanocrystalline materials due to issues such as peak broadening. These type of systems can be analysed using with programs such as PDFgui[46] but are still limited by the need for a crystal structure as an input. More complex analytical techniques have been utilised in the understanding of materials such as RMC modelling.[48,49] This type of analysis allows the modelling of a material with combined short, medium and long range structure whilst having no symmetry constraints. Furthermore, it allows the analysis of a supercell in comparison to the small box method used in Rietveld analysis.
- *Interatomic correlations*: The PDF is calculated from the Fourier transformation of the S(Q). Firstly, this means that any scattering due to the background, setup etc., will be seen in the PDF if the corrections are not done properly. Secondly, all

interatomic correlations will be seen in the PDF. There are some methods that can be utilised to overcome this. For example this can be done, in the case of supported catalysts, by the subtraction of the plain support PDF from that of the PDF for the catalyst and support.[50] This allows for the isolation of the PDF for the catalyst itself. Another way in which this can be done is through the use of anomalous dispersion of X-rays near an absorption edge[51]. This allows for the removal of certain contributions to the PDF from other elements, such as Gd-Gd correlations in mixed ceria-gadolinia systems. In the case of NPDF this can be accomplished using isotopic substitution.

2.7 Methodologies for Data analysis

The collection of the data from either synchrotron or neutron sources is the start of a long process in order to get the data in the correct form in order to be analysed. Initially the subtraction of background, experimental setup ought to be done. This is very important in the case of any total scattering experiment, as any contribution from these, will be undergo a Fourier Transformation and might manifest as spurious peaks in the PDF which may be modelled during analysis. Once these corrections are done correctly, then the analysis can be performed. The basic premise of analysis for XAFS, PDF and XRD is the fitting of a theoretical pattern and/or spectra for a structure by the refinement of structural and experimental parameters. The driving force for this is the minimisation of the difference between the data and theory. This is most commonly done by a nonlinear least-squares curve fitting.

2.8 Analysis of X-ray and Neutron Diffraction data

2.8.1 X-ray and Neutron based Diffraction data

The initial processing performed in order to extract PDF data is the transformation of a 2D image (from a 2D x-ray detector) into a 1D graph of intensity vs. 2θ/Q-space/D-space. The X-ray in-situ was processed using Fit2D.[52] This allows for the masking of any experimental setup such as a furnace or beam stop, allows for the averaging of the intensity over the diffraction cones, allows for the removal of the dark image whilst also allowing the calibration of the detector-sample distance, tilt of detector, beam centre, background subtraction etc. Fit2D also fortunately includes a batch processing as modern synchrotron beam lines with 2D image detectors allow for quick acquisition for *in-situ* experiments which can lead to the gathering of 1000s of data sets.

This is enough pre-processing to be done before analysis by Le Bail or Rietveld based methods can be performed. This is performed using GSAS[53] with the EXPGUI interface[54] which allows the ability to easily analyse the data. It has numerous parameters that can be refined such as lattice parameters, atomic displacement parameters, occupancies, scaling factors, background functions etc.

Furthermore, diffraction data can be analysed with TOPAS[55] or GSAS-II this allows for analysis by Pawley or Rietveld based methods.

2.8.2 Analysis of Total Scattering data

2.8.2.1 X-ray based PDF data correction

The initial processing performed in order to extract PDF data is the transformation of a 2D image (from a 2D x-ray detector) into a 1D graph of intensity vs. 2θ/Q-space/D-space. For example, data obtained from ID15B is processed using Fit2D.[52] This allows for the masking of any experimental setup such as a furnace or beam stop, allows for the averaging of the intensity over the diffraction cones, allows for the removal of the dark image whilst also allowing the calibration of the detector-sample distance, tilt of detector, beam centre, background subtraction etc. Fit2D, also fortunately, includes batch processing as modern PDF beam lines with 2D image detectors allow for quick acquisition for *in-situ* experiments which can lead to the gathering of 1000s of data sets.

Once this is performed, the data must be pre-processed in order to look at only the coherent scattering as the total intensity measured is made of 4 parts; coherent-, incoherent-, background- and multi-scattering.

This background scattering must be removed otherwise any contribution from this will be seen within the S(Q) or G(r) data *c.f.* in Rietveld refinement either the background is subtracted from the raw data or ignored completely as no pre-processing and fitted with background functions. This correction and Fourier Transformation can be performed using either PDFgetX2[56] or PDFgetX3.[57]

2.8.2.2 Neutron based PDF data correction

The initial processing of the neutron data was performed using GudrunN. This is a piece of ‘In-House’ software at ISIS. This merges numerous data sets as scans normally are taken in one hour sections. This then normalises the data with respect to a vanadium rod and the sample environment *e.g.* vanadium cans for ex-situ experiments or silica tubes for in-situ experiments. Once numerous values such as sample composition and number density are inputted, Gudrun will perform corrections to give the F(Q) and G(r). Further to this merged and corrected data can be Fourier transformed in order to obtain G(r) using STOG, which is distributed as part of RMCProfile.[58]

2.8.2.3 PDF data analysis

It must be noted that different programs output different formalisms for different functions. A thorough comparison of all the formalisms has been discussed by Keen.[35] Once, either the XPDF or NPDF data is processed, the G(r) is analysed using PDFgui.[46] Analysis using this type of methodology is analogous to a Rietveld refinement on real space data as it uses a similar ‘small box’ approach, though this can be expanded to a supercell unlike Rietveld refinements. Similarly to GSAS, PDFgui is able to simultaneously model both XPDF and NPDF data sets in order to highlight contributions to the PDF from both low- and high-z scatterers due to the different manners in which these radiation sources interact with atoms. In addition there are no limitations on the number of phases that could be refined. The parameters that can be refined are scale factor, lattice parameter, atomic displacement parameters, occupancies, interatomic correlation parameters etc.

2.8.3 Analysis of XAS data

2.8.3.1 Data Processing

Several programs, such as Athena,[28] Viper[59] and EDA,[60] are available for the processing and extraction of χ(k). In this thesis, a combination of Athena was used to process and extract data. The advantage of using Athena in data processing is the merging of datasets, the ability to process one data set and use those parameters across the whole experiment, multiple excitation event correction etc. Though these are limited by the samples having a similarity between their composition and structures.

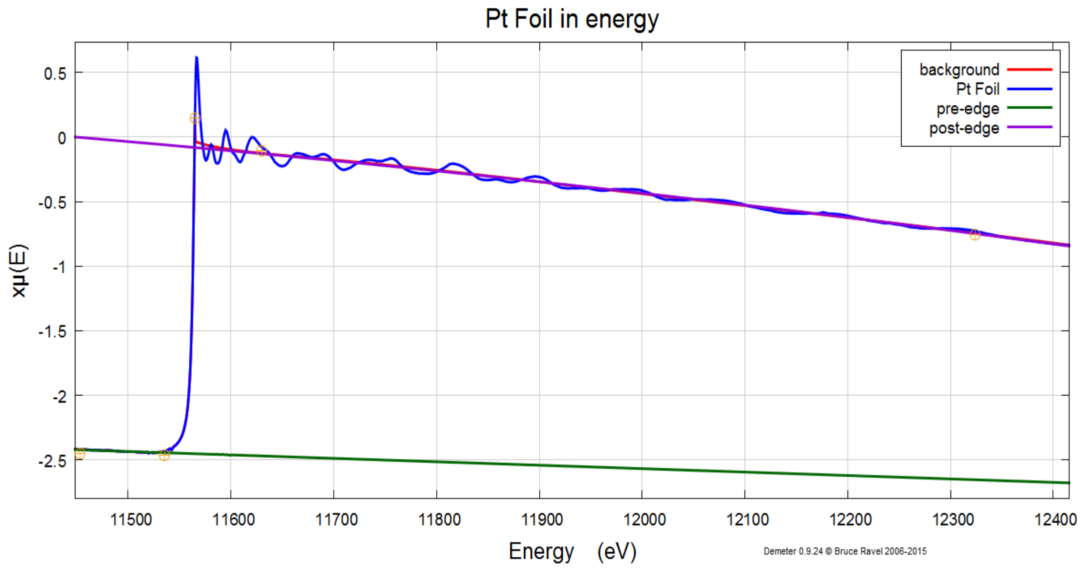

Figure 2-20: An example of an absorption spectrum (measured on the Pt L_3-edge) showing the background, pre-edge and post-edge lines

The spectrum (Figure 2-20) shows that ~11565 eV there is a sharp increase in the intensity, μ(E), of the peak.

$$\mu(E) = \ln \frac{I_0}{I}$$

This is the absorption edge *e.g.* Pt L_3-edge and its intensity is proportional to the concentration of the probed atom within the sample. This value is seldom known due to the sample thickness, homogeneity of sample within matrix, x-ray absorption by binder etc. This is overcome by the normalisation process which μ(E) is divided by edge jump thus leading to an edge step of one.[26] The edge jump is calculated by fitting the pre- and post-edge regions with polynomials, though care must be taking in fitting the post-edge region as the EXAFS region can influence the normalisation process. Further to this, choosing the correct E_0 is important as this will affect the analysis later on in the process. This value is normally obtained/refined when using a known standard, such as a metal Pt foil as seen in Figure 2-20). The figure is normally determined by using the inflection point in the derivative of μ(E) or the value at half the edge step. The μ(E) can then be converted onto a k-space grid (Å^{-1}).

$$k = \sqrt{\frac{2m(E - E_0)}{\hbar^2}}$$

Once this value and normalisation is performed, the background can be subtracted from the absorption spectrum. This relates to an ideal single atom absorption spectrum, μ_0(E), without any neighbours influencing, giving rise to oscillations in the EXAFS region and determined with a cubic spline.[61] Care must be taken in subtracting μ_0(E) as this could remove contributions from the subtle oscillations in μ(E) leading to subtle changes in the final analysis. As the data can be converted to k-space, the background function can have different weightings. This can be represented as k^n, where n = 1,2 or 3, which influences the fit in either lower or high regions of E in μ(E).

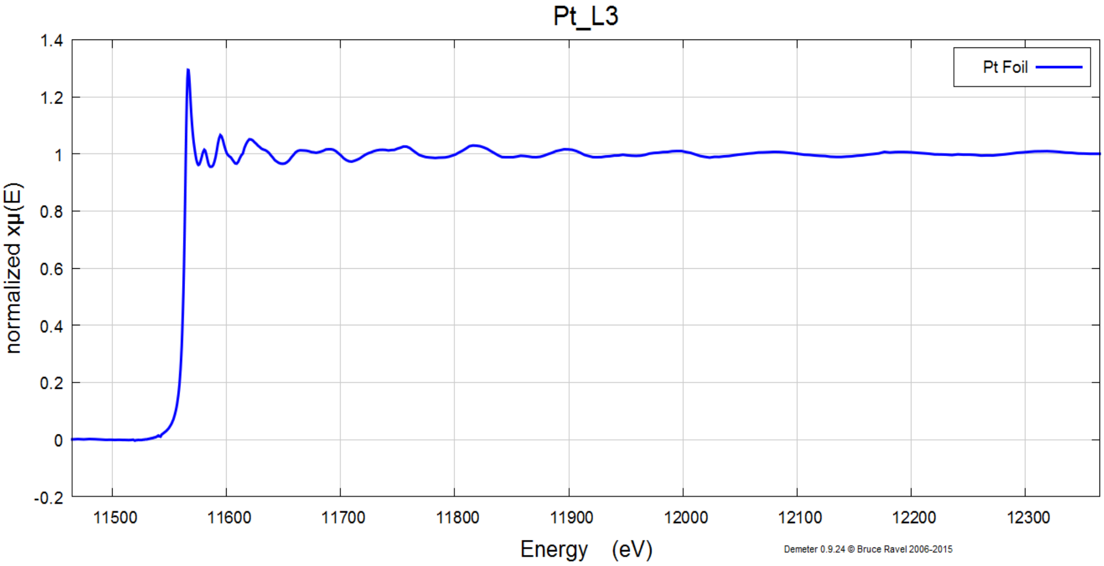

Figure 2-21: Normalised μ(E) for Pt Foil after subtraction of the background contribution from single atom scattering

In addition to using different k-weights to improve the fit in different regions of k, Athena uses smoothing functions *e.g.* Rbkg and spline clamps, that may improve the background fitting.

Once a satisfactory normalisation process has been accomplished the data is transformed into χ(k) where:

$$\chi = \frac{\mu_{total} - \mu_{atomic}}{\mu_{atomic}}$$

In order to model the data in real space, χ(k) is Fourier transformed to χ(R). This can also emphasise different R-space ranges dependent on the k-weighting used.

2.8.3.2 Analysis of XANES

As discussed previously, XANES is sensitive to the electronic configuration and co-ordination number of the probed atom in the experiment. This relates to the binding energy of the probed absorption edge, therefore any changes to the local structure *e.g.* phase change during reduction is observable. The simplest and an effective manner in which the materials can be analysed is to measure standard reference materials with a known structure and oxidation state and comparing with the sample. This has the advantages of not needing to perform XANES calculations and overcoming issues with shifts in the absorption energy measured at different beamlines. This shows the importance of running standards for every experiment at different beamlines, as a shift in the absorption energy can relate to a mixture of different valences for the probed atom. In addition to the change in absorption edge, the intensity of the white line[62] is dependent on the co-ordination number/geometry and what neighbouring atom is present.

Though a comparison of the XANES spectra of the references and the reference materials is informative of the phases present, the ability to model the unknown sample and have numeric values to the amount of the phases present is important in the comprehension of what is occurring in the sample. This analytical process is called linear combination fitting (LCF). This requires the measurement of known standards across the spectrum of the probed atom *e.g.* reduction of PtO_2 to Pt, need to measure Pt oxides and Pt foil standards. Though there are certain caveats that the analysis is based on the standards measured and that if the wrong standards are measured or too many datasets are allowed to fit the experimental data therefore incorrect answers can be found.[63]

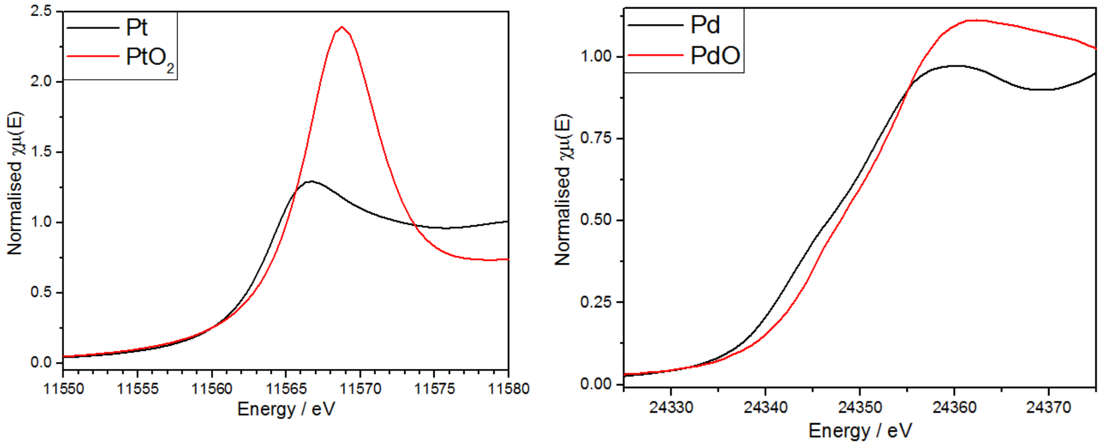

Figure 2-22: Comparison of the normalised μ(E) for Platinum Group Metal and its' respective oxide (Left) Platinum and Platinum Oxide (Right) Palladium and Palladium oxide

Figure 2-22 shows the comparison of the XANES spectra for PGM and PGM oxide species. The comparison of the normalised μ(E) for Pt and PtO_2 shows the change in both the edge position and the white line intensity. For Pd and PdO, there is a small change in edge position and white line intensity but also some subtle change in the peak shape.

2.8.3.3 Analysis of EXAFS

The EXAFS equation is a good approximation for use in the interpretation and analysis of EXAFS data. This equation allows for the refinement of parameters allowing for the understanding of the structure of the material. Though care has to be taken as these parameters may be correlated and be influenced by the starting values used.

$$\chi(k) = \sum_{j} \frac{N_j f_j(\mathrm{k}) \exp(-2k^2\alpha_j^2)}{kR_j^2} \sin(2kR_j + \delta_j(k))$$

Where N is the number of neighbouring atoms with $f_j(k)$ and $\delta_j(k)$ being the scatting properties of the neighbouring atoms. R is the distance between the excited atom and its respective neighbouring atoms and σ^2 is the square of the mean disorder for R.

The EXAFS analysis performed in this thesis used Artemis,[28] part of the Demeter software package. This uses the FEFF[29] code for the determination of phase shifts and scattering amplitudes by calculating self-consistent real space multiple-scattering.[64,65] FEFF, regularly, uses a crystallographic information file (CIF) to generate single and multiple scattering paths for a cluster of atoms of a set radii, r. This calculation also estimates the importance of the single or multiple scattering paths, allowing for the optimisation of what paths are important in the analysis. If no CIF calculates paths that match with the data then Artemis presents the option of a quick first shell fit, based on the absorber, neighbouring atom and the interatomic distance.

Artemis has been developed in conjunction with Athena giving the ability to easily import the normalised XAFS data. Artemis allows for the options of fitting in k- or r-space, using different k-weightings, adjusting k_{min} and k_{max}, optimising r_{min} and r_{max} etc.

Artemis uses separate terms (FEFF is defined by different parameters[66]) representing the following:

- N, the degeneracy of each path
- S_0^2, the amplitude reduction factor
- E_0, the energy correction
- R, the path length
- σ^2, the Debye-Waller factor

N, is fixed for each path so there is no change in the degeneracy, instead it is multiplied by an arbitrary factor and this is refined to map out the change in the co-ordination. S_0^2 can be refined for each path or fixed for paths of similar distances *e.g.* in the case of the refinement of ex-situ ceria samples, S_0^2 was refined using a highly crystalline reference then fixed for the other samples. Artemis does not the actual value of R but instead refines ΔR, the difference between the actual distance and that of the crystalline input from FEFF. Ideally this should be less than ~0.1 Å otherwise new phase shifts and scattering amplitudes would need to be recalculated. In an ideal world we'd refine each parameter separately but can group parameters together for different paths to reduce the number of variables.

Using a crystallographic based input for FEFF[67,68] calculations and EXAFS refinements has both positives and setbacks. If no CIF is available or the local structure is drastically differing to that of the known crystal structures, then the only way to model using Artemis is by the use of quick shell fits which normally limits to first shell analysis.

Furthermore, LCF can be used to analyse EXAFS data by similarly modelling with known standards. This type of analysis is hindered by relatively weak scattering of low-Z atoms *e.g.* oxygen, nitrogen or carbon. Similarly EXAFS has difficulties in differentiating between neighbouring atoms on the periodic table.

A note must be made for the analysis of Ce L_3-edge as extra corrections need to be performed before EXAFS analysis can be performed. A double excitation component needs to be subtracted to determine reliable structural information. The correction of the $\chi(k)$, for the double excitation event due to the $2p,4d \rightarrow 5d^2$ transition at 5854 eV[69] is performed by fitting a Lorentzian peak to model the transition resonance to the data with 3 parameters: width, height and position. Figure 2-23 illustrates the fitting of the Lorentzian peak showing the initial and final $\chi(k)$.

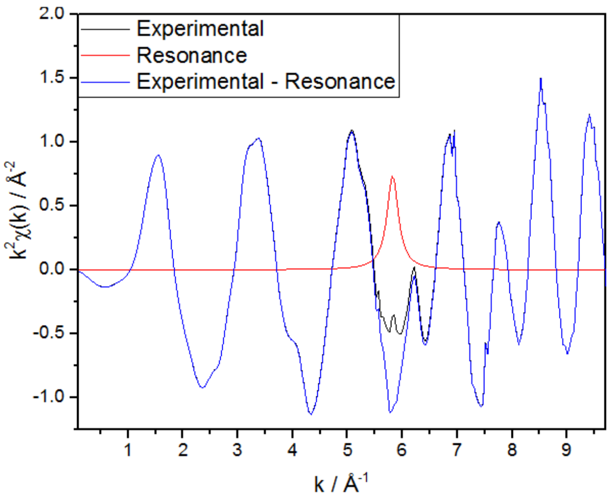

Figure 2-23: A comparison of initial and final $\chi(k)$ for the NIST Ceria sample illustrating the Lorentzian peak fitted for removal of the $2p,4d \rightarrow 5d2$ resonance feature on the Ce L_3-edge.[70]

In addition to the above mentioned techniques Temperature Programmed Reduction (TPR) was used to support the described methods. This measures the release or uptake of Hydrogen over a programmed temperature ramping cycle.

In summary, the details of the main techniques are provided in this chapter. All the details of the *insitu* and *exsitu* experiments, beamline configurations, wavelengths, q or k-range, and method of data collection are given in respective chapters.

2.9 Bibliography

1 R. I. Frankel, *West. J. Med.*, 1996, **164**, 497–501.

2 F. R. Elder, A. M. Gurewitsch, R. V Langmuir and H. C. Pollock, *Phys. Rev.*, 1947, **71**, 829–830.

3 D. H. Bilderback, P. Elleaume and E. Weckert, *J. Phys. B At. Mol. Opt. Phys.*, 2005, **38**, S773.

4 A. Lienard, *L'Eclairage Elec.*, 1898, **16**, 5.

5 H. C. Pollock, *Phys. Rev.*, 1946, **69**, 125.

6 H. C. Pollock, *Am J. Phys.*, 1983, **51**, 278.

7 M. L. Perlman, E. M. Rowe and R. E. Watson, *Phys. Today*, 1974, **27**, 30–37.

8 P. L. Hartman and D. H. Tomboulian, *Phys. Rev.*, 1953, **91**, 1577–1578.

9 D. H. Tomboulian and P. L. Hartman, *Phys. Rev.*, 1956, **102**, 1423–1447.

10 K. Codling, *J. Synchrotron Radiat.*, 1997, **4**, 316–333.

11 S. Doniach, K. Hodgson, I. Lindau, P. Pianetta and H. Winick, *J. Synchrotron Radiat.*, 1997, **4**, 380–395.

12 D. W. Lynch, *J. Synchrotron Radiat.*, 1997, **4**, 334–343.

13 R. E. Gerig, J. M. Gibson, D. M. Mills, W. G. Ruzicka, L. Young and A. Zholents, *Nucl. Instruments Methods Phys. Res. Sect. A Accel. Spectrometers, Detect. Assoc. Equip.*, 2011, **649**, 1–2.

14 Y. Sakurai, M. Oura, H. Sakae, T. Usui, H. Kimura, Y. Oikawa, H. Kitamura, T. Konishi, H. Shiwaku, A. Nakamura, H. Amamoto and T. Harami, *Rev. Sci. Instrum.*, 1995, **66**, 1771–1773.

15 http://extranet2.diamond.ac.uk/ISV/Flipping/2014/index.html#6-7 Date Accessed: 2015-07-03

16 J. F. Haw, in *In-Situ Spectroscopy in Heterogeneous Catalysis*, Wiley-VCH Verlag GmbH & Co. KGaA, 2004, pp. 1–14.

17 B. M. Weckhuysen, *In-situ Spectroscopy of Catalysts*, American Scientific Publishers, Stevenson Ranch, CA., 2004.

18 A. M. Beale, S. D. M. Jacques and B. M. Weckhuysen, *Chem. Soc. Rev.*, 2010, **39**, 4656–4672.

19 T. Shido and R. Prins, *Curr. Opin. Solid State Mater. Sci.*, 1998, **3**, 330–335.

20 F. M. Cano, A. P. Molina and A. M. Molenbroek, *Synchrotron Radiat. News*, 2009, **22**, 12–16.

21 http://diamond.ac.uk/Home/About/Synchrotrons/Machine.html Date Accessed: 2013-12-10

22 M. de Broglie, *C. R. Acad. Sci.*, 1913, **157**, 924–926.

23 H. Fricke., *Phys. Rev.*, 1920, **16**, 202–215.

24 R. de L. Kronig, *Zeitschrift für Phys. Phys.*, 1931, **70**, 317–323.

25 F. W. Lytle, *J. Synchrotron Radiat.*, 1999, **6**, 123–134.

26 M. Newville, 2004.

27 D. E. Sayers, E. A. Stern and F. W. Lytle, *Phys. Rev. Lett.*, 1971, **27**, 1204–1207.

28 B. Ravel and M. Newville, *J. Synchrotron Radiat.*, 2005, **12**, 537–541.

29 J. J. Rehr, J. M. de Leon, S. I. Zabinsky and R. C. Albers, *J. Am. Chem. Soc.*, 1991, **113**, 5135–5140.

30 J. Chadwick, *Proc. R. Soc. London A Math. Phys. Eng. Sci.*, 1932, **136**, 692–708.

31 J. Chadwick, *Proc. R. Soc. London A Math. Phys. Eng. Sci.*, 1933, **142**, 1–25.

32 R. I. Smith and S. Hull. http://www.isis.stfc.ac.uk/instruments/polaris/documents/user-guide-for-the-polaris-powder-diffractometer-at-isis7278.pdf Date Accessed: 2014-02-19

33 P. Debye, *Ann. Phys. (Berlin, Ger.)*, 1915, **351**, 809–823.

34 F. Zernike and J. A. Prins, *Z. Phys.*, 1927, **41**, 184.

35 D. A. Keen, *J. Appl. Crystallogr.*, 2001, **34**, 172–177.

36 B. E. Warren, H. Krutter and O. Morningstar, *J. Am. Ceram. Soc.*, 1936, **19**, 202–206.

37 P. Debye and H. Menke, *Phys. Zeit*, 1930, **31**, 797.

38 N. S. Gingrich, *Rev. Mod. Phys.*, 1943, **15**, 90–110.

39 R. E. Franklin, *Acta Crystallogr.*, 1950, **3**, 107–121.

40 W. Cochran, *Acta Crystallogr.*, 1948, **1**, 54–56.

41 G. T. Clayton and L. Heaton, *Phys. Rev.*, 1961, **121**, 649–653.

42 D. G. Henshaw, *Phys. Rev.*, 1960, **119**, 9–13.

43 R. Kaplow, T. A. Rowe and B. L. Averbach, *Phys. Rev.*, 1968, **168**, 1068–1079.

44 H. Ocken and C. N. J. Wagner, *Phys. Rev.*, 1966, **149**, 122–130.

45 R. R. Fessler, R. Kaplow and B. L. Averbach, *Phys. Rev.*, 1966, **150**, 34–43.

46 C. L. Farrow, P. Juhas, J. W. Liu, D. Bryndin, E. S. Božin, J. Bloch, T. Proffen and S. J. L. Billinge, *J. Phys. Condens. Matter*, 2007, **19**, 335219.

47 L. Malavasi, *Dalt. Trans.*, 2011, **40**, 3777–3788.

48 M. G. Tucker, M. T. Dove and D. A. Keen, *J. Appl. Crystallogr.*, 2001, **34**, 630–638.

49 D. A. Keen, M. G. Tucker and M. T. Dove, *J. Phys. Condens. Matter*, 2005, **17**, S15.

50 J. Keating, G. Sankar, T. I. Hyde, S. Kohara and K. Ohara, *Phys. Chem. Chem. Phys.*, 2013, **15**, 8555–8565.

51 M. Allieta, M. Brunelli, M. Coduri, M. Scavini and C. Ferrero, *Z. Krist. Proc.*, 2011, **2011**, 15–20.

52 A. P. Hammersley, S. O. Svensson, M. Hanfland, A. N. Fitch and D. Hausermann, *High Press. Res.*, 1996, **14**, 235–248.

53 A. C. Larson and R. B. Von Dreel, *Los Alamos Nation Lab. Rep. LAUR*, 1994, 86–748.

54 B. H. Toby, *J. Appl. Crystallogr.*, 2001, **34**, 210–213.

55 A. A. Coelho, *J. Appl. Crystallogr.*, 2003, **36**, 86–95.

56 X. Qiu, J. W. Thompson and S. J. L. Billinge, *J. Appl. Crystallogr.*, 2004, **37**, 678.

57 P. Juhás, T. Davis, C. L. Farrow and S. J. L. Billinge, *J. Appl. Crystallogr.*, 2013, **46**, 560–566.

58 M. G. Tucker, D. A. Keen, M. T. Dove, A. L. Goodwin and Q. Hui, *J. Phys. Condens. Matter*, 2007, **19**, 335218.

59 K. V Klementev, *J. Phys. D Appl. Phys.*, 2001, **34**, 209–217.

60 A. Kuzmin, *Phys. B Condens. Matter*, 1995, **208**–**209**, 175–176.

61 J. W. Cook and D. E. Sayers, *J. Appl. Phys.*, 1981, **52**, 5024–5031.

62 J. W. Sobczak, E. Sobczak, A. Drelinkiewicz, M. Hasik and E. Wenda, *J. Alloy. Compd.*, 2004, **362**, 162–166.

63 T. I. Hyde, P. W. Ash, D. A. Boyd, G. Randlshofer, K. Rothenbacher and G. Sankar, *Platin. Met. Rev.*, 2011, **55**, 233–245.

64 J. J. Rehr and R. C. Albers, *Phys. Rev. B*, 1990, **41**, 8139–8149.

65 J. J. Rehr, R. C. Albers and S. I. Zabinsky, *Phys. Rev. Lett.*, 1992, **69**, 3397–3400.

66 M. Jaouen, G. Hug, B. Ravel, A. L. Ankudinov and J. J. Rehr, *EPL*, 2000, **49**, 343.

67 J. J. Rehr, J. J. Kas, M. P. Prange, A. P. Sorini, Y. Takimoto and F. Vila, *Comptes Rendus Phys.*, 2009, **10**, 548–559.

68 J. J. Rehr, *Rev. Mod. Phys.*, 2000, **72**, 621–654.

69 J. Chaboy, A. Marcelli and T. A. Tyson, *Phys. Rev. B*, 1994, **49**, 11652.

70 H. R. Marchbank, A. H. Clark, T. I. Hyde, H. Y. Playford, M. G. Tucker, D. Thompsett, J. M. Fisher, K. W. Chapman, K. A. Beyer, M. Monte, A. Longo and G. Sankar, *ChemPhysChem*, 2016, **17**, 3494–3503.

Chapter 3: Structure of nano-sized Ceria materials: a combined spectroscopic and scattering investigation

3.1 Abstract

The structures of several nano-sized ceria (CeO_2), systems were investigated using neutron and X-ray diffraction, and X-ray absorption spectroscopy. Bragg Diffraction and total scattering techniques revealed that in all the samples the occupancy of both Ce^{4+} and O^{2-} are stoichiometric, and analysis using reverse Monte Carlo (RMC) revealed significant disorder around oxygen atoms in the nano sized ceria materials in contrast to the highly crystalline Ceria NIST Diffraction standard. The analysis showed that the main differences observed in the pair correlations from various techniques were attributed to the differences in particle size of the CeO_2 prepared by three different methodologies. The detailed analysis of the Ce L_3- and K-edge EXAFS data supports this observation; the decrease in higher shell coordination numbers, with respect to the highly crystalline Ceria NIST Diffraction standard, are attributed to differences in particle size.

3.2 Introduction

Ceria has been used, over decades, for numerous applications. Ceria is widely used in emission based catalytic control within the automotive industries,[1–5] due to the ability to change oxidation state from Ce (IV) to Ce (III) and vice versa at a moderate temperatures (<600°C)[3] allowing it to store and release oxygen from its structure.

$$CeO_2 \rightleftharpoons CeO_{2-x} + \frac{x}{2}O_2$$

The fluorite structure (space group ($Fm\bar{3}m$), Ce: 4a, 0, 0, 0 and O: 8c, ¼, ¼, ¼,)[6] of ceria allows oxide ions to diffuse 'easily'[3]; ensuring, when either being reduced or oxidised, oxygen can enter or leave the structure. The non-stoichiometry of oxygen within the material creates vacancies within the structure whilst reducing Ce (IV) to Ce (III), whilst retaining the fluorite structure.

$$O_o \rightleftharpoons \frac{1}{2}O_2 + V_o^{\cdot\cdot} + 2e'$$
$$2Ce^{4+} + 2e' \rightleftharpoons 2Ce^{3+}$$

Ceria has been used in different areas, for example in hydrocarbon oxidation[7] and reforming,[8] and partial oxidation of methane[9] in combination with various transition or platinum group metals. Ceria is used in catalytic wet oxidation reactions, in conjunction with high temperatures and high oxygen pressure, to remove organic waste residues found in water supplies.[10]

Numerous methods have been reported for the preparation of CeO_2.[11] This area attracts attention to improve the performance/properties of this material; defect structures created in these systems are thought to be essential for their applications dependent on the preparation methods. Many of the materials are in a relatively crystalline form (some methods yield lower crystallinity compared to the others), but it is problematic to rely on one specific technique to determine the nature of any defects. For example, X-ray diffraction is routinely used, though this technique will provide accurate information about cerium atoms and less accurate about the nature of oxygen in the system. Neutron diffraction methods are desirable for their ability to probe oxygen atoms within the metal oxide material. It has been found[12] that, by using Rietveld[13] based refinement methods of the neutron diffraction data and Pair-Distribution Function (PDF) analysis reveal that there are interstitial oxygen defects within the fluorite structure and these oxide ions provide the mobility that allows ceria to act as an oxygen store for catalysis.

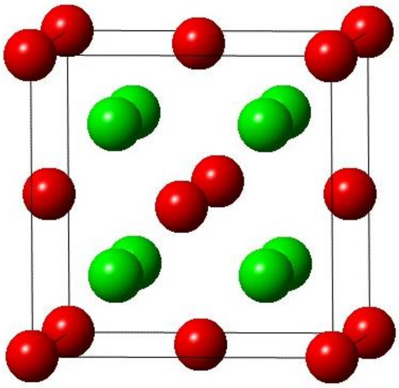

Figure 3-1: Ceria adopts the fluorite structure (space group Fm-3m, Ce (red): 4a, 0, 0, 0 and O (green): 8c ¼, ¼, ¼)

The PDF method provides short, medium and longer-range order information, depending on the range of r-space used in the analysis, the data represent a weighted histogram of all interatomic distances in the sample and only through modelling can insight be gained into specific pairwise interactions.[14] An element specific technique, such as X-ray absorption spectroscopy (XAS, consisting of X-ray absorption near edge structure (XANES) and Extended X-ray absorption fine structure (EXAFS)) is highly complementary. XANES is used to investigate the oxidation state of metal ions present in the materials whereas EXAFS provides information about the coordination environment of the probed ions present in the sample. [15]

In order to fully understand the structure, defects and particle size in ceria prepared by various methods, various techniques, in particular XAS (at the Ce L_3 and K-edges), PDF analysis of the total scattering data and Rietveld analysis of the X-ray and neutron diffraction data.

3.3 Experimental

3.3.1 Sample Preparation

Four ceria samples were examined in this work. Two Ceria samples were prepared from the respective Ce (III) and Ce (IV) precursor salts. For the Ce (III) precursor salt sample, concentrated NH_3 (30ml, 0.44mol) was added to 1L demineralised water and the solution was stirred. Cerium nitrate.6H_2O (63.4g, 0.146mol) was dissolved in water (60ml) and carefully added to the stirred base solution. An immediate yellow precipitate formed. After 30min stirring the product was recovered by filtration, thoroughly washed, dried at 105°C and fired 500°C for 2 hours (ramp rate 10°C min^{-1}). This is referred to as “Ce (III) precursors”. For the Ce (IV) precursor salt sample, concentrated NH_3 (40ml, 0.59mol) was added to 1L demineralised water and the solution was stirred. Cerric ammonium nitrate (80g, 0.146mol) was dissolved in water (60ml) and carefully added to the stirred base solution. An immediate yellow precipitate formed. After 30min stirring the product was recovered by filtration, thoroughly washed, dried at 105°C and fired 500°C for 2 hours (ramp rate 10°C min^{-1}). This is referred to as “Ce (IV) precursors”. A commercially available Rhodia high surface area ceria (referred to as HSA in the thesis) from Solvay was used after calcination to 500°C for 2 hours. A Ceria Standard Reference Material® (SRM 674b) for XRD Quantitative Powder Diffraction from the National Institute of Standards & Technology (NIST), Gaithersburg, MD was used 'as received’.

3.3.2 X-ray and Neutron Total Scattering and Bragg diffraction

All four materials were measured on the POLARIS[16] instrument at the ISIS Facility, Rutherford Appleton Laboratory, UK. Data was collected using the low angle, 90° and back scattering banks data over $28° < 2\theta < 42°$, $85° < 2\theta < 95°$ and $130° < 2\theta < 160°$ respectively. Data was collected in six 1 hour scans and then merged. The ceria samples were ground into a fine powder and loaded into 8mm diameter vanadium cans. These cans were loaded into an automatic sample changer and placed into the detector tank then the atmosphere was evacuated. The raw Neutron Diffraction data was processed using MantidPlot.[17]

X-ray total scattering data of all the samples were collected at the 11-ID-B beamline at APS. The samples were ground into a fine powder and loaded into 1mm diameter kapton tubes. The kapton tubes were loaded into an automatic sample changer. Total scattering and Bragg diffraction patterns were collected using a Perkin Elmer Amorphous silicon 2D detector in ambient conditions. The diffraction patterns were collected using $\lambda = 0.1430$ Å; for Bragg diffraction data were collected between 2θ = 0.0 to 17.3° and for total scattering patterns were collected over a Q-range = 0.7 to 26 Å^{-1}. The raw 2D images was processed using Fit2D[18] to create 1D plots of intensity vs 2θ (or nm^{-1}).

3.3.3 X-ray absorption spectroscopy (XAS) at Ce L_3 and K-edges

Exsitu XAS data was collected at the Ce L_3-edge (5723.4 eV) at room temperature at BM26A[19] beam line, at the European Synchrotron Research Facility (ESRF) which operates at 6 GeV with a typical current of ca 100 mA. A Si (111) double crystal monochromator was used to collect the L_3 edge data and was collected in transmission geometry using ionisation chambers. Approximately 10mg of sample was ground with approximately 90mg of fumed silica and made into a pellet. The XAS data was measured in step scans in an E-range of 5623.0 and 6154.0 eV. *Ex-situ* XAS data at the Ce K-edge (40443 eV) was obtained at room temperature on BM23,[20] at the ESRF. The data was collected using a Si (311) double crystal monochromator. The data was collected in transmission mode using ionisation chambers. Circa 95mg of sample was ground in combination with approximately 15mg of cellulose and pressed into a pellet. The XAS data was measured in step scans in an E-range of 40200 and 41423 eV.

Analysis of the XAS datasets was performed using ATHENA and ARTEMIS software[21]. FEFF6L[22] with Hedin-Lundqvist muffin-tin like potentials were used for all the scattering path calculations.

3.4 Data Analysis

3.4.1 Neutron Total Scattering

3.4.1.1 Reciprocal Space refinement

Analysis of the data, the Rietveld method,[13] was performed using the graphical interface, EXPGUI,[23] of the GSAS software.[24] The refinement used data from four of POLARIS detector banks, allowing a combined d-spacing range of 0.25 – 3.25 Å to be fitted simultaneously. The background and profile parameters were refined along with the cell parameter, isotropic thermal displacement parameters (U_{iso}) and oxygen occupancy.

3.4.1.2 Real Space refinement

The data correction (of the neutron datasets) for real space analysis was performed using GUDRUN[25]. This performs normalisation, merging of data sets and correction for the general sample environment and containers. The Fourier transformation of the S(Q) to result in the G(r) was performed using STOG, distributed as part of the RMCProfile package.[26] If needed, a sloping background on the S(Q) was corrected using a Fourier filter, where a low-r region of the PDF (0 – 2 Å) was back transformed and the result subtracted from the Q-space function.

$$G(r) = 4\pi r[\rho(r) - \rho_0] = \frac{2}{\pi}\int_{Q=0}^{Q_{max}} Q[S(Q) - 1]\sin(Qr)\,dQ$$

This results in a weighted histogram of interatomic distances giving the visualisation of the probability of an atom pair being found at distance, r. In this study a Q_{max} = 40 $Å^{-1}$ was used.

Analysis of the PDF data was performed using PDFgui[27] to provide a structural refinement. The refinement used the ceria fluorite structure. The refined parameters used were general scale factor, lattice parameter, particle diameter, U_{iso} for both cerium and oxygen atoms as well as oxygen occupancy. R_w is a measure of the 'goodness of fit' produced by PDFgui. The values of the refined U_{iso} parameters for PDF data is higher than those obtained from Rietveld refinement. This is due to the multiplication of the data by Q being Fourier transformed therefore amplifying any noise at high Q.

3.5 X-ray Total Scattering

3.5.1 Reciprocal Space refinement

Analysis of X-ray Bragg diffraction data was performed in conjunction with the neutron diffraction data.

3.5.2 Real Space refinement

Fit2D[18] was initially used to process the 2D detector images to give 1D diffraction patterns of Q vs intensity. PDFgetX2[28] was utilised to process the raw data. This program corrects such as sample container and Compton scattering. The Q_{min} and Q_{max} were 1.75 and 26 $Å^{-1}$ respectively. The real space refinement of the X-ray total scattering data was performed in the same manner seen for neutron total scattering data, though not in combination, due to software limitations.

3.6 XAS data correction and refinement

The XAS data is processed using EDA[29] software for both K- and L_3-edge. An additional correction was applied to the L_3-edge data to model a double excitation event at 5856 eV.[30] Artemis[21] was used to analyse the EXAFS *($\chi(k)$)* data to extract structural parameters. Phase-shifts and amplitude factors were calculated using FEFF6l using crystallographic data of ceria fluorite structure Hedin-Lundqvist potentials were used to calculate phase shifts and backscattering factors. For the L_3-edge the fitting was performed between k = 2.89 and 9.18

$Å^{-1}$ and r = 1 and 2.60 Å. For the K-edge the fitting was performed between k = 2.01 and 14.76 $Å^{-1}$ and r = 1 and 5.5 Å. The amplitude reduction factor (SO2) was refined using ceria NIST as a reference material with a fixed coordination number of 8 for the first Ce-O path. These values were 0.72 for the L3-edge and 1.00 for the K-edge. Simultaneous combined edge analysis was performed that gave satisfactory fits for respective data sets.

3.7 Results and Discussion

First the results from the combined X-ray and Neutron diffraction data are presented followed by XANES and EXAFS (combined refinement of both L_3 and K-edge EXAFS data) then finally the analysis of PDF data along with RMC modelling describing the nature of disorder present in the ceria materials is shown.

3.7.1 Joint X-ray and Neutron Rietveld refinement

The diffraction patterns of all the four samples recorded using Neutron and X-ray radiations are shown in Figure 3-2. The diffraction patterns show phase pure samples but show considerable broadening in many of the reflections indicating the particle sizes of the synthesised samples are significantly smaller compared to the NIST standard. The combination of Neutrons and X-rays is useful as they interact with the nuclei and electron density, respectively. The interaction with many low-Z materials is stronger with neutrons than X-rays. The neutron scattering cross sections for Ce and O are 2.94 and 4.232 barns respectively[31] whilst the X-ray scattering cross section for cerium is larger than that of oxygen.[32] This allows the emphasis of both cerium and oxygen depending on the radiation source, giving a more accurate overview of atomic arrangement within ceria.

A combined Rietveld refinement of the neutron and X-ray data was performed to yield a single structural model for each sample**.** The Rietveld refinements of all 4 samples show that the Bragg peaks correspond to the ceria fluorite structure (Figure 3-3 and Figure 3-4). Table 3-1 shows the refined lattice and structural parameters showing they are relatively similar. Peak broadening for the synthesised ceria samples is indicative of a smaller crystallite size.

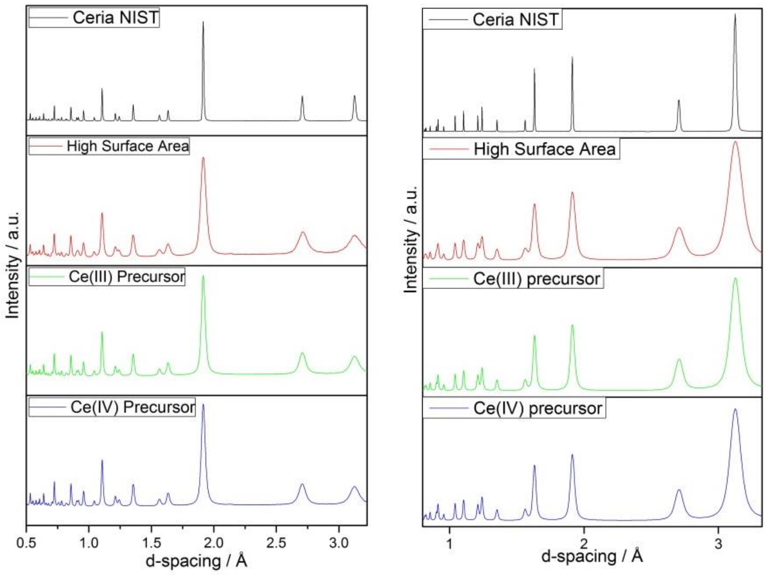

Figure 3-2: Neutron Diffraction patterns (Left) and X-ray Diffraction patterns (Right) for the 4 samples are shown. These show subtle variations in peak position, intensity and peak broadening indicative of changes in lattice parameter, crystallite size, atomic disorder etc.

The refinement of the atomic displacement parameters (ADPs) shows that the synthesised samples have greater disorder with respect to the ceria NIST standard. Though it is interesting to note that the ADPs for the Ce (III) precursor ceria sample have similar values for that of the ceria NIST. The refined values of the atom occupancies show that all samples are stoichiometric to within experimental error.

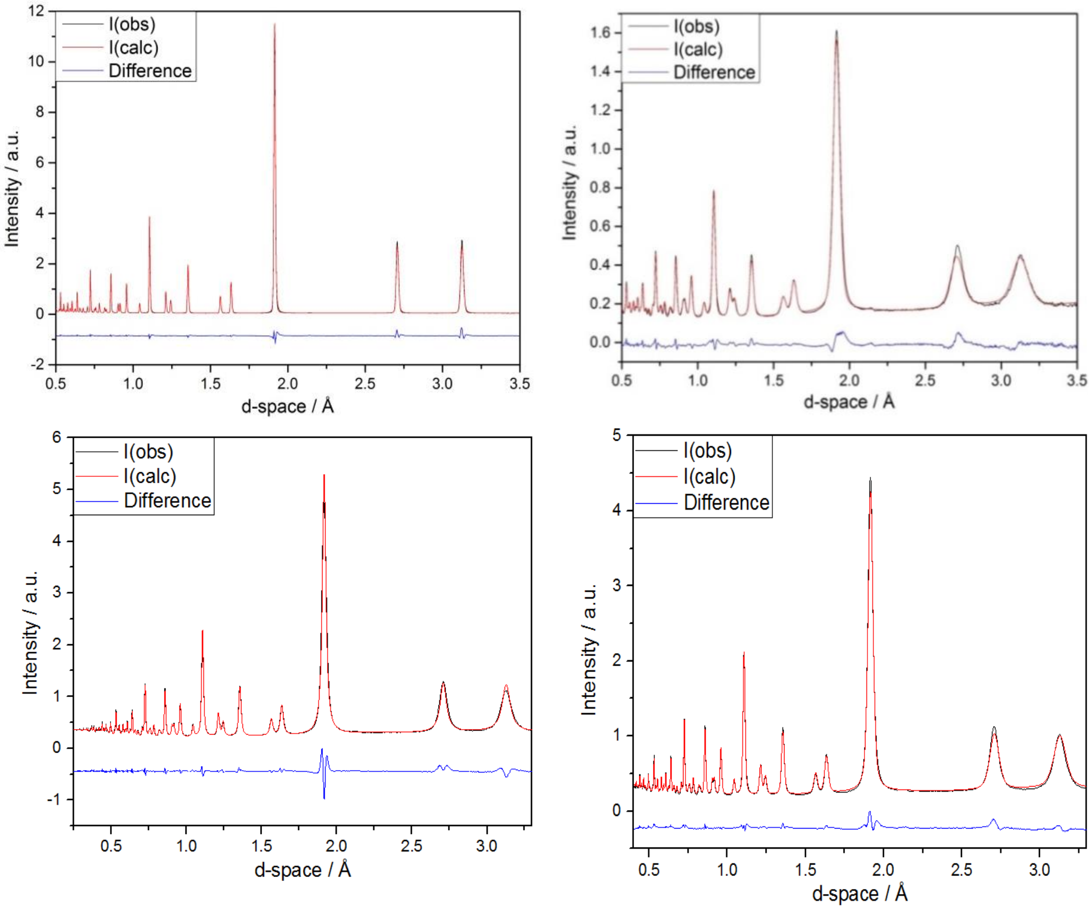

Figure 3-3: Comparison of observed (Iobs) and calculated (Icalc) neutron diffraction pattern: (Top left) Ceria NIST, (Top right) HSA Ceria, (Bottom left) Ceria prepared from Ce (III) precursor and (Bottom right) for Ceria prepared from Ce (IV) Precursor.

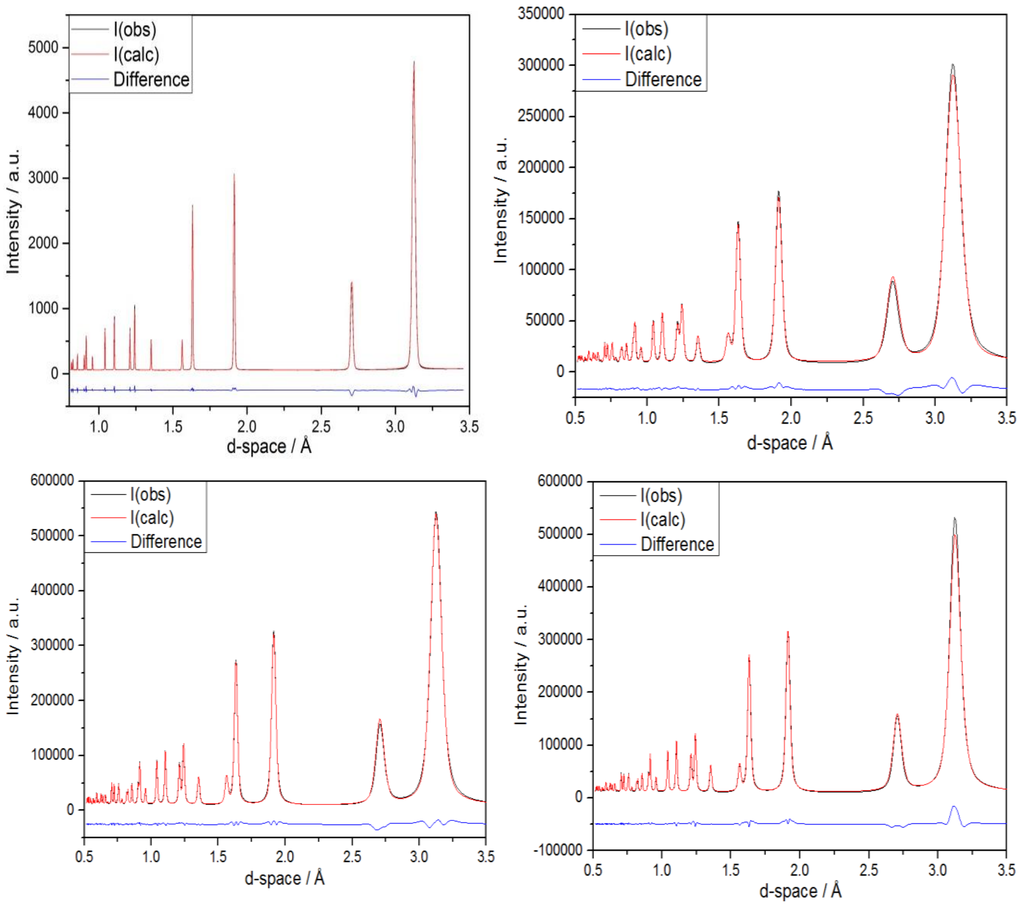

Figure 3-4: Comparison of observed (Iobs) and calculated (Icalc) X-ray diffraction patterns: (Top left) Ceria NIST, (Top right) HSA Ceria, (Bottom left) Ceria prepared from Ce (III) precursor and (Bottom right) for Ceria prepared from Ce (IV) Precursor.

Table 3-1: Results of Rietveld refinement of joint X-ray and neutron diffraction data of four Ceria materials. *fixed as the diffraction standard and zero refined and set for other samples.

	Ceria NIST	HSA	Ce (III) Precursor	Ce (IV) Precursor
a / Å	5.411651*	5.4099(37)	5.4121(79)	5.4128(31)
U_{iso} Ce / $Å^2$	0.003285(27)	0.00431(4)	0.00364(4)	0.00437(4)
U_{iso} O / $Å^2$	0.00558(18)	0.008199(35)	0.00572(4)	0.007624(26)
Occupancy Ce / a.u.	0.998(1)	0.996(1)	1.00(1)	0.995(1)
Occupancy O / a.u.	1.004(1)	1.005(1)	1.000(1)	1.004(1)
R_{wp} factor / %	4.7	4.01	3.21	3.88

3.7.2 XAS analysis

An X-ray absorption spectroscopic study at the Ce L_3-edge was used to understand whether any local structural disorder and mixed oxidation states present in the system. The datasets (Figure 3-5) reveals that for all four ceria samples, Cerium ions are found to be principally in the +4 oxidation states as a characteristic doublet is seen, marked as **iii** and **iv**. The XANES region has a characteristic pre-edge feature (feature A at 5719 eV) which has been assigned to delocalisation of the d orbital at the bottom of the conduction band within large clusters, 2p→5d transition.[33] Feature **ii** in the XANES is a low-energy shoulder relating to a $2p \rightarrow 4f^1 5de_g \underline{L}$ transition at 5724 eV due to the crystal-field splitting of the Ce 5d states.[34] With **iii** being $2p \rightarrow 4f^1 5dt_{2g} \underline{L}$ transition at 5728 eV.[34] Here the experimental crystal-field energy splitting for the Ce 5d is approximately 4 eV which is in good agreement with previously published experimental and theoretical values of 3.6 eV[35] and 4 eV[33] respectively. **iv** is then associated to the $2p \rightarrow 4f^0 5d$ transition at 5735 eV.

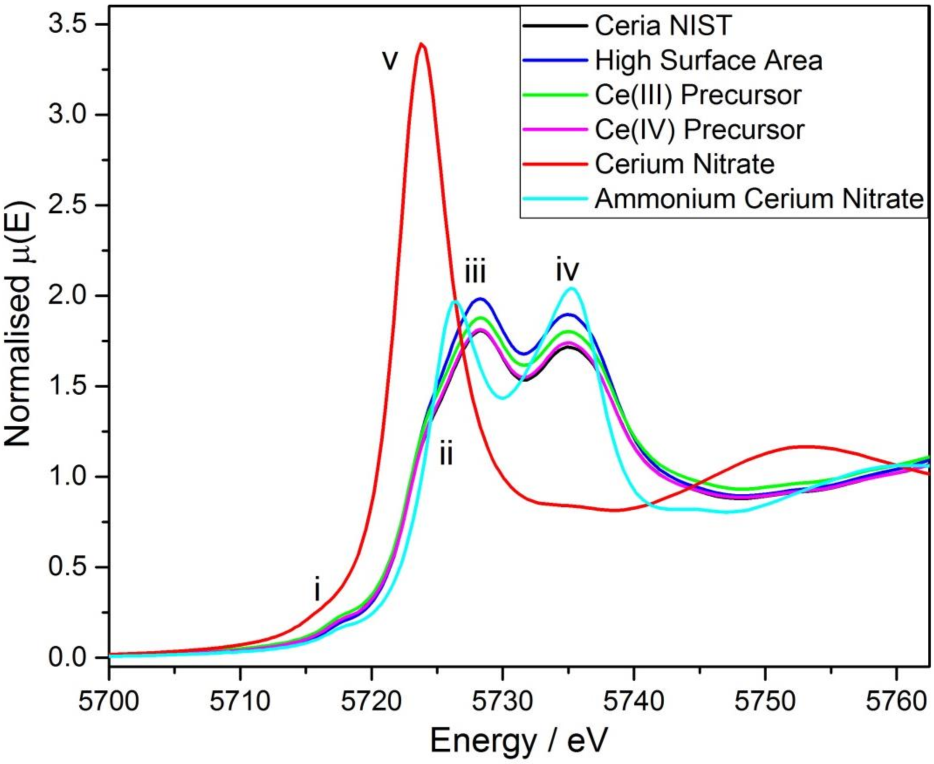

Figure 3-5: A comparison of the L3-edge for all four Ceria samples and Cerium Nitrate and Ammonium Cerium Nitrate standards with characteristic features labelled. i, pre-edge feature associated to the delocalisation of the d orbital at the bottom of the conduction band within large clusters. ii, a low energy shoulder associated to the crystal-field splitting within the cubic fluorite structure. iii and iv the characteristic doublet for the 2p→4f0,15d transitions. v, singlet for the 2p→4f15d for Ce atom with 3+ oxidation state[35]

Figure 3-5 also shows the XANES observed for Cerium Nitrate, where Ce is in +3 oxidation state, which characteristically shows a singlet at 5724 eV associated to a 2p→4f^{1}5d transition. Ammonium Cerium nitrate is also shown, here the Ce is in a Ce (IV) oxidation state, as seen by the distinctive doublet feature, however there is no crystal-field

XANES analysis was performed on all four samples and the results are given in Table 3-2. The analysis indicates that all the samples have spectral features that appear closely similar in energy for Ce^{4+} with peak assignments made according the aforementioned transitions using the Athena software package. [25] A large error in position of the pre-edge feature (i) is due the magnitude of this feature being small, as can be seen in Figure 3-6. Four Gaussian peaks are satisfactory to replicate the experimental data within good agreement in position of the peaks across all samples. The edge-position is given from the position of the arctangent function and is consistent for all four samples. As the peak positions and edge position are consistent over all the samples it can be concluded that they are all close to the ideal stoichiometry with only subtle differences.

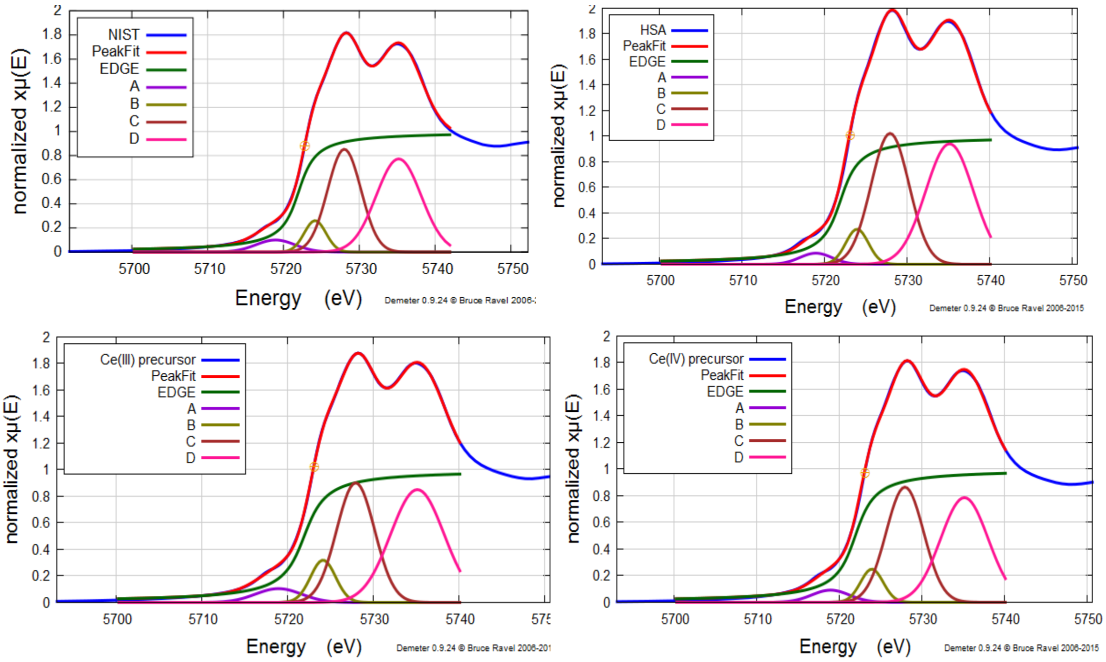

Figure 3-6: Typical XANES peak fitting showing the Ceria NIST (Top left), HSA Ceria (Top right), (Bottom left) Ceria prepared from Ce (III) precursor and (Bottom right) for Ceria prepared from Ce (IV) Precursor with component peaks visible. The edge structure has been fitted with an arctangent function and 4 Gaussian peaks associated to different transitions that have been identified within crystalline Ceria. i, pre-edge feature associated to the delocalisation of the d orbital at the bottom of the conduction band within large clusters. ii, a low energy shoulder associated to the crystal-field splitting within the cubic fluorite structure. iii and iv the characteristic doublet for the 2p→4f0,15d transitions. v, singlet for the 2p→4f15d for Ce atom with 3+ oxidation state[35].

Table 3-2: Results of XANES peak fitting using the Ce L3 edge XAS data

	Sample			
Peak Position / eV	**Ceria NIST**	**HSA**	**Ce (III) Precursor**	**Ce (IV) Precursor**
Edge Position	**5722.0 ± 0.3**	**5722.4 ± 0.3**	**5722.0 ± 0.4**	**5722.1 ± 0.3**
(i) $2p \rightarrow 5d$	**5719 ± 3**	**5719 ± 3**	**5719 ± 3**	**5719 ± 3**
(ii) $2p\rightarrow4f^1 5de_g\underline{L}$	**5724.1 ± 0.2**	**5724.0 ± 0.5**	**5724.2 ± 0.2**	**5724.0 ± 0.3**
(iii) $2p\rightarrow4f^1 5dt_{2g}\underline{L}$	**5728.0 ± 0.1**	**5728.0 ± 0.1**	**5728.0 ± 0.1**	**5728.0 ± 0.1**
(iv) $2p\rightarrow4f^0 5d$	**5735.2 ± 0.1**	**5735.2 ± 0.1**	**5735.2 ± 0.1**	**5735.2 ± 0.1**

3.7.3 Extended X-ray absorption fine structure

Analysis of the Ce L_3 edge EXAFS data was performed, assuming the Ceria NIST sample does not suffer from particle size affects and is defect free so has been used to determine the amplitude reduction factors (SO2). The EXAFS fitting was performed in r-space, though a correction is needed to remove the double excitation component in order obtain reliable structural information from the L_3 edge data. This was performed by fitting a Lorentzian peak (in $\chi(k)$) to model the transition resonance to the data with 3 parameters: width, height and position,[36] corresponding to a $2p,4d\rightarrow5d^2$ transition at 5854 eV[30] for a double excitation event.

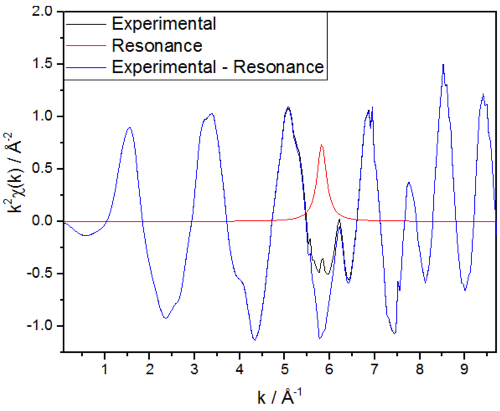

Figure 3-7: A comparison of initial and final χ(k) for the NIST Ceria sample illustrating the Lorentzian peak fitted for removal of the 2p,4d→5d2 resonance feature on the Ce L3 edge.

Figure 3-7 illustrates the fitting of the Lorentzian peak showing the initial and final χ(k). The refinement of the Ce-O distance without resonance correction was refined to be 2.30(8) Å which is similar to 2.30(6) Å reported by Fonda el al[30] and is significantly smaller than the crystallographic value of 2.343 Å.

The L_3-edge spectra provides high quality information relating to the first shell, though is unable to provide accurate parameters regarding second neighbour Ce-Ce distance, due to the limited k range as the Ce L_2 edge overlaps at 6164 eV or approximately k = 10.4 Å^{-1}. More accurate information on the second and higher neighbour contributions was obtained on the Ce K-edge. As there is core-hole lifetime broadening at high energy absorption edge, the K-edge data may not provide accurate structural parameters of the first shell. Therefore, a combined refinement of Ce L_3 and K-edges to determine accurately the first and higher neighbour correlations was required.

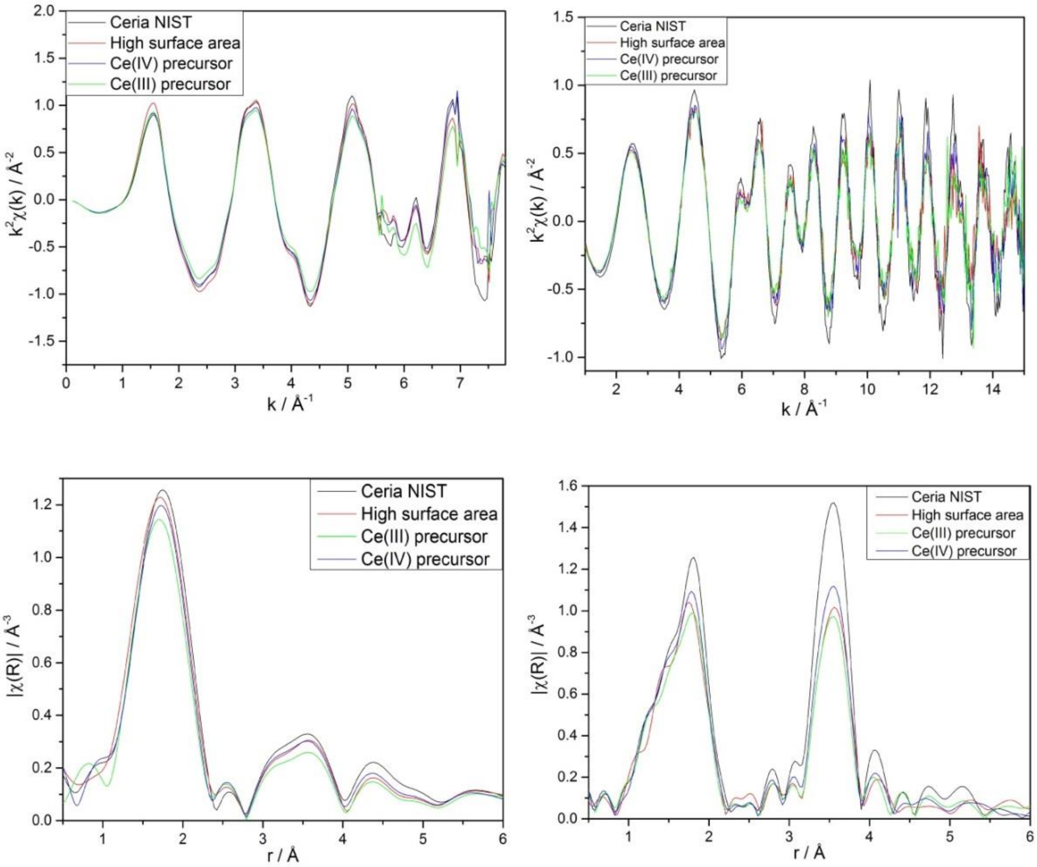

Figure 3-8 shows a comparison of the $k_2\chi(k)$ and $|\chi(R)|$ of the four samples for the L_3- and K-edge respectively. Where the $\chi(k)$ has been Fourier transformed between k of 2.89 and 9.18 Å^{-1} for the L_3-edge data and between 2.01 and 14.76 Å^{-1} for the K-edge data. The r-space data shows that all three samples are closely similar to that of ceria NIST standard, whilst having variations in peak intensity suggesting some alterations in the local structure.

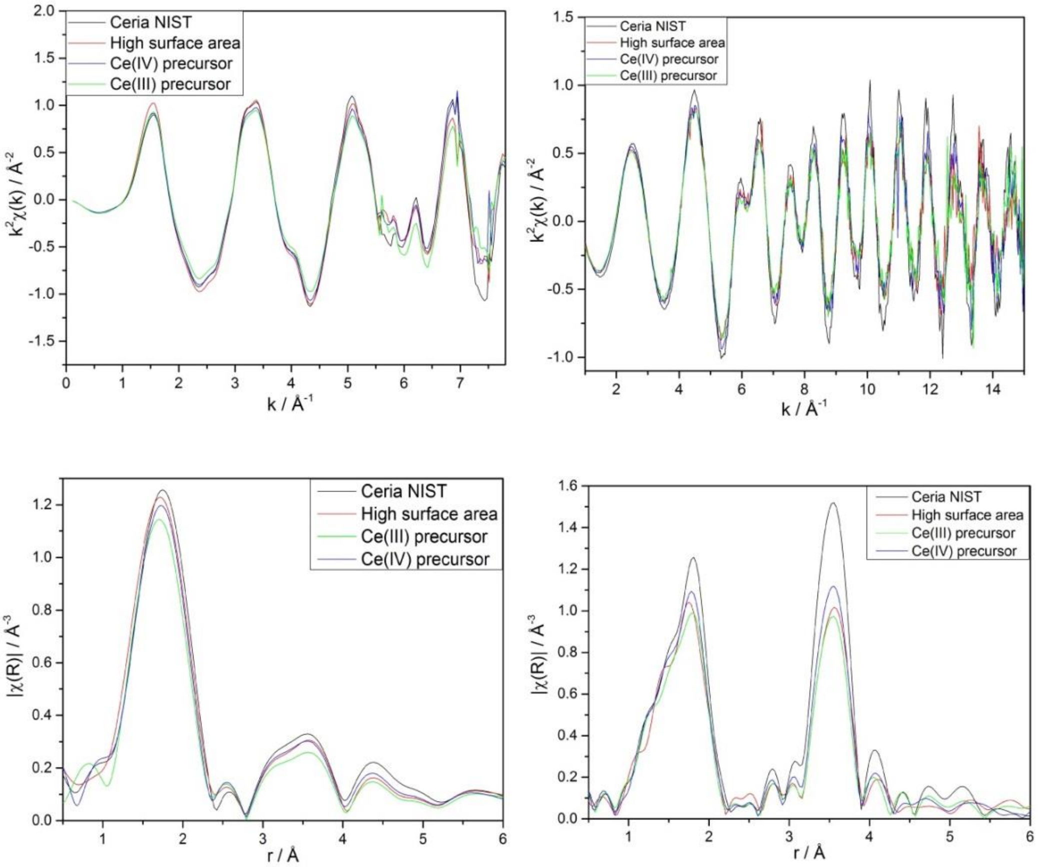

Figure 3-8: A comparison of the k2χ(k) (Top left) and |χ(R)| (Bottom left) for all four samples measured at the L_3-edge. A comparison of the k2χ(k) (Top right) and |χ(R)| (Bottom right) for all four samples measured at the K-edge. This shows all have the ceria fluorite structure with subtle subtle variations in intensity and peak position.

A joint edge refinement allows for the importance of both first and second shell contributions in r-space. Figure 3-9 and Figure 3-10 illustrate the experimental data and the calculated fit obtained with this approach.

Table 3-3: Structural parameters obtained using combined EXAFS of the L_3- and K-edges.

Sample	Path	N	σ^2	R / Å
Ceria NIST	O.1	8**	0.0044 ± 0.00023	2.31 ± 0.004
	Ce.1*	12**	0.00038 ± 0.00042	3.34 ± 0.006
HSA	O.1	8.1 ± 0.8	0.0064 ± 0.00028	2.30 ± 0.003
	Ce.1*	9.2 ± 0.9	0.0045 ± 0.00065	3.83 ± 0.008
Ce (III) Precursor	O.1	7.8 ± 0.8	0.0066 ± 0.00053	2.30 ± 0.002
	Ce.1*	8.9 ± 0.9	0.0046 ± 0.00025	3.84 ± 0.007
Ce (IV) Precursor	O.1	7.7 ± 0.8	0.0060 ± 0.00032	2.31 ± 0.003
	Ce.1*	9.4 ± 0.9	0.0042 ± 0.00064	3.83 ± 0.007

*refined using K-edge only
**held constant for refinement of amplitude reduction factor

Table 3-3 shows the results obtained from the best fit for the ceria samples. The refinement of the first Ce-O path shows that the synthesised samples have larger σ^2 values than the highly crystalline ceria NIST, in agreement with the combined diffraction analysis. With respect to crystallographic values, contraction of the first shell is observed with all samples showing smaller than 2.34 Å.

For all the synthesised samples the coordination number of the nearest Ce-Ce neighbour is significantly lower in comparison to the ceria NIST standard and σ^2 appears to be slightly higher for the Ce-Ce path compared to ceria NIST. The decrease in coordination number could be interpreted as due to particle size effect or cation defects present in the system. As the Ce-O coordination numbers appear to be close that of NIST standard, this implies that the ceria particles are oxygen terminated.

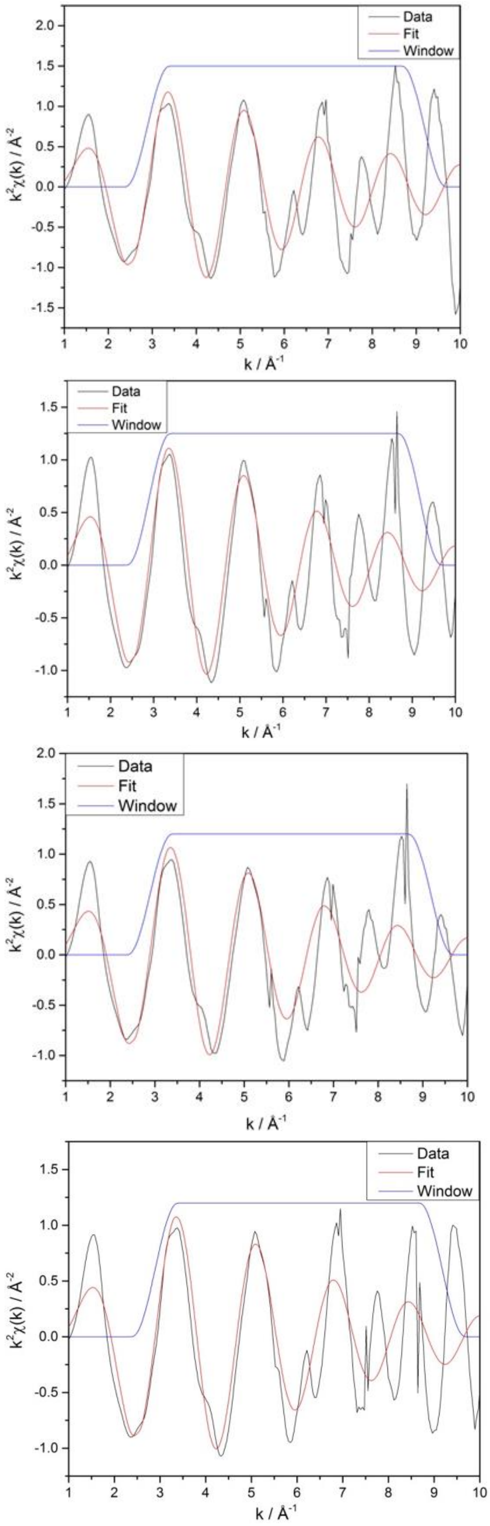

Figure 3-9: A comparison of the k2χ(k) data and fit: Top Ceria NIST, 2nd HSA Ceria, 3rd Ceria prepared from Ce (III) precursor and bottom Ceria prepared from Ce (IV) precursor.

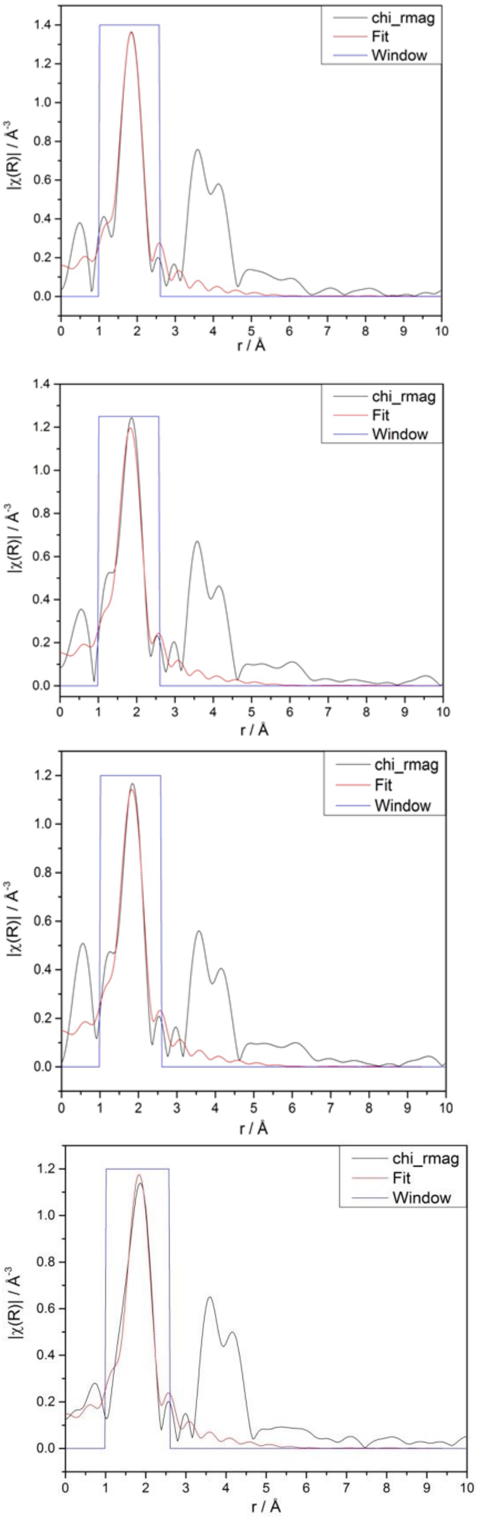

Figure 3-10: A comparison of the |χ(R)| data and fit: Top Ceria NIST, 2nd HSA Ceria, 3rd Ceria prepared from Ce (III) precursor and bottom Ceria prepared from Ce (IV) precursor.

3.7.4 X-ray and Neutron total scattering data analysis

Pair distribution function (PDF) analysis since it allows the structure to be probed over a larger R-range in contrast with XAS. PDF analysis is a Rietveld-like approach wherein a structural model is refined to obtain the best possible fit to the PDF, thus producing a model that is biased to local rather than long-range structure. The X-ray and neutron PDF data sets were analysed independently, due to limitations in the analysis software.

3.7.4.1 Neutron PDF data analysis

In contrast to the Rietveld refinement, different refined parameters are found when looking at the short and medium range structure. The refinement of the lattice parameter for all samples shows a different trend to that seen in the Rietveld refinement. Figure 3-11 and Figure 3-12 shows a comparison of the PDFs for all four samples alongside an example fit undertaken on the Ceria NIST sample. This shows that the local structure of all the samples is consistent with the fluorite structure. In the synthesized samples, the amplitude of the oscillations in D(r) shows significant dampening relative to the ceria NIST sample. Since the instrumental parameters were the same in all cases, this suggests that the HSA ceria, and the samples prepared using Ce (III) and Ce (IV) precursors have smaller crystallite size.

It is also observed that the synthesised samples have higher ADP parameters than that of the reference material. The refined occupancies of both cerium and oxygen atoms are consistent with a fully stoichiometric material.

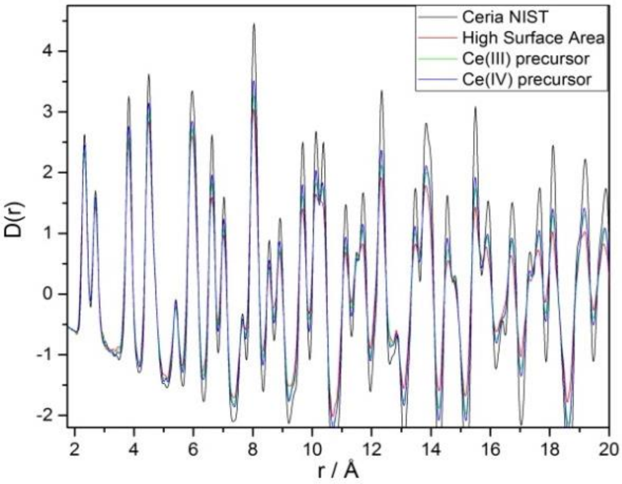

Figure 3-11: Comparison of the neutron G(r) data and calculated G(r) for Ceria NIST

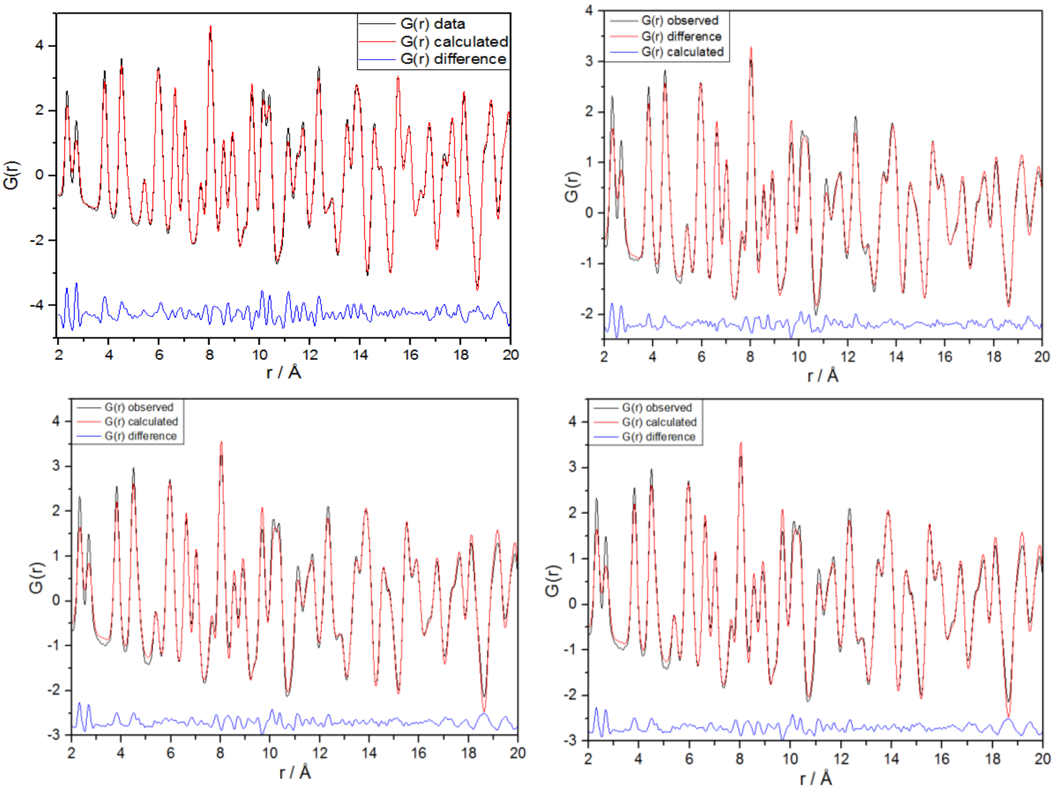

Figure 3-12: Comparison of the neutron G(r) data and calculated G(r): (Top left) Ceria NIST, (Top right) HSA Ceria, (Bottom left) Ceria prepared from Ce (III) precursor and (Bottom right) for Ceria prepared from Ce (IV) Precursor.

Table 3-4: Results of NPDF refinement of four Ceria materials.

	Ceria NIST	HSA	Ce (III) Precursor	Ce (IV) Precursor
a / Å	5.412(01)	5.404(71)	5.409(33)	5.407(93)
U_{iso} Ce / Å^2	0.0038(04)	0.00671(47)	0.0059(94)	0.0049(63)
U_{iso} O / Å^2	0.0085(95)	0.012(30)	0.012(38)	0.011(02)
Occupancy Ce / a.u.	1.01(70)	1.01(36)	1.00(60)	1.00(72)
Occupancy O / a.u.	1.01(55)	1.03(47)	1.02(79)	1.02(87)
R_w factor / %	8.7144	13.4436	14.424	14.243

3.7.4.2 X-ray PDF data analysis

Figure 3-13 and Figure 3-14 shows a comparison of the PDFs for all four samples. The modelling of XPDF data was performed with fixed occupancies from the equivalent NPDF analysis. The refined ADPs shows that the HSA, Ce (III) and Ce (IV) precursor ceria samples are more disordered than the ceria NIST material. In addition, the dampening of amplitudes in higher r region in G(r) is greater for the synthesised ceria samples in comparison to the ceria NIST supporting the NPDF results.

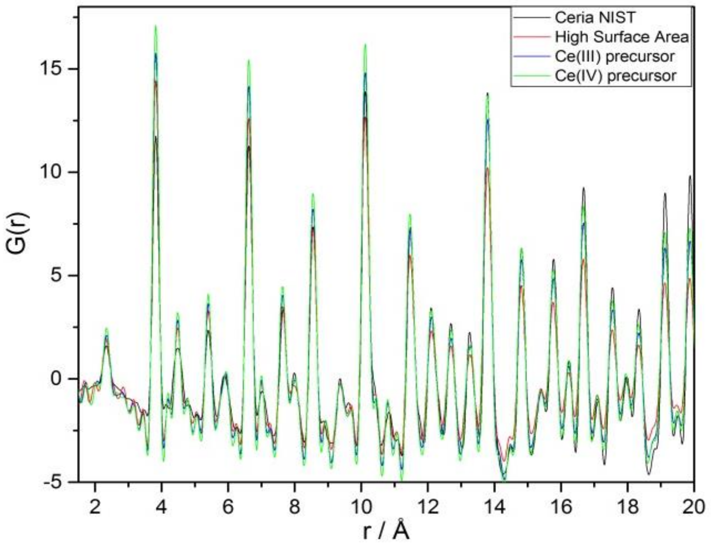

Figure 3-13: Comparison of the X-ray G(r) data and calculated G(r) for Ceria NIST

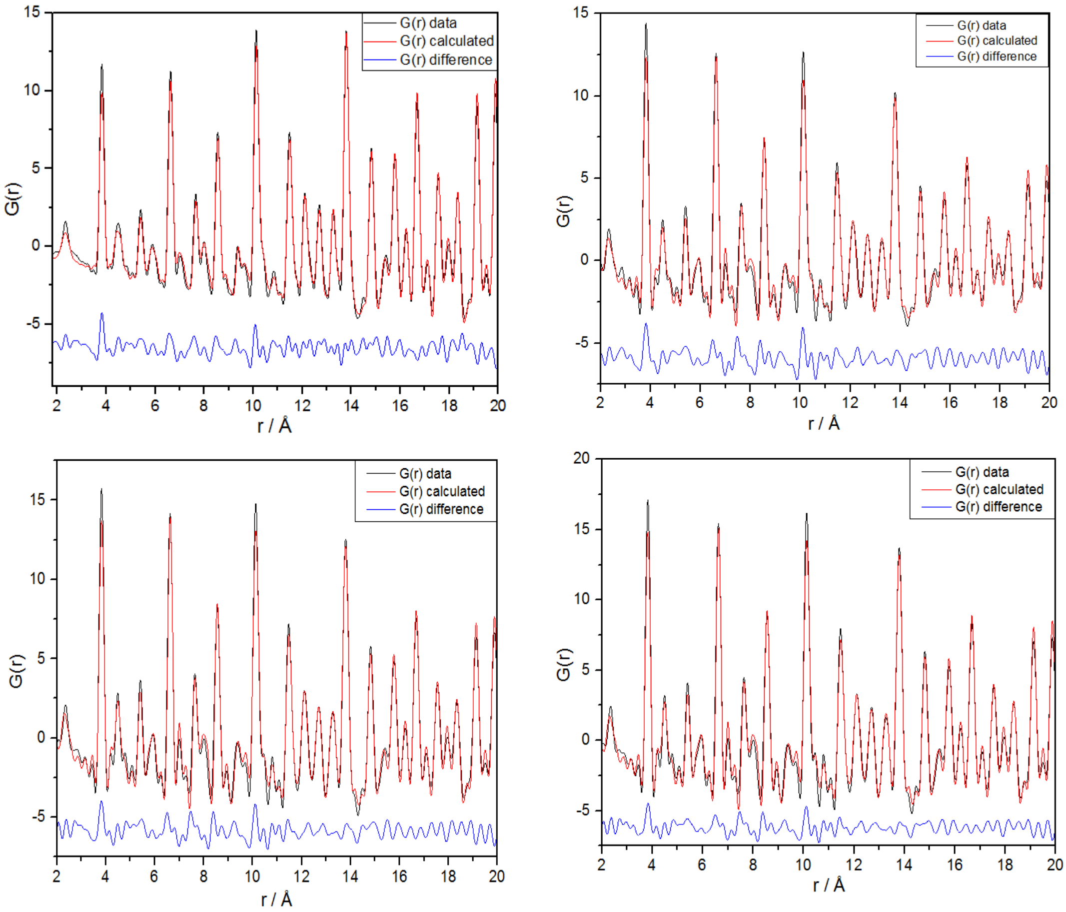

Figure 3-14: Comparison of the neutron G(r) data and calculated G(r): (Top left) Ceria NIST, (Top right) HSA Ceria, (Bottom left) Ceria prepared from Ce (III) precursor and (Bottom right) for Ceria prepared from Ce (IV) Precursor.

Table 3-5: Results of XPDF refinement of four Ceria materials.

	Ceria NIST	HSA	Ce (III) Precursor	Ce (IV) Precursor
a / Å	5.411(23)	5.408(34)	5.412(07)	5.407(97)
U_{iso} Ce / Å^2	0.0050(85)	0.0055(22)	0.0050(72)	0.0045(98)
U_{iso} O / Å^2	0.027(34)	0.039(81)	0.0050(72)	0.0045(98)
Occupancy Ce / a.u.	1.01(70)	1.01(36)	1.00(60)	1.00(72)
Occupancy O / a.u.	1.01(55)	1.03(47)	1.02(79)	1.02(87)
R_w factor / %	11.24	15.0585	13.8793	14.1365

3.8 Size effect

Both combined XRD/ND analysis and independent XPDF and NPDF analysis suggest all the system studied here are stoichiometric with site occupancies close to 1 (see Figure 3-15). Whereas, EXAFS analysis indicates that the synthesised ceria sample have lower coordination number for the Ce-Ce second neighbour pair-correlation. Although the Ce-O coordination number for samples prepared using Ce (III) and Ce (IV) precursors is slightly less than bulk. When combined, these observations suggest that the particles are oxygen terminated, which would result in full or nearly-full Ce-O shells, but under-coordinated Ce-Ce "shells".

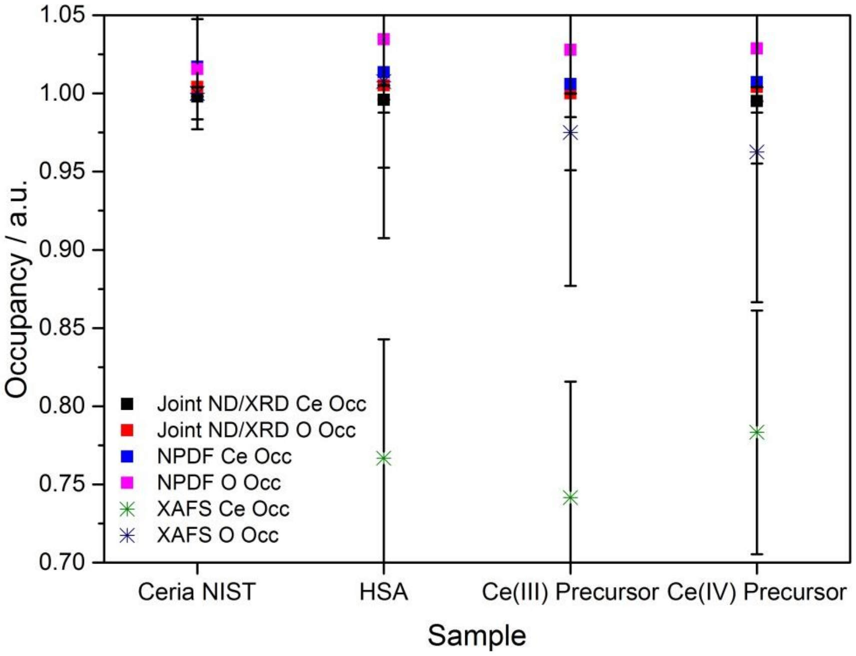

Figure 3-15: A comparison of the Cerium and Oxygen Occupancies for all four materials analysed with different techniques. In the case of EXAFS, the occupancy number refers to the actual coordination number divided by 8 (for Ce-O) and 12 (for Ce-Ce)

The occupancies based on EXAFS analysis are given in fractions obtained by dividing the obtained coordination number with bulk value (8 for Ce-O and 12 for Ce-Ce). Therefore, combining the information gained from X-ray and neutron diffraction studies, it is proposed that the decrease seen in the Ce-Ce coordination number is likely to be due to size effect rather than oxygen defects within the structure.

A comparison of the particle/crystallite size determined from joint ND/XRD, NPDF, XPDF and XAFS analysis shows different values. Sizes obtained from joint XRD/ND based analysis is based purely on any crystallites that have the fluorite structure and ignores any contribution from very small and/or amorphous particles. Whereas XPDF, NPDF and

EXAFS give an average information on all types of particle sizes present in the sample, which would explain why the values observed are lower than those seen from joint XRD/ND Rietveld analysis.

The comparison of particle sizes (See Figure 3-16) obtained from all the different techniques show that HSA, Ce (III) and Ce (IV) precursor ceria samples have a smaller particle size than that of the reference material.

The results obtained from diffraction based analysis give an average crystallite size assuming spherical particle. Particle sizes obtained from N- and XPDF are obtained from analysing the dampening in the intensity of G(r) with increasing r, assuming a spherical particle. EXAFS analysis assumes Ceria NIST to be a bulk crystalline material and the sizes for the synthesised materials were obtained by considering the change in coordination number of the Ce-Ce (second neighbour) with respect to the NIST standard then comparing the refined values with respect to model particles. The variations seen between these methods is that diffraction analysis takes only the crystalline components of the sample and PDF analysis takes into account both crystalline and poorly-crystalline part of the sample. Both methods estimate particle size based on the experimental data; EXAFS derived particle size are based on an assumed model to match the coordination number. It has been noted that when cross-correlating EXAFS with other techniques, in particular TEM and XRD EXAFS gives smaller sizes.[37]

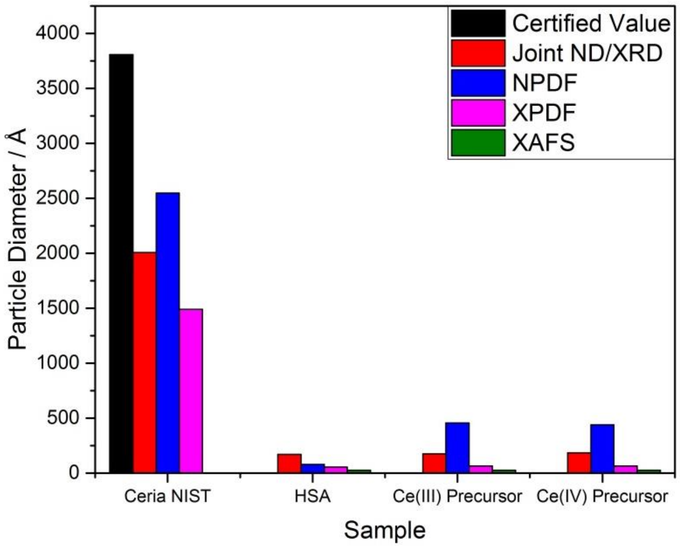

Figure 3-16: A comparison of particle sizes derived from different techniques. The certified value is the reported value from NIST[39]

3.9 Disorder

To understand the nature of disorder present in the synthesised samples, reverse Monte Carlo (RMC) analysis of the neutron data using RMCProfile software was performed, as Rietveld studies clearly suggested that the neutron scattering data are better suited for this analysis due to the X-ray data being dominated by Ce-Ce correlations. RMCProfile modelling was implemented using a 6x6x6 supercell constructed from the Rietveld-obtained model. The supercell comprised of 864 cerium cations and 1728 oxygen anions. For each material, 10 simulations were carried out starting from the perfect fluorite structure then the atoms were randomly moved by a set amount to imitate disorder before modelling. The results were averaged over all 10 simulations per sample to minimize the potential for uniqueness problems.

The advantage of using the RMCProfile suite of software is that it takes simultaneously the Bragg diffraction data and the PDF data (one can define more than one r-range so that short and medium range order can be considered) and analyse them together to get the best model that fits both short, medium and long-range concurrently. For these samples, the G(r) datasets were separated into 2 distinct ranges, with one being fitted between 1 – 5 Å and the other between 1 – 15 Å, in order to give a greater weighting to the short range data.

The best fits obtained between experimental neutron diffraction data, NPDF, for two different ranges are shown in Figure 3-17. In all cases, the Bragg data and the short-range NPDF data are fitted very well. However, the quality of the fits decreases with increasing r. This occurs as the software cannot take into account the particle size effects and instrumental resolution when fitting in real space.

The output models of the RMCProfile analysis can be visualised by reducing the 6x6x6 supercell down onto the original unit cell, overlaying all cerium and oxygen atoms together into “clouds” which are roughly equivalent to thermal ellipsoids generated from Rietveld refinement. The models generated based on this procedure are displayed in Marchbank *et al*.[38] It is observed that the distribution of both Ce and O atoms are very narrow in the case of ceria NIST in comparison to the synthesised samples. In particular, the oxygen atoms in the HSA20 sample show maximum deviation from their ideal positions. MSD values of Ce-O distances follow the trend HSA> Ce (IV) precursor > Ce (III) precursor >> NIST standard.[38] Therefore, the disorder present in the oxygen could be one of the reasons for HSA to be more effective in oxygen mobility and catalytic processes.

Ceria NIST

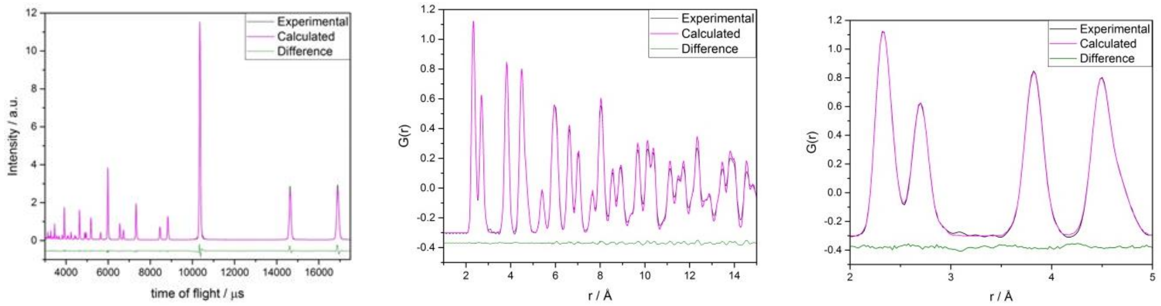

High Surface Area Ceria

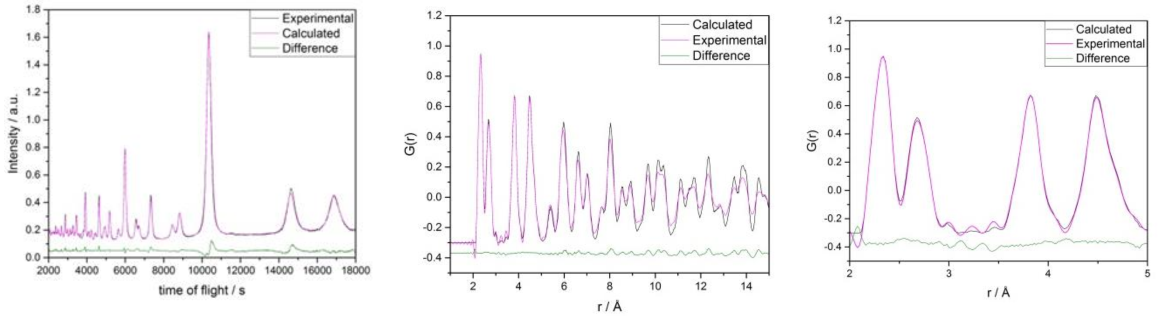

Ce (III) Precursor

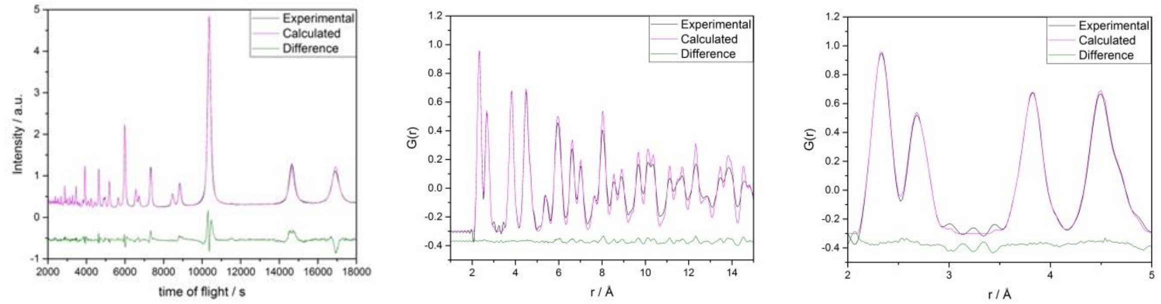

Ce (IV) Precursor

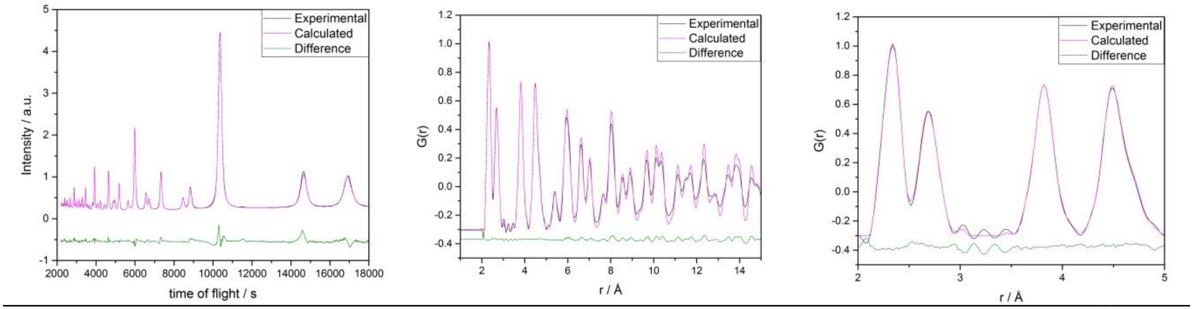

Figure 3-17: Comparison of the calculated and experimental data sets for Bragg Diffraction (Left), G(r) 1 – 15 Å (Centre) and G(r) 1 – 5 Å (Right)

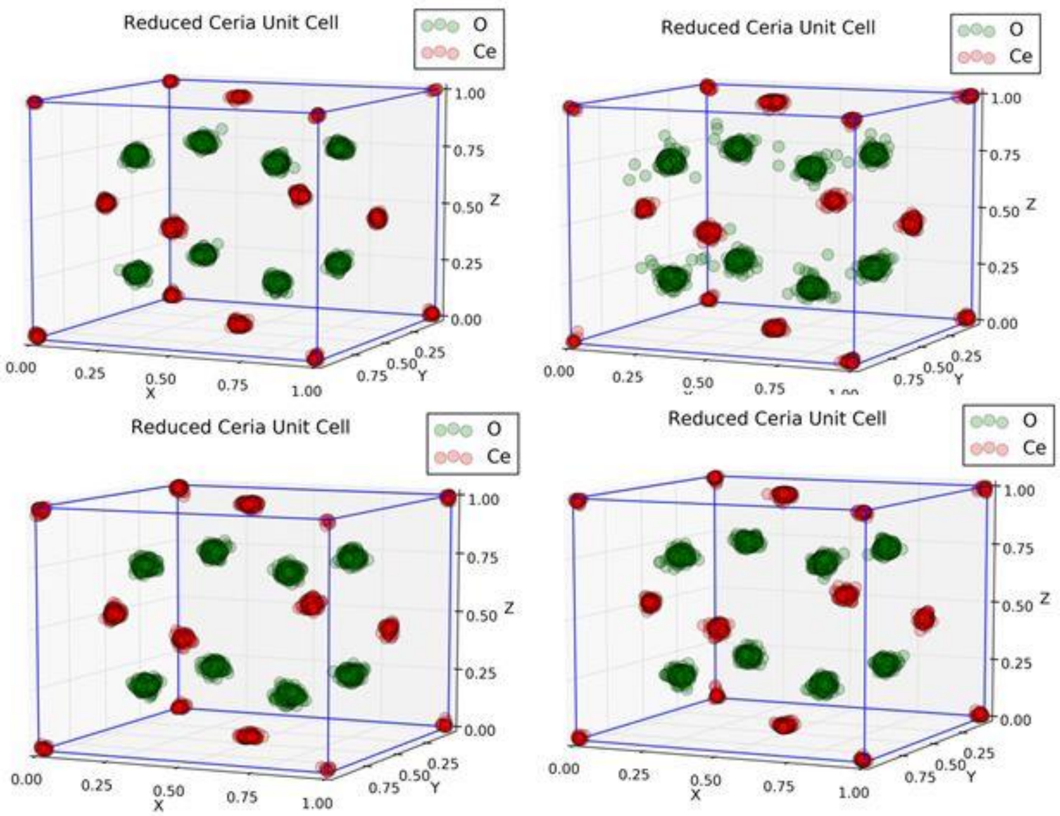

Figure 3-18: Reduced configuration to an over laid single unit cell. NIST ceria standard (top left), HSA ceria (top right), Ce (III) precursor (bottom left), Ce (IV) precursor (bottom right)[38]

3.10 Summary

In this work it is shown that the reliance on purely one form of characterisation technique may give only a single viewpoint of the structure of the material, hence utilising more than one technique is important to understand the material characteristics. All the techniques used show that no matter the synthesis procedure, the phase pure ceria fluorite structure is observed and the composition is close to stoichiometric CeO_2. Combined Rietveld analysis of ND and XRD data shows that the HSA ceria, Ce (III) and Ce (IV) precursor ceria samples are more disordered than that of a ceria NIST standard. Neutron and X-ray PDF studies support this observation. Dampening of the amplitudes of the PDFs of the synthesized samples is observed at r > 10Å which indicates a smaller crystallite size compared to the NIST sample that has an average crystallite size of 380.6 nm.[39] EXAFS analysis of both the Ce L_3- and K-edges agrees with PDF analysis and Rietveld refinement of diffraction data showing crystallite sizes smaller than that of the NIST sample. EXAFS data analysis clearly indicates that the disorder is more in the oxygen site in all the synthesised samples compared to NIST standard and more significant disorder is seen for high-surface area material than other synthesised samples. It is difficult to say from these data whether the disorder associated with oxygen is related to the increased ratio of surface-oxygen in the smaller particles. More surface sensitive techniques that can determine structure near to the particle surface would be required to establish this. Analysis of the RMC models of all the materials further support the conclusion that more disorder is observed on the oxygen site for the ceria samples in comparison to the Ceria NIST material.

3.11 Bibliography

1 R. J. Farrauto and R. M. Heck, *Catal. Today*, 1999, **51**, 351–360.

2 J. Kašpar, P. Fornasiero and N. Hickey, *Catal. Today*, 2003, **77**, 419–449.

3 A. Trovarelli, Ed., *Catalysis by Ceria and Related Materials*, Imperial College Press, London, 2002.

4 A. Trovarelli, C. De Leitenburg, M. Boaro and G. Dolcetti, *Catal. Today*, 1999, **50**, 353–367.

5 V. A. M. Selvan, R. B. Anand and M. Udayakumar, *ARPN J. Eng. Appl. Sci.*, 2009, **4**, 1–6.

6 A. Trovarelli, *Catalysis by Ceria and Related Materials*, Imperial College Press, London, 2002.

7 R. M. Heck and R. J. Farrauto, *Appl. Catal., A*, 2001, **221**, 443–457.

8 R. Craciun, B. Shereck and R. J. Gorte, *Catal. Lett.*, 1998, **51**, 149–153.

9 P. Pantu, K. Kim and G. R. Gavalas, *Appl. Catal., A*, 2000, **193**, 203–214.

10 Y. I. Matatov-meytal and M. Sheintuch, *Ind. Eng. Chem. Res.*, 1998, **37**, 309–326.

11 R. I. Walton, *Prog. Cryst. Growth. Charact. Mater.*, 2011, **57**, 93–108.

12 E. Mamontov and T. Egami, *J. Phys. Chem. Solids*, 2000, **61**, 1345–1356.

13 H. M. Rietveld, *J. Appl. Crystallogr.*, 1969, **2**, 65–71.

14 E. Takeshi and S. J. L. Billinge, in *Underneath the Bragg Peaks Structural Analysis of Complex Materials*, eds. T. Egami and S. J. L. Billinge, Pergamon, 2012, vol. 16, pp. 1–25.

15 S. Yamazaki, T. Matsui, T. Ohashi and Y. Arita, *Solid State Ionics*, 2000, **136–137**, 913–920.

16 S. Hull, R. I. Smith, W. I. F. David, A. C. Hannon, J. Mayers and R. Cywinski, *Phys. B Condens. Matter*, 1992, **180–181**, 1000–1002.

17 O. Arnold, J. C. Bilheux, J. M. Borreguero, A. Buts, S. I. Campbell, L. Chapon, M. Doucet, N. Draper, R. Ferraz Leal, M. A. Gigg, V. E. Lynch, A. Markvardsen, D. J. Mikkelson, R. L. Mikkelson, R. Miller, K. Palmen, P. Parker, G. Passos, T. G. Perring, P. F. Peterson, S. Ren, M. A. Reuter, A. T. Savici, J. W. Taylor, R. J. Taylor, R. Tolchenov, W. Zhou and J. Zikovsky, *Nucl. Instruments Methods Phys. Res. Sect. A Accel. Spectrometers, Detect. Assoc. Equip.*, 2014, **764**, 156–166.

18 A. P. Hammersley, S. O. Svensson, M. Hanfland, A. N. Fitch and D. Hausermann, *High Press. Res.*, 1996, **14**, 235–248.

19 S. Nikitenko, A. M. Beale, A. M. J. Van Der Eerden, S. D. M. Jacques, O. Leynaud, M. G. O'Brien, D. Detollenaere, R. Kaptein, B. M. Weckhuysen and W. Bras, *J. Synchrotron Radiat.*, 2008, **15**, 632–640.

20 O. Mathon, A. Beteva, J. Borrel, D. Bugnazet, S. Gatla, R. Hino, I. Kantor, T. Mairs, M. Munoz, S. Pasternak, F. Perrin and S. Pascarelli, *J. Synchrotron Radiat.*, 2015, **22**, 1548–1554.

21 B. Ravel and M. Newville, *J. Synchrotron Radiat.*, 2005, **12**, 537–541.

22 J. J. Rehr, R. C. Albers, S. I. Zabinsky, A. L. Ankudinov and M. J. Eller, *Phys. Rev. B*, 1995, **52**, 2995.

23 B. H. Toby, *J. Appl. Crystallogr.*, 2001, **34**, 210–213.

24 A. C. Larson and R. B. Von Dreel, *Los Alamos Nation Lab. Rep. LAUR*, 1994, 86–748.

25 A. K. Soper, http://www.isis.stfc.ac.uk/instruments/sandals/data-analysis/gudrun8864.html, Date Accessed 05/10/2015.

26 M. G. Tucker, D. A. Keen, M. T. Dove, A. L. Goodwin and Q. Hui, *J. Phys. Condens. Matter*, 2007, **19**, 335218.

27 C. L. Farrow, P. Juhas, J. W. Liu, D. Bryndin, E. S. Božin, J. Bloch, T. Proffen and S. J. L. Billinge, *J. Phys. Condens. Matter*, 2007, **19**, 335219.

28 X. Qiu, J. W. Thompson and S. J. L. Billinge, *J. Appl. Crystallogr.*, 2004, **37**, 678.

29 A. Kuzmin, *Phys. B Condens. Matter*, 1995, **208**–**209**, 175–176.

30 J. Chaboy, A. Marcelli and T. A. Tyson, *Phys. Rev. B*, 1994, **49**, 11652.

31 V. F. Sears, *Neutron News*, 1992, **3**, 26–37.

32 W. H. McMaster, N. K. Del Grande, J. H. Mallett and J. H. Hubbell, *Lawrence Livermore Lab., Rep. UCRL-50174*, 1969.

33 A. V. Soldatov, T. S. Ivanchenko, S. Della Longa, A. Kotani, Y. Iwamoto and A. Bianconi, *Phys. Rev. B*, 1994, **50**, 5074–5080.

34 C. Paun, O. V Safonova, J. Szlachetko, P. M. Abdala, M. Nachtegaal, J. Sa, E. Kleymenov, A. Cervellino, F. Krumeich and J. A. van Bokhoven, *J. Phys. Chem. C*, 2012, **116**, 7312–7317.

35 J. Zhang, Z. Wu, T. Liu, T. Hu, Z. Wu and X. Ju, *J. Synchrotron Radiat.*, 2001, **8**, 531–532.

36 E. Fonda, D. Andreatta, P. E. Colavita and G. Vlaic, *J. Synchrotron Radiat.*, 1999, **6**, 34–42.

37 S. W. T. Price, N. Zonias, C.-K. Skylaris, T. I. Hyde, B. Ravel and A. E. Russell, *Phys. Rev. B*, 2012, **85**, 75439.

38 H. R. Marchbank, A. H. Clark, T. I. Hyde, H. Y. Playford, M. G. Tucker, D. Thompsett, J. M. Fisher, K. W. Chapman, K. A. Beyer, M. Monte, A. Longo and G. Sankar, *ChemPhysChem*, 2016, **17**, 3494–3503.

39 https://www-s.nist.gov/srmors/certificates/674B.pdf Date Accessed 28/03/2017

Chapter 4: *Insitu* Neutron Diffraction, X-ray Total scattering and X-ray absorption spectroscopy study of Platinum group metal loaded ceria under reducing conditions

4.1 Abstract

A combination of both x-ray and neutron in situ pair distribution function (PDF) analysis, Ce L_3- and K-edge, Pd K-edge and Pt L_3-edge XAS were performed on, plain high surface area ceria and 5wt% Pd and 5wt% Pt loaded high surface area ceria samples under reducing conditions. This allowed for a thorough and in depth study of how pure ceria behaves and the effect of Pd and Pt on the support and its behaviour under reducing conditions. Detailed analysis of PDF and XAS data for the pure ceria support show a reduction under heating in H_2:N_2 whilst under cooling ceria 'reoxidises' to it' original stoichiometry of CeO_2. In contrast both the addition of Pd and Pt to the ceria support shows enhanced reduction of the ceria upon heating and no or little reoxidation takes place upon cooling under a reducing atmosphere.

4.2 Introduction

Though ceria can be utilised within catalysis,[1] it is extensively used as a support for catalysts such as transition metals[2] or platinum group metals[3] (PGMs).[4] These can be used as a single metallic or in combination with other PGMs as a bimetallic system. These PGMs are costly but their long life makes them cost effective[5] and their ability to be dispersed onto a support will reduce the cost but increase efficiency due to an increased surface area to volume ratio[6] and noble metals can enhance the redox performance and the OSC of the support on which the PGM has been dispersed.[7–10]

This is further complicated by strong metal support interaction (SMSI) which describes the interaction between the metal and the metal support and how this affects the reactions. This effect was first reported by Tauser *et al.* investigating the reduction of metals supported on titania. This showed that CO and H_2 chemisorption was inhibited though not explicable by poisoning, sintering of metal particles and the encapsulation of metals.[11] This affect is important in three way catalysis whilst improve dispersion of the metals on a support as well as reduce sintering, for example the Pt-O-Ce interaction acts as an anchor point from which there is a limitation in the sintering of Pt particles on the surface support.[12] Furthermore the loading of PGMs on a ceria support aids in the surface reduction and removal of oxygen.[13]

In the case of Pd dispersed/loaded onto a ceria support, there is an increase in the OSC, catalytic ability and aid in the reduction from Pd(II) to Pd metal because of a synergistic relationship[14–16] between the Pd ions and the ceria support. The surface interaction between Pd-Ce has been reported[17,18] showing the formation of metal clusters and of a mixed metal phase $Pd_xCe_{1-x}O_2$.. NO_x and CO conversion[19,20] is promoted by Pd on ceria by a Pd-Ce interaction, NO dissociation is favoured by oxygen vacancies formed by Pd-Ce interactions but a decrease in its activation.

There are a few mechanisms in which the SMSI can be justified through such as alloy formation,[21,22] diffusion of metal into the support/encapsulated by the support[23,24] and formation of bonds between the metal and support (via an intermediary oxygen).[25,26]

The electronic interactions forming PGM-M or PGM-O-M structures have been observed by numerous methodologies. Pt and Pd surface-support interactions have been reported to exist using Raman spectroscopy whilst resulting in a highly dispersed metal.[27]

EXAFS of Pt L_3-edge for Pt supported onto catalyst supports show that for alumina only Pt-Pt bond formation occurs, indicating metal particle formation. If the Pt is supported onto a ceria based support there is the formation of a Pt-O-Ce bond suppressing any sintering of Pt particles whilst aging. When treated under reducing conditions, the Pt-O-Ce interaction breaks down and Pt metal particles are dispersed across the ceria based support.[12,28] Due to the support dependent nature of this effect,[28] it would imply the electron density of the oxygen in the support could be the root of this effect. Lin *et al.* reported that using a combined methodology that there is a dependent sensitive nature of Pt oxide showing the complete dispersion of the Pt nanoparticles across the ceria support and partial reduction of the ceria by hydrogen spill over.[29]

Furthermore the SMSI can be justified by alloy formation or the encapsulation of the metal within the support. The main driving force for the encapsulation is to minimise the surface energy. SMSI is prone to occur in catalytic support materials with low surface energy e.g. ceria, titania in comparison to silica or alumina.[30] The drive to minimise the surface energy is evidently seen using HRTEM[31] as this shows Pd particles covered by a layer of the ceria based support. The incorporation can expand the lattice parameter of the ceria based support and induce strain into the material which can be a driving force for anion migration in the support. The encapsulation, generally, only occurs under reducing conditions above 500°C whilst alloy formation is encountered above 900°C e.g. $CePt_5$ phases are reported when reducing Pt/Ceria reduced at 900°C.[21] Furthermore these alloys can be treated under reducing atmospheres to results in Pt/ceria systems.[22]

The level and nature in which the PGM and support interaction can occur is dependent on nature of synthesis procedure,[23] the support,[32] precious metal loaded etc.[33] Pd and Pt on ceria are found to be more active for NO conversion in comparison to the respective metals on alumina, silica or zirconia.[34] Further to this the amount of PGM used can influence the chemical behaviour. With increasing Pt loading, the Pt oxide phase present in the dispersed PGM will increase until saturated, which from then on will form PdO.[35] These systems can form Pt-O-Ce under the appropriate conditions, slowing the sintering process and dispersing the particles. Lower Pt amounts loaded have a higher preference against sintering dependent on the treatment, so that at high temperatures the surface area stability is independent of the amount of Pt loaded onto the support.[36] This is complicated by the size of the support as a decrease in crystallite size increase the interaction between PGM and ceria support. The type of PGM present on the catalytic support has different interactions. Pd-O-Ce and Rh-O-Ce are still present after calcination at 800°C whilst Pt-O-Ce are found below 500°C leading to the order of affinity for ceria being Pd > Pt.[32]

It was decided to perform the study on local and average structure at operating conditions as these samples will have significantly different structures compared to those taken at ambient conditions. This dual study of local and average structure will also help with the understanding of what happens within the material and whether the material has different structural characteristics on a local length scale which has already been found for other doped materials.

Insitu X-ray total scattering was utilised to investigate the local structure. This was performed using synchrotron radiation as this has been proven to help in the understanding of how the local structure differs or is similar to the average structure whilst allowing *insitu* experimentation which is important for studies of materials undergoing a dynamic change.

Neutron Powder Diffraction (ND) was used to investigate the average structure in order to allow us a complete crystallographic understand of the bulk properties of the samples. This was utilised as the oxygen neutron scattering length is greater than that of cerium.

4.3 Experimental Section

The pure ceria support is a commercially available Rhodia high surface area ceria (referred to as HSA in the thesis) from Solvay and the Pd and Pt samples were made by impregnation. The required amount of Pd and Pt nitrate solutions (commercially available from JM) diluted to a volume appropriate to fill the pore volume of the HSA ceria support. Materials were dried at 105°C and fired at 500°C.

4.3.1 X-ray absorption spectroscopy (XAS) at Pt L_3-edge

Insitu XAS data was acquired at the Pt L_3-edge (11564 eV) at the BM23 beam line,[37] European Synchrotron Research Facility (ESRF). A Si (111) double crystal monochromator was used to collect the L_3-edge data and all datasets were collected in transmission geometry and using ionisation chambers. Pellets were made from 10mg of the ceria sample was ground with 90mg of fumed silica. The XAS data were measured in step scans in an E-range of 11400 and 12425 eV. The samples were purged under a continuously flowing N_2 atmosphere then switched to the continuously flowing reducing atmosphere of H_2:N_2. Data was collected at RT then the temperature was ramped from 10°C to 450°C. The samples were then cooled under a reducing atmosphere to room temperature and data was collected.

4.3.2 X-ray absorption spectroscopy (XAS) at Pd K-edge

Insitu XAS data was acquired at the Pd K-edge (24350 eV) at the BM01 (The Swiss-Norwegian beam line), ESRF. A Si (111) double crystal monochromator was used to collect the K-edge data and all datasets were collected in transmission geometry and using ionisation chambers. A quartz capillary was loaded with 100mg of sample and placed above a hot air blower. The XAS data were measured in step scans in an E-range of 24150 and 25600 eV. The samples were purged under a continuously flowing N_2 atmosphere then switched to the continuously flowing reducing atmosphere of H_2:N_2. All the samples were measured at 30, 50, 100, 200, 300, 400 and 450 °C during heating, with a 5 °C min^{-1} ramp, held at 450 °C for 10 minutes then allowed to cool to RT whilst the samples were measured at 400, 300, 200, 100 and 50°C.

4.3.3 X-ray absorption spectroscopy (XAS) at Ce L_3-edge

Insitu XAS data was acquired at the Ce L_3-edge (5723.4 eV) at the BM26A beam line, ESRF. A Si (111) double crystal monochromator was used to collect the L_3-edge data and all datasets were collected in transmission geometry and using ionisation chambers. Pellets were made from 10mg of the ceria sample was ground with 90mg of fumed silica. The XAS data were measured in step scans in an E-range of 5623.0 and 6154.0 eV. The samples were purged under a continuously flowing N_2 atmosphere then switched to the continuously flowing reducing atmosphere of H_2:N_2. Data was collected at RT then the temperature was ramped from 10°C to 450°C. The samples were then cooled under a reducing atmosphere to room temperature and data was collected.

4.3.4 X-ray absorption spectroscopy (XAS) at Ce K-edge

Insitu XAS data was obtained at the Ce K-edge (40443 eV) on the BM23 beam line,[37] at the ESRF. The beamline uses a Si (311) double crystal monochromator and all the data were collected in transmission mode using ionisation chambers. Pellets were made from 10mg of the ceria sample was ground with 90mg of fumed silica. The XAS data was measured in step scans in an E-range of 40200 and 41423 eV. The samples were purged under a continuously flowing N_2 atmosphere then switched to the continuously flowing reducing atmosphere of H_2:N_2. Data was collected at RT then the temperature was ramped from 10°C to 450°C. The samples were then cooled under a reducing atmosphere to room temperature and data was collected.

4.3.5 Temperature Programmed Reduction (TPR)

TPR was performed using an Altamira Instruments AMI-200. The samples were heated from 25°C to 1100°C at 10°C min^{-1} under 10% H_2/Ar flowing at 30 ml min^{-1}. TPR measures the uptake of hydrogen as a sample undergoes a heating cycle.

4.3.6 X-ray Total scattering

X-ray total scattering patterns were obtained on the ID15B at the European Synchrotron Research Facility (ESRF), using a mar345 2D detector. The wavelength was λ=0.1438001 Å with a Q range = 1 - 23 Å^{-1}. The samples were prepared to produce monodisperse grain sizes to aid in gas flow over the sample. These were loaded into a 1mm diameter quartz capillary mounted on a bespoke gas rig cell over a hot air blower.

The empty quartz capillary was scanned in order to remove the background at RT due to negligible change in temperature and low thermal expansion.

All the samples were measured at 30, 50, 100, 200, 300, 400 and 450 °C during heating, with a 5 °C min^{-1} ramp, held at 450 °C for 10 minutes then allowed to cool to RT whilst the samples were measured at 400, 300, 200, 100 and 50°C. The samples were purged under a continuously flowing N_2 atmosphere for 10 minutes then switched to the continuously flowing reducing atmosphere of H_2(5%)/N_2.

4.3.7 Neutron diffraction (ND)

The ND patterns were obtained on POLARIS[38] at the ISIS Facility, Rutherford Appleton Laboratory. Data was acquired over $28° < 2\theta < 42°$, $85° < 2\theta < 95°$ and $130° < 2\theta < 160°$ with a low angle, 90° and back scattering bank respectively. The samples were loaded onto a glass frit within a silica tube. This tube was then place into another silica tube, allowing gas flow through the sample whilst being able to evacuate the detector tank removing any scattering from air.

The samples were purged in continuously flowing nitrogen at RT and a ND pattern was measured. Then the gas was switched to continuously flowing reducing atmosphere of H_2(5%)/N_2 at RT and another ND pattern was measured. The sample was heated to 200 °C at a 5 °C min^{-1} ramp, held for 3 hours and a ND pattern was measured. The sample was then heated to 400 °C at a 5 °C min^{-1} ramp, held for 3 hours and a ND pattern was measured. The sample was then allowed to cool down to RT and once reaching RT, another ND pattern was measured.

4.4 Data analysis

4.4.1 XAS data correction and refinement

All XAS datasets underwent background subtraction and normalisation using Athena[39] software for Pd K-edge, Pt and Ce L_3-edges, and Ce K-edge. Linear combination fitting (LCF), using the procedure described in the Experimental Chapter, was performed using Athena[39] where Pd foil and PdO were used as standards for Pd K-edge data, and HSA Ceria and Cerium nitrate for the Ce L_3-edge data. Analysis was performed using Artemis software.[39] This extracts structural parameters from the EXAFS ($\chi(k)$). FEFF6l was used to calculate Phase-shifts and amplitude factors using the ceria fluorite structure. Hedin-Lundqvist potentials were used to calculate backscattering factors and phase shifts.

For the K-edge the fitting was performed between k = 3.9 and 14.3 Å^{-1} and r = 2.5 and 3.9 Å. The amplitude reduction factor (SO2) was refined using ceria NIST as a reference material and set as 1.00 for the K-edge.

4.4.2 Real space analysis

The raw diffraction patterns were then processed using PDFgetX3[40] between $0.6<Q<23$Å^{-1} as this offers rapid batch processing of the data.

The analysis of the data in Real space was performed using the PDFfit2 software in the graphical interface of PDFgui.[41] The unit cell parameters and ADPs were refined.

4.4.3 Reciprocal space analysis

The ND patterns were processed using MantidPlot. The XRD 2D images were processed using FIT2D.[42] The analysis of the data (the Rietveld Method[43]) was performed using the graphical interface, EXPGUI[44], of the GSAS software.[45] This analysis used Chebyshev polynomials to fit the background whilst using a pseudo voigt,[46] modified to account for asymmetric correction,[47] to fit the line profile of the data.

The background and profile parameters were refined along with the cell parameter, atomic displacement parameters (ADPs) and occupancies. These ADPs are a measure of the mean square displacements for the atoms present in the material and can be seen as a measure of the disorder present in the material either due to defects and/or thermal effects.

4.5 Results

First the Rietveld refinement of the diffraction data (combined analysis of neutron and X-ray diffraction) is discussed first followed by discussion of X-ray Analysis Spectroscopy and then finally the combination of all techniques and their respective results.

4.5.1 Joint ND/XRD Rietveld Refinement

The combination of ND and XRD diffraction patterns in Rietveld refinement is important as these types of radiation interact differently with atoms. This emphasises different types of atoms due to their respective scattering cross sections. All the samples show that they have the fluorite ceria structure throughout the experiments with subtle changes in peak position and intensities relating to changes in the lattice parameters, atomic displacement parameters (ADPs) and occupancies.

All three samples show that all material has the ceria fluorite structure throughout the heating and cooling under reducing conditions. No evidence of crystalline PdO/PtO_2 or Pd or Pt metal is observed at the outset of the experiments. Once the sample is under a hydrogen atmosphere the formation of Pd or Pt metal is observed.

Figure 4-1 shows the comparison of the diffraction patterns for both X-ray and Neutron diffraction techniques for the High surface area ceria support and the 5wt% Pd and Pt loaded samples respectively. For the High surface area ceria support, it shows a slight shift in all peak positions to a lower Q value, showing a larger unit cell size. For the 5wt% Pd on a High surface area ceria support, it shows a slight shift in the peak position to a lower Q value, showing a larger unit cell size. It is also noticeable that a peak forms around 2.8 $Å^{-1}$ at 200°C suggesting some reduction to Pd metal. For the 5wt% Pt on a High surface area ceria support, it shows a slight shift in the peak position to a lower Q value, showing a larger unit cell size. It is also noticeable that a peak forms around 2.8 $Å^{-1}$ at 400°C suggesting some reduction to Pt metal.

The refinement of the lattice parameters (Figure 4-2) show that both Pd and Pt loaded ceria have subtly larger unit cells, suggesting that some quantity of PGM might be incorporated into the fluorite structure. The results show that for all samples that the heating under a reducing atmosphere results in a lattice expansion. For all 3 samples this may be due to both thermal expansion of the fluorite structure and the reduction of Ce (IV) to Ce (III), as Ce (III) (1.143 Å) has larger ionic radii compared to Ce (IV) (0.97 Å). Under cooling, in a reducing atmosphere, there are contractions in the lattice parameters for all 3 samples. There are marked differences between the start and end values for both Pd and Pt loaded ceria in comparison to the pure ceria support. This suggests that both Pd and Pt aid in the reduction of ceria and the removal of oxygen from the structure implying Ce (III) formation. However, there was no evidence for Ce_2O_3 phase present in the sample and the diffraction data of the cooled sample correspond to only Fluorite structure.

The analysis of both cerium and oxygen ADPs show that as the samples are heated under H_2:N_2 there is increase in both the disorder of the cerium and oxygen atoms in the materials, being at its most disordered state at 400^{o}C. As the samples are cooled these values decrease for both the cerium and oxygen atoms. These values at the end of the experiment do not return to those seen at the start of the experiment suggesting that there might be some thermally induced disorder or disorder caused by vacancies.

Examination of the oxygen occupancies shows the influence of PGM on the ceria support. The refined occupancies for the pure ceria support shows that during heating there is a loss in oxygen which would normally indicate the sample has been reduced. It is noticeable that after cooling there is a ‘reoxidation’.

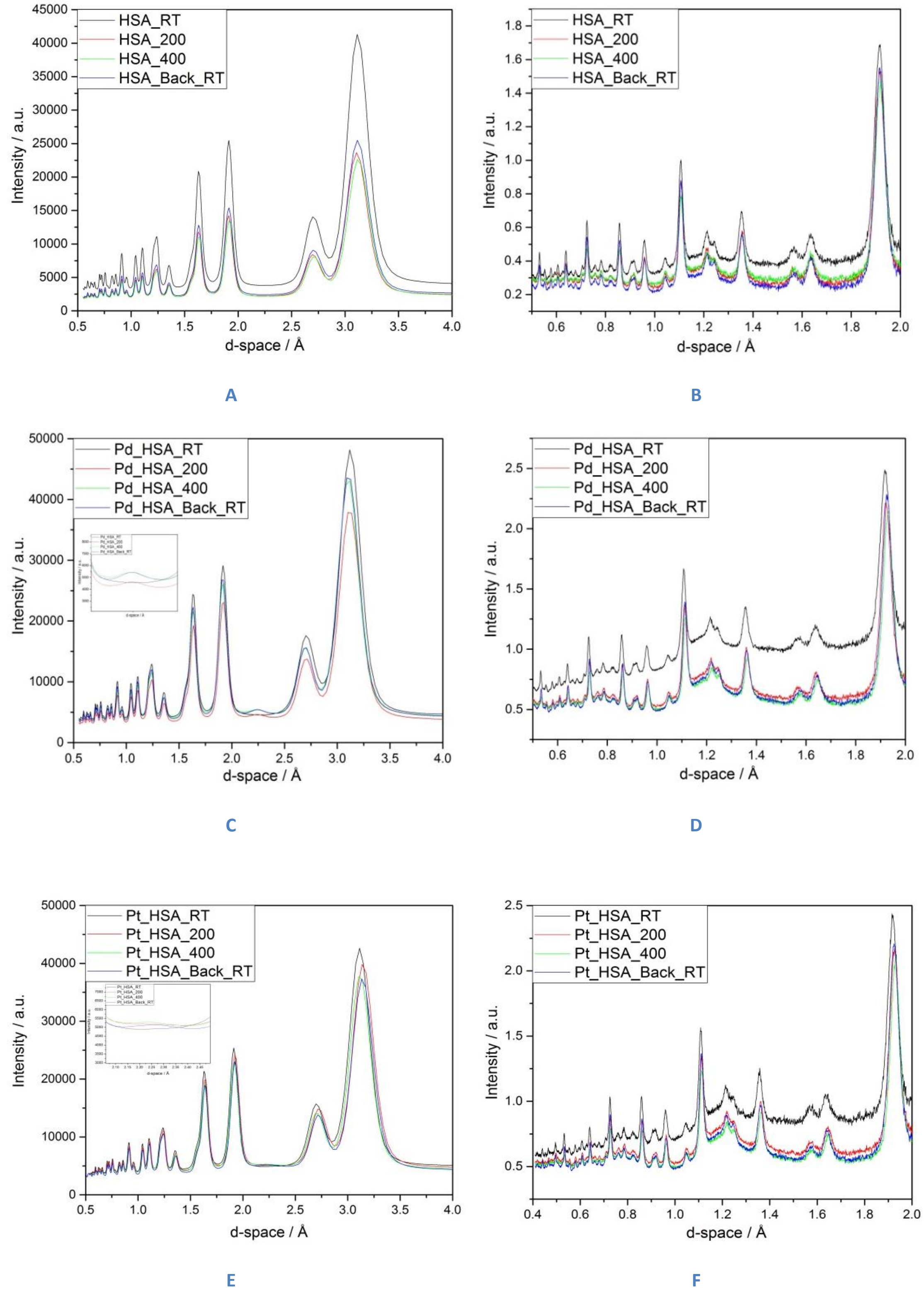

A B C D E F

Figure 4-1: (A) Comparison of the X-ray and (B) Neutron diffraction patterns at Room Temperature, 200°C, 400°C and returned to Room Temperature for the High Surface Area ceria support. (C) Comparison of the X-ray and (D) Neutron diffraction patterns at Room Temperature, 200°C, 400°C and returned to Room Temperature for 5 wt% Pd on a High Surface Area ceria support. (E) Comparison of the X-ray and (F) Neutron diffraction patterns at Room Temperature, 200°C, 400°C and returned to Room Temperature for 5 wt% Pt on a High Surface Area ceria support

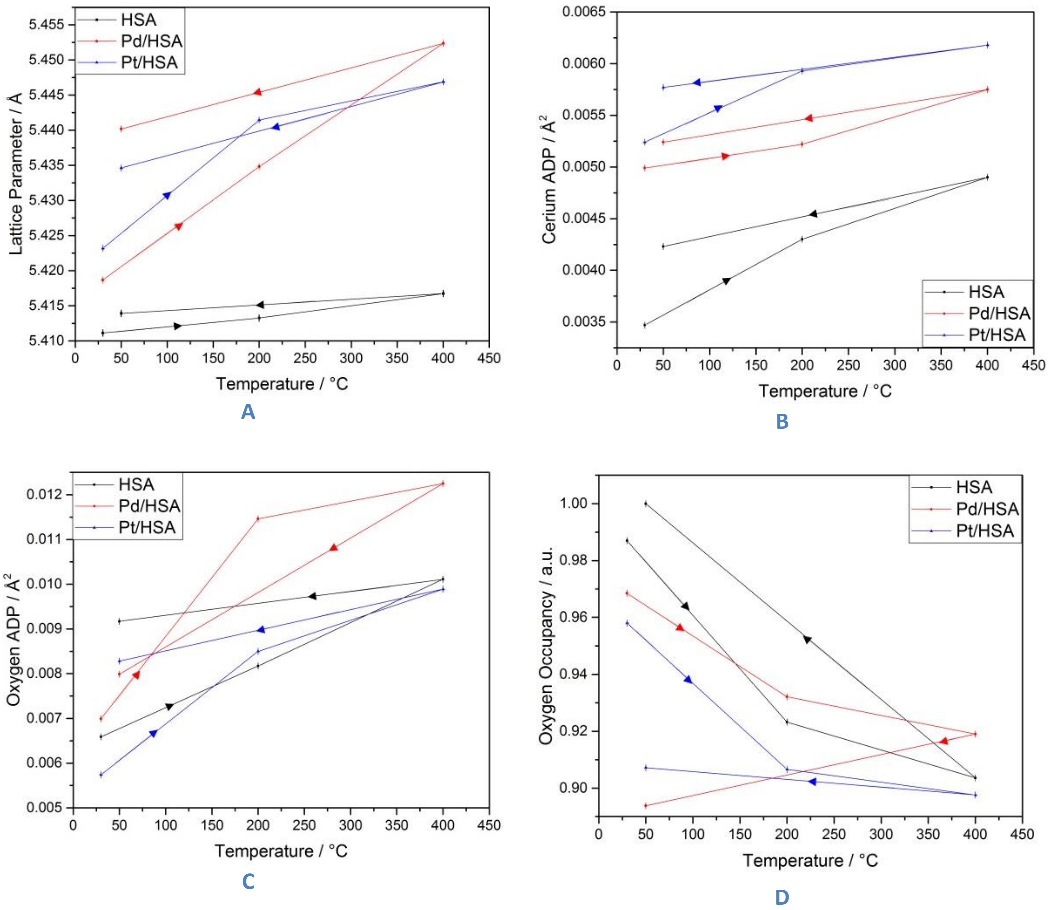

A

B

C

D

Figure 4-2: (A) Lattice Parameters for the Ceria support and respective PGM loaded ceria samples (B) Cerium atom isotropic atomic displacement parameters for the Ceria support and respective PGM loaded ceria samples (C) Oxygen atom isotropic atomic displacement parameters for the Ceria support and respective PGM loaded ceria samples (D) Oxygen occupancies for the Ceria support and respective PGM loaded ceria samples. These show variations in the lattice parameter and disorder present in the samples throughout the heating and cooling cycles. The direction of the heating and cooling is designated by the direction of arrows located on the graphs.

This would suggest that up to 400°C there is no or little reduction of the pure ceria support and any reduction could be masked by an increase in the ADP of the oxygen atoms. For both Pd and Pt loaded ceria samples there is an observable reduction in the oxygen occupancy, similarly seen for the pure ceria support. After the PGM loaded ceria samples are cooled, there is no return in the oxygen occupancy to the starting values. This would suggest that both the reduction is ‘real’ and that the loading of PGM onto ceria aids in the reduction of the ceria support.

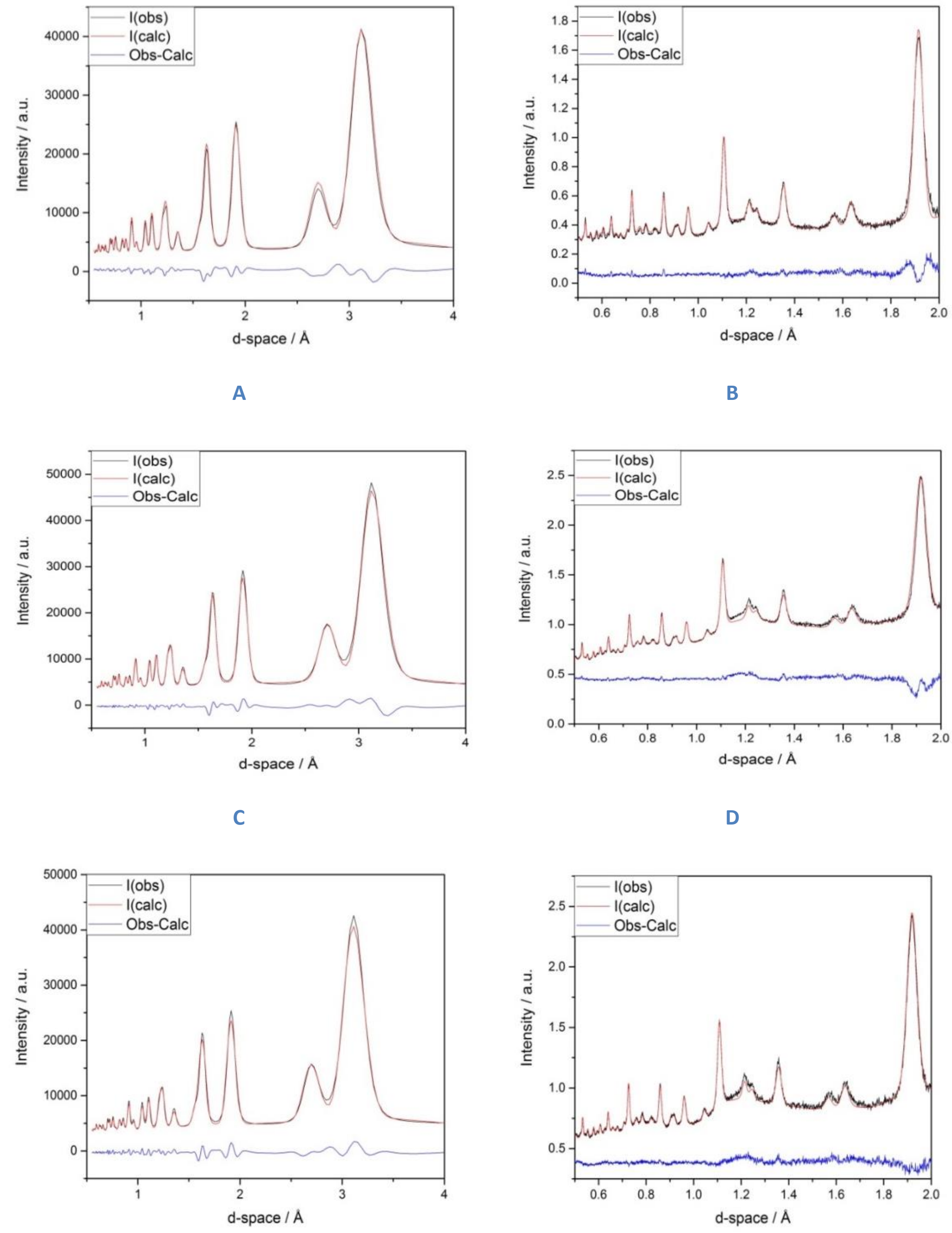

A B

C D

E F

Figure 4-3: Comparison of the Observed experimental data and the calculated data for the respective XRD and ND datasets using the Rietveld Method. (A) XRD for HSA (B) ND for HSA (C) XRD for 5 wt% Pd on HSA (D) ND for 5 wt% Pd on HSA (E) XRD for 5 wt% Pt on HSA (F) ND for 5 wt% Pt on HSA

4.5.4 Real Space data

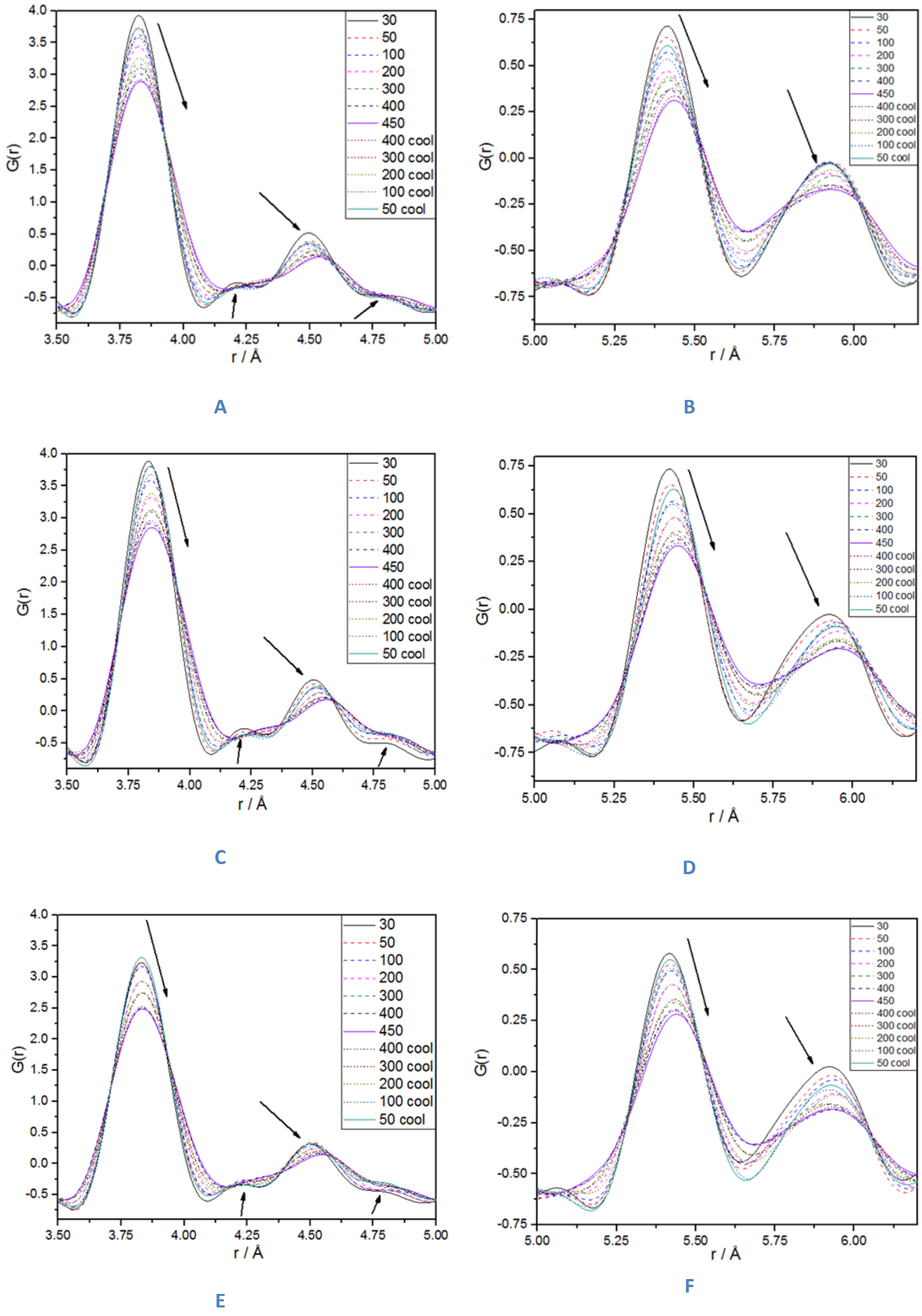

Figure 4-4: (A and B) G(r) curves for the high surface area ceria support, highlighting different sections and the effect of temperature upon the short range structure (C and D) G(r) curves for 5wt% Pd loaded onto ceria, highlighting different sections and the effect of temperature upon the short range structure (E and F) G(r) curves for 5wt% Pt loaded onto ceria, highlighting different sections and the effect of temperature upon the short range structure

The changes in position and intensity relate to the disorder in the material that may be occurring in the ceria. The 1st Ce-Ce and 2nd Ce-O (Figure 4-4) are present at approximately 3.8 Å and 4.5 Å respectively. For all the samples it is found that the 1st Ce-Ce bond decreases in intensity whilst no discernible change in the bond length. For all 3 samples, there is both a decrease in intensity and increase the bond length seen for the 2nd Ce-O shell. This expansion could be indicative of thermal expansion of the sample. Similarly, to the 1st Ce-O bond, shoulders are present for both the 1st Ce-Ce and 2nd Ce-O peaks. Tentatively these shoulders could be due to dynamic effects within the material such as an increase in the Debye-Waller factors.

These G(r) positions can further be evaluated by looking at the 2nd Ce-Ce and 3rd Ce-O found at approximately 5.4 Å and 5.9 Å respectively (Figure 4-4). For all the samples there is an increase in the peak position with a broadening of the peak for the 2nd Ce-Ce pair. This could be seen as both a combination of thermal expansion and reduction of Ce (IV) to Ce (III) leading to Ce (IV) - Ce (III) atom pairs. Similarly, for the 3rd Ce-O atom pair there is a broadening of the peak with an increase in peak position which can be explained which can be assigned to both a combination of thermal expansion and reduction of Ce (IV) to Ce (III) leading to the larger Ce (III) - O atom pair. Overall these materials do not undergo a phase change i.e. CeO_2 to Ce_2O_3 and the only changes observed for all 3 materials is a thermal expansion and increased disorder of both cerium and oxygen atoms upon heating.

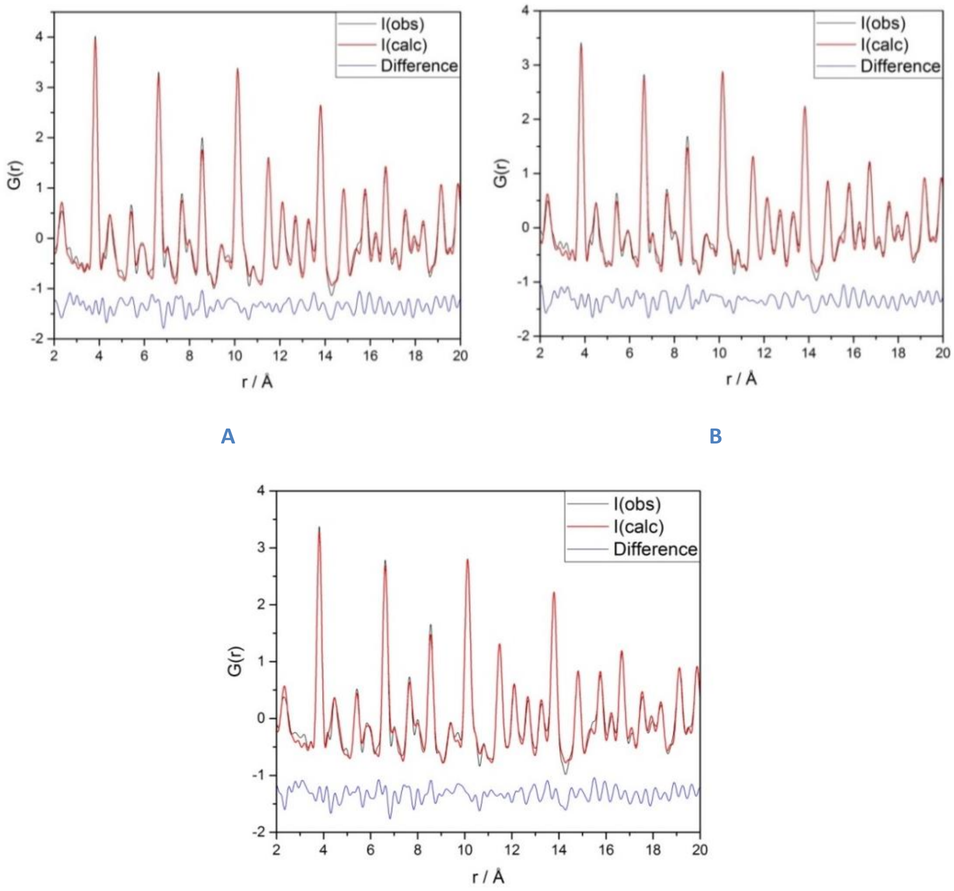

A

B

C

Figure 4-5: Example of the fits for the PDF analysis, showing a comparison of the Observed Data (I(obs)), Calculated Data (I(calc)) and the difference between these respective data sets (A) High Surface area ceria support (B) 5 wt% Pd on a High Surface area ceria support (C) 5 wt% Pt on a High Surface area ceria support

4.5.2 X-ray absorption near edge structure (XANES) analysis

Figure 4-6 shows the comparison of the High Surface Area Ceria, and the respective 5 wt% Pd and Pt loaded samples with 2 standards. These standards are Cerium Nitrate and Ceria NIST, consisting of Ce (III) and Ce (IV) ions respectively. This shows that at room temperature that the samples consist of Ce (IV) ions and no noticeable amount of Ce (III) ions is present. Figure 4-7 shows a comparison of the Ce-L_3 edge XANES spectra for the high surface area ceria support, 5wt% Pd and Pt both supported on the high surface area ceria support. These show, for all the samples, there are some changes in peak position and intensity, which is attributable to the reduction of Ce (IV) to Ce (III) though, does not reduce fully to Ce_2O_3. For the pure ceria support, the initial material and final material have similar

XANES spectra suggesting that before and after the reducing cycle the sample has a similar structure. In comparison to the PGM loaded samples which show marked changes in both peak shape and peak position after undergoing the reducing experiment, indicating a marked changed in the structure of the ceria.

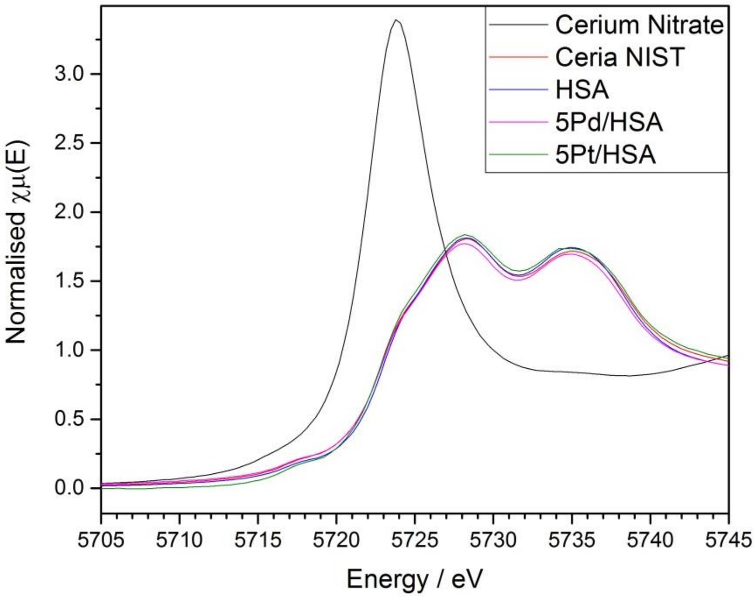

Figure 4-6: Comparison of the 3 samples with 2 ceria based standards. Cerium Nitrate consists of Ce (III) ions whereas Ceria NIST consists of a highly crystalline ceria sample made of Ce (IV) ions. This shows that all the samples consist of Ce (IV) ions.

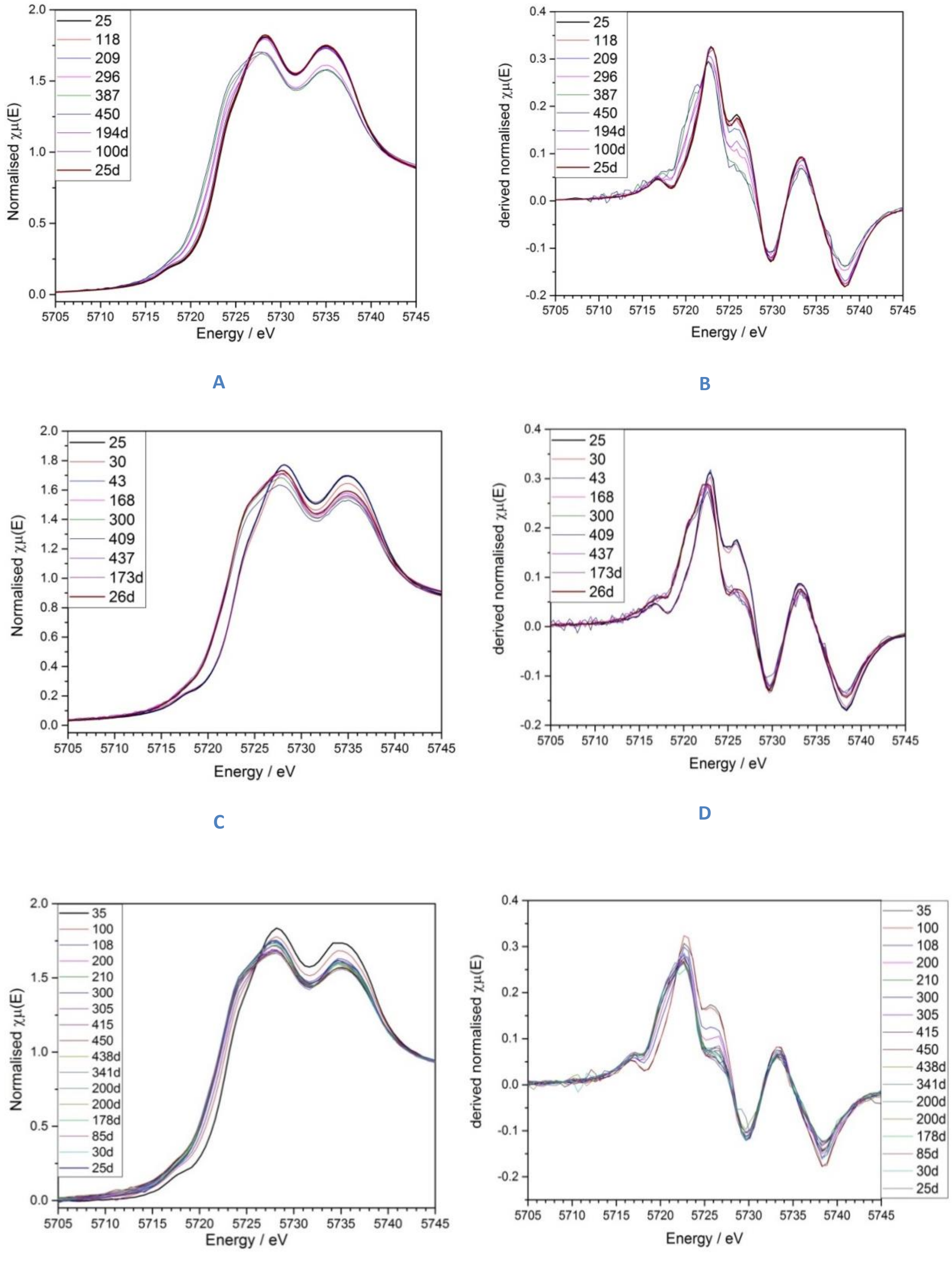

A

B

C

D

E

F

Figure 4-7: (A) Comparison of the Ce L_3-edge XANES spectra for the High surface area support (B) Comparison of the Ce L_3-edge 1st derivative XANES spectra for the High surface area support (C) Comparison of the Ce L_3-edge XANES spectra for 5wt% Pd on a High surface area support (D) Comparison of the Ce L_3-edge 1st derivative XANES spectra for 5wt% Pd on a High surface area support (E) Comparison of the Ce L_3-edge XANES spectra for 5wt% Pt on a High surface area support (F) Comparison of the Ce L_3-edge 1st derivative XANES spectra for 5wt% Pt on a High surface area support

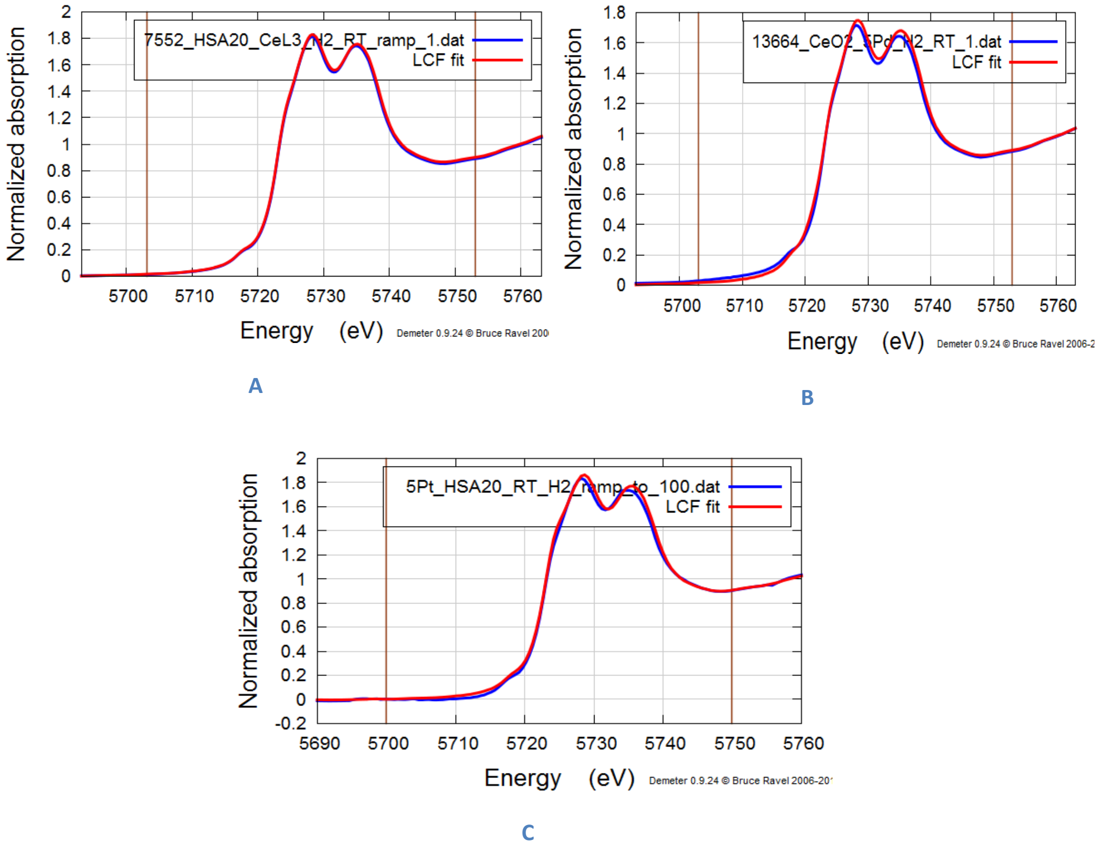

A

B

C

Figure 4-8: Comparison of the Observed XANES spectra (for the Ce L_3-edge)and Linear Combination Fitting (LCF) (A) the pure High Surface area support for varying temperatures (B) 5 wt% Pd on HSA (C) 5 wt% Pt on HSA

Figure 4-9 shows the comparison of the Pd K-edge normalised μ(E) with respect to a PdO and Pd foil standard. This shows that initially any Pd present is in the form of PdO on the ceria support. After heating to 50°C in a reducing atmosphere, the PdO is reduced to Pd metal and it remains as metallic Pd throughout the rest of the heating and cooling cycle. Figure 4-9 shows the comparison of the Pt L_3-edge normalised μ(E) with respect to a PtO_2 and Pt foil standard. This shows that initially any Pt present is in the form of PtO_2 on the ceria support. Whilst heating between 35°C and 140°C in a reducing atmosphere, the PtO_2 is reduced to Pt metal and it remains as metallic Pt throughout the rest of the heating and cooling cycle. This is similar seen in the XRD patterns where the formation of a peak d = ~2.25Å is observed for both Pd and Pt loaded ceria samples at similar temperatures observed in XAS.

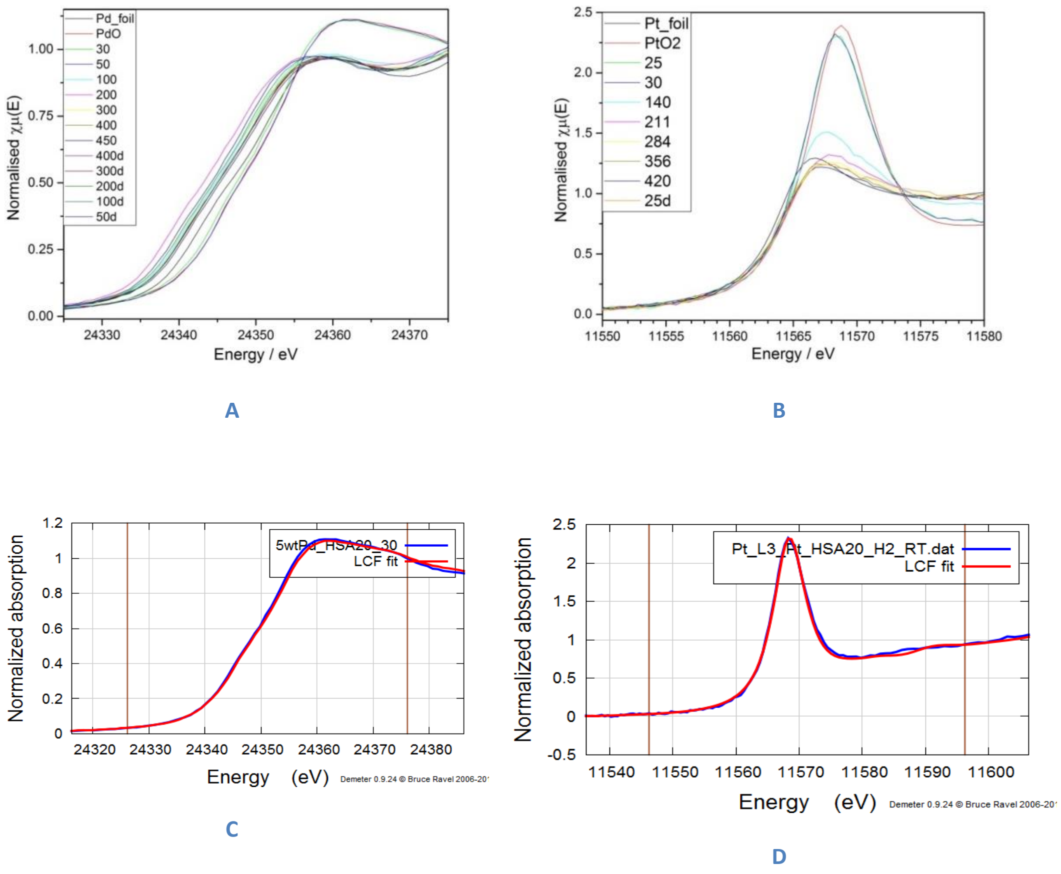

A

B

C

D

Figure 4-9: (A) Comparison of the normalised μ(E) for the Pd K-edge XAS data under heating and cooling cycle, PdO and Pd foil standards (B) Comparison of the normalised μ(E) for the Pt L3-edge XAS data under heating and cooling cycle, PtO2 and Pt foil standards (C) Example of the LCF for XAS data measured on the Pd K-edge (D) Example of the LCF for XAS data measured on the Pt L3-edge

Figure 4-10 shows the values for the Ce (III) fraction obtained from LCF for the high surface area ceria support and respective Pd and Pt loaded samples, undergoing heating and cooling in a reducing atmosphere. During heating within a reducing atmosphere the Ce (IV) ions present in ceria should be reduced to Ce (III) ions due to the removal of oxygen from the ceria lattice. For the High surface area ceria support, an increase in the amount of Ce (III) ions present within the sample is observed as the sample is heated. As the sample is cooled from 450°C back to room temperature the amount of Ce (III) present, as refined using LCF, reduces until it reaches the initial values observed at the outset of the experiment. If the sample was truly reduced then no return to purely Ce (IV) ions would be seen. In this case, this occurs which suggests that a pseudo reduction is observed. This would seem to suggest that a surface reduction might occur and the bulk of the reduction seen in XAS is due to an extensive temperature dependant oxygen migration throughout the sample.

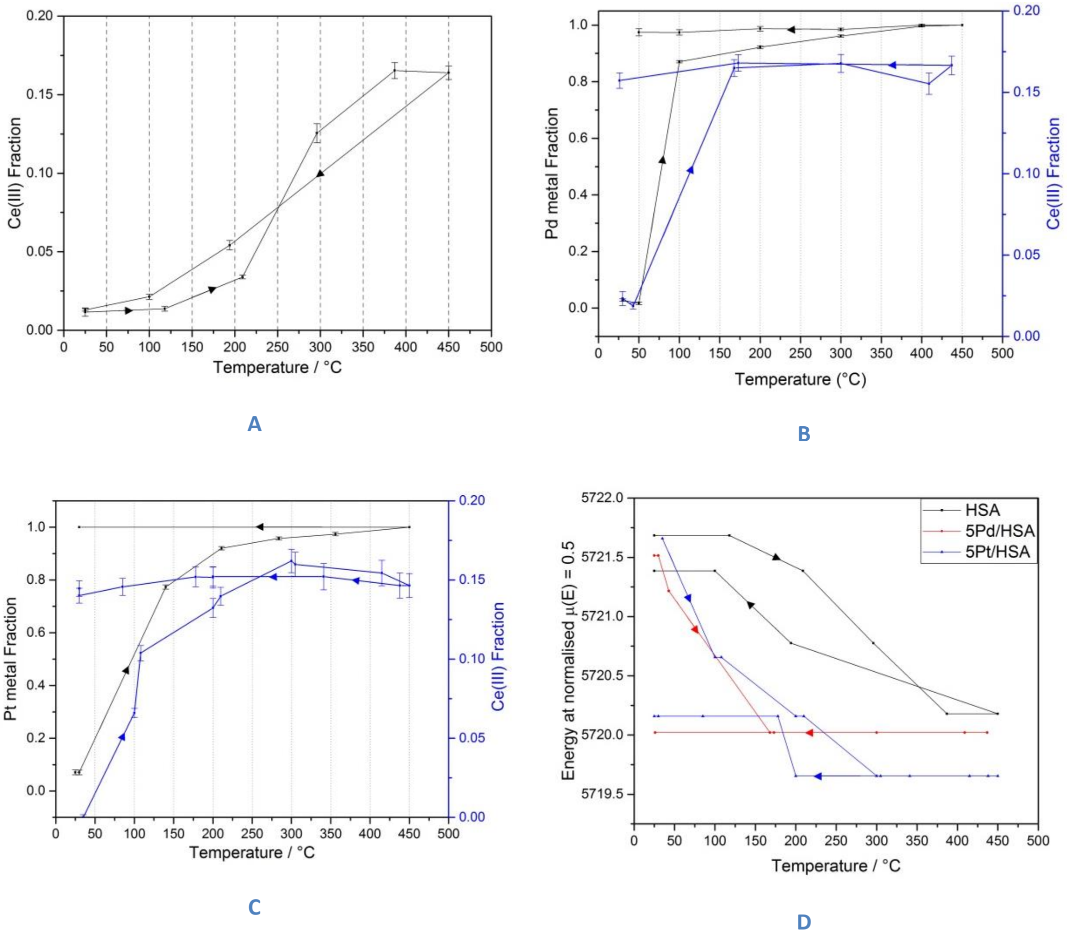

A

B

C

D

Figure 4-10: (A) Refined Ce (III) fractions obtained from LCF for the High Surface area ceria support. The red and blue arrows indicate the heating and cooling (of the sample) respectively (B) Comparison of the refined phase fractions for Pd metal and Ce (III) for 5wt% Pd on a high surface are ceria support. The red and blue arrows indicate the heating and cooling (of the sample) respectively (C) Comparison of the refined phase fractions for Pt metal and Ce (III) for 5wt% Pt on a high surface area ceria support. (D) Comparison of the Energy at normalised μ(E) = 0.5 for the High Surface area ceria support and the 5wt% Pd and Pt loaded samples respectively. The direction of the heating and cooling is designated by the direction of arrows located on the graphs.

The Ce (III) fractions obtained by LCF of the Ce L_3-edge for the 5wt% Pd on a high surface area ceria support, shows the reduction of Ce (IV) to Ce (III) whilst heating. This occurs simultaneously with the reduction of PdO to Pd metal, suggesting that the formation of Pd metal aids the reduction of ceria. Upon cooling back to 30°C, whilst under a reducing atmosphere, the amount of the Ce (III) does not decrease, in contrast to the High Surface area ceria support (Figure 4-10). This would suggest that there is no reformation of Ce (IV) and that the inclusion of Pd aids in the removal of oxygen from the lattice leading to the creation, and retention, of Ce (III) ions.

The behaviour observed for 5wt% Pt on a high surface area ceria support is similarly to the 5wt% Pd on a high surface area ceria support, the LCF shows the reduction of Ce (IV) to Ce (III) at similar temperatures with respect to the reduction of PtO_2. Upon cooling back to

30°C, whilst under a reducing atmosphere, the amount of the Ce (III) does not decrease, in contrast to the High Surface area ceria support.

Upon cooling the PGM/CeO_2 samples back to 30°C, whilst under a reducing atmosphere, the amount of the Ce (III) does not decrease, in contrast to the High Surface Area ceria support. This would suggest that there is no reformation of Ce (IV) and that the inclusion of Pt or Pd aids in the removal of oxygen from the lattice leading to the creation, and retention, of Ce (III) ions. Furthermore as can be seen in the case of both the Pd and Pt samples the onset of Ceria reduction is found to coincide with the reduction of the PGM metal, which is below the observed reduction of the Ceria support. This indicates that the PGM reduction aids the reduction of Ceria. In comparison to reported literature[32] there is no preference in the affinity of either Pd or Pt to ceria as the rate of Ce (III) creation for both samples are similar and the amount of Ce (III) formed by 450°C are similar.

Furthermore, the comparison of the energy position at normalised $\mu(E) = 0.5$, shows for all samples that upon heating in a reducing atmosphere, the energy decreases. This suggests that for all the samples that Ce (IV) is being reduced to Ce (III). For the pure High surface ceria support, the energy position returns to approximately its' original position, suggesting that any Ce (III) that was formed has been reoxidised back to Ce (IV). In comparison, the 5wt% Pd and Pt loaded samples, the energy position doesn't return close to the original value which is indicative of Ce (III) present still in the samples after cooling.

To ensure that these effects were not due to the presence of the PGM loaded onto the ceria and due to the preparation method, the same reactions were performed using a physical mixture of PdO and PtO_2 with the high surface area ceria support respectively.

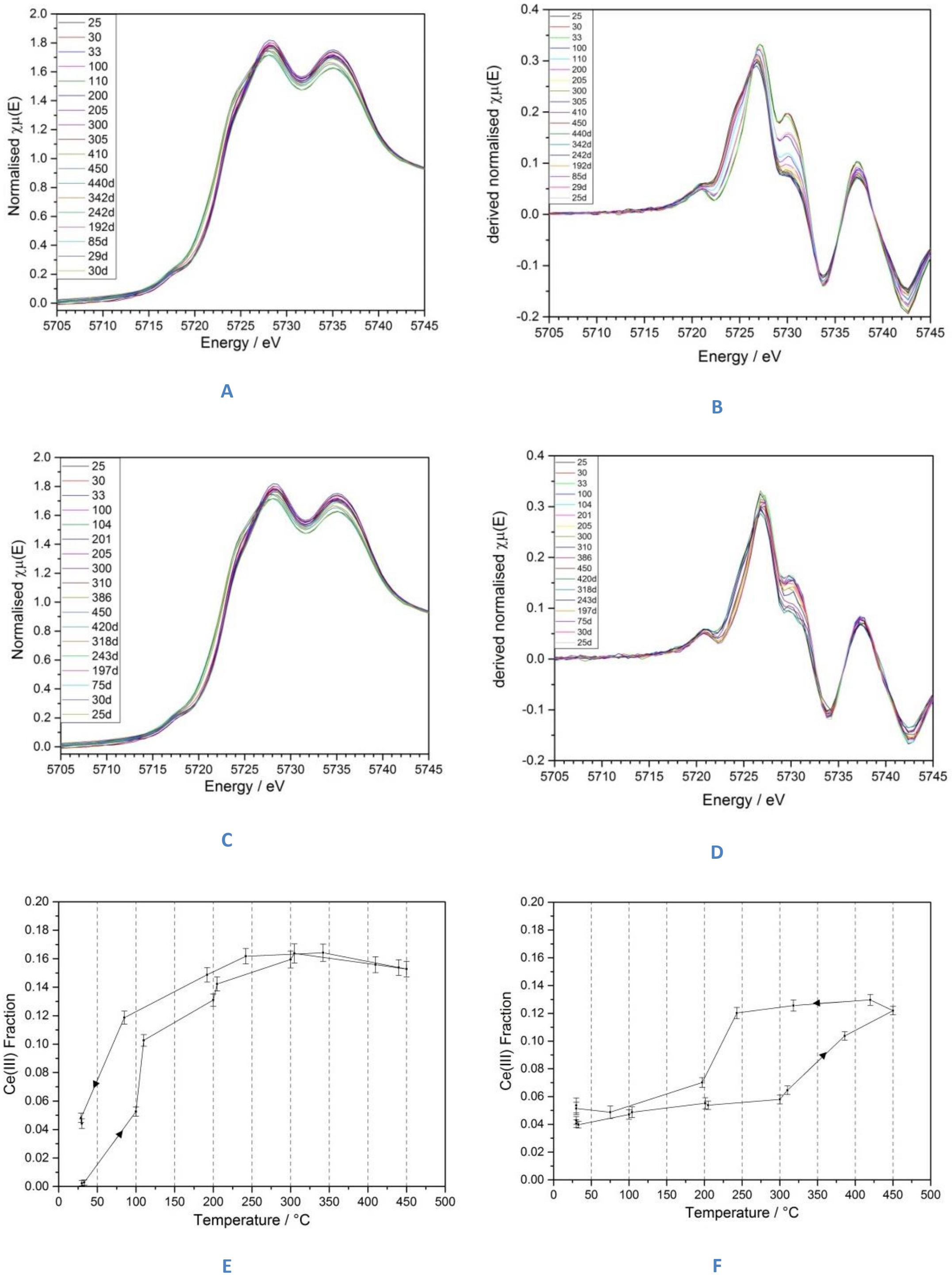

Figure 4-11: (A) Comparison of the Ce L_3-edge XANES spectra for the physical mixture of PdO and High surface area support (B) Comparison of the Ce L_3-edge 1st derivative XANES spectra for the physical mixture of PdO and High surface area support (C) Comparison of the Ce L_3-edge XANES spectra for the physical mixture of PtO_2 and High surface area support (D) Comparison of the Ce L_3-edge 1st derivative XANES spectra for the physical mixture of PtO_2 and High surface area support (E) Refined Ce (III) fractions obtained from LCF for the physical mixture of PdO and High Surface area ceria support (F) Refined Ce (III) fractions obtained from LCF for the physical mixture of PtO_2 and High Surface area ceria support. The direction of the heating and cooling is designated by the direction of arrows located on the graphs.

Figure 4-11 shows the comparison of the XANES spectra and the refined Ce (III) fractions from LCF for the physical mixture of PdO and PtO_2 with the High Surface area ceria support respectively. The comparison of the XANES spectra for both PdO/HSA and PtO_2/HSA show subtle variations in peak position and intensity, indicating that upon heating in a reducing atmosphere there is some reduction of Ce (IV) to Ce (III). Though this amount decreases as the samples are cooled from 450°C back to room temperature. The refined values of the Ce (III) fraction show that for both samples there is an increase in the amount of Ce (III) present as they are heated under the reducing atmosphere. As both samples are cooled there is a decrease in the amount of Ce (III) present, though both do not return to their original values suggesting some Ce (III) is present after the heating cycle. In contrast to the samples where Pd and Pt have been impregnated onto the ceria support, these samples show some 'reoxidation' after cooling. This suggests that, though the inclusion of PGM into the sample by incipient wetness impregnation, aids in the removal of oxygen from the ceria structure.

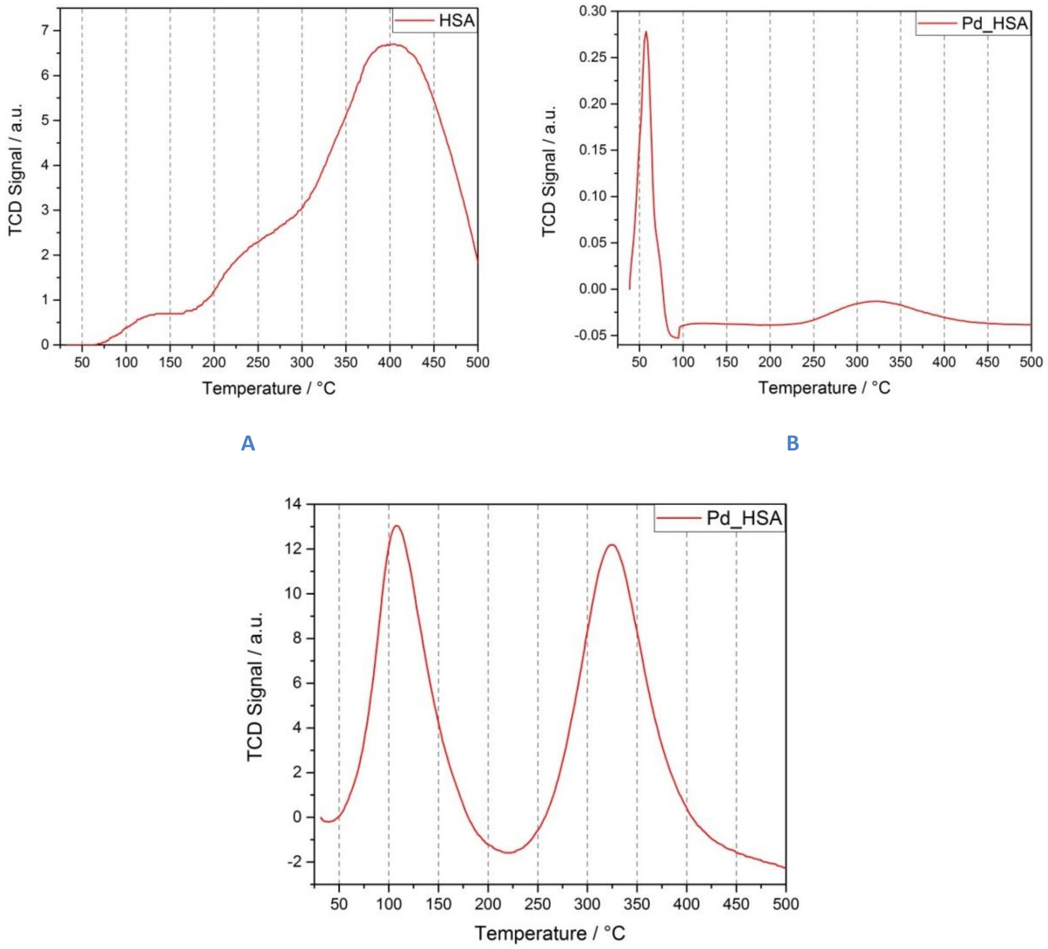

A

B

C

Figure 4-12: (A) TPR Profile of the High Surface Area Ceria support between Room Temperature and 500°C (B) TPR Profile of 5wt% Pd on a High Surface Area Ceria support between Room Temperature and 500°C (C) TPR Profile of 5wt% Pt on a High Surface Area Ceria support between Room Temperature and 500°C

The TPR profile, Figure 4-12, of the high surface area ceria support shows one main feature (~400°C) in the temperature range for this series of experiments.[48] This can be assigned to the reduction of surface ceria and the start of the reduction for bulk ceria. The TPR profile for 5 wt% Pd on ceria, there are 2 main features. The first ~60°C can be attributed to the reduction of surface ceria[49] and PdO to Pd, whereas the broad feature ~300°C for bulk ceria. For 5 wt% Pt on ceria, there are 2 main features in the TPR profile, the first (~100°C) can be assigned to the reduction of PtO_2 to Pt,[50] which is seen in the corresponding LCF analysis and of the surface ceria, and the second broad feature (~325°C) is attributed to further bulk reduction of ceria.[51]

4.5.3 Extended X-ray Fine Structure (EXAFS) analysis

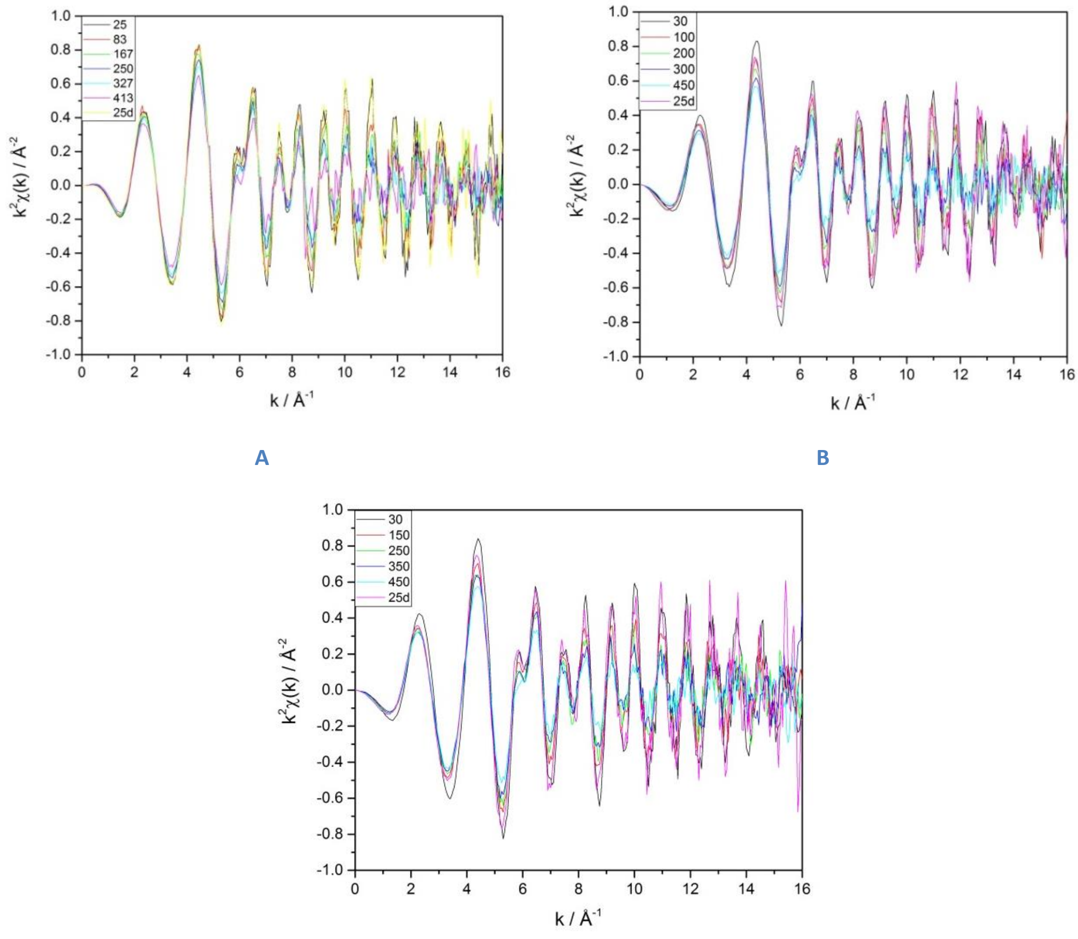

A

B

C

Figure 4-13: (A) Comparison of the $k^2\chi(k)$ for the High Surface Area ceria support and the respective 5 wt% Pd and 5 wt% Pt loaded samples (B and C) respectively. These show that under a reducing atmosphere and upon heating there are subtle variations in peak position and intensity. All graphs showing the data at the starting temperature, highest temperature and end temperature.

Figure 4-13 show comparison of the $k^2\chi(k)$ for the High Surface Area ceria support and the respective 5 wt% Pd and 5 wt% Pt loaded samples obtained on the Ce K-edge. These show that they all have the ceria fluorite structure with subtle variations in both the peak position and intensity dependent on temperature.

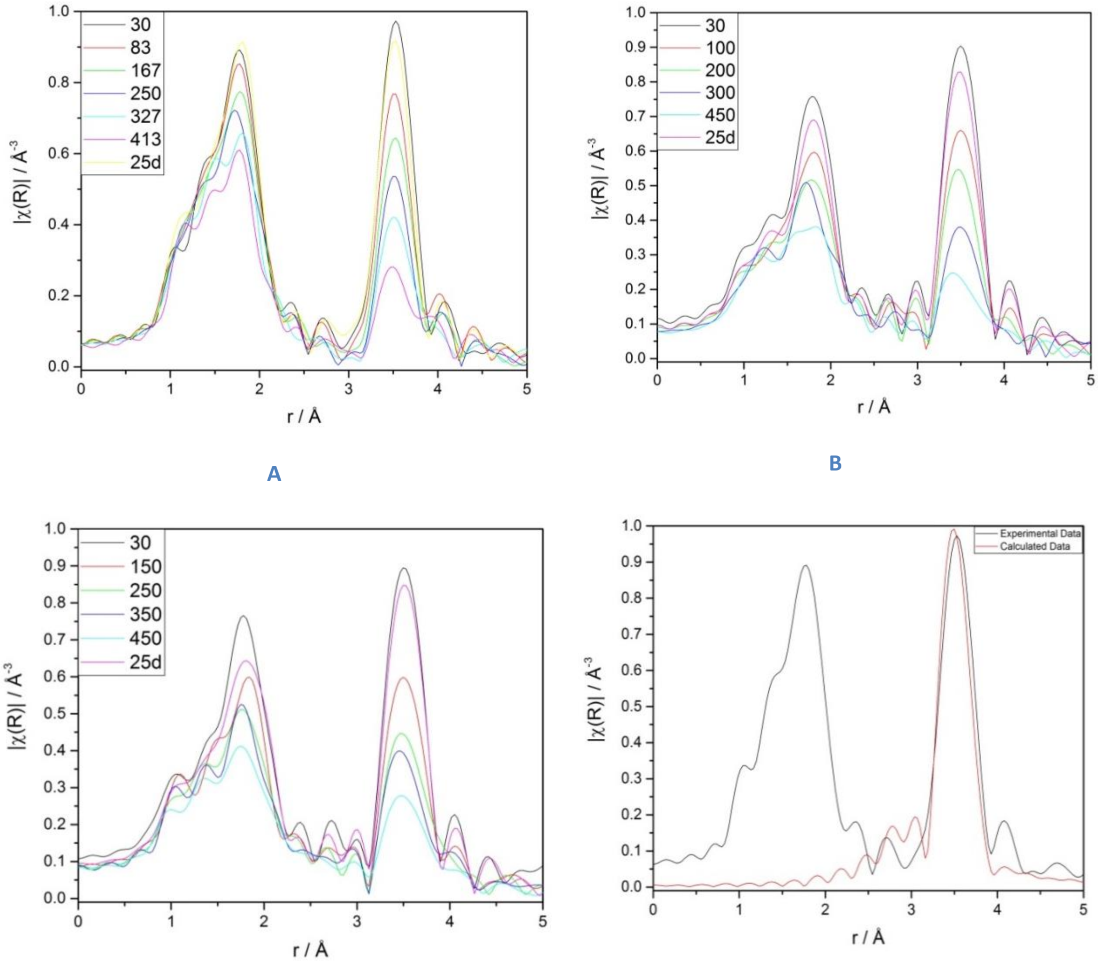

A

B

C

D

Figure 4-14: (A) Comparison of the |χ(R)| for the High Surface Area ceria support and the respective 5 wt% Pd and 5 wt% Pt loaded samples (B and C) respectively. These show that under a reducing atmosphere and upon heating there are variations in peak position and intensity. All graphs showing the data at the starting temperature, highest temperature and end temperature. (D) A typical fit obtained for the experimental data showing the fitting of Ce-Ce interatomic distance.

The fitting procedure was performed on the 1st Ce-Ce interatomic distance as the K-edge data might not result in accurate structure parameters for the first shell due to a core-hole lifetime broadening at a high energy absorption edge.

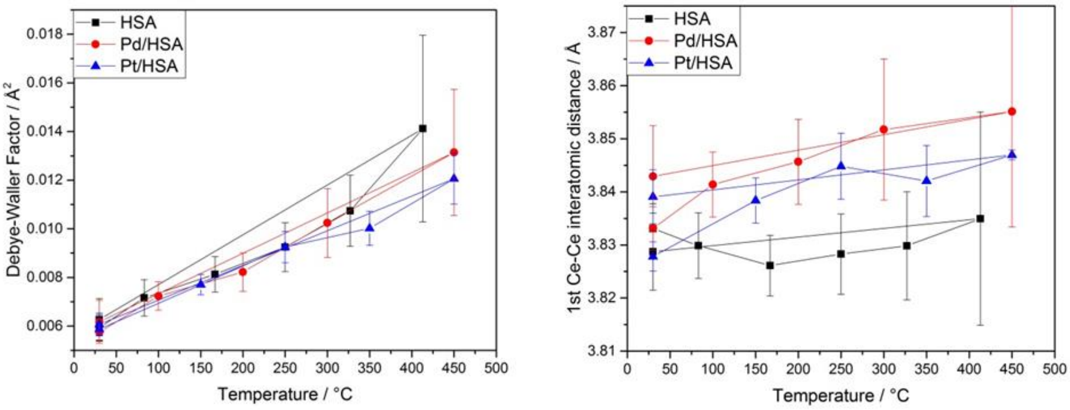

A

B

Figure 4-15: (A) Comparison of the refined DW factors from K-edge EXAFS for the High Surface Area ceria support, and the 5 wt% Pd and 5 wt% Pt loaded samples. (B) Comparison of the refined Ce-Ce interatomic distances for the High Surface Area ceria support, and the 5 wt% Pd and 5 wt% Pt loaded samples.

Figure 4-15 shows the comparison of the refined Debye Waller Factors and 1st Ce-Ce interatomic distances obtained from analysis of K-edge EXAFS. The Debye-Waller factors show for all the samples that there is an increase in the disorder of the cerium ions in the structure as the samples are heated which return to similar values upon cooling back to room temperature. The refined interatomic distances for the 1st Ce-Ce shells, show for the pure ceria support, there a slight decrease as the samples are heated to ca. 150°C, then the distance increase upon heating to 450°C. After the pure ceria support is cooled, there is a contraction in the Ce-Ce distance to similar values observed at the outset of the experiment. In contrast for both the Pd and Pt loaded samples, from the outset of the experiment, there is an increase in the Ce-Ce distance upon heating under hydrogen, reaching its maximum distance after heating to 450°C. After cooling back to room temperature, there is a contraction of the Ce-Ce distance. The noticeable difference is that the distance obtained after cooling is not similar to those refined from the outset of the experiment. This indicates some disorder remaining in the sample after undergoing the reducing cycle. Though these observations are well within the errors of the refined parameters which make this observation to be certain of and are later compared with PDF to ascertain the validity of these values.

4.6 Combination and comparison between different characterisation techniques

Figure 4-16 shows the comparison of the refined lattice parameters of the high surface area support and the respective Pd and Pt loaded ceria samples on heating and cooling under a reducing atmosphere. The lattice parameter for the pure ceria support shows and increase under heating then returning back to its original value upon cooling indicative of a thermal expansion and no reduction of the pure ceria support. In addition to this the Rietveld refinement of the pure ceria support shows hysteresis during the heating and cooling cycling. The PGM loaded samples show an increase in the lattice parameter with heating under hydrogen and a decrease upon cooling but not to their starting values. This shows upon heating there is a combination of thermal expansion and reduction and on cooling the sample is still in a reduced state.

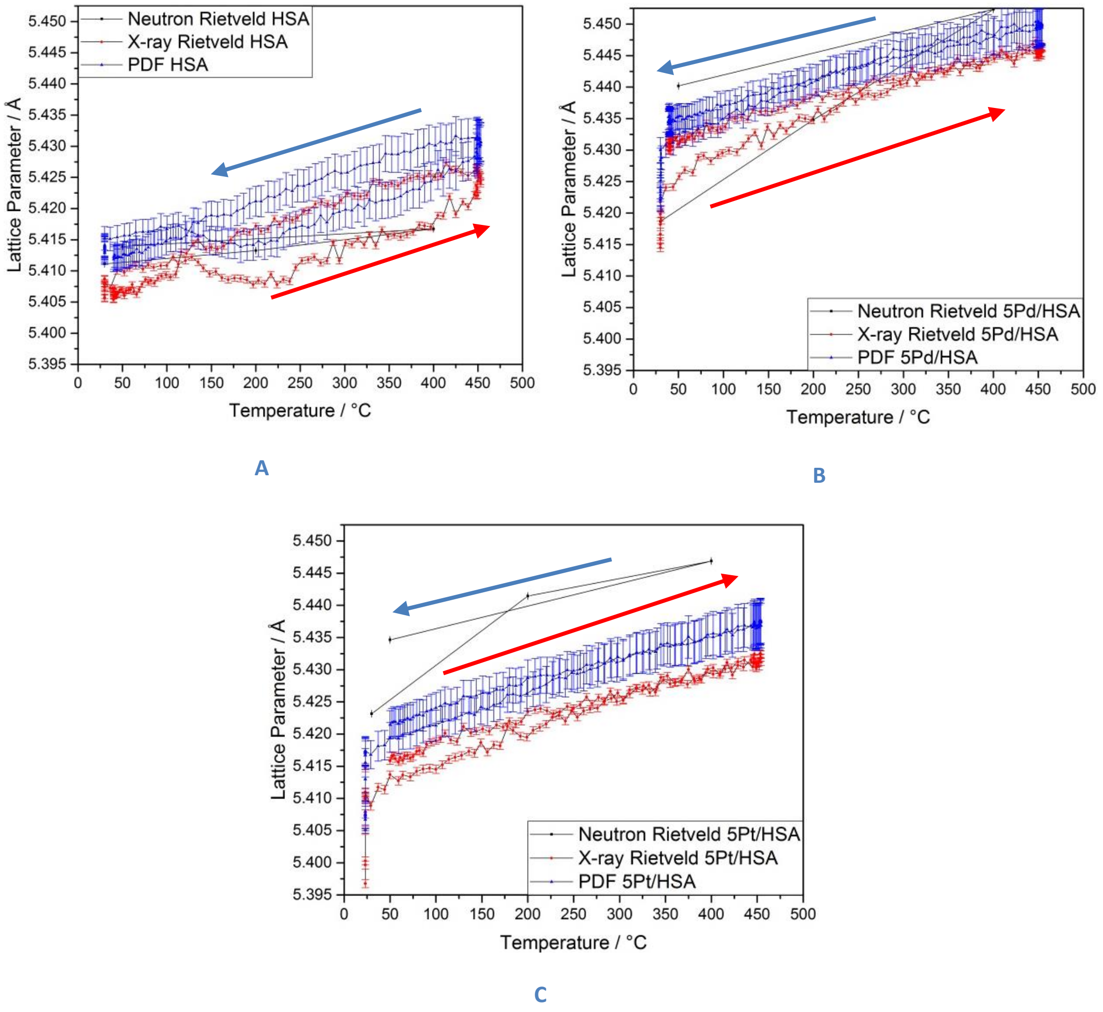

A

B

C

Figure 4-16: Comparison of the Lattice Parameters derived from Rietveld and PDF (between 2-20 Å) for High surface area ceria (A) and the Pd and Pt loaded samples (B and C) respectively. The red and blue arrows indicate the heating and cooling (of the sample) respectively.

Figure 4-17 shows the comparison of the refined 1st Ce-Ce interatomic distances found using EXAFS and PDF techniques, for all 3 samples. These show how the Ce-Ce interatomic changes under a reducing atmosphere. This shows for the pure ceria support, we observe a slight contraction in the distance for both PDF and EXAFS before the bond distance increases under further heating. In contrast the Pd and Pt loaded samples show a similar correlation between both EXAFS and PDF. Both these techniques indicate that after the start of heating under a reducing atmosphere there’s a noticeable increase in the interatomic distance as the sample is heated further. Though the EXAFS, XRD or PDF data alone do not give a full story, the comparison of the respective datasets show how the lattice parameter behaves under the reducing conditions, showing that over the short, medium and long range similar characteristics are seen. It must be noted that there is a sharp increase in lattice parameter as the samples are at room temperature. This could be attributed to the sample settling as gas is introduced to the capillary. The offset between Rietveld and PDF results may be a result of the data correction process.

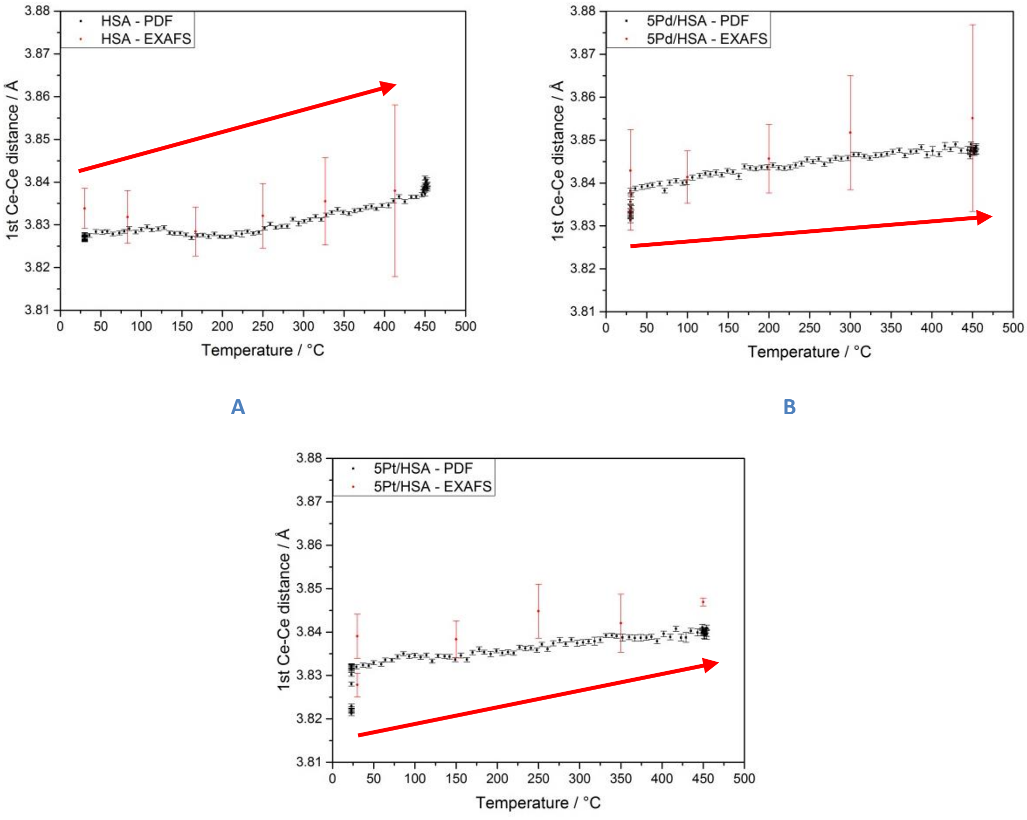

A

B

C

Figure 4-17: Comparison of the 1st Ce-Ce distance derived from k-edge EXAFS and PDF for High surface area ceria (A) and 5wt% Pd and Pt loaded samples (B and C) respectively. The red arrow indicates the direction of heating.

4.7 Conclusion

To conclude, this work has successfully shown that a combination of techniques is important in the comprehension of how catalytic materials behave under reducing conditions. Neutron diffraction and x-ray total scattering methodologies both show the fluorite structure is observed from the outset and throughout the reducing cycle. Neutron diffraction methods show the reduction of ceria and the loss of oxygen whereas XPDF showing the increase in disorder upon heating, and perhaps the formation of Ce (III)-O bonds. The XPDF shows increases in lattice parameters during the cycle consistent with previously reported metal loaded ceria systems under reducing conditions.[52] A combination of refined lattice parameters and refined oxygen occupancies, from ND, show that heating to 400°C that pure ceria support and the respective Pd and Pt loading on ceria are reduced by ca. 10%. With an increase in the lattice parameter which is a combination of thermal disorder and formation of Ce (III) ions. A similar observation has been seen using ND under reducing conditions where the loss of oxygen and the increase in lattice parameters and thermal parameters upon heating.[53] The important differences between the pure support and PGM loaded materials is on cooling that the pure support returns to a similar lattice parameter value and oxygen occupancy whereas for PGM loaded samples do not return to their original values.

The analysis of XANES data gives important information of the electronic and coordination of the probed atom. For the Ce L_3-edge of the high surface area ceria support, we can observe the reduction from Ce (IV) to Ce (III) under heating then oxidation back to Ce (IV). This trait has been observed previously in cerium based oxides.[54] In contrast to the reported literature, no particle size growth was seen i.e. no definitive peak sharpening in diffraction, suggesting that the increase in particle size and loss of oxide deficient surfaces was not the cause of the reoxidation of the ceria under reducing and cooling conditions. The comparison of the Pd K-edge and Pt L_3-edge with the respective Ce L_3-edge data shows the reduction of the PGM metal simultaneously with the onset of Ce (IV) to Ce (III) reduction, at a lower temperature than pure ceria. This indicates that PGM are important to aid in the reduction of ceria suggesting that PGM leads to a spill over mechanism. Furthermore the amount of Ce (III) present upon cooling stays consistent on cooling (matching the lack of reoxidation seen in Neutron Diffraction). In addition the Pd K-edge EXAFS shows the reduction of PdO to Pd metal, though not fully, suggesting a small particle formation and no incorporation of Pd into the ceria lattice by this synthesis procedure or subsequent treatment.[55]

A combination of these techniques would suggest that for the pure ceria support, though reduction is observed this could actually be an extensive migration of oxygen from their ideal sites in the structure which is mimicking a reduction then the subsequent oxidation in reducing conditions. In comparison Pd and Pt loaded onto ceria, show a reduction upon heating and no oxidation upon cooling. This indicates that both Pd and Pt are important in the removal of oxygen from the ceria lattice. This work indicates that Pd and Pt both have similar influence on the ceria support by the amount of reduction observed. This is contrary to reported literature indicating that Pd has stronger metal support interactions than Pt.[56]

Further work for this would be to use neutron PDF to probe further into the migration of oxygen atoms throughout the lattice then to combine all datasets and use RMC based methods to model these materials to investigate further how oxygen atoms in the ceria lattice behave under reducing conditions.

4.8 Acknowledgements

I thank the U.K. Science and Technology Facilities Council for allocating neutron beam time at the ISIS facility. I acknowledge the European Synchrotron Radiation Facility for provision of synchrotron radiation facilities.

4.9 Bibliography

1 A. Trovarelli, *Catalysis by Ceria and Related Materials*, Imperial College Press, London, 2002.

2 D. Astruc, in *Nanoparticles and Catalysis*, Wiley-VCH Verlag GmbH & Co. KGaA, 2008, pp. 1–48.

3 H. Renner, G. Schlamp, I. Kleinwächter, E. Drost, H. M. Lüschow, P. Tews, P. Panster, M. Diehl, J. Lang, T. Kreuzer, A. Knödler, K. A. Starz, K. Dermann, J. Rothaut, R. Drieselmann, C. Peter and R. Schiele, in *Ullmann's Encyclopedia of Industrial Chemistry*, Wiley-VCH Verlag GmbH & Co. KGaA, 2000.

4 J. J. McKetta Jr, *Chemical Processing Handbook*, CRC Press, 1993.

5 J. A. Rabo, *Catal. Today*, 1994, **22**, 201–234.

6 M. E. Dry, *Catal. Today*, 2002, **71**, 227–241.

7 L. F. Liotta, A. Longo, A. Macaluso, A. Martorana, G. Pantaleo, A. M. Venezia and G. Deganello, *Appl. Catal. B Environ.*, 2004, **48**, 133–149.

8 H. He, H. X. Dai, L. H. Ng, K. W. Wong and C. T. Au, *J. Catal.*, 2002, **206**, 1–13.

9 L. F. Liotta, A. Longo, G. Pantaleo, G. Di Carlo, A. Martorana, S. Cimino, G. Russo and G. Deganello, *Appl. Catal. B Environ.*, 2009, **90**, 470–477.

10 P. Fornasiero, J. Kašpar, V. Sergo and M. Graziani, *J. Catal.*, 1999, **182**, 56–69.

11 S. J. Tauster, S. C. Fung and R. L. Garten, *J. Am. Chem. Soc.*, 1978, **100**, 170–175.

12 H. Shinjoh, M. Hatanaka, Y. Nagai, T. Tanabe, N. Takahashi, T. Yoshida and Y. Miyake, *Top. Catal.*, 2009, **52**, 1967–1971.

13 B. Harrison, A. F. Diwell and C. Hallett, *Platin. Met. Rev.*, 1988, **32**, 73–83.

14 M. F. Luo and X. M. Zheng, *Appl. Catal. A Gen.*, 1999, **189**, 15–21.

15 G. P. Osorio, S. F. Moyado, V. Petranovskii and A. Simakov, *Catal. Letters*, 2006, **110**, 53–60.

16 M. F. Luo, Z. Y. Hou, X. X. Yuan and X. M. Zheng, *Catal. Letters*, 1998, **50**, 205–209.

17 A. I. Boronin, E. M. Slavinskaya, I. G. Danilova, R. V. Gulyaev, Y. I. Amosov, P. A. Kuznetsov, I. A. Polukhina, S. V. Koscheev, V. I. Zaikovskii and A. S. Noskov, *Catal. Today*, 2009, **144**, 201–211.

18 R. V Gulyaev, E. M. Slavinskaya, S. A. Novopashin, D. V Smovzh, A. V Zaikovskii, D. Y. Osadchii, O. A. Bulavchenko, S. V Korenev and A. I. Boronin, *Appl. Catal. B Environ.*, 2014, **147**, 132–143.

19 P. Fornasiero, G. R. Rao, J. Kašpar, F. L’Erario and M. Graziani, *J. Catal.*, 1998, **175**, 269–279.

20 G. Ranga Rao, P. Fornasiero, R. Di Monte, J. Kašpar, G. Vlaic, G. Balducci, S. Meriani, G. Gubitosa, A. Cremona and M. Graziani, *J. Catal.*, 1996, **162**, 1–9.

21 S. Bernal, J. J. Calvino, M. A. Cauqui, J. M. Gatica, C. Larese, J. A. Pérez Omil and J. M. Pintado, *Catal. Today*, 1999, **50**, 175–206.

22 C. Hardacre, T. Rayment and R. M. Lambert, *J. Catal.*, 1996, **158**, 102–108.

23 S. Suhonen, M. Valden, M. Hietikko, R. Laitinen, A. Savimäki and M. Härkönen, *Appl. Catal. A Gen.*, 2001, **218**, 151–160.

24 S. Bernal, F. J. Botana, J. J. Calvino, G. A. Cifredo, J. A. Pe´rez-Omil and J. M. Pintado, *Catal. Today*, 1995, **23**, 219–250.

25 S. Hinokuma, H. Fujii, M. Okamoto, K. Ikeue and M. Machida, *Chem. Mater.*, 2010, **22**, 6183–6190.

26 H. Hirata, K. Kishita, Y. Nagai, K. Dohmae, H. Shinjoh and S. Matsumoto, *Catal. Today*, 2011, **164**, 467–473.

27 L. L. Murrell, S. J. Tauster and D. R. Anderson, in *Catalysis and Automotive Pollution Control II*, ed. A. Crucq, Elsevier Science PUBL B V, Amsterdam, 1991, vol. 71, pp. 275–289.

28 Y. Nagai, T. Hirabayashi, K. Dohmae, N. Takagi, T. Minami, H. Shinjoh and S. Matsumoto, *J. Catal.*, 2006, **242**, 103–109.

29 W. Lin, A. A. Herzing, C. J. Kiely and I. E. Wachs, 2008, 5942–5951.

30 G. Ertl, H. Knozinger and J. Weitkamp, in *Handbook of Heterogeneous Catalysis*, Wiley-VCH Verlag GmbH, 1997, pp. 1–48.

31 H. P. Sun, X. P. Pan, G. W. Graham, H.-W. Jen, R. W. McCabe, S. Thevuthasan and C. H. F. Peden, *Appl. Phys. Lett.*, 2005, **87**.

32 S. Hosokawa, M. Taniguchi, K. Utani, H. Kanai and S. Imamura, *Appl. Catal. A Gen.*, 2005, **289**, 115–120.

33 M. Hatanaka, N. Takahashi, T. Tanabe, Y. Nagai, K. Dohmae, Y. Aoki, T. Yoshida and H. Shinjoh, *Appl. Catal. B Environ.*, 2010, **99**, 336–342.

34 K. Okumura, T. Motohiro, Y. Sakamoto and H. Shinjoh, *Surf. Sci.*, 2009, **603**, 2544–2550.

35 H. Yao, M. Sieg and H. Plummer Jr, *J. Catal.*, 1979, **59**, 365–374.

36 L. L. Murrell, S. J. Tauster and D. R. Anderson, *Stud. Surf. Sci. Catal.*, 1991, **71**, 275.

37 O. Mathon, A. Beteva, J. Borrel, D. Bugnazet, S. Gatla, R. Hino, I. Kantor, T. Mairs, M. Munoz, S. Pasternak, F. Perrin and S. Pascarelli, *J. Synchrotron Radiat.*, 2015, **22**, 1548–1554.

38 R. I. Smith, S. Hull and A. R. Armstrong, in *EPDIC 3, PTS 1 AND 2: Proceedings Of the 3RD European Powder Diffraction Conference*, ed. E. Delhez, R and Mittemeijer, Transtec Publications LTD, Zurich, 1994, vol. 166, pp. 251–256.

39 B. Ravel and M. Newville, *J. Synchrotron Radiat.*, 2005, **12**, 537–541.

40 P. Juhás, T. Davis, C. L. Farrow and S. J. L. Billinge, *J. Appl. Crystallogr.*, 2013, **46**, 560–566.

41 C. L. Farrow, P. Juhas, J. W. Liu, D. Bryndin, E. S. Božin, J. Bloch, T. Proffen and S. J. L. Billinge, *J. Phys. Condens. Matter*, 2007, **19**, 335219.

42 A. P. Hammersley, S. O. Svensson, M. Hanfland, A. N. Fitch and D. Hausermann, *High Press. Res.*, 1996, **14**, 235–248.

43 H. M. Rietveld, *J. Appl. Crystallogr.*, 1969, **2**, 65–71.

44 B. H. Toby, *J. Appl. Crystallogr.*, 2001, **34**, 210–213.

45 A. C. Larson and R. B. Von Dreel, *Los Alamos Nation Lab. Rep. LAUR*, 1994, 86–748.

46 P. Thompson, D. E. Cox and J. B. Hastings, *J. Appl. Crystallogr.*, 1987, **20**, 79–83.

47 L. W. Finger, D. E. Cox and A. P. Jephcoat, *J. Appl. Crystallogr.*, 1994, **27**, 892–900.

48 E. Rocchini, A. Trovarelli, J. Llorca, G. W. Graham, W. H. Weber, M. Maciejewski and A. Baiker, *J. Catal.*, 2000, **194**, 461–478.

49 N. Acerbi, S. Golunski, S. C. Tsang, H. Daly, C. Hardacre, R. Smith and P. Collier, *J. Phys. Chem. C*, 2012, **116**, 13569–13583.

50 D. Rodríguez, J. Sánchez and G. Arteaga, *J. Mol. Catal. A Chem.*, 2005, **228**, 309–317.

51 S. Damyanova and J. M. . Bueno, *Appl. Catal. A Gen.*, 2003, **253**, 135–150.

52 J. C. Hanson, R. Si, W. Xu, S. D. Senanayake, K. Mudiyanselage, D. Stacchiola, J. A. Rodriguez, H. Zhao, K. A. Beyer, G. Jennings, K. W. Chapman, P. J. Chupas and A. Martínez-Arias, *Catal. Today*, 2014, **229**, 64–71.

53 S. Hull, S. T. Norberg, I. Ahmed, S. G. Eriksson, D. Marrocchelli and P. A. Madden, *J. Solid State Chem.*, 2009, **182**, 2815–2821.

54 D. R. Modeshia, C. S. Wright, J. L. Payne, G. Sankar, S. G. Fiddy and R. I. Walton, *J. Phys. Chem. C*, 2007, **111**, 14035–14039.

55 C. I. Hiley, J. M. Fisher, D. Thompsett, R. J. Kashtiban, J. Sloan and R. I. Walton, *J. Mater. Chem. A*, 2015, **3**, 13072–13079.

56 C. de Leitenburg, A. Trovarelli and J. Kašpar, *J. Catal.*, 1997, **166**, 98–107.

Chapter 5: *Insitu* X-ray absorption spectroscopy and X-ray total scattering characterisation of Palladium loaded ceria

5.1 Abstract

The effect of Pd loading on ceria was examined by using combined in situ XAS (at the Pd K-edge)/High resolution x-ray diffraction (HRXRD) as well as in situ PDF techniques. In addition, Ce L_3-edge studies were conducted on 1, 2.5 and 5wt% Pd loaded on high-surface ceria samples. All methods showed that an increase in the Pd loading decreased the reduction temperature for both the Ceria support and PdO to Pd metal conversion. Both XAS and HRXRD show the reduction of all samples upon heating, whereas on cooling there is no or little reoxidation of Ce (III) to Ce (IV) for the Pd loaded samples in comparison to the pure support. The method in which the Pd is incorporated onto ceria is appears to be important (strong metal support interaction) as the reoxidation is observed for a physical mixture sample of PdO and ceria.

5.2 Introduction

Ceria (CeO_2), on its own, has extensive uses in the field of catalysis[1] and numerous other areas.[2–5] In addition, platinum group metals (PGMs)[6] and transition metals[7] can be loaded onto a ceria support either as a sole metal or in conjunction with other metals e.g. bimetallic systems. The metals that are dispersed onto the metal oxide support are normally found as either atomic clusters or particles. As the size of the metal particles decrease further to cluster, the catalytic properties are changed. This is to increase their efficiency[8] as surface area increases with decreasing particle volume whilst reducing their cost.[9]Additionally, the combination of PGMs and the support, can improve the oxygen storage capacity (OSC) and redox operation.[10,11]

The use of Pd on ceria has been well documented in uses such as automotive exhaust catalysts,[12] steam reforming,[13] methanol synthesis[14] etc. This combined system is useful due to a combination to both the OSC of the ceria support and the ability for catalysis to be performed by the noble metal nanoparticles. These systems are normally theorised to have the support enhanced activity of the noble metal catalysis due to Strong metal support interaction (SMSI). This interaction is generally found when it is induced by the reduction of an oxide support, leading to the change in the chemical properties for the noble metals dispersed onto the surface support. As well as being a reversible process,[15] there is improved reducibility of the support. The SMSI effect has been rationalised by H_2 dissociated into atomic hydrogen by the noble metal then the removal of oxygen atoms located on the support surface in the vicinity of the noble metal particle.

Charge transfer can occur between the metal oxide support and the metal nanoparticle via electronic interactions between the respective components in the system. Chemical interactions complicate this further e.g. by a redox reaction. These interactions often influence the catalytic performance and reducibility of the loaded metal.[16–18] There are numerous ways where SMSI can be explained e.g. formation of PGM-O-Ce bonds ,[19] alloy formation,[20] diffusion of the PGM into the support and/or encapsulation of the PGM by the support,[21] partial reduction of the ceria by the PGM creating bridging hydroxyl moieties[22] and electronic interactions creating a "catalytic nanodiode"

It was important to study both the local, medium and long range structure simultaneously whilst under reducing conditions as these might show if there are any differences how the reduction proceeds over different length scales.

Insitu X-ray diffraction (XRD) was used to study the average structure whilst *insitu* X-ray Pair Distribution Function (XPDF) was used to investigate the local and medium structure. *Insitu* X-ray absorption spectroscopy (XAS) was utilised in probing the geometric and electronic structure of both the Ce and Pd atoms present.

5.3 Experimental Section

The pure ceria support is a commercially available Rhodia high surface area ceria (referred to as HSA in the thesis) from Solvay and the Pd and Pt samples were made by impregnation. The required amount of Pd nitrate solution (commercially available from JM) diluted to a volume appropriate to fill the pore volume of the HSA ceria support. Materials were dried at 105°C and fired at 500°C.

5.3.1 Temperature Programmed Reduction (TPR)

TPR was performed using a Micromeritics AutoChem II 2920 instrument. The samples were heated from 25°C to 1100°C at 10°C min^{-1} and held for 10 minutes under 5% H_2:N_2 flowing at 30 ml min^{-1}. TPR measures the uptake of hydrogen as a sample undergoes a heating cycle.

5.3.2 X-ray absorption spectroscopy (XAS) at Pd K-edge

Insitu XAS data was attained at the Pd K-edge (24350 eV) at BM01 (The Swiss-Norwegian beam line), European Synchrotron Research Facility (ESRF). A quartz capillary was loaded with approximately 100mg of the sample and loaded into a rig above a hot air blower. A Si

(111) double crystal monochromator was used to obtain the data in transmission geometry and using ionisation chambers. The data was collected between 24150 and 25600 eV in step scans. The samples were purged under Argon then switched to the continuously flowing reducing atmosphere of 5% H_2:N_2. The datasets were measured at 30, 50, 100, 200, 300, 400 and 450 °C during heating, with a 5 °C min^{-1} ramp, held at 450 °C for 10 minutes then allowed to cool to RT whilst the samples were measured at 400, 300, 200, 100 and 50°C.

5.3.3 X-ray absorption spectroscopy (XAS) at Ce L_3-edge

Insitu XAS data was acquired at the Ce L_3-edge (5723.4 eV) on the BM26A[23] beam line, ESRF (for the 2.5 wt% and 5 wt% Pd on a high surface area ceria support samples). All datasets were collected in transmission geometry and using ionisation chambers A Si (111) double crystal monochromator was used to collect the L_3-edge data. Pellets were made from 10mg of the ceria sample was ground in conjunction with 90mg of fumed silica. The XAS data were measured in step scans in an E-range of 5623.0 and 6154.0 eV. The samples were purged under N_2 then switched to 5% H_2:N_2. Data was obtained at room temperature then the temperature was ramped from 10°C to 450°C at 10°Cmin^{-1}. The samples were then cooled under 5% H_2:N_2 to room temperature whilst data was collected.

5.3.4 X-ray absorption spectroscopy (XAS) at Ce L_3-edge

Insitu XAS data was acquired at the Ce L_3-edge (5723.4 eV) on the BM23 beam line,[24] ESRF (for the 1 wt% on a high surface area ceria support sample). All datasets were collected in transmission geometry and using ionisation chambers A Si (111) double crystal monochromator was used to collect the L_3-edge data. Pellets were made from 10mg of the ceria sample was ground in conjunction with 90mg of fumed silica. The XAS data were measured in step scans in an E-range of 5623.0 and 6154.0 eV. The samples were purged under N_2 then switched to 5% H_2:N_2. Data was obtained at room temperature then the temperature was ramped from 10°C to 450°C at 10°C min^{-1}. The samples were then cooled under 5% H_2:N_2 to room temperature whilst data was collected.

5.3.5 X-ray diffraction (XRD)

Insitu XRD data was measured at BM01, ESRF using a PILATUS2M 2D detector. The wavelength was λ=0.5060 Å with a 2θ range = 8 - 34°. A quartz capillary was loaded with approximately 100mg of the sample and loaded into a rig above a hot air blower. The samples were purged under N_2 then switched to the continuously flowing reducing atmosphere of 5% H_2:N_2. The datasets were measured at 30, 50, 100, 200, 300, 400 and 450

°C during heating, with a 5 °C min^{-1} ramp, held at 450 °C for 10 minutes then allowed to cool to RT whilst the samples were measured at 400, 300, 200, 100 and 50°C.

5.3.6 X-ray Total scattering

X-ray total scattering patterns were obtained on the ID15B at the ESRF, using a mar345 2D detector. The wavelength was λ=0.1438001 Å and Q = 0.6 - 23 Å^{-1}. The samples were prepared to produce monodisperse grain sizes to aid in gas flow over the sample. These were loaded into a 1mm diameter quartz capillary mounted above a hot air blower.

The samples were purged under N_2 before switching to 5% H_2:N_2. All the samples were measured at 30, 50, 100, 200, 300, 400 and 450 °C during heating, with a 5 °C min^{-1} ramp, held at 450 °C for 10 minutes then allowed to cool to RT whilst the samples were measured at 400, 300, 200, 100 and 50°C.

5.4 Data analysis

5.4.1 XAS data correction and refinement

All XAS datasets underwent background subtraction and normalisation using Athena[25] software for Pd K-edge and Ce L_3-edges. Phase-shifts and amplitude factors were calculated using FEFF6l using crystallographic data of ceria fluorite structure Hedin-Lundqvist potentials were used to calculate phase shifts and backscattering factors. For the Pd K-edge the fitting was performed between k = 1.65 and 11 Å^{-1} and r = 1 and 4 Å. Due to issues with data quality, only analysis on the XANES spectra was performed for the Ce L_3-edge. For the Pd K-edge the amplitude reduction factor (SO2) was refined using Pd foil with a fixed coordination number of 8 and 12 respectively.

5.4.2 XRD analysis

The XRD 2D images were processed using a program on the SNBL beamline.

The analysis was performed using the Rietveld method.[26] This was performed using the graphical interface, EXPGUI[27], of the GSAS software.[28] The background, profile parameters, lattice parameter, isotropic thermal displacement parameters (U_{iso}) and oxygen occupancy were refined.

Batch refinements of the *Insitu* datasets was performed using the SrRietveld which allows for the automation of GSAS based refinements.[29]

5.4.3 Real space analysis

The 2D images were processed using Fit2D.[30] The raw diffraction patterns were then processed using PDFgetX3[31] between $1 < Q < 23$ Å^{-1} as this offers rapid batch processing of the data.

The analysis was performed using the PDFfit2 software in the graphical interface of PDFgui.[32]

5.5 Results and Discussion

The approach to data analysis used numerous steps in order to investigate thoroughly how the materials behave under reducing conditions and how the short, medium and long range structural order is affected.

5.5.1 X-ray diffraction

XRD is a powerful technique in the comprehension and characterisation of the bulk/average structure of the material allowing the understanding of the long range structural properties.

Figure 5-1 shows the comparison of the XRD patterns collected for 1, 2.5 and 5 wt% Pd on ceria respectively. The peaks correspond to the fluorite structure. Differences in peak position and intensity suggest subtle variations in lattice parameters. Further to this, peak broadening is indicative of a combination of increased disorder and/or smaller crystallite size.

Figure 5-2 shows examples of the fits for the respective samples showing good agreement between the data and models.

Figure 5-3 shows the comparison of the refined parameters from HRXRD for the pure ceria support and the respective 1, 2.5 and 5 wt % Pd samples. The refined lattice parameters (Top left) shows that on heating the lattice expands, which is due to the combination of thermal expansion and the formation of Ce (III) ions. In the case of 5wt% Pd on ceria, a small peak forms at d = ~2.25 Å, suggesting the formation of Pd metal.

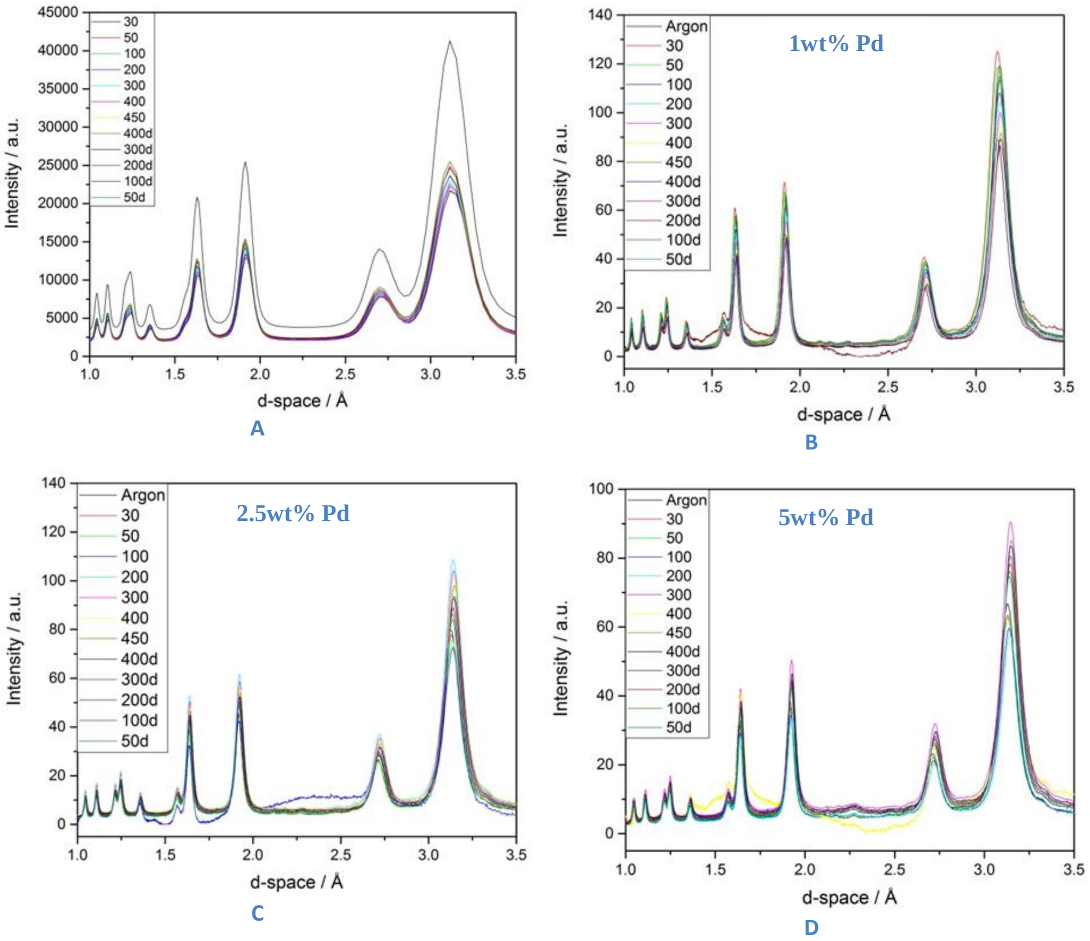

A B C D

Figure 5-1: Comparison of the XRD Patterns for the (A) ceria support and the respective (B) 1, (C) 2.5 and (D) 5wt% Pd loaded samples. This shows that all the samples have the ceria fluorite structure. Certain data sets show a varying background in comparison to a majority of the data collected which is attributed to beam top up.

Upon cooling, the lattice parameter for the pure ceria support, returns to its original value whereas this is not the case for any of the Pd loaded samples. This might suggest some disorder has been retained upon cooling.

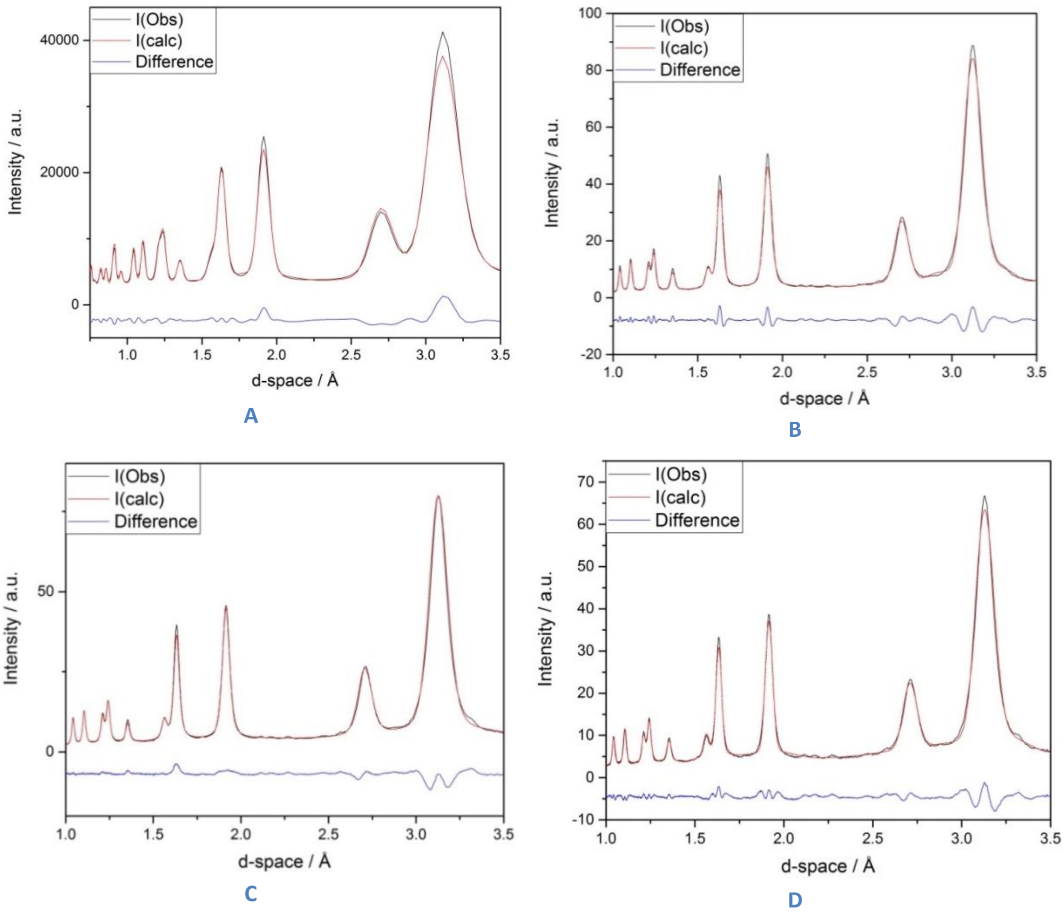

A

B

C

D

Figure 5-2: Examples of the XRD Patterns and their respective fits for the (A) ceria support and the respective (B) 1, (C) 2.5 and (D) 5wt% Pd loaded samples. This shows that all the samples have the ceria fluorite structure.

The atomic displacement parameters for both cerium and oxygen atoms (Top right and Bottom left of Figure 5-3 respectively) show that on heating, all the atoms become more disorder and that on cooling the atoms become less disordered. The refined oxygen occupancies (Bottom right) show that for all samples that upon heating in a reducing atmosphere the occupancy decreases. This would suggest that oxygen is removed from the lattice. However, on cooling, under a reducing atmosphere, the occupancy increases. For the pure support the occupancy returns to its original value whereas for the Pd loaded samples, less oxygen is present after cooling back to 50°C. This would indicate that on heating both reduction and extensive migration of oxide ions from their ideal sites is present. On cooling, oxide ions return to their original sites which would mimic reoxidation under hydrogen.

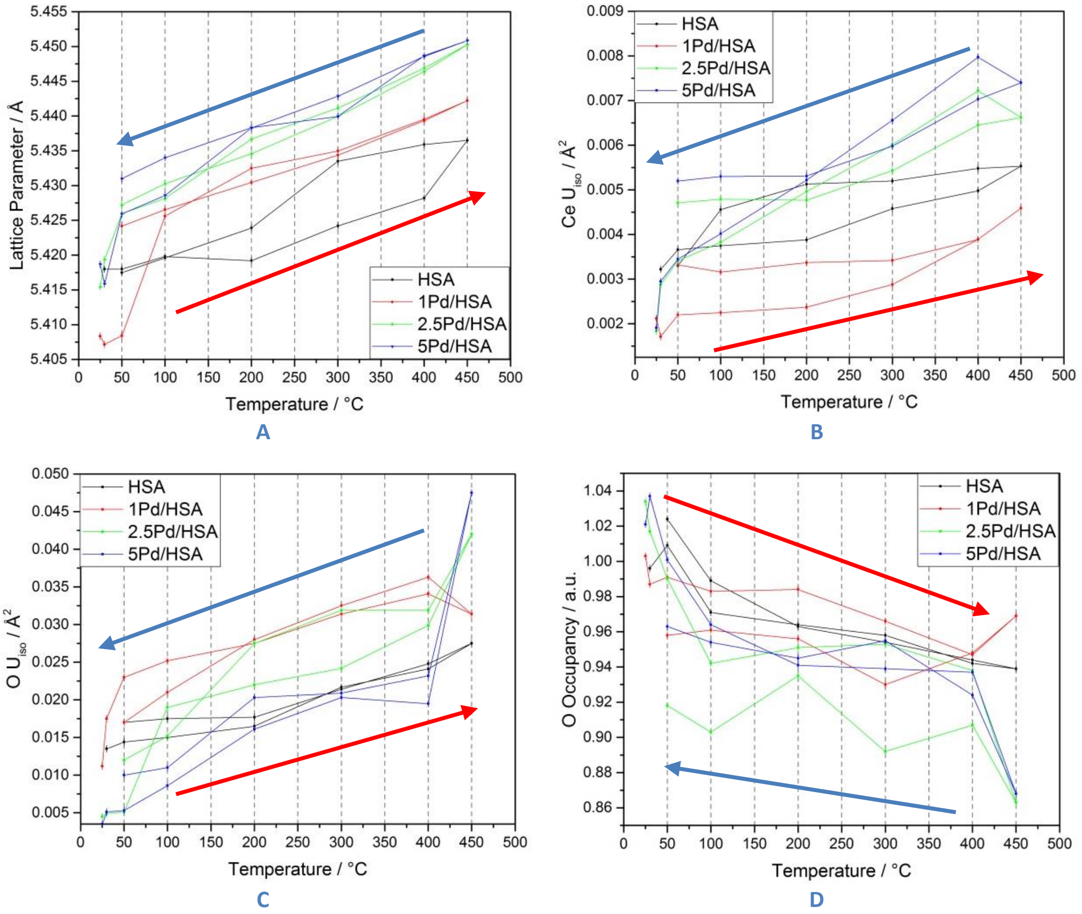

Figure 5-3: (A) Lattice Parameters for the Ceria support and respective Pd loaded ceria samples, (B) Cerium atom isotropic atomic displacement parameters for the Ceria support and respective Pd loaded ceria samples, (C) Oxygen atom isotropic atomic displacement parameters for the Ceria support and respective Pd loaded ceria samples and (D) Oxygen occupancies for the Ceria support and respective Pd loaded ceria samples. These show variations in the lattice parameter and disorder present in the samples throughout the heating and cooling cycles. The red and blue arrows indicate the heating and cooling (of the sample) respectively.

5.5.2 X-ray absorption Spectroscopy

XAS is an important technique in order to comprehend the geometric and electronic structure of the probed atoms. This allows the understanding how the local structure varies under the reaction conditions.

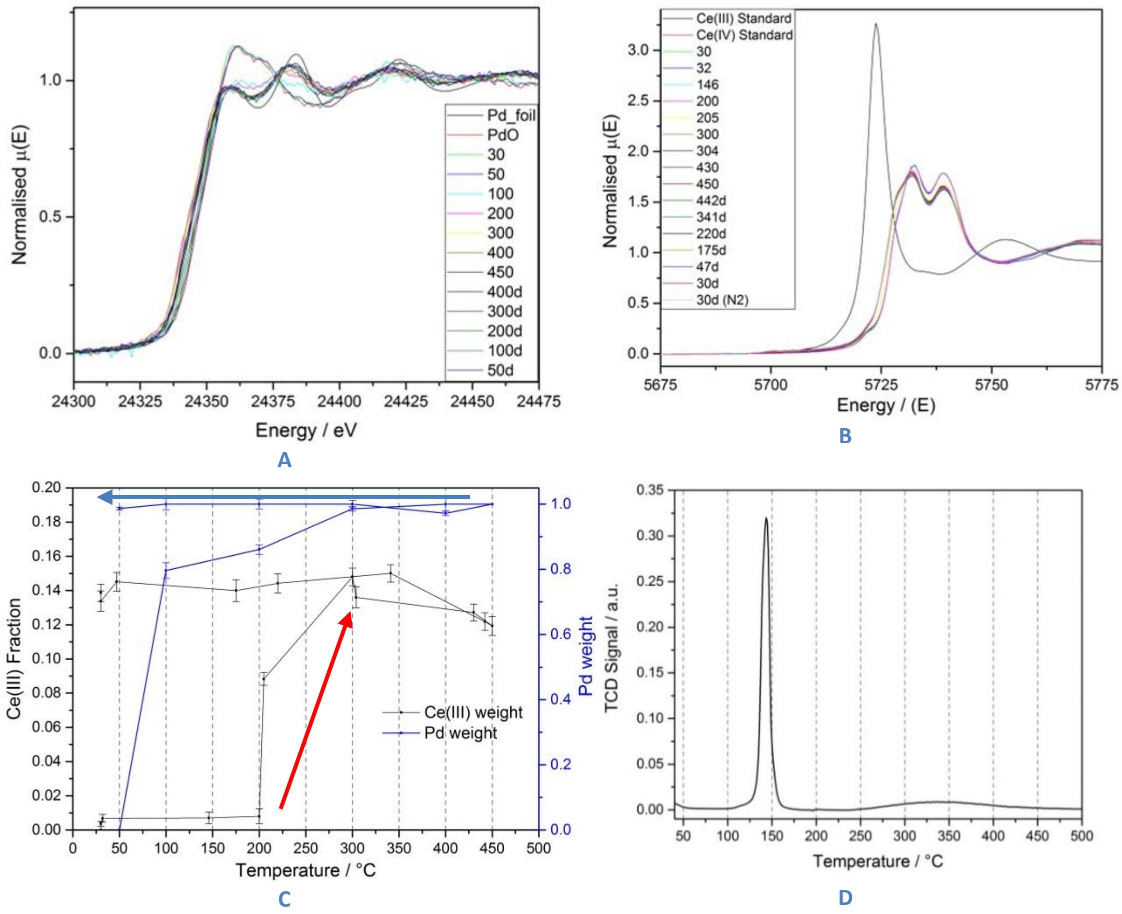

Figure 5-4: (A) Comparison of the normalised μ(E) for Pd K-edge obtained on heating and cooling for 1wt%Pd on ceria. (B) Comparison of the normalised μ(E) for Ce L_3-edge obtained on heating and cooling for 1wt%Pd on ceria. (C) Comparison of the Ce (III) weight and Pd metal weight obtained through LCF of the Ce L_3-edge and Pd K-edge respectively. The red and blue arrows indicate the heating and cooling (of the sample) respectively. (D) The TPR Profile for 1wt% Pd on ceria

Figure 5-4 shows the comparison of the XANES spectra of the Pd K-edge and Ce L_3-edge as well as the linear combination fitting (LCF) showing the Pd metal and Ce (III) weights respectively, for 1wt% Pd on Ceria. The XANES spectra for the Pd K-edge shows initially there is PdO present which then reduces to Pd metal once the sample is heated under 5% H_2:N_2.

The XANES spectra for the Ce L_3-edge show that the sample is initially Ce (IV) (in comparison to the Ce (III) standard), as the sample is heated under a reducing atmosphere a noticeable shoulder starts forming indicating the formation of Ce (III) in the sample. The LCF for the Pd K-edge shows the reduction of PdO to Pd metal, though it does not reduce fully to Pd metal. The LCF for the Ce L_3-edge shows the reduction of Ce (IV) to Ce (III) as the sample is heated to 450°C. As the sample is cooled the amount of Ce (III) in the sample stays consistent. Whereas for the pure ceria support the amount of Ce (III) decreases on cooling back to original vales suggesting that the Pd is important in the reduction and removal of oxygen from the lattice. The TPR profile of 1wt% Pd on the high surface area ceria support shows 2 features, a sharp peak ca. 140°C and a small broad feature ca. 350°C. These can be assigned to the reduction of PdO[33] and the reduction of surface ceria[34] respectively.

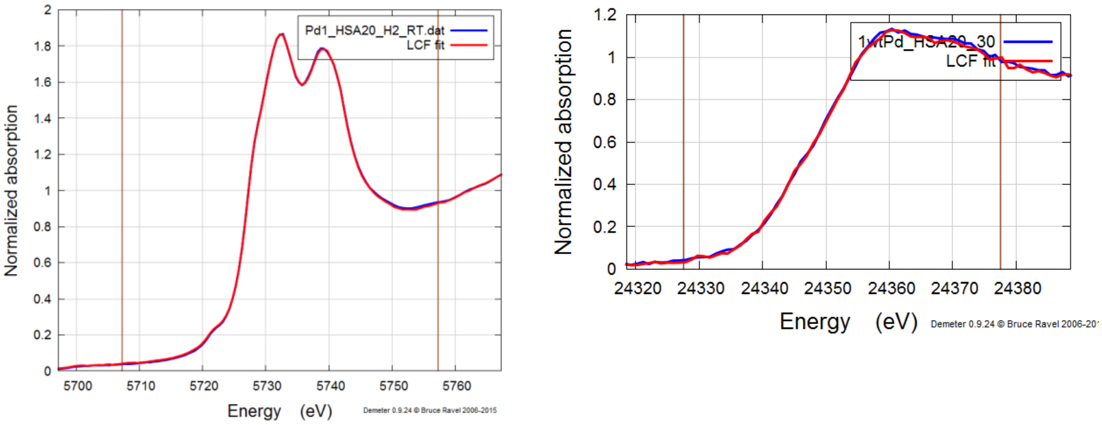

Figure 5-5: (Left) Example LCF for 1 wt% Pd on ceria obtained on the Ce L_3-edge (Right) Example LCF for 1 wt% Pd on ceria obtained on the Ce K-edge

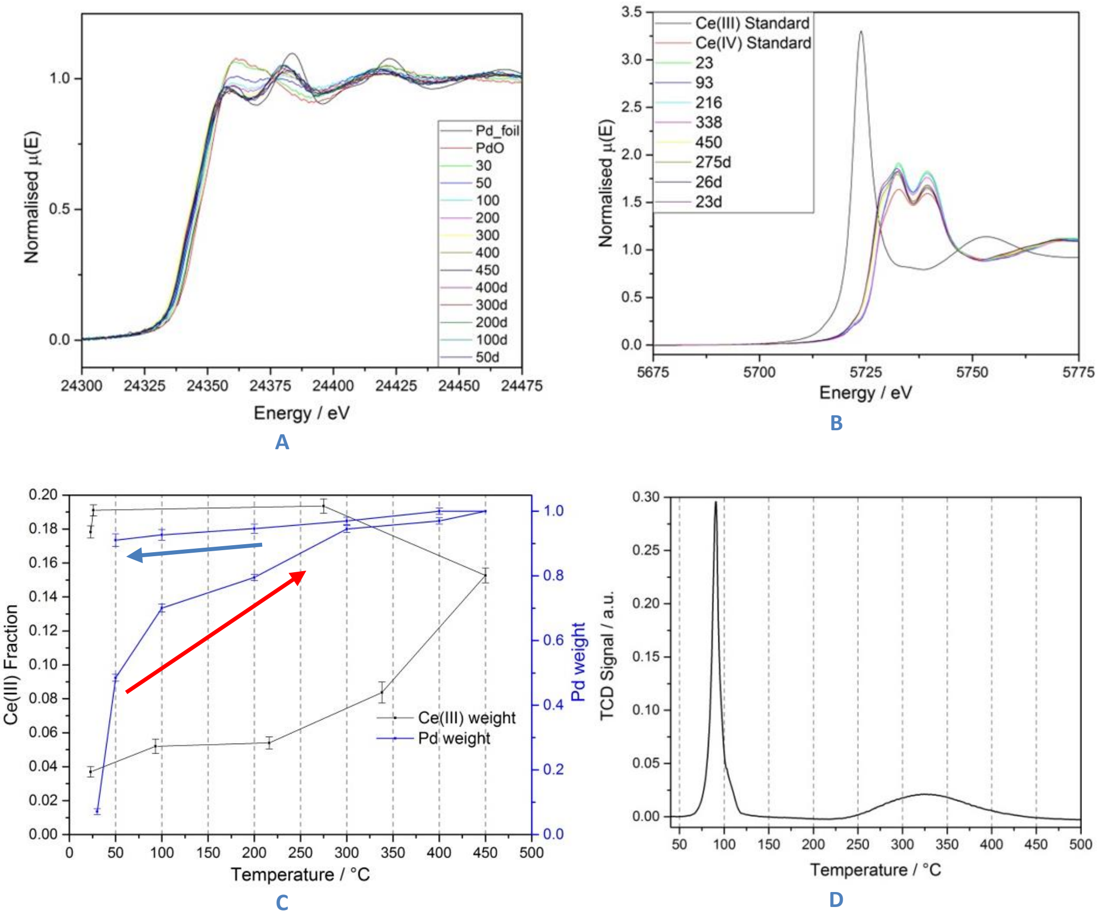

Figure 5-6: (A) Comparison of the normalised μ(E) for Pd K-edge obtained on heating and cooling for 2.5wt% Pd on ceria. (B) Comparison of the normalised μ(E) for Ce L_3-edge obtained on heating and cooling for 2.5wt% Pd on ceria. (C) Comparison of the Ce (III) weight and Pd metal weight obtained through LCF (D) The TPR Profile for 2.5wt% Pd on ceria

Figure 5-6 shows the comparison of the XANES spectra of the Pd K-edge and Ce L_3-edge as well as the linear combination fitting (LCF) showing the Pd metal and Ce (III) weights respectively, for 2.5wt% Pd on Ceria. The XANES spectra for the Pd K-edge shows initially there is PdO present which then reduces to Pd metal once the sample is heated under 5% H_2:N_2. The XANES spectra for the Ce L_3-edge show that the sample is initially Ce (IV) (in comparison to the Ce (III) standard), as the sample is heated under a reducing atmosphere a noticeable shoulder starts forming indicating the formation of Ce (III) in the sample. The LCF for the Pd K-edge shows the reduction of PdO to Pd metal, though it does not reduce fully to Pd metal. The LCF for the Ce L_3-edge shows the reduction of Ce (IV) to Ce (III) as the sample is heated to 450°C. As the sample is cooled the amount of Ce (III) in the sample stays consistent. Whereas for the pure ceria support the amount of Ce (III) decreases on cooling back to original vales suggesting that that the Pd is important in the reduction and removal of oxygen from the lattice. The TPR profile of 2.5wt% Pd on the high surface area ceria support shows 2 features, a sharp peak ca. 90°C and a small broad feature ca. 325°C.

These can be assigned to the reduction of PdO[33] and the reduction of surface ceria[34] respectively.

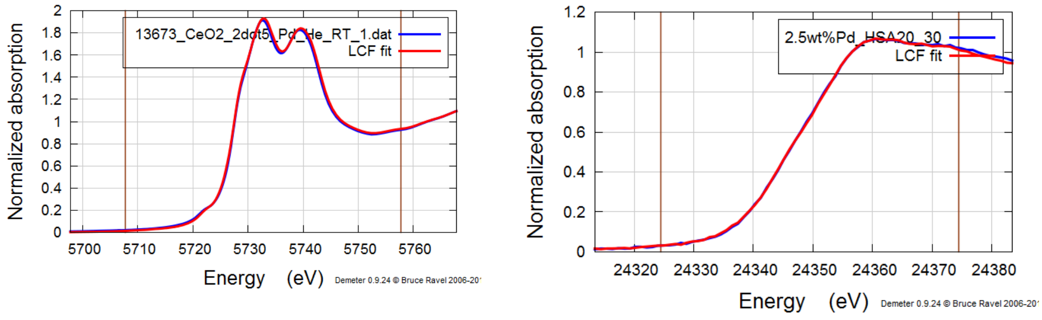

Figure 5-7: (Left) Example LCF for 2.5 wt% Pd on ceria obtained on the Ce L_3-edge (Right) Example LCF for 2.5 wt% Pd on ceria obtained on the Ce K-edge

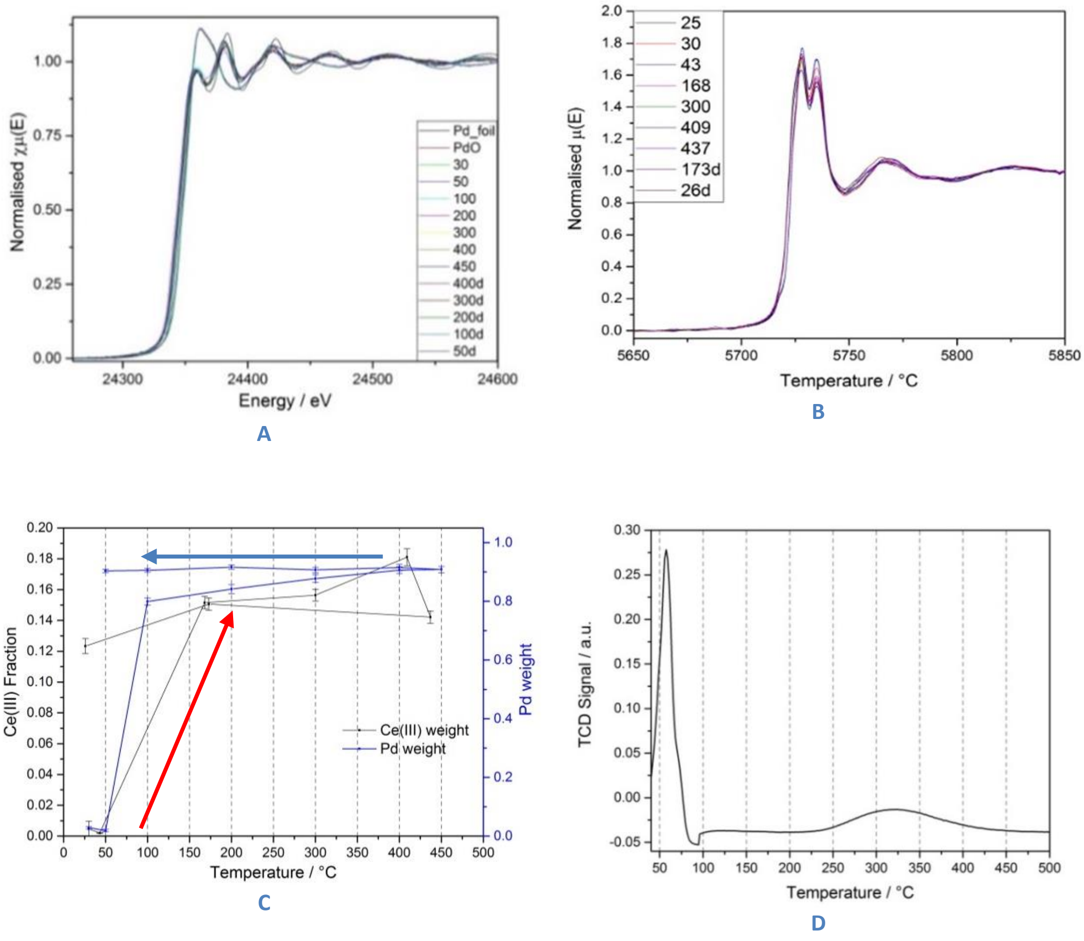

A

B

C

D

Figure 5-8: (A) Comparison of the normalised μ(E) for Pd K-edge obtained on heating and cooling for 5wt% Pd on ceria. (B) Comparison of the normalised μ(E) for Ce L_3-edge obtained on heating and cooling for 5wt% Pd on ceria. (C) Comparison of the Ce (III) weight and Pd metal weight obtained through LCF (D) The TPR Profile for 5wt% Pd on ceria

Figure 5-8 shows the comparison of the XANES spectra of the Pd K-edge and Ce L_3-edge as well as the linear combination fitting (LCF) showing the Pd metal and Ce (III) weights respectively, for 5wt% Pd on Ceria. The XANES spectra for the Pd K-edge shows initially there is PdO present which then reduces to Pd metal once the sample is heated under 5% H_2:N_2. The XANES spectra for the Ce L_3-edge show that the sample is initially Ce (IV) (in comparison to the Ce (III) standard), as the sample is heated under a reducing atmosphere a noticeable shoulder starts forming indicating the formation of Ce (III) in the sample. The LCF for the Pd K-edge shows the reduction of PdO to Pd metal, though it does not reduce fully to Pd metal. The LCF for the Ce L_3-edge shows the reduction of Ce (IV) to Ce (III) as the sample is heated to 450°C. As the sample is cooled the amount of Ce (III) in the sample stays consistent. Whereas for the pure ceria support the amount of Ce (III) decreases on cooling back to original vales suggesting that that the Pd is important in the reduction and removal of oxygen from the lattice. The TPR profile of 5wt% Pd on the high surface area ceria support shows 2 features, a sharp peak ca. 60°C and a small broad feature ca. 320°C. These can be assigned to the reduction of PdO[33] and the reduction of surface ceria[34] respectively. It is also observed that as more Pd is loaded onto the ceria support, the first main peak decreases in its position, suggesting a decrease in reduction temperature as more Pd is loaded.

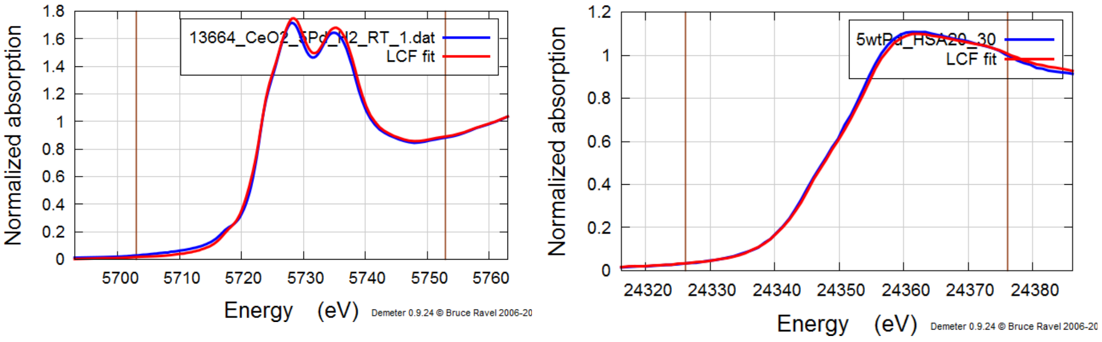

Figure 5-9: (Left) Example LCF for 5 wt% Pd on ceria obtained on the Ce L_3-edge (Right) Example LCF for 5 wt% Pd on ceria obtained on the Ce K-edge

Figure 5-10 shows the XANES spectra (left) and LCF (right) for the pure ceria support. This shows the formation of a shoulder as the sample is reduced under a ramping temperature which then disappears as the sample is cooled. This would seem counterintuitive as there would be no oxidising agent present in the H_2/N_2 gas stream flowing over the sample. One mechanism in which this could be accomplished is by the surface reduction of oxygen or terminating hydroxyl species from the ceria. Then during the reduction cycle there could be extensive migration of oxygen throughout the bulk of the ceria material. On cooling these oxygen return to their ideal sites in the crystal lattice mimicking the return of Ce (IV) even though the sample has been cooled under reducing conditions.

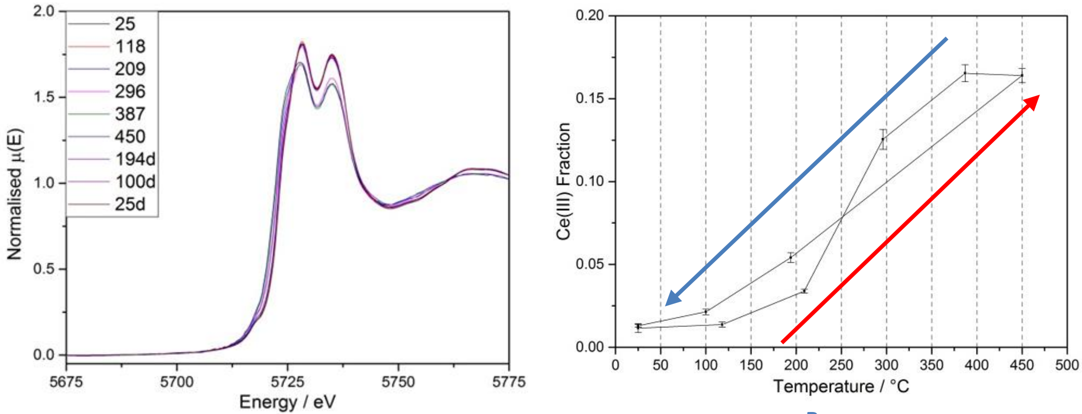

A

B

Figure 5-10: (A) Comparison of the normalised μ(E) for the pure ceria support showing the formation of a shoulder upon heating under a reducing atmosphere. (B) the Ce (III) weight refined from LCF showing the reduction of Ce (IV) to Ce (III) on heating. The red and blue arrows indicate the heating and cooling (of the sample) respectively.

The LCF values refined for Ce (III) shows an increase in the amount of Ce (III) present as the sample is heated to 450°C under a reducing atmosphere, though as the sample is cooled under hydrogen the amount of Ce (III) decreases to a negligible amount suggesting that the introduction of Pd onto the ceria aids in the removal of oxygen from the ceria structure. The addition of Pd metal to the ceria support also decreases the temperature at which Ce (IV) will reduce to Ce (III). It is noticeable that across all the samples that the reduction of PdO to Pd occurs before the reduction of Ce (IV) to Ce (III).

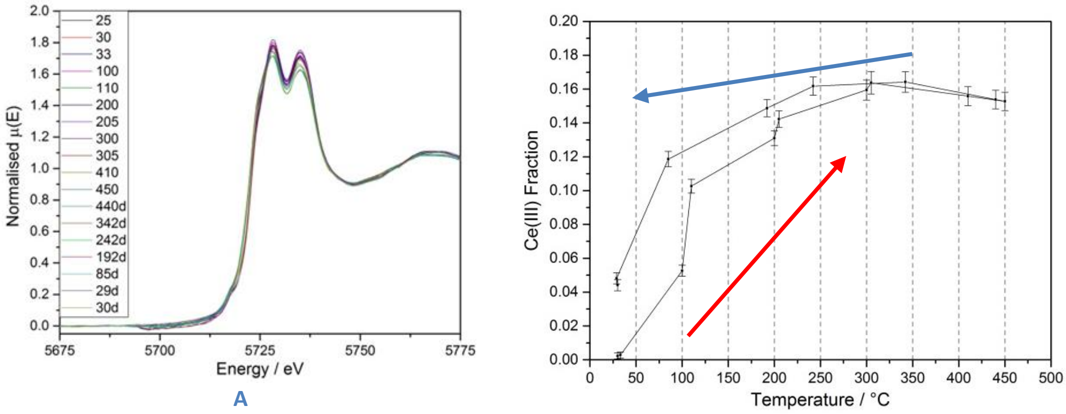

A

B

Figure 5-11: (A) Comparison of the normalised μ(E) for a mixture of PdO and the pure ceria support showing the formation of a shoulder upon heating under a reducing atmosphere. (B) the Ce (III) weight refined from LCF showing the reduction of Ce (IV) to Ce (III) on heating. The red and blue arrows indicate the heating and cooling (of the sample) respectively.

For comparison, Figure 5-11, the same experiment was performed using a physical mixture of PdO and the high surface area ceria support prepared by grinding these materials together. This shows similar levels of Ce (III) are formed under a reducing atmosphere though this proceeds at a lower temperature than for the pure ceria support. On cooling the amount of Ce (III) decreases, but not to the original value c.f. pure ceria support. This indicates that Pd influences the reduction and removal of oxygen from ceria but more importantly the manner in which the Pd is loaded onto the ceria support influences the reduction and that there must be a chemical interaction between the Pd and Ceria support. This would suggest that the samples undergo a spill over mechanism where the H_2 dissociates upon the Pd and migrates towards the ceria, as the monoatomic hydrogen will migrate from H-rich to H-low areas. Upon interacting with the ceria support, the monoatomic hydrogen will react with the oxygen present in ceria, forming water and leaving the system. In addition as more Pd is loaded onto the ceria support, the reduction temperature for the surface ceria layer is lowered. This would be due to the larger amount of Pd present on the surface and the resulting greater number of Pd-O-Ce interactions between the dispersed Pd nanoparticles and the ceria support.

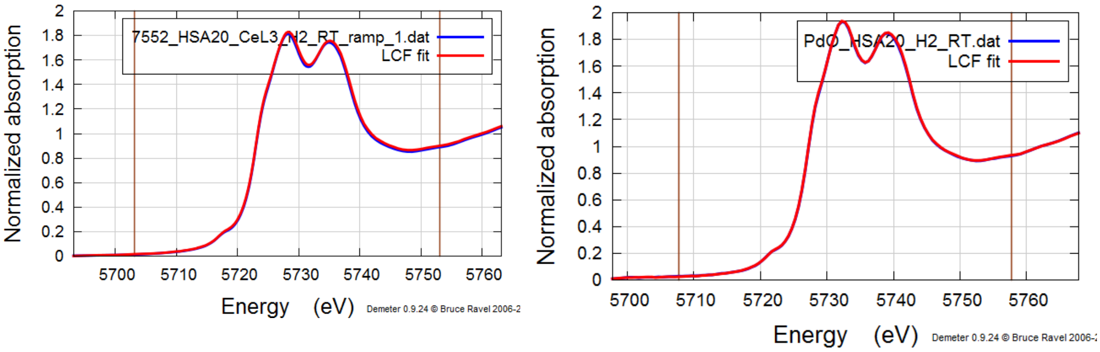

Figure 5-12: (Left) Example LCF for the Ceria support obtained on the Ce L3-edge (Right) Example LCF for the physical mixture of PdO and ceria support obtained on the Ce K-edge

5.5.2 Extended X-ray Absorption Fine Structure

Figure 5-13 shows the comparison of the 2.5 and 5 wt % Pd loaded onto a high surface area ceria support. EXAFS analysis was not performed on 1 wt% Pd loaded on ceria due to data quality. Both graphs show that initially any Pd present in both samples is PdO which may be reasoned by the fact that the samples are calcined for 2 hours at 500°C.

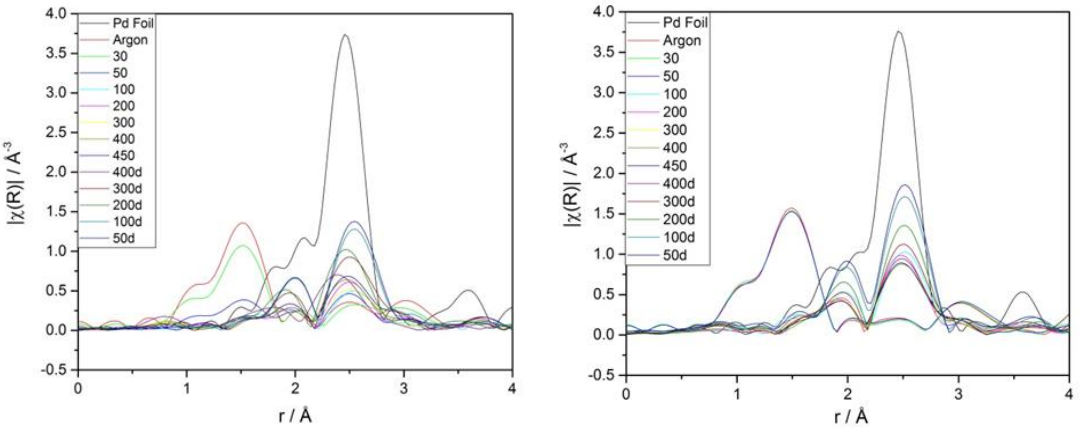

A B

Figure 5-13: Comparison of the |(R)| for 2.5 wt% Pd on Ceria (Left) and 5 wt% Pd on Ceria (right). These graphs both show the reduction of PdO to Pd metal after heating above 50°C under H_2:N_2

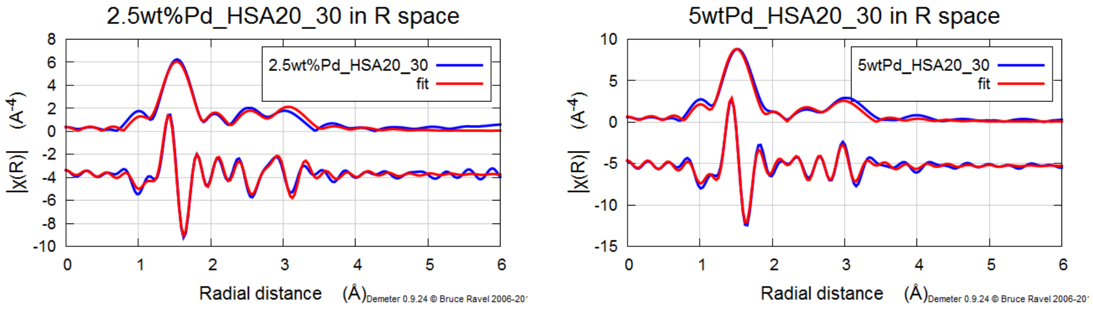

Figure 5-14: Comparison of the EXAFS fitting in R-space and k-space (Left) 2.5 wt% Pd on ceria (Right) 5 wt% Pd on ceria

This correlates with the observations seen in the LCF of the XANES data (Figure 5-6 and Figure 5-8), that upon heating there is the formation of Pd metal. In contrast though LCF shows the Pd metal is formed at a lower temperature and in greater amounts compared to EXAFS for both samples respectively. This would seem the data contradicts but could be explained by the fact that XAS is more sensitive to lower levels of the probed element in contrast to the EXAFS fitting.

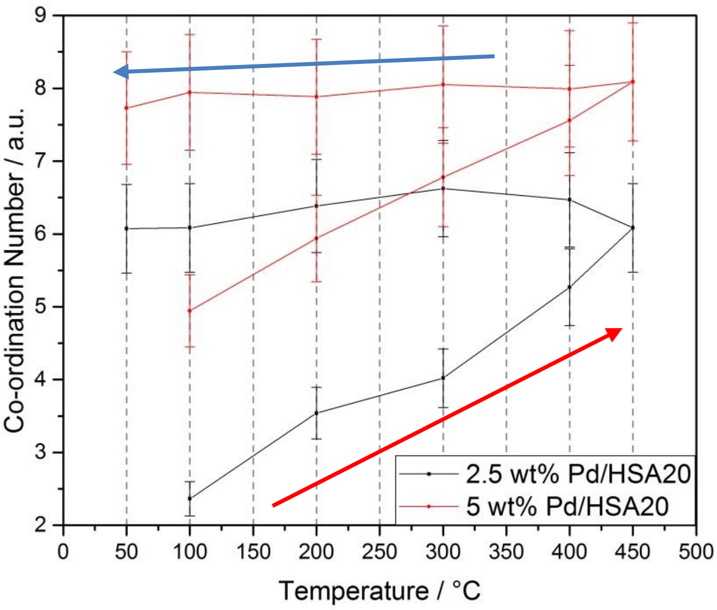

Figure 5-15: Comparison of the refined co-ordination numbers from Pd K-edge EXAFS, showing an increase in co-ordination number upon heating under a reducing atmosphere. The red and blue arrows indicate the heating and cooling (of the sample) respectively.

Figure 5-15 shows the comparison of the refined co-ordination numbers (CN) for both the 2.5 wt% and 5 wt% Pd on ceria. Once the PdO has been reduced to Pd, the CN is approximately 2.25 and 5 for 2.5 wt% and 5 wt% Pd on ceria respectively. This would indicate that once PdO has reduced to Pd metal there are Pd nanoparticles present[35] (cf. the CN for Pd foil is 12). As the samples heated, under 5% H_2:N_2, there is an increase in the CN, which would indicate that there is a growth in the particle size. As the samples are cooled, in a reducing atmosphere, there is no further increase in the CN. This would suggest that there is no further particle growth. No values are reported below 100°C as there is a phase change from PdO to Pd metal.

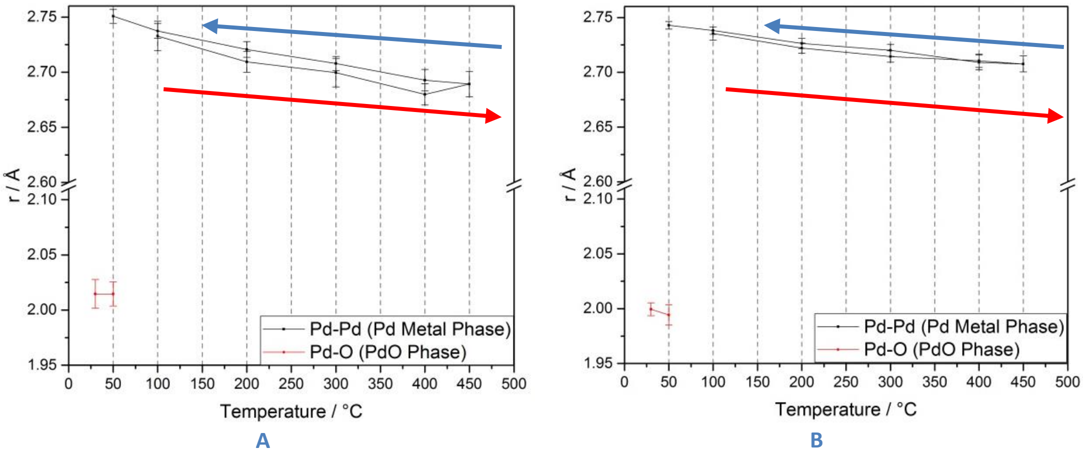

Figure 5-16: Comparison of the Pd-Pd interatomic distances for both 2.5 wt% Pd on ceria (A) and 5 wt% Pd on ceria (B). These both show that, on heating under a reducing atmosphere, the Pd-Pd distances contract, whilst on cooling these distances expand. The red and blue arrows indicate the heating and cooling (of the sample) respectively.

Figure 5-16 shows the comparison of the refined Pd-Pd interatomic distances for 2.5 wt% Pd and 5 wt% Pd on ceria refined from EXAFS. The results show that, after the initial PdO phase has been reduced to Pd metal, there is a decrease in the Pd-Pd interatomic distance with heating, under a reducing atmosphere. This would seem counterintuitive as we would assume there would be thermal expansion (as seen for the ceria support in this paper). This has been observed for numerous supported nanoparticle systems.[36,37] As the samples are cooled there is an increase in the Pd-Pd interatomic distance, this would suggest some further particle size growth.

5.5.4 Real Space data

The changes in position, peak width and intensity relate to the disorder and changes to the structure of the material. Over the short and medium ranges, the PDF for all the samples shows there are no major structural changes and the ceria fluorite structure is observed throughout the whole experiment.

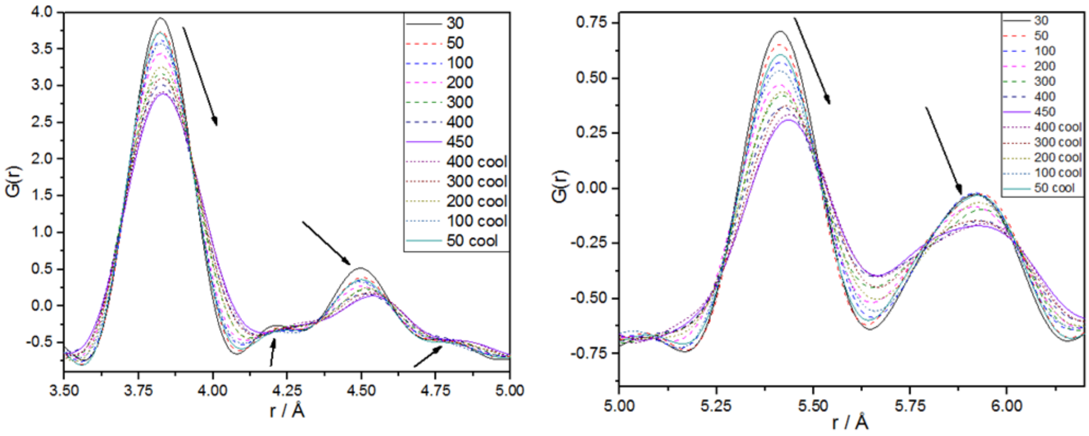

Figure 5-17: The G(r) for the high surface area ceria support, highlighting different sections and the effect of temperature upon the short range structure

The G(r) for ceria support (Figure 5-17), 1 wt% Pd (Figure 5-18), 2.5 wt% Pd (Figure 5-19) and 5 wt% Pd (Figure 5-20) samples are shown respectively. The 1st Ce-Ce and 2nd Ce-O at approx. 3.8 Å and 4.5 Å respectively. All the samples show no apparent change in the in the distance for the 1st Ce-Ce correlation.

All samples exhibit, for the 2nd Ce-O shell, an increase in distance whilst decrease in intensity which would imply thermal expansion of the lattice. Shoulders for the 1st Ce-Ce and 2nd Ce-O could be cautiously assigned to dynamic effects within the ceria material.

These G(r) positions can further be evaluated by looking at the 2nd Ce-Ce and 3rd Ce-O found at approximately 5.4 Å and 5.9 Å respectively. For all 3 samples there is an increase in the peak position with a broadening of the peak for the 2nd Ce-Ce pair. This could be seen as both a combination of thermal expansion and reduction of Ce (IV) to Ce (III) leading to Ce (IV)-Ce (III) atom pairs. Similarly for the 3rd Ce-O atom pair there is a broadening of the peak with an increase in peak position which can be explained which can be assigned to both a combination of thermal expansion and reduction of Ce (IV) to Ce (III) leading to the larger Ce (III)-O atom pair.

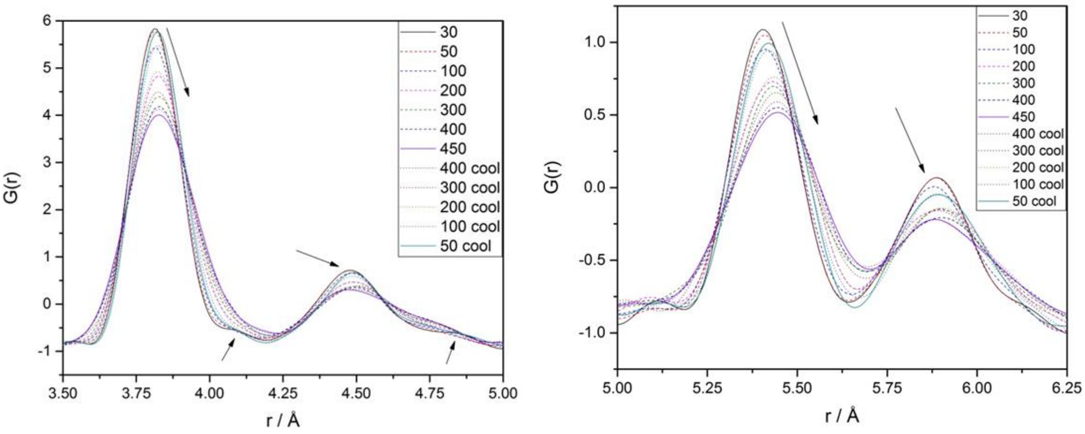

Figure 5-18: The G(r) for 1wt% Pd loaded onto ceria, highlighting different sections and the effect of temperature upon the short range structure

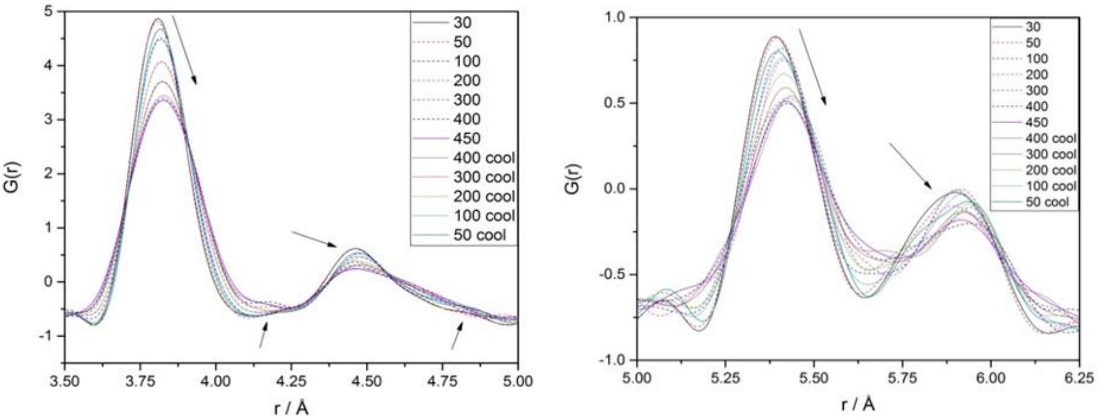

Figure 5-19: The G(r) for 2.5 wt% Pd loaded onto ceria, highlighting different sections and the effect of temperature upon the short range structure

Figure 5-22 shows the comparison of the lattice parameters derived from both the Rietveld and PDF based techniques. Though, both Rietveld and PDF, show subtle differences in the refined values, it suggests a similar correlation between the temperature and the lattice parameter.

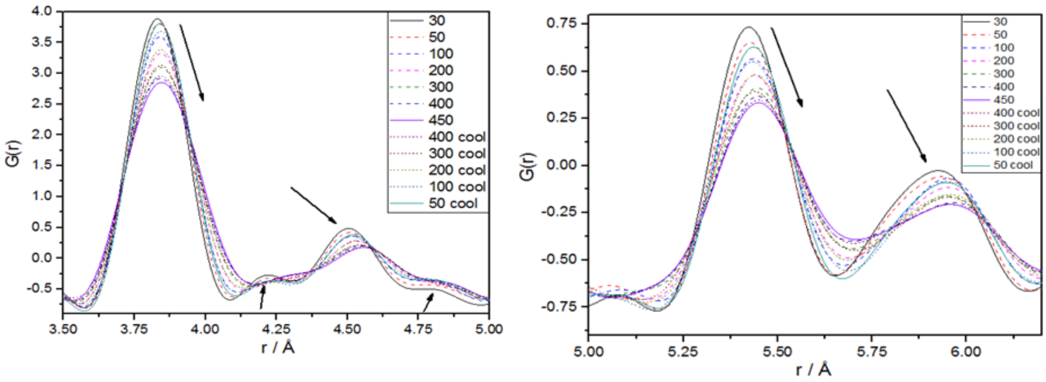

Figure 5-20: The G(r) for 5wt% Pd loaded onto ceria, highlighting different sections and the effect of temperature upon the short range structure

(A) High surface area ceria support shows that on heating there is a thermal expansion and that upon cooling back to 50°C there are similar values to those observed at the outset of the experiment. For 1 wt% Pd on ceria

(B) There is a slow increase in the lattice parameter on heating and this increases markedly above 350°C. This would indicate the start of the observable reduction of ceria and this continues upon cooling under a reducing atmosphere.

(C) Both 2.5 wt% Pd on ceria and 5 wt% Pd on ceria have similar shapes to their respective correlations between temperature and lattice parameter. This indicates that the reduction of the ceria support occurs faster as more Pd is loaded onto the support. Both samples also show that on cooling, the lattice parameters to not return to their original values. Any offset between the starting and ending values for the lattice parameter would signify a combination of increased disorder and increased number of Ce (III) ions present showing the sample has been reduced to an extent.

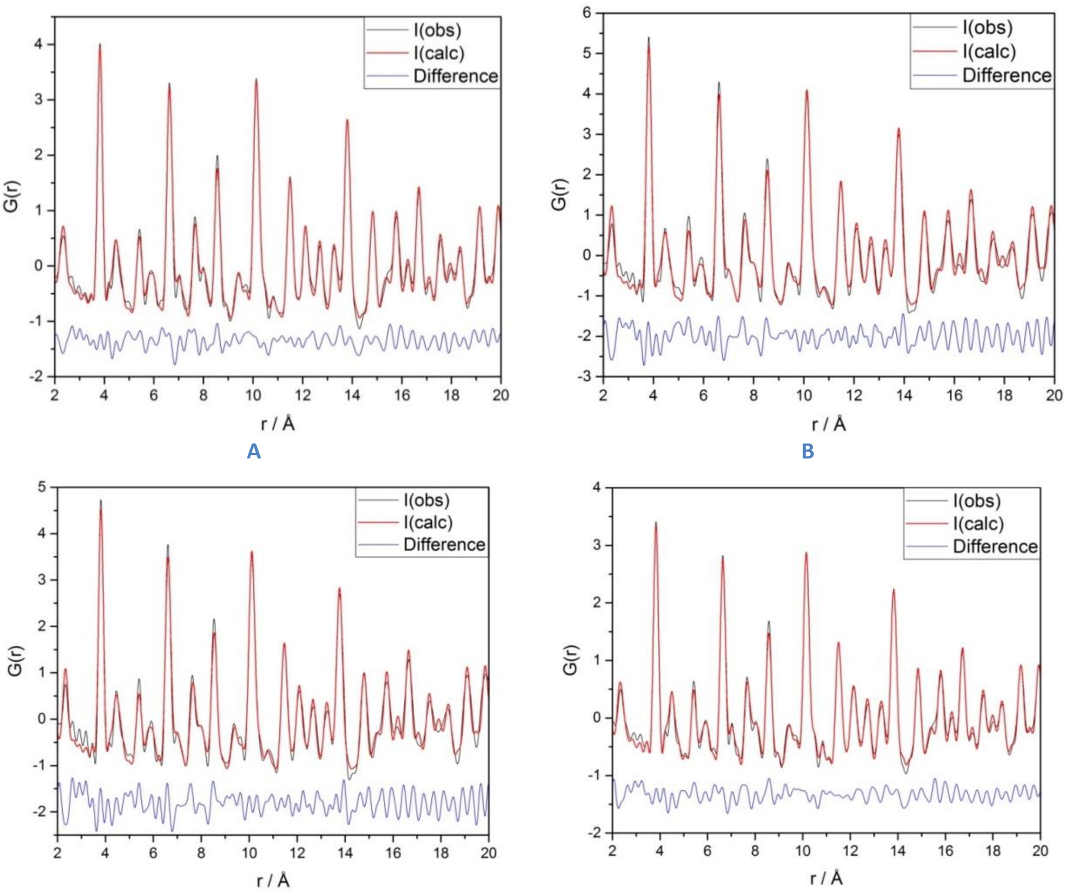

A

B

C

D

Figure 5-21: Examples of the PDF and their respective fits for the (A) ceria support and the respective (B) 1, (C) 2.5 and (D) 5wt% Pd loaded samples. This shows that all the samples have the ceria fluorite structure.

5.6 Conclusion

This investigation shows how a sole technique does not illustrate fully how materials behave under industrially relevant conditions. XAS analysis shows that for the pure ceria support the sample is reduced upon heating but returns to its original state after cooling which is a previously reported property of ceria based materials.[38]

In comparison the loading of Pd onto the high surface area ceria support, decreases the reduction temperature of the ceria support but upon cooling there is no reoxidation. Increasing the amount of Pd loaded onto the ceria support, decreases the temperature at which the metal reduces and at which the ceria will start to reduce. The XAS also indicates that for the Pd loaded onto ceria samples, the metal must reduce from PdO to Pd before the onset of the reduction for the ceria support.

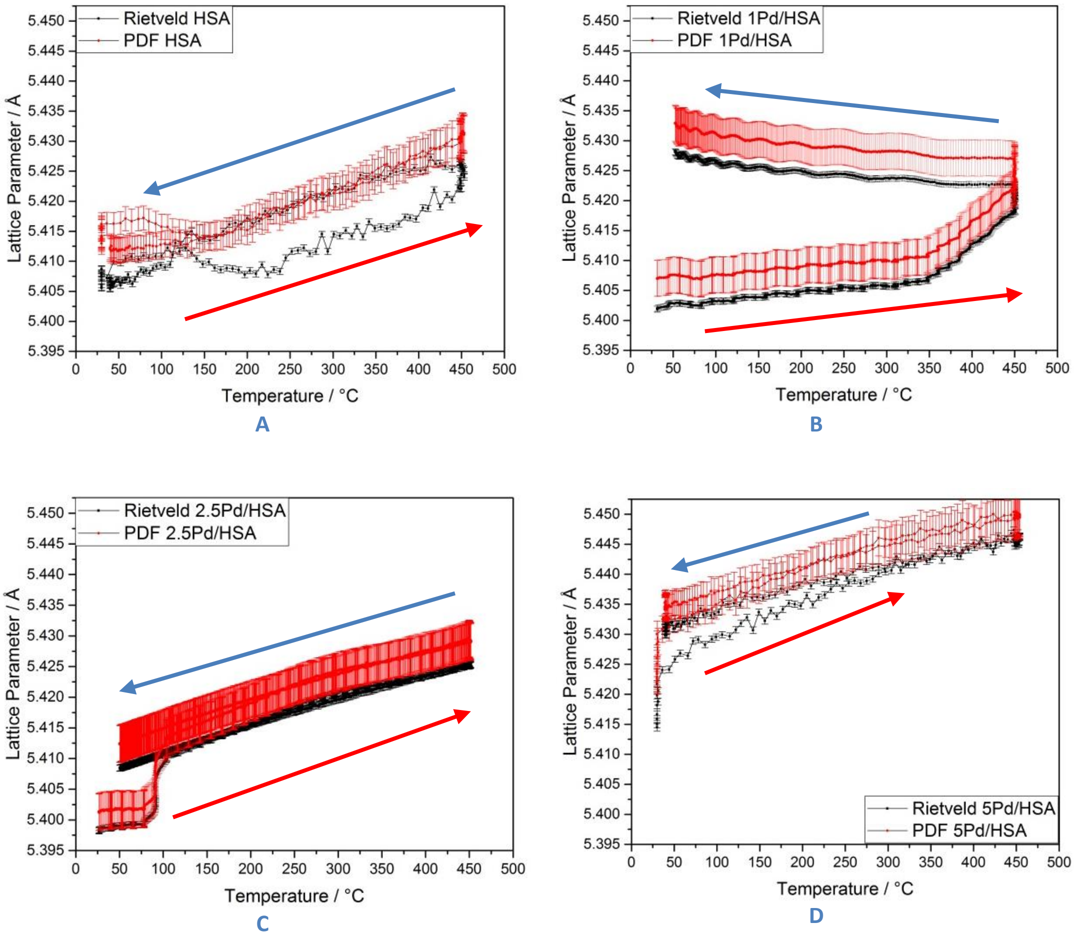

Figure 5-22: Comparison of the Lattice Parameters derived from Rietveld and PDF (between 2-20 Å) for the High Surface Area support (A), 1wt% Pd on ceria (B), 2.5wt% Pd on ceria (C) and 5wt% Pd on ceria (D). The red and blue arrows indicate the heating and cooling (of the sample) respectively.

In contrast, a physical mixture of PdO and the high surface area support shows a decrease in the reduction temperature for the ceria support. It does not reoxidise to the same extent as the pure ceria support though does not behave in the same manner as the Pd loaded ceria samples as analysed with XANES. The respective EXAFS analysis for the 2.5 and 5 wt% Pd samples show the reduction of PdO to Pd. The refinement of the co-ordination numbers show that neither samples have an average co-ordination of 12 (c.f. the Pd foil). This would indicate that the Pd present is found in a nanoparticulate form. Furthermore, comparison of the respective EXAFS spectra with Hiley *et al*,[39] confirm that no Pd is present in square planar geometry within the high surface area ceria support.

The HRXRD shows that for all the samples the ceria fluorite is observed throughout the reduction experiments and no other ceria based phases are present. The refined parameters show the reduction and loss of oxygen from the lattice whilst heating. For the pure ceria support there is reoxidation back to stoichiometric values whereas for the Pd loaded materials, there is a loss of oxygen. The addition of Pd into the lattice does not improve the fits indicating a highly dispersed PdO phase at the outset of the experiments and nanoparticulate Pd after the reduction from PdO to Pd metal. This behaviour matches that of previously reported literature on the reduction of PdO to Pd under hydrogen.[40] This is supported by XPDF experiments of the same samples under the same operating conditions. PDF based techniques indicate an increased disorder of Ce and O ions upon heating and the formation of Ce (III)-O bonds. The comparison of the refined lattice parameters from both Rietveld and PDF show both similar values and similar correlations between an increase in temperature and the lattice parameter. For the Pd loaded samples, the lattice parameter does not return to its original values in comparison to the pure ceria support, indicating increased disorder and the presence of Ce (III) ions. Though for 1wt% Pd on ceria shows a further expansion on cooling for both Rietveld and PDF based analytical methods. This is in contrast to XAS which indicates that less Ce (III) is present on cooling, leading to a smaller lattice parameter. Furthermore, upon cooling, less thermal energy is imparted to the PGM/ceria system leading, in theory, to a more ordered system. This would suggest that the experiment could have had issues as this result is counterintuitive to what is both chemically and physically possible. This could be due to incorrect temperature measurements, variation in sample position, variations in gas composition etc.

The TPR profile shows that with increasing amounts of Pd there is a decrease in the temperature at which reduction takes place. This has been attributed to the reduction of PdO to Pd metal. This behaviour matches previously reported results on PGM loaded ceria supports.[41] The decrease in reduction temperature can be assigned to the Pd present on the 1 wt% Pd on ceria sample being highly dispersed in contrast to the 5 wt% Pd on ceria sample.

All the techniques combined show for the ceria support that there is reoxidation in a reducing atmosphere which seems counter intuitive. In reality the reduction observed could be migration of oxygen mirroring the removal of oxygen and reduction of the support. Whereas for the Pd loaded samples, the inclusion of Pd onto the systems shows that it is important in the removal of oxygen from the lattice as no reoxidation is observed upon cooling.

5.7 Bibliography

1 A. Trovarelli, *Catalysis by Ceria and Related Materials*, Imperial College Press, London, 2002.

2 R. M. Heck and R. J. Farrauto, *Appl. Catal., A*, 2001, **221**, 443–457.

3 R. Craciun, B. Shereck and R. J. Gorte, *Catal. Lett.*, 1998, **51**, 149–153.

4 P. Pantu, K. Kim and G. R. Gavalas, *Appl. Catal., A*, 2000, **193**, 203–214.

5 Y. I. Matatov-meytal and M. Sheintuch, *Ind. Eng. Chem. Res.*, 1998, **37**, 309–326.

6 H. Renner, G. Schlamp, I. Kleinwächter, E. Drost, H. M. Lüschow, P. Tews, P. Panster, M. Diehl, J. Lang, T. Kreuzer, A. Knödler, K. A. Starz, K. Dermann, J. Rothaut, R. Drieselmann, C. Peter and R. Schiele, in *Ullmann's Encyclopedia of Industrial Chemistry*, Wiley-VCH Verlag GmbH & Co. KGaA, 2000.

7 D. Astruc, in *Nanoparticles and Catalysis*, Wiley-VCH Verlag GmbH & Co. KGaA, 2008, pp. 1–48.

8 M. E. Dry, *Catal. Today*, 2002, **71**, 227–241.

9 J. A. Rabo, *Catal. Today*, 1994, **22**, 201–234.

10 L. F. Liotta, A. Longo, A. Macaluso, A. Martorana, G. Pantaleo, A. M. Venezia and G. Deganello, *Appl. Catal. B Environ.*, 2004, **48**, 133–149.

11 L. F. Liotta, A. Longo, G. Pantaleo, G. Di Carlo, A. Martorana, S. Cimino, G. Russo and G. Deganello, *Appl. Catal. B Environ.*, 2009, **90**, 470–477.

12 H.-W. Jen, G. . Graham, W. Chun, R. . McCabe, J.-P. Cuif, S. . Deutsch and O. Touret, *Catal. Today*, 1999, **50**, 309–328.

13 R. Craciun, W. Daniell and H. Knözinger, *Appl. Catal. A Gen.*, 2002, **230**, 153–168.

14 N. Tsubaki and K. Fujimoto, *Top. Catal.*, **22**, 325–335.

15 S. J. Tauster, S. C. Fung and R. L. Garten, *J. Am. Chem. Soc.*, 1978, **100**, 170–175.

16 S. Golunski and A. Walker, *Chem. Commun.*, 2000, 1593–1594.

17 G. Sankar, C. N. R. Rao and T. Rayment, *J. Mater. Chem.*, 1991, **1**, 299–300.

18 C. M. Y. Yeung and S. C. Tsang, *J. Phys. Chem. C*, 2009, **113**, 6074–6087.

19 H. Hirata, K. Kishita, Y. Nagai, K. Dohmae, H. Shinjoh and S. Matsumoto, *Catal. Today*, 2011, **164**, 467–473.

20 S. Bernal, J. J. Calvino, M. A. Cauqui, J. M. Gatica, C. Larese, J. A. Pérez Omil and J. M. Pintado, *Catal. Today*, 1999, **50**, 175–206.

21 S. Suhonen, M. Valden, M. Hietikko, R. Laitinen, A. Savimäki and M. Härkönen, *Appl. Catal. A Gen.*, 2001, **218**, 151–160.

22 G. Jacobs, U. Graham, E. Chenu, P. Patterson, A. Dozier and B. Davis, *J. Catal.*, 2005, **229**, 499–512.

23 S. Nikitenko, A. M. Beale, A. M. J. Van Der Eerden, S. D. M. Jacques, O. Leynaud, M. G. O'Brien, D. Detollenaere, R. Kaptein, B. M. Weckhuysen and W. Bras, *J. Synchrotron Radiat.*, 2008, **15**, 632–640.

24 O. Mathon, A. Beteva, J. Borrel, D. Bugnazet, S. Gatla, R. Hino, I. Kantor, T. Mairs, M. Munoz, S. Pasternak, F. Perrin and S. Pascarelli, *J. Synchrotron Radiat.*, 2015, **22**, 1548–1554.

25 B. Ravel and M. Newville, *J. Synchrotron Radiat.*, 2005, **12**, 537–541.

26 H. M. Rietveld, *J. Appl. Crystallogr.*, 1969, **2**, 65–71.

27 B. H. Toby, *J. Appl. Crystallogr.*, 2001, **34**, 210–213.

28 A. C. Larson and R. B. Von Dreel, *Los Alamos Nation Lab. Rep. LAUR*, 1994, 86–748.

29 P. Tian, W. Zhou, J. Liu, Y. Shang, C. L. Farrow, P. Juh??s and S. J. L. Billinge, *J. Appl. Crystallogr.*, 2013, **46**, 255–258.

30 A. P. Hammersley, S. O. Svensson, M. Hanfland, A. N. Fitch and D. Hausermann, *High Press. Res.*, 1996, **14**, 235–248.

31 P. Juhás, T. Davis, C. L. Farrow and S. J. L. Billinge, *J. Appl. Crystallogr.*, 2013, **46**, 560–566.

32 C. L. Farrow, P. Juhas, J. W. Liu, D. Bryndin, E. S. Božin, J. Bloch, T. Proffen and S. J. L. Billinge, *J. Phys. Condens. Matter*, 2007, **19**, 335219.

33 S. Komhom, O. Mekasuwandumrong, J. Panpranot and P. Praserthdam, *Ind. Eng. Chem. Res.*, 2009, **48**, 6273–6279.

34 E. Rocchini, A. Trovarelli, J. Llorca, G. W. Graham, W. H. Weber, M. Maciejewski and A. Baiker, *J. Catal.*, 2000, **194**, 461–478.

35 S. I. Sanchez, L. D. Menard, A. Bram, J. H. Kang, M. W. Small, R. G. Nuzzo and A. I. Frenkel, *J. Am. Chem. Soc.*, 2009, **131**, 7040–7054.

36 D. E. Ramaker, J. de Graaf, J. a. R. van Veen and D. C. Koningsberger, *J.*

Catal., 2001, **203**, 7–17.

37 Y. Zhang, M. L. Toebes, A. van der Eerden, W. E. O’Grady, K. P. de Jong, D. C. Koningsberger and W. E. O’Grady, *J. Phys. Chem. B*, 2004, **108**, 18509–18519.

38 D. R. Modeshia, C. S. Wright, J. L. Payne, G. Sankar, S. G. Fiddy and R. I. Walton, *J. Phys. Chem. C*, 2007, **111**, 14035–14039.

39 C. I. Hiley, J. M. Fisher, D. Thompsett, R. J. Kashtiban, J. Sloan and R. I. Walton, *J. Mater. Chem. A*, 2015, **3**, 13072–13079.

40 A. Baylet, P. Marécot, D. Duprez, P. Castellazzi, G. Groppi and P. Forzatti, *Phys. Chem. Chem. Phys.*, 2011, **13**, 4607–4613.

41 C. de Leitenburg, A. Trovarelli and J. Kašpar, *J. Catal.*, 1997, **166**, 98–107.

Chapter 6: *Insitu* X-ray total scattering study of the phase transformation of ceria-zirconia kappa and fluorite materials

6.1 Abstract

X-ray diffraction and PDF was used in the study of the reduction and oxidation of Ceria-Zirconia kappa and fluorite materials, and how the introduction of Pd into these systems influences the reduction behaviour. The Fluorite based materials show no phase change under heating in either oxidising or reducing atmospheres there are no phase changes observed. In contrast, the heating of the Kappa based materials under reducing conditions show the loss of oxygen from the lattice and the conversion to the pyrochlore structure. Upon cooling and treating with air, these are converted back to the Kappa structure.

6.2 Introduction

The understanding of zirconia and zirconia based materials is of importance due to numerous uses in areas such as catalysis, highly mobile oxygen storage materials,[1–3] chlorine production[4] etc. To understand fully the phase transformation of these materials is importance as they can be developed to avert unwanted chemical or mechanical transformations when used in ‘real world’ or ‘industrially relevant’ applications.[5] The inclusion of ceria into zirconia based materials is important due to improvement in oxygen storage capacity (OSC)[6] and thermal stability,[7] in industrially relevant conditions. Figure 6-1 shows the binary phase diagram and how the variation in the mol% of ZrO_2 and CeO_2 influences the structure of the resulting CeO_2-ZrO_2 material.[8] Below 1000°C, above 80 mol% CeO2 the cubic phase is observed, below 10% CeO_2 the monoclinic form is seen. Three tetragonal phases are observed, t, t’ and t” where t is the stable form and t’ and t” are metastable forms. The t” is an intermediate between t’ and c showing no tetragonal nature of the cation sub lattice but displacement of oxygen from the ideal fluorite sites. Therefore this is often referred to as a cubic structure with $Fm\overline{3}m$ space group.

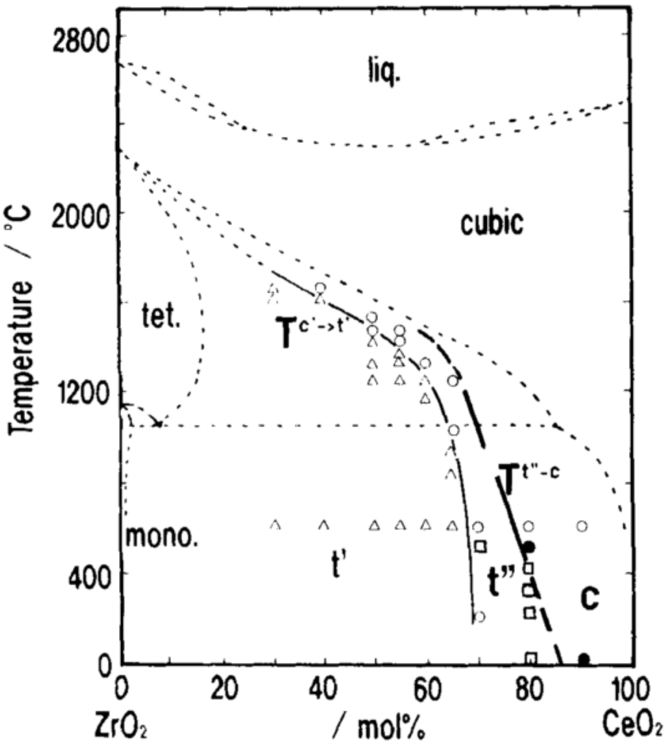

Figure 6-1: Binary phase diagram for CeO_2-ZrO_2 systems adapted from Yashima *et al*.[9] Key mono – monoclinic, tet. – tetragonal (stable), t' and t" are both metastable tetragonal phases, and c is cubic

This is attributed to the cation sub lattice generating the XRD pattern. It has been shown that converting the t-phase $CeZrO_4$ into a kappa phase $CeZrO_4$ where a statistical distribution of cations has been converted into an ordered cation sub lattice. The κ-$Ce_2Zr_2O_8$ can further be converted into the pyrochlore on which is releases oxygen and forms pyr-$Ce_2Zr_2O_7$. This improved OSC has been shown to be of use in the combustion of halogenated materials.[10]

The steps in which κ-$Ce_2Zr_2O_8$ can be formed by from the reduction of t- $Ce_2Zr_2O_8$ but dependent on the temperature this can further be reduced to pyr-$Ce_2Zr_2O_7$. It is important to find synthetic procedures in which this can be avoided and a stable κ-$Ce_2Zr_2O_8$ can be formed.

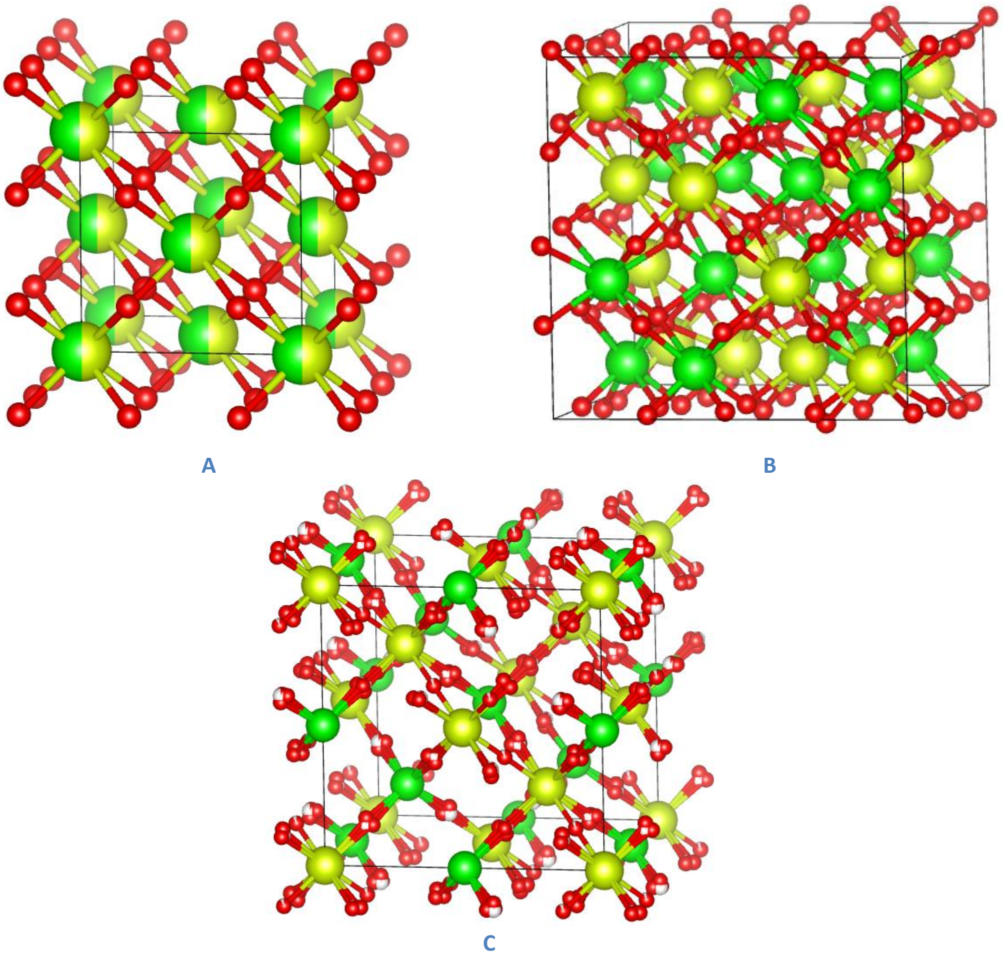

Figure 6-2: (A) Fluorite $Ce_{0.5}Zr_{0.5}O_2$ (B) κ-$Ce_{0.5}Zr_{0.5}O_2$ (C) pyr-$Ce_{0.5}Zr_{0.5}O_2$. Cerium (Yellow) Zirconium (Green) Oxygen (Red). The partially white spheres represent partially occupied oxygen sites.

6.3 Experimental Section

The treated $Ce_{0.5}Zr_{0.5}O_2$ was prepared by treating a commercially available disordered $Ce_{0.5}Zr_{0.5}O_2$ at 950°C under 10% H_2:N_2 for 6 hours. Palladium loaded samples were prepared by the required amount of Pd nitrate solution (commercially available from JM) diluted to a volume appropriate to fill the pore volume of the $Ce_{0.5}Zr_{0.5}O_2$ support. Materials were dried at 105°C and fired at 500°C.

XRD patterns of all the samples were collected on the 11-ID-B beamline at APS.

The samples were prepared to produce monodisperse grain sizes and loaded into quartz capillary of 1mm diameter, mounted on a gas rig cell over a hot air blower. The diffraction patterns were collected using $\lambda = 0.1430$ Å; data was collected between $2\theta = 0.0$ to 17°.

Two experiments were performed on the κ-$Ce_{0.5}Zr_{0.5}O_2$ and $Ce_{0.5}Zr_{0.5}O_2$ fluorite materials and respective Palladium loaded samples, 1Pd/ κ-$Ce_{0.5}Zr_{0.5}O_2$ and $Ce_{0.5}Zr_{0.5}O_2$ fluorite. The first set of experiments were performed by heating the samples in air. The samples were first purged under helium; the samples were then heated at 10 °C min^{-1} from room temperature to 500°C and held for 30 minutes. The samples were then heated further to 900°C, held for 30 minutes and then the samples were allowed to cool.

The second set of experiments was a cycling of reducing and oxidising conditions. The samples were firstly purged under helium; the samples were then heated in 3.5% H_2:N_2 at 10°Cmin^{-1} from room temperature to 900°C and held for 30 minutes. The samples were allowed to cool to room temperature then purged with Helium. The samples were then heated under air at 10°Cmin^{-1} from room temperature to 500°C and held for 30 minutes. The samples were then heated further to 900°C, held for 30 minutes and then the samples were allowed to cool.

6.4 Data Processing and Analysis

The raw 2D image data underwent processing with Fit2D.[11] Rietveld refinement was performed using Topas[12] with reflection profiles modelled using a modified Pseudo Voigt with reference data collected from Ceria NIST (SRM674b). Crystallite sizes have been calculated using the volume weighted column height LVol-IB method.[13]

6.5 Results and Discussion

6.5.1 Insitu characterisation of samples cycling under an oxidising atmosphere

The initial set of experiments were performed by heating the κ-$Ce_{0.5}Zr_{0.5}O_2$, 1Pd/κ-$Ce_{0.5}Zr_{0.5}O_2$ and 1Pd/$Ce_{0.5}Zr_{0.5}O_2$ fluorite materials under air, holding at 500°C and 900°C respectively.

Figure 6-3 shows the comparison of the diffraction patterns taking at 30°C, 500°C, 900°C and after cooling at 30°C for (A) κ-$Ce_{0.5}Zr_{0.5}O_2$ (B) 1Pd/κ-$Ce_{0.5}Zr_{0.5}O_2$ (C) 1Pd/$Ce_{0.5}Zr_{0.5}O_2$ fluorite samples respectively.

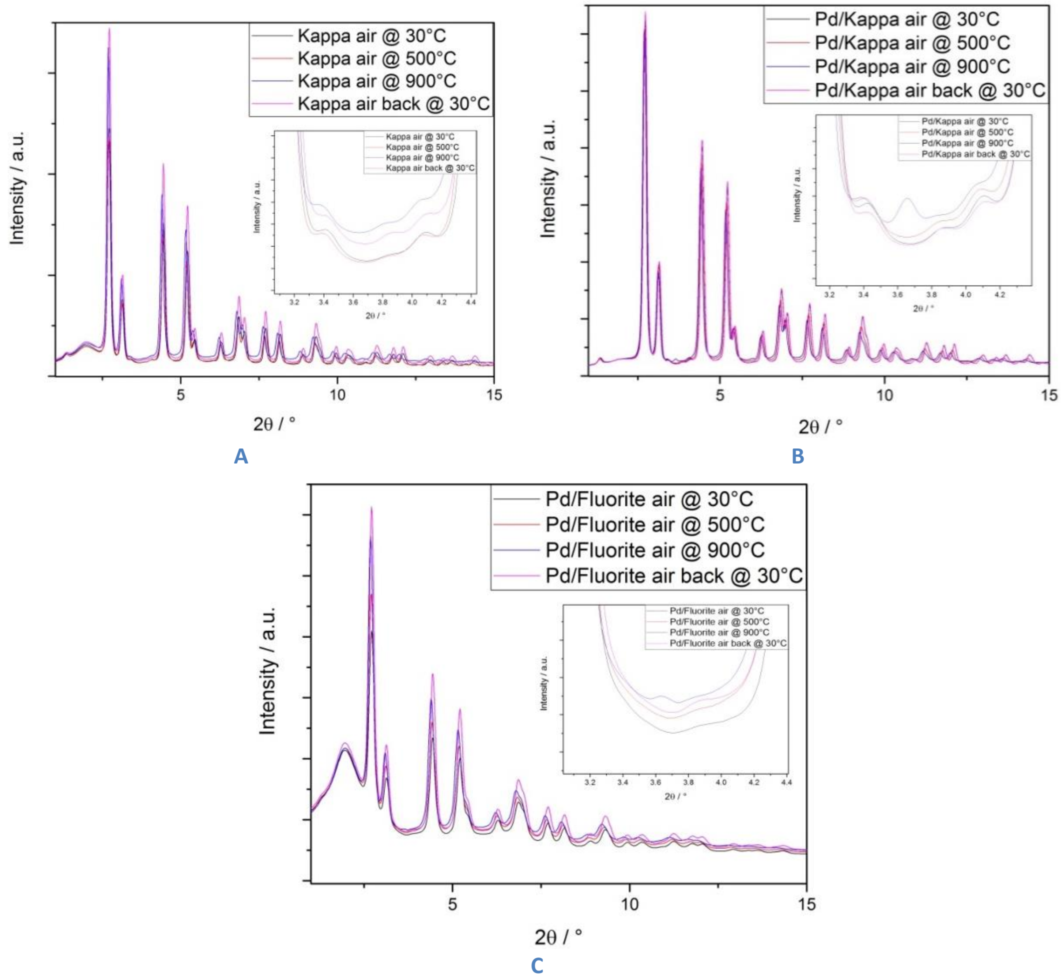

A

B

C

Figure 6-3: Comparison of the diffraction patterns taking at 30°C, 500°C, 900°C and after cooling at 30°C for (A) κ-$Ce_{0.5}Zr_{0.5}O_2$ (B) 1Pd/κ-$Ce_{0.5}Zr_{0.5}O_2$ (C) 1Pd/$Ce_{0.5}Zr_{0.5}O_2$ fluorite samples respectively. The diffraction patterns show that upon heating there are subtle variations in peak position, intensity and width.

For the plain κ-$Ce_{0.5}Zr_{0.5}O_2$, the super lattice reflections are evident throughout the experiment, suggesting that under heating in air that this sample does not convert to the fluorite structure. For 1Pd/κ-$Ce_{0.5}Zr_{0.5}O_2$, the superlattice reflections are evident throughout the experiment, suggesting that under heating in air that this sample does not convert to the fluorite structure. In addition a further peak is formed after heating suggesting the formation of a Pd phase. For 1Pd/$Ce_{0.5}Zr_{0.5}O_2$ fluorite, the fluorite structure is found throughout the experiment with no evident peak sharpening occurring. This would indicate no discernible particle size growth after heating. In addition a further subtle peak, between 2θ = 3.6° and 3.8°, is formed after heating suggesting the formation of a Pd metal phase. Note the broad peak at approximately 2θ = ~2° is assigned to the quartz capillary.

Table 6-1: Results obtained using Rietveld analysis for κ-$Ce_{0.5}Zr_{0.5}O_2$ for a sample that has been heated to and held at 900°C under a reducing atmosphere. Lattice Parameter a = 10.8193(7) Å, Space Group $P2_13$, R_{wp} = 2.63%, B_{eq} is the isotropic temperature factor ($B_{eq} = 8\pi^2U_{iso}$)

Atom	Site	X	y	z	Beq	Site Occupancy Factor (S.O.F.)
Ce1	**4a**	**0.369**	**0.369**	**0.369**	**1.91(3)**	**1**
Ce2	**12b**	**0.13**	**0.125**	**0.377**	**1.86(2)**	**1**
Zr1	**4a**	**0.87**	**0.87**	**0.87**	**0.6(7)**	**1**
Zr2	**12b**	**0.12**	**0.132**	**0.873**	**0.461(4)**	**1**
O1	**4a**	**0.5**	**0.5**	**0.5**	**8.94(3)**	**0.588(3)**
O2	**4a**	**-0.01**	**-0.01**	**-0.01**		
O3	**4a**	**0.75**	**0.75**	**0.75**		
O4	**4a**	**0.26**	**0.26**	**0.26**		
O5	**12b**	**0**	**0.01**	**0.23**	**4.7(3)**	**0.99(4)**
O6	**12b**	**0.25**	**0.25**	**0.52**		
O7	**12b**	**0.29**	**0.29**	**-0.01**		
O8	**12b**	**0.01**	**0.01**	**0.77**		

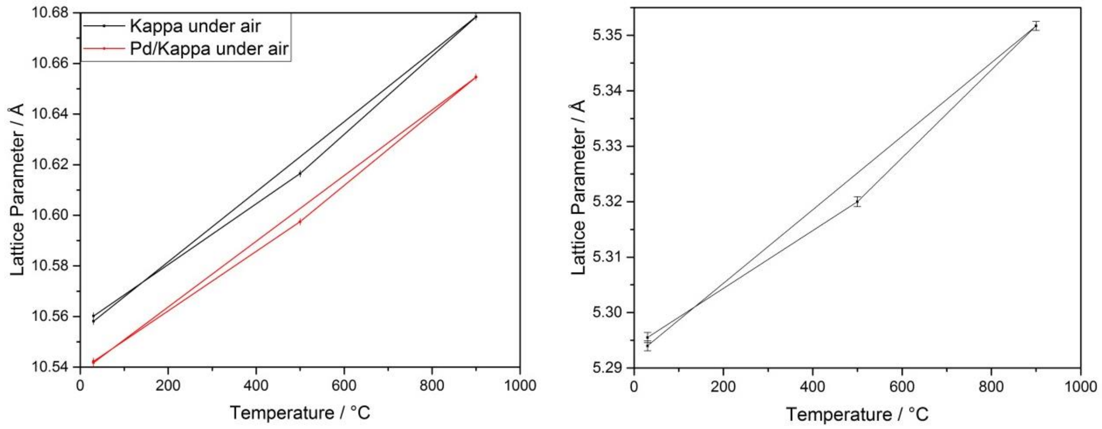

Figure 6-4: Comparison of lattice parameter vs Temperature for κ-$Ce_{0.5}Zr_{0.5}O_2$ and 1Pd/κ- $Ce_{0.5}Zr_{0.5}O_2$ (left) 1Pd/ $Ce_{0.5}Zr_{0.5}O_2$ (right). This shows that upon heating the lattice expands and on cooling the unit cell size returns to original size.

Figure 6-4 shows the comparison of the lattice parameter vs temperature and how this reacts to heating under an oxidising atmosphere. This shows that for all 3 samples that the lattice expands upon heating up to 500 and 900°C respectively. On cooling the unit cell size decreases and relaxes back to its original value. This relates to the subtle variation in peak position. This correlates furthermore that the atomic displacement parameters which mirror this increase in thermal disorder on heating, returning to the original values upon cooling.

Furthermore for all samples, no discernible peak sharpening occurs, indicating that no particle size growth occurs during the experiment.

6.5.2 *Insitu* characterisation of samples cycling under a reducing then oxidising atmospheres

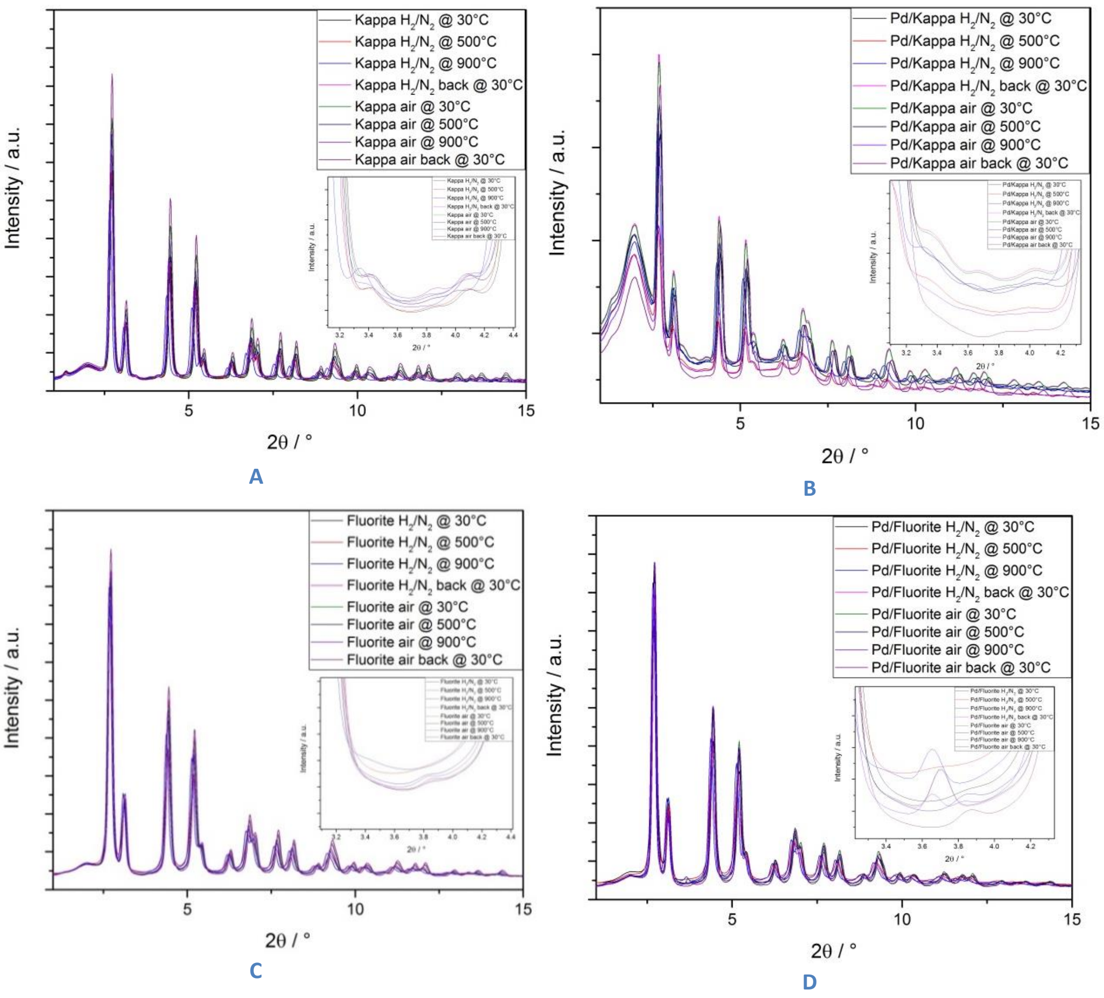

Figure 6-5: Comparison of the diffraction patterns taking at 30°C, 500°C, 900°C and after cooling at 30°C under H_2:N_2 then Air for (A) κ-$Ce_{0.5}Zr_{0.5}O_2$ (B) 1Pd/κ-$Ce_{0.5}Zr_{0.5}O_2$ (C) $Ce_{0.5}Zr_{0.5}O_2$ fluorite (D) 1Pd/ $Ce_{0.5}Zr_{0.5}O_2$ fluorite samples respectively. The diffraction patterns show that upon heating there are subtle variations in peak position, intensity and width.

Figure 6-5 shows the comparison of the diffraction patterns taken at 30°C, 500°C, 900°C and after cooling at 30°C under H2:N2 then Air for (A) κ-$Ce_{0.5}Zr_{0.5}O_2$ (B) 1Pd/ κ-$Ce_{0.5}Zr_{0.5}O_2$ (C) $Ce_{0.5}Zr_{0.5}O_2$ fluorite (D) 1Pd/$Ce_{0.5}Zr_{0.5}O_2$ fluorite samples respectively. For all samples there are observable changes in in peak position and intensity. For all samples, there are no observable kappa to fluorite phase transitions for the kappa based materials.

Though for the Pd loaded materials, a peak is formed between 2θ = 3.6° and 3.8° which is indicative of the formation of Pd metal. No discernible peak sharpening occurs during the cycling, indicating no particle size growth for all samples. Note the broad peak at approximately 2θ = ~2° is assigned to the quartz capillary.

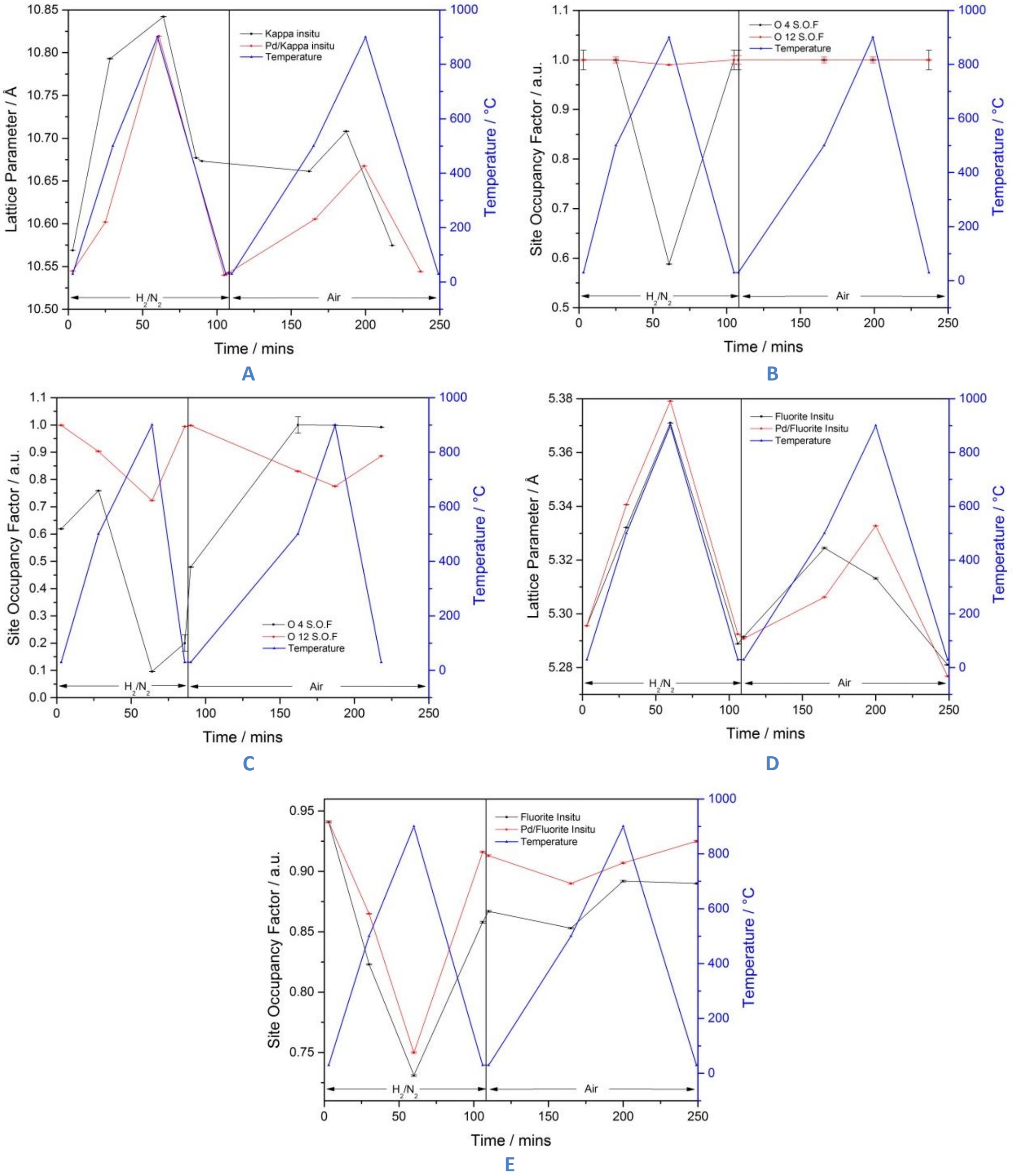

Figure 6-6: (A) Comparison of the refined unit cell size for κ-$Ce_{0.5}Zr_{0.5}O_2$ and 1Pd/κ-$Ce_{0.5}Zr_{0.5}O_2$ (B) Comparison of the refined Site Occupancy Factor (S.O.F.) for κ-$Ce_{0.5}Zr_{0.5}O_2$ (C) Comparison of the refined S.O.F. for 1Pd/κ-$Ce_{0.5}Zr_{0.5}O_2$ (D) Comparison of the refined unit cell size for fluorite $Ce_{0.5}Zr_{0.5}O_2$ and 1Pd/$Ce_{0.5}Zr_{0.5}O_2$ (E) Comparison of the refined S.O.F. for fluorite $Ce_{0.5}Zr_{0.5}O_2$ and 1Pd/$Ce_{0.5}Zr_{0.5}O_2$

Figure 6-6 shows the comparison of numerous refined parameters for both kappa and fluorite based materials. Figure 6-6 (A) shows the refined lattice parameter values for κ-$Ce_{0.5}Zr_{0.5}O_2$ and 1Pd/κ-$Ce_{0.5}Zr_{0.5}O_2$ respectively. For both samples the lattice expands as they heated from room temperature to 900°C. This is due to a combination of both thermal expansion (from heating the samples) and the reduction of Ce (IV) to Ce (III). It is noticeable that under a reducing atmosphere that the lattice expansion is of a greater magnitude, for both samples, compared to the expansion observed under an oxidising atmosphere. This would suggest that the reduction of the samples and removal of oxygen from the lattice is a causative process in the lattice expansion during the cycling experiments. Furthermore the rate of expansion is greater for the Pd loaded kappa material in comparison to the bare support, indicating that the inclusion of Pd to the system aids in the reduction of the sample. Figure 6-6 (B) and (C) show the refined Structure Occupancy Factor (S.O.F.) for κ-$Ce_{0.5}Zr_{0.5}O_2$ and 1Pd/κ-$Ce_{0.5}Zr_{0.5}O_2$ respectively. For the pure κ-$Ce_{0.5}Zr_{0.5}O_2$ material, there is loss of oxygen under reducing conditions of the O 4 site whereas for 1Pd/κ-$Ce_{0.5}Zr_{0.5}O_2$ there is loss of oxygen from both the O 4 and O 12 sites. This indicates that the κ-$Ce_{0.5}Zr_{0.5}O_2$ support could be reduced to the pyrochlore material with the loss of oxygen and creation of oxygen defects within the system.[14] For 1Pd/κ-$Ce_{0.5}Zr_{0.5}O_2$ there is greater amount of loss of oxygen on both sites, supporting the idea that the Pd provides a site where H_2 could be disassociated upon and react with oxygen in the lattice forming water. Upon cooling, the amount of oxygen increase for both κ-$Ce_{0.5}Zr_{0.5}O_2$ and 1Pd/κ-$Ce_{0.5}Zr_{0.5}O_2$. This would seem to be counterintuitive as the samples are cooled under a reducing environment. This could be a result of the correlation between atomic displacement and S.O.F. Upon cooling to room temperature (~100 minutes), the pure κ-$Ce_{0.5}Zr_{0.5}O_2$ shows that the O site is fully occupied whereas for 1Pd/κ-$Ce_{0.5}Zr_{0.5}O_2$ the S.O.F. = ~0.5 for the O 4 site. This would imply that for κ-$Ce_{0.5}Zr_{0.5}O_2$, either no reduction occurs and there is extensive disordering of the Oxygen sites, or increase in atomic disorder and small amounts of reduction. In comparison, for 1Pd/κ-$Ce_{0.5}Zr_{0.5}O_2$, there are oxygen defects are cooling, suggesting reduction of the ceria zirconia material.

Figure 6-6 (D) shows the comparison of the lattice parameters for both the fluorite $Ce_{0.5}Zr_{0.5}O_2$ and 1Pd/$Ce_{0.5}Zr_{0.5}O_2$ materials. Similarly to the kappa materials, the lattice parameter expands upon heating to 900°C under reducing or oxidising atmospheres, and contracts upon cooling. For both samples the amount of expansion is larger under reducing conditions compared to oxidising conditions, suggesting the creation of Ce (III) ions under reducing conditions, which has a larger ionic radius in comparison to Ce (IV). Refinement of the S.O.F. (Figure 6-6 (E)) for both plain and Pd loaded fluorite samples show there is loss of oxygen from the lattice. Upon cooling these values increase though not to their original values. This suggests that the values observed on heating are both a combination of the reduction of the support and the increase in the disorder of the atoms within the lattice (as both S.O.F. and atomic displacement correlate). It is further noticeable that upon heating under an oxidising atmosphere that the fluorite materials do not become fully stoichiometric in comparison to the kappa based materials.

6.6 Summary

The oxidation cycle of fluorite and κ-$Ce_{0.5}Zr_{0.5}O_2$ based materials show no phase transition from their respective starting materials. The analysis shows that upon heating under an oxidising atmosphere that there is a lattice expansion and disordering of the atoms within the structure. Upon cooling under this atmosphere, the lattice contracts to its original size, suggesting less disorder upon cooling. The only noticeable difference is that for the Pd loaded samples, there is the formation of Pd metal. This would seem counterintuitive as most likely the initial Pd phase would be dispersed PdO on the surface of the support but the conversion of PdO to Pd under oxidising conditions is documented.[15] It is of note that no discernible sintering of the fluorite $Ce_{0.5}Zr_{0.5}O_2$ material is observed in comparison to previously reported findings.[16]

In contrast the reduction and oxidising of both fluorite and kappa materials show greater changes under the respective atmospheres. The fluorite $Ce_{0.5}Zr_{0.5}O_2$ materials show that under reducing conditions that there is a lattice expansion. This can attributed to both thermal expansion and the loss of oxygen from the lattice. Under oxidising conditions, the amount of thermal expansion is less than that observed in reducing conditions supporting the loss of oxygen being observed. Though overall the samples are not converted to either a kappa or pyrochlore ceria-zirconia material c.f. the synthesis of the kappa materials for this experiment was performed by heating the fluorite ceria zirconia materials for 6 hours under reducing conditions.

For the kappa ceria-zirconia materials, both are converted to the pyrochlore structure under a reducing atmosphere. The kappa and pyrochlore phases being related by having a similar sub lattice of both cations and anions, but the pyrochlore only filling 7/8 oxygen sites present. Under oxidising conditions the pyrochlore structures are then oxidised back to their respective kappa ceria zirconia starting materials. This would indicate that the time at which the samples at 900°C was not long enough to induce a pyrochlore formation as under oxidising conditions the samples readily convert to the kappa starting material. The 1Pd/κ-$Ce_{0.5}Zr_{0.5}O_2$ material shows an marked increase in the loss of oxygen from the lattice compared to the plain κ-$Ce_{0.5}Zr_{0.5}O_2$ materials which has been previously reported.[6] This redox treatment has been utilised before[10] showing that κ-$Ce_{0.5}Zr_{0.5}O_2$ is still found post treatment.

For both the plain and Pd loaded κ-$Ce_{0.5}Zr_{0.5}O_{2,}$ the lattice parameters return to similar values post redox treatment indicating that any Ce (III) formed during the reduction phase has been oxidised back to Ce (IV).[17]

Further work for the comprehension of these materials would be to heat the samples for longer than used in these series of experiments to form a stable pyrochlore ceria zirconia material at ambient conditions. More analysis is required into the structure of the formed pyrochlore structures and how this structure transforms back to the κ-$Ce_{0.5}Zr_{0.5}O_2$ starting materials.[18] In addition the use of EXAFS of both the Ce and Zr atoms present within the support material would aid in the understanding of the short range structure whereas the use of Pd EXAFS would help in comprehending the conversion of the dispersed Pd (or PdO) into Pd metal under either reducing or oxidising conditions. Furthermore, more characterisation is required using Neutron Total scattering techniques to probe, more accurately, the oxygen disorder within these samples and whether certain cerium or zirconium rich regions are found.[19]

6.7 Bibliography

1 B. J. Wuensch, K. W. Eberman, C. Heremans, E. M. Ku, P. Onnerud, E. M. E. Yeo, S. M. Haile, J. K. Stalick and J. D. Jorgensen, *Solid State Ionics*, 2000, **129**, 111–133.

2 M. Pirzada, R. W. Grimes, L. Minervini, J. F. Maguire and K. E. Sickafus, *Solid State Ionics*, 2001, **140**, 201–208.

3 P. J. Wilde and C. R. A. Catlow, *Solid State Ionics*, 1998, **112**, 173–183.

4 M. Moser, C. Mondelli, T. Schmidt, F. Girgsdies, M. E. Schuster, R. Farra, L. Szentmiklósi, D. Teschner and J. Pérez-Ramírez, *Appl. Catal. B Environ.*, 2013, **132–133**, 123–131.

5 M. Yashima, M. Kakihana and M. Yoshimura, *Solid State Ionics*, 1996, **86–88**, 1131–1149.

6 P. Fornasiero, R. Dimonte, G. R. Rao, J. Kaspar, S. Meriani, A. Trovarelli and M. Graziani, *J. Catal.*, 1995, 151, 168–177.

7 M. Pijolat, M. Prin, M. Soustelle, O. Touret and P. Nortier, *J. Chem. Soc.{,} Faraday Trans.*, 1995, **91**, 3941–3948.

8 T. a. Lee, C. R. Stanek, K. J. McClellan, J. N. Mitchell and A. Navrotsky, *J. Mater. Res.*, 2008, **23**, 1105–1112.

9 M. Yashima, H. Arashi, M. Kakihana and M. Yoshimura, *J. Am. Ceram. Soc.*, 1994, **77**, 1067–1071.

10 B. De Rivas, R. López-Fonseca, M. Á. Gutiérrez-Ortiz and J. I. Gutiérrez-Ortiz, *Catal. Today*, 2011, **176**, 470–473.

11 A. P. Hammersley, S. O. Svensson, M. Hanfland, A. N. Fitch and D. Hausermann, *High Press. Res.*, 1996, **14**, 235–248.

12 A. A. Coelho, *J. Appl. Crystallogr.*, 2003, **36**, 86–95.

13 F. Bertaut and P. Blum, *C.R. Acad. Sci. Paris*, 1949, **229**, 666.

14 S. Urban, P. Dolcet, M. Möller, L. Chen, P. J. Klar, I. Djerdj, S. Gross, B. M. Smarsly and H. Over, *Appl. Catal. B Environ.*, 2015, **197**, 23–34.

15 J. Keating, G. Sankar, T. I. Hyde, S. Kohara and K. Ohara, *Phys. Chem. Chem. Phys.*, 2013, **15**, 8555–8565.

16 D. Terribile, *Catal. Today*, 1998, **43**, 79–88.

17 J. B. Thomson, A. Robert Armstrong and P. G. Bruce, *J. Am. Chem. Soc.*, 1996, **118**, 11129–11133.

18 S. N. Achary, S. K. Sali, N. K. Kulkarni, P. S. R. Krishna, A. B. Shinde and A. K. Tyagi, *Chem. Mater.*, 2009, **21**, 5848–5859.

19 E. Mamontov, R. Brezny, M. Koranne and T. Egami, *J. Phys. Chem. B*, 2003, **107**, 13007–13014.

Chapter 7: Conclusion and future work

This work has shown that the combination of advanced characterisation techniques is important in the comprehension of catalysts and that understanding the short-, medium- and long-range structure highlights how using one analytical method is a poor choice for characterisation. Though these are relatively basic systems, this thesis gives a solid basis to further work in both ceria based systems and combined characterisation methodologies.

7.1 Structure of nano-sized Ceria materials: a combined spectroscopic and scattering investigation

The initial work, that formed a basis for later work, was to understand the structure of ceria materials, whether the synthesis procedure influenced the structure and how a combination of techniques can influence the observed results. It was shown that the synthetic procedure only influenced the materials by the formation of different particle size and no obvious defects or extreme disordering from the ideal fluorite structure was found. The results obtained by combined Rietveld analysis of ND and XRD data shows that the HSA ceria, Ce (III) and Ce (IV) precursor ceria samples are more disordered than that of a ceria NIST standard. Neutron and X-ray PDF studies support this observation. Dampening of the amplitudes of the PDFs of the synthesized samples is observed at $r > 10Å$ which indicates a smaller crystallite size compared to the NIST sample that has an average crystallite size of 380.6 nm.[1] EXAFS analysis of both the Ce L_3- and K-edges agrees with PDF analysis and Rietveld refinement of diffraction data showing crystallite sizes smaller than that of the NIST sample. EXAFS data analysis clearly indicates that the disorder is more in the oxygen site in all the synthesised samples compared to NIST standard and more significant disorder is seen for high-surface area material than other synthesised samples. It is difficult to say from these data whether the disorder associated with oxygen is related to the increased ratio of surface-oxygen in the smaller particles. More surface sensitive techniques that can determine structure near to the particle surface would be required to establish this. Analysis of the RMC models of all the materials further support the conclusion that more disorder is observed on the oxygen site for the ceria samples in comparison to the Ceria NIST material.

Future work for the study of *ex*-situ ceria samples would be improved by the inclusion of more surface sensitive techniques that can determine structure near to the particle surface such as X-ray Photoelectron spectroscopy which would help verify the oxidation state of the surface cerium atoms. Furthermore the inclusion of other complimentary techniques such as Raman, Oxygen (^{17}O) NMR and electron diffraction would not only help with the comparison of the ceria samples but their inclusion into the RMCProfile modelling would improve the accuracy in the resultant models.

7.2 *Insitu* Neutron diffraction, X-ray Total scattering, and X-ray absorption study of platinum group metal loaded ceria under reducing conditions

To conclude, this work has successfully shown that a combination of techniques is important in the comprehension of how catalytic materials behave under reducing conditions.

Neutron/X-ray diffraction and x-ray total scattering methodologies both show the fluorite structure is observed from the outset and throughout the reducing cycle. Neutron diffraction methods show the reduction of ceria and the loss of oxygen whereas XPDF showing the increase in disorder upon heating, and perhaps the formation of Ce (III)-O bonds. The XPDF shows increases in lattice parameters during the cycle consistent with previously reported metal loaded ceria systems under reducing conditions.[2] A combination of refined lattice parameters and refined oxygen occupancies, from ND, show that heating to 400°C that pure ceria support and the respective Pd and Pt loading on ceria are reduced by ca. 10%. With an increase in the lattice parameter which is a combination of thermal disorder and formation of Ce (III) ions. A similar observation has been seen using ND under reducing conditions where the loss of oxygen and the increase in lattice parameters and thermal parameters upon heating.[3] The important differences between the pure support and PGM loaded materials is on cooling that the pure support returns to a similar lattice parameter value and oxygen occupancy whereas for PGM loaded samples do not return to their original values.

The analysis of XANES data gives important information of the electronic and coordination of the probed atom. For the Ce L_3-edge of the high surface area ceria support, we can observe the reduction from Ce (IV) to Ce (III) under heating then oxidation back to Ce (IV). This trait has been observed previously in cerium based oxides.[4] In contrast to the reported literature, no particle size growth was seen i.e. no definitive peak sharpening in diffraction, suggesting that the increase in particle size and loss of oxide deficient surfaces was not the cause of the reoxidation of the ceria under reducing and cooling conditions. The comparison of the Pd K-edge and Pt L_3-edge with the respective Ce L_3-edge data shows the reduction of the PGM metal simultaneously with the onset of Ce (IV) to Ce (III) reduction, at a lower temperature than pure ceria. This indicates that PGM are important to aid in the reduction of ceria suggesting that PGM leads to a spill over mechanism. Furthermore the amount of Ce (III) present upon cooling stays consistent on cooling (matching the lack of reoxidation seen in Neutron Diffraction). In addition the Pd K-edge EXAFS shows the reduction of PdO to Pd metal, though not fully, suggesting a small particle formation and no incorporation of Pd into the ceria lattice by this synthesis procedure or subsequent treatment.[5]

A combination of these techniques would suggest that for the pure ceria support, though reduction is observed this could actually be an extensive migration of oxygen from their ideal sites in the structure which is mimicking a reduction then the subsequent oxidation in reducing conditions. In comparison Pd and Pt loaded onto ceria, show a reduction upon heating and no oxidation upon cooling. This indicates that both Pd and Pt are important in the removal of oxygen from the ceria lattice. This work indicates that Pd and Pt both have similar influence on the ceria support by the amount of reduction observed. This is contrary to reported literature indicating that Pd has stronger metal support interactions than Pt.[6]

Further work for this would be to use neutron PDF to probe further into the migration of oxygen atoms throughout the lattice then to combine all datasets and use RMC based methods to model these materials to investigate further how oxygen atoms in the ceria lattice behave under reducing conditions.

7.3 *Insitu* X-ray absorption spectroscopy and X-ray total scattering characterisation of Palladium on ceria with different loading levels

Once again this part of the work shows how a combination of techniques allows for the determination of how materials behave under in operando conditions.

This investigation shows how a sole technique does not illustrate fully how materials behave under industrially relevant conditions. XAS analysis shows that for the pure ceria support the sample is reduced upon heating but returns to its original state after cooling which is a previously reported property of ceria based materials.[4]

In comparison the loading of Pd onto the high surface area ceria support, decreases the reduction temperature of the ceria support but upon cooling there is no reoxidation. Increasing the amount of Pd loaded onto the ceria support, decreases the temperature at which the metal reduces and at which the ceria will start to reduce. The XAS also indicates that for the Pd loaded onto ceria samples, the metal must reduce from PdO to Pd before the onset of the reduction for the ceria support. In contrast, a physical mixture of PdO and the high surface area support shows a decrease in the reduction temperature for the ceria support. It does not reoxidise to the same extent as the pure ceria support though does not behave in the same manner as the Pd loaded ceria samples as analysed with XANES. The respective EXAFS analysis for the 2.5 and 5 wt% Pd samples show the reduction of PdO to Pd. The refinement of the co-ordination numbers show that neither samples have an average co-ordination of 12 (c.f. the Pd foil). This would indicate that the Pd present is found in a nanoparticulate form. Furthermore, comparison of the respective EXAFS spectra with Hiley *et al*,[5] confirm that no Pd is present in square planar geometry within the high surface area ceria support.

The HRXRD shows that for all the samples the ceria fluorite is observed throughout the reduction experiments and no other ceria based phases are present. The refined parameters show the reduction and loss of oxygen from the lattice whilst heating. For the pure ceria support there is reoxidation back to stoichiometric values whereas for the Pd loaded materials, there is a loss of oxygen. The addition of Pd into the lattice does not improve the fits indicating a highly dispersed PdO phase at the outset of the experiments and nanoparticulate Pd after the reduction from PdO to Pd metal. This behaviour matches that of previously reported literature on the reduction of PdO to Pd under hydrogen.[7] This is supported by XPDF experiments of the same samples under the same operating conditions. PDF based techniques indicate an increased disorder of Ce and O ions upon heating and the formation of Ce (III)-O bonds. The comparison of the refined lattice parameters from both Rietveld and PDF show both similar values and similar correlations between an increase in temperature and the lattice parameter. For the Pd loaded samples, the lattice parameter does not return to its original values in comparison to the pure ceria support, indicating increased disorder and the presence of Ce (III) ions. Though for 1wt% Pd on ceria shows a further expansion on cooling for both Rietveld and PDF based analytical methods. This is in contrast to XAS which indicates that less Ce (III) is present on cooling, leading to a smaller lattice parameter. Furthermore, upon cooling, less thermal energy is imparted to the PGM/ceria system leading, in theory, to a more ordered system. This would suggest that the experiment could have had issues as this result is counterintuitive to what is both chemically and physically possible. This could be due to incorrect temperature measurements, variation in sample position, variations in gas composition etc.

The TPR profile shows that with increasing amounts of Pd there is a decrease in the temperature at which reduction takes place. This has been attributed to the reduction of PdO to Pd metal. This behaviour matches previously reported results on PGM loaded ceria supports.[6] The decrease in reduction temperature can be assigned to the Pd present on the 1 wt% Pd on ceria sample being highly dispersed in contrast to the 5 wt% Pd on ceria sample.

All the techniques combined show for the ceria support that there is reoxidation in a reducing atmosphere which seems counter intuitive. In reality the reduction observed could be migration of oxygen mirroring the removal of oxygen and reduction of the support. Whereas for the Pd loaded samples, the inclusion of Pd onto the systems shows that it is important in the removal of oxygen from the lattice as no reoxidation is observed upon cooling.

Further work for this would be to use neutron PDF to probe further into the migration of oxygen atoms throughout the lattice. In addition using Ce K-edge XAS would be a complimentary technique in investigating the ceria support. Furthermore all datasets could be combined and RMC based methods can model these materials to investigate further how oxygen atoms in the ceria lattice behave under reducing conditions, combining short, medium and long range structural investigations.

7.4 *Insitu* x-ray total scattering study of the phase transformation of ceria-zirconia kappa and fluorite materials

The oxidation cycle of fluorite and κ-$Ce_{0.5}Zr_{0.5}O_2$ based materials show no phase transition from their respective starting materials. The analysis shows that upon heating under an oxidising atmosphere that there is a lattice expansion and disordering of the atoms within the structure. Upon cooling under this atmosphere, the lattice contracts to its original size, suggesting less disorder upon cooling. The only noticeable difference is that for the Pd loaded samples, there is the formation of Pd metal. This would seem counterintuitive as most likely the initial Pd phase would be dispersed PdO on the surface of the support but the conversion of PdO to Pd under oxidising conditions is documented.[8] It is of note that no discernible sintering of the fluorite $Ce_{0.5}Zr_{0.5}O_2$ material is observed in comparison to previously reported findings.[9]

In contrast the reduction and oxidising of both fluorite and kappa materials show greater changes under the respective atmospheres. The fluorite $Ce_{0.5}Zr_{0.5}O_2$ materials show that under reducing conditions that there is a lattice expansion. This can attributed to both thermal expansion and the loss of oxygen from the lattice. Under oxidising conditions, the amount of thermal expansion is less than that observed in reducing conditions supporting the loss of oxygen being observed. Though overall the samples are not converted to either a kappa or pyrochlore ceria-zirconia material c.f. the synthesis of the kappa materials for this experiment was performed by heating the fluorite ceria zirconia materials for 6 hours under reducing conditions.

For the kappa ceria-zirconia materials, both are converted to the pyrochlore structure under a reducing atmosphere. The kappa and pyrochlore phases being related by having a similar sub lattice of both cations and anions, but the pyrochlore only filling 7/8 oxygen sites present. Under oxidising conditions the pyrochlore structures are then oxidised back to their respective kappa ceria zirconia starting materials. This would indicate that the time at which the samples at 900°C was not long enough to induce a pyrochlore formation as under oxidising conditions the samples readily convert to the kappa starting material. The 1Pd/κ-$Ce_{0.5}Zr_{0.5}O_2$ material shows an marked increase in the loss of oxygen from the lattice compared to the plain κ-$Ce_{0.5}Zr_{0.5}O_2$ materials which has been previously reported.[10] This redox treatment has been utilised before[11] showing that κ-$Ce_{0.5}Zr_{0.5}O_2$ is still found post treatment.

For both the plain and Pd loaded κ-$Ce_{0.5}Zr_{0.5}O_{2,}$ the lattice parameters return to similar values post redox treatment indicating that any Ce (III) formed during the reduction phase has been oxidised back to Ce (IV).[12]

Further work for the comprehension of these materials would be to heat the samples for longer than used in these series of experiments to form a stable pyrochlore ceria zirconia material at ambient conditions. More analysis is required into the structure of the formed pyrochlore structures and how this structure transforms back to the κ-$Ce_{0.5}Zr_{0.5}O_2$ starting materials.[13] In addition the use of EXAFS of both the Ce and Zr atoms present within the support material would aid in the understanding of the short range structure whereas the use of Pd EXAFS would help in comprehending the conversion of the dispersed Pd (or PdO) into Pd metal under either reducing or oxidising conditions.

Further work into this area would be to perform the experiments again but over a longer time scale i.e. heating the fluorite precursor material for longer than 30 minutes at 900°C, and instead heat for similar time scales to those used in the synthesis of the experiment. The addition of both Ce and Zr XAS would help in the understanding of the short range structure. These datasets could then combined to perform an RMC based analysis to simultaneously model both edges. Characterisation is required using Neutron Total scattering techniques to probe, more accurately, the oxygen disorder within these samples and whether certain cerium or zirconium rich regions are found.[14]

In summary, the work presented in the thesis showed the use of appropriate structural characterisation methods which are sensitive to short, medium and long-range order of crystalline material is crucial to understand their unusual behaviour both in the nano particulate form and under reaction conditions. The study also highlights the importance of studying materials under in situ conditions as opposed to the investigation of end members of a reaction as it could mislead or provide misleading information of a catalytic system.

7.5 Bibliography

1 https://www-s.nist.gov/srmors/certificates/674B.pdf Date Accessed 28/03/2017

2 J. C. Hanson, R. Si, W. Xu, S. D. Senanayake, K. Mudiyanselage, D. Stacchiola, J. A. Rodriguez, H. Zhao, K. A. Beyer, G. Jennings, K. W. Chapman, P. J. Chupas and A. Martínez-Arias, *Catal. Today*, 2014, **229**, 64–71.

3 S. Hull, S. T. Norberg, I. Ahmed, S. G. Eriksson, D. Marrocchelli and P. A. Madden, *J. Solid State Chem.*, 2009, **182**, 2815–2821.

4 D. R. Modeshia, C. S. Wright, J. L. Payne, G. Sankar, S. G. Fiddy and R. I. Walton, *J. Phys. Chem. C*, 2007, **111**, 14035–14039.

5 C. I. Hiley, J. M. Fisher, D. Thompsett, R. J. Kashtiban, J. Sloan and R. I. Walton, *J. Mater. Chem. A*, 2015, **3**, 13072–13079.

6 C. de Leitenburg, A. Trovarelli and J. Kašpar, *J. Catal.*, 1997, **166**, 98–107.

7 A. Baylet, P. Marécot, D. Duprez, P. Castellazzi, G. Groppi and P. Forzatti, *Phys. Chem. Chem. Phys.*, 2011, **13**, 4607–4613.

8 J. Keating, G. Sankar, T. I. Hyde, S. Kohara and K. Ohara, *Phys. Chem. Chem. Phys.*, 2013, **15**, 8555–8565.

9 D. Terribile, *Catal. Today*, 1998, **43**, 79–88.

10 P. Fornasiero, R. Dimonte, G. R. Rao, J. Kaspar, S. Meriani, A. Trovarelli and M. Graziani, *J. Catal.*, 1995, 151, 168–177.

11 B. De Rivas, R. López-Fonseca, M. Á. Gutiérrez-Ortiz and J. I. Gutiérrez-Ortiz, *Catal. Today*, 2011, **176**, 470–473.

12 J. B. Thomson, A. Robert Armstrong and P. G. Bruce, *J. Am. Chem. Soc.*, 1996, **118**, 11129–11133.

13 S. N. Achary, S. K. Sali, N. K. Kulkarni, P. S. R. Krishna, A. B. Shinde and A. K. Tyagi, *Chem. Mater.*, 2009, **21**, 5848–5859.

14 E. Mamontov, R. Brezny, M. Koranne and T. Egami, *J. Phys. Chem. B*, 2003, **107**, 13007–13014.

Chapter 8: Appendices

Appendix for Chapter 3

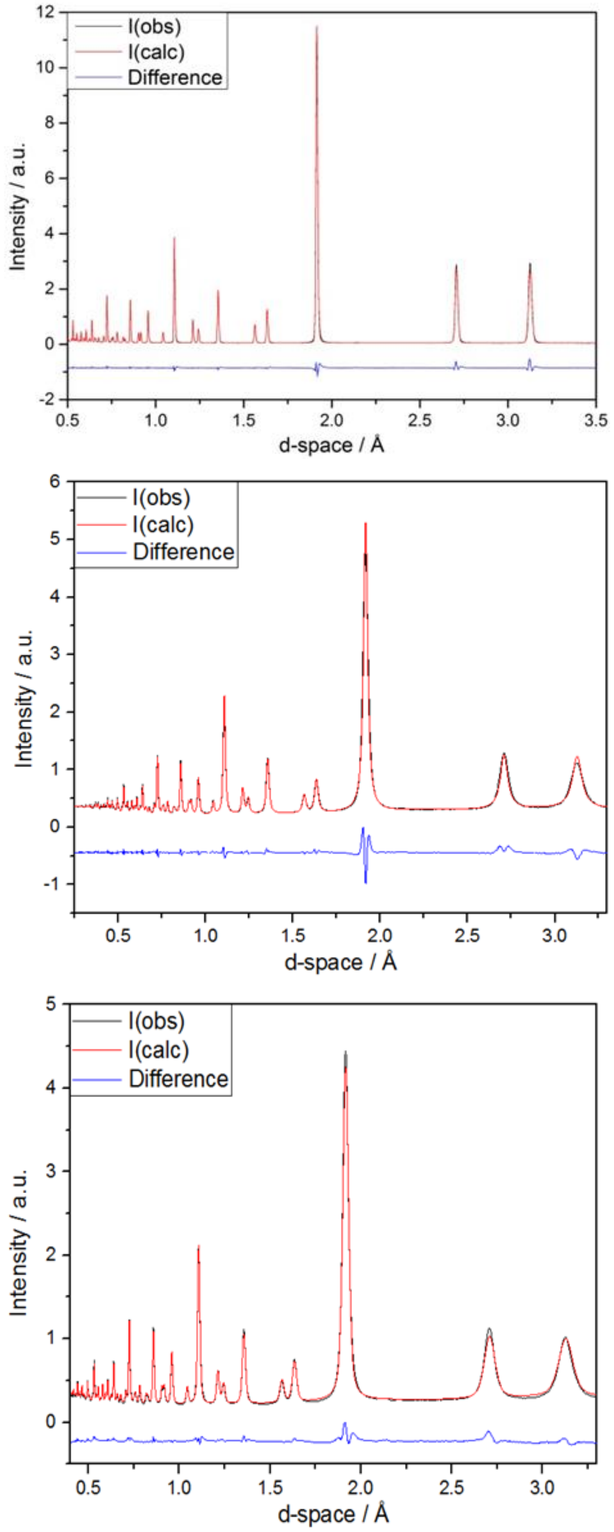

Figure S1: Comparison of observed (Iobs) and calculated (Icalc) neutron diffraction pattern (Top) Ceria NIST (Middle) Ceria prepared from Ce (III) precursor (Bottom) for Ceria prepared from Ce (IV) Precursor.

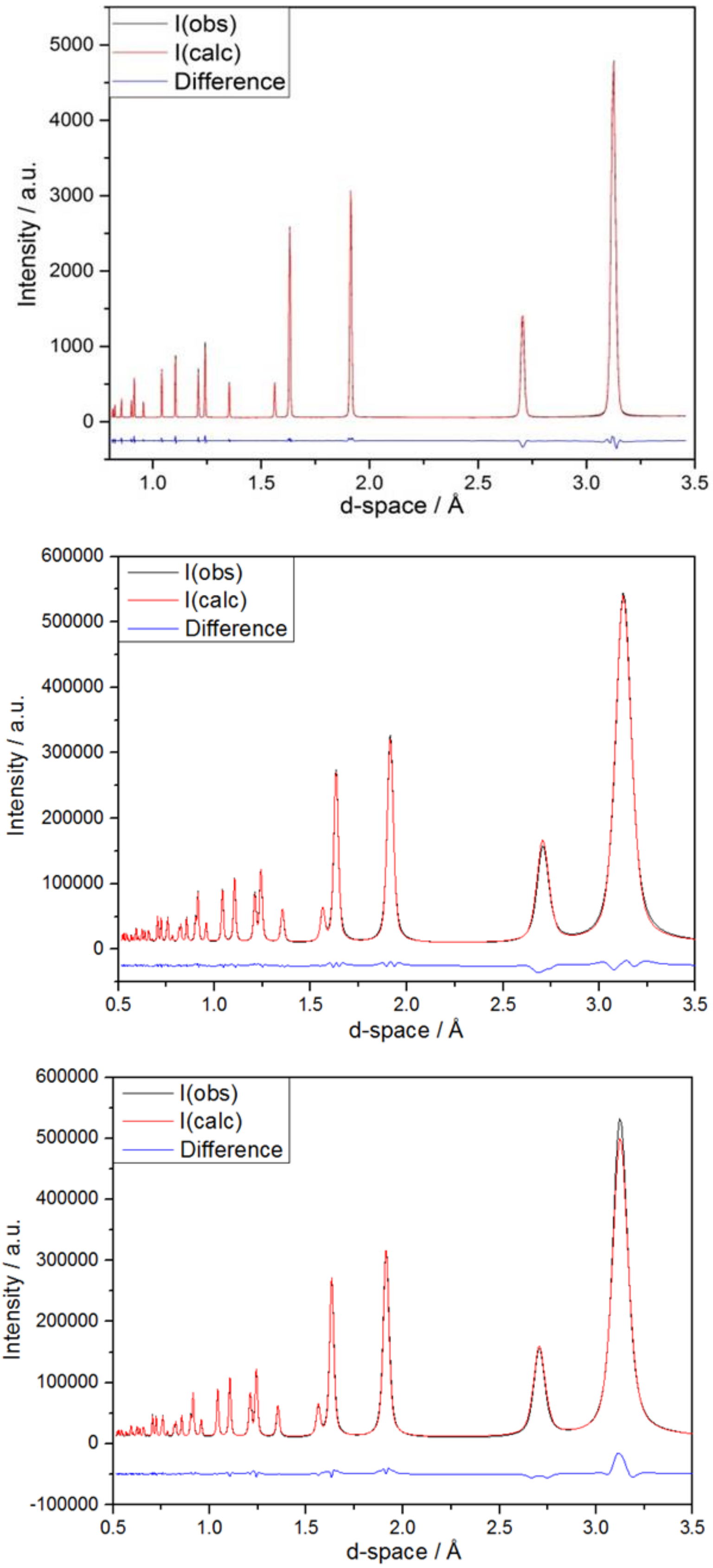

Figure S2: Comparison of observed (Iobs) and calculated (Icalc) X-ray diffraction pattern (Top) Ceria NIST (Middle) Ceria prepared from Ce (III) precursor (Bottom) for Ceria prepared from Ce (IV) Precursor.

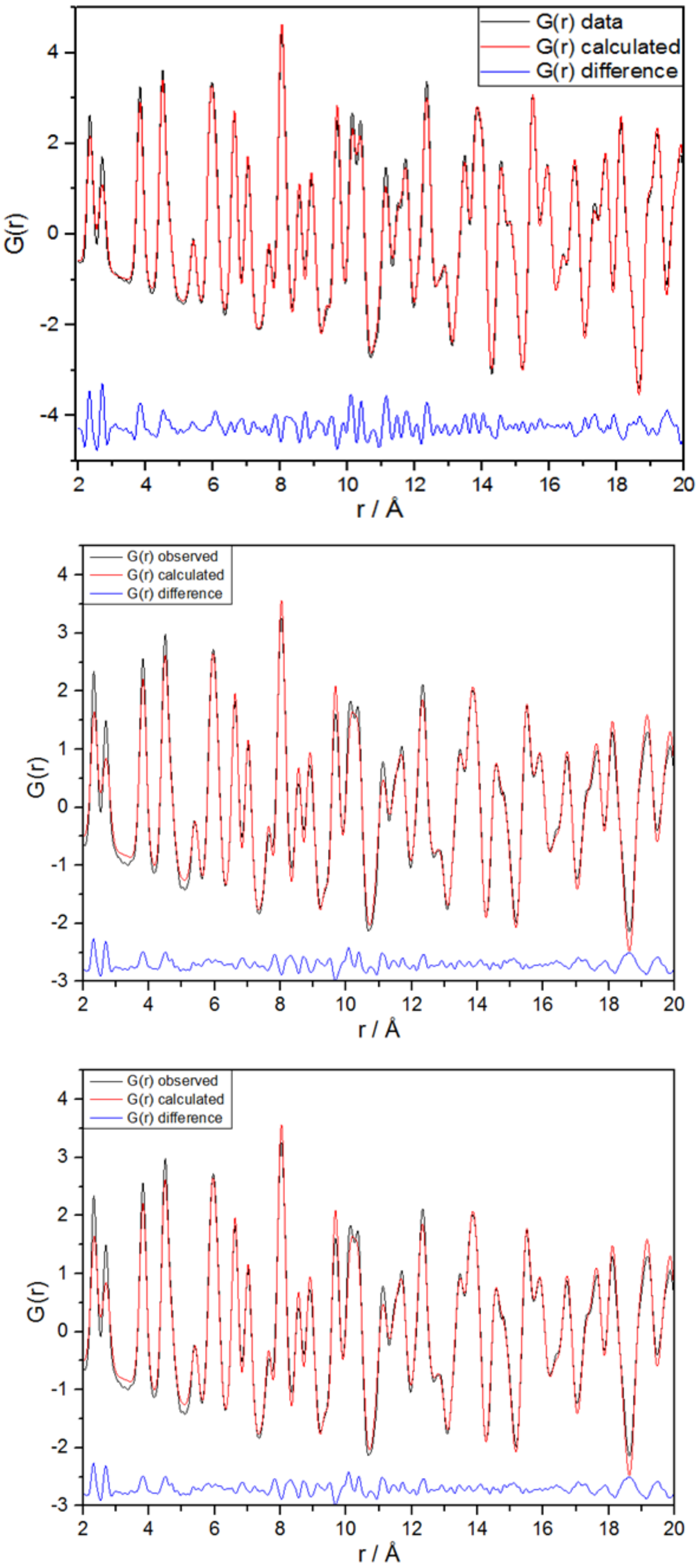

Figure S3: Comparison of the neutron G(r) data and calculated G(r) (Top) Ceria NIST (Middle) Ceria prepared from Ce (III) precursor (Bottom) for Ceria prepared from Ce (IV) Precursor.

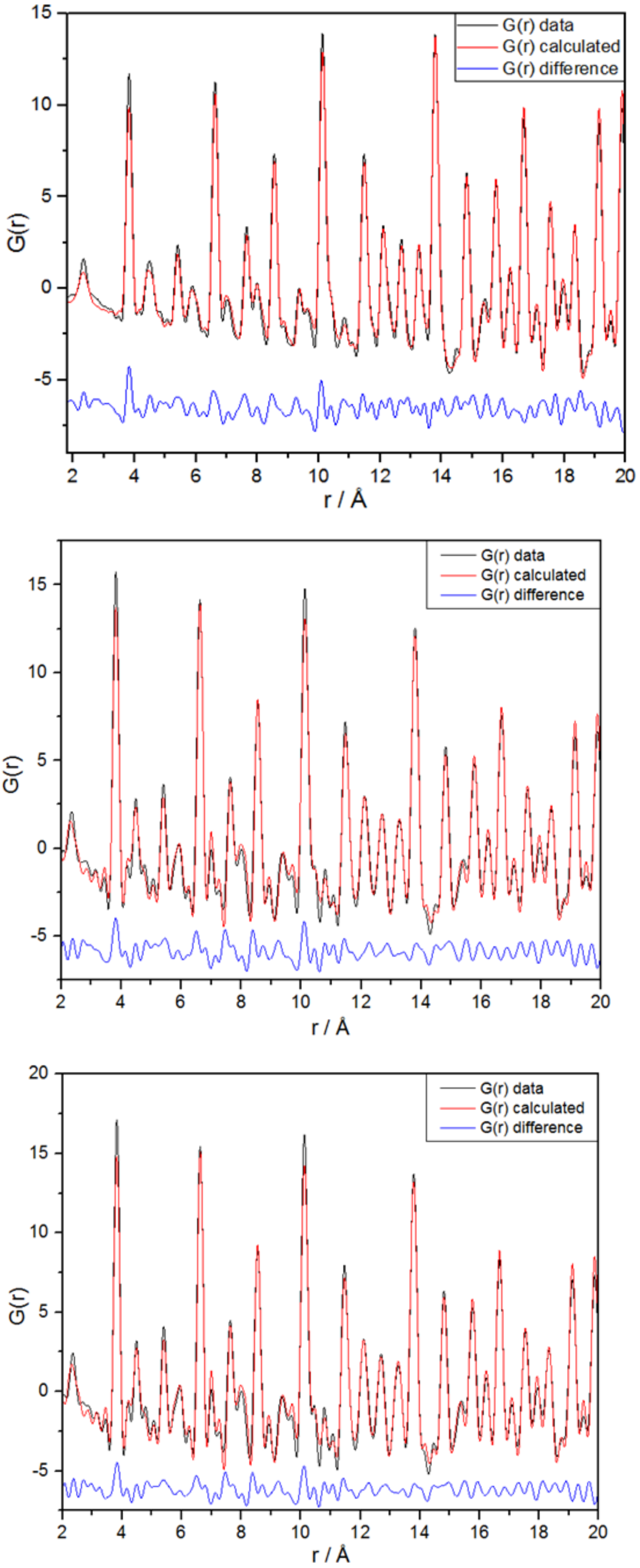

Figure S4: Comparison of the x-ray G(r) data and calculated G(r) (Top) Ceria NIST (Middle) Ceria prepared from Ce (III) precursor (Bottom) for Ceria prepared from Ce (IV) Precursor.

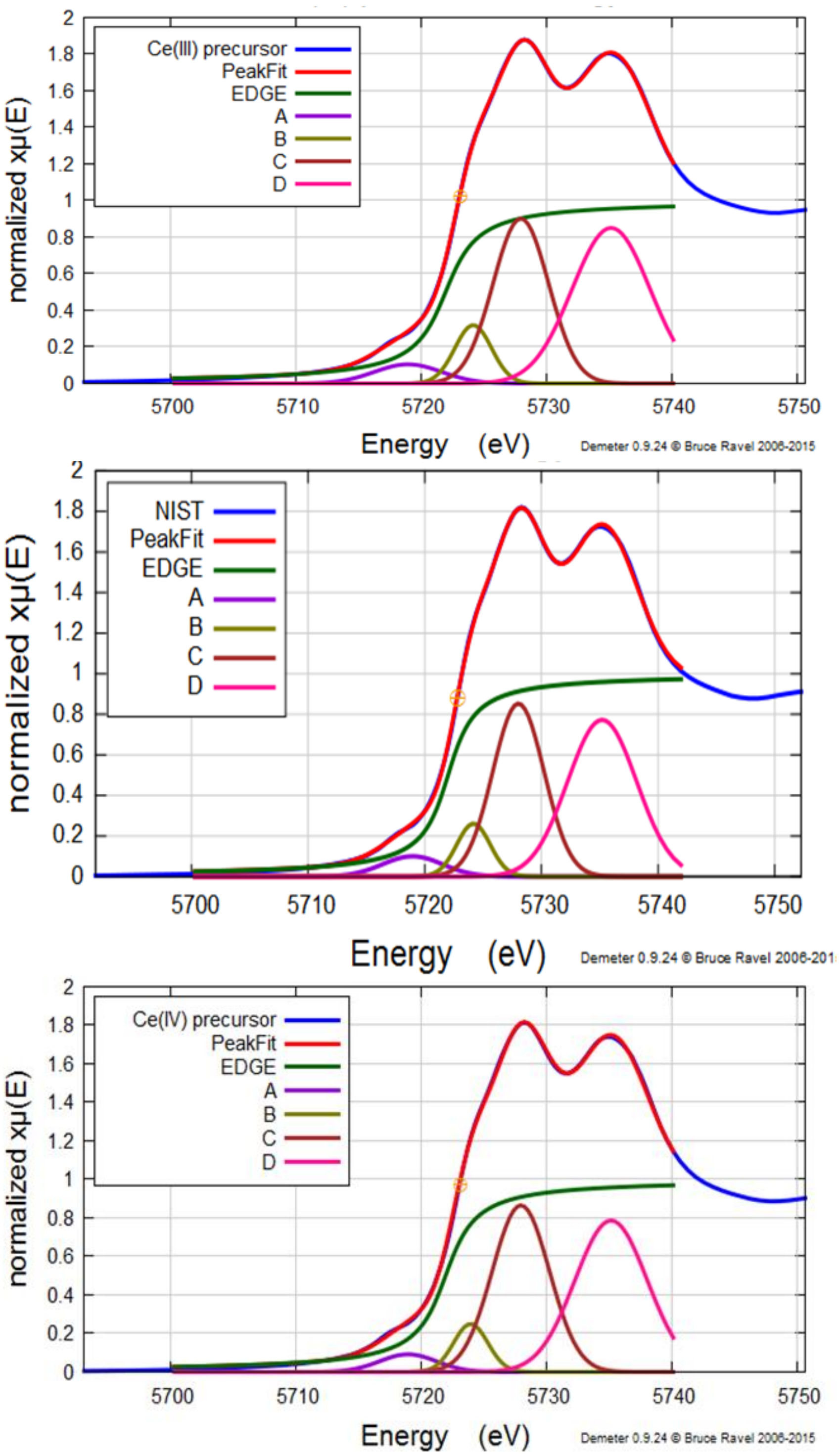

Figure S5: Typical XANES peak fitting with component peaks visible. The edge structure has been fitted with an arctangent function and 4 Gaussian peaks associated to different transitions that have been identified within crystalline Ceria. A, pre-edge feature associated to the delocalisation of the d orbital at the bottom of the conduction band within large clusters. B, a low energy shoulder associated to the crystal-field splitting within the cubic fluorite structure. C and D the characteristic doublet for the 2p→4f0,15d transitions. (Top) Ceria NIST (Middle) Ceria prepared from Ce (III) precursor (Bottom) for Ceria prepared from Ce (IV) Precursor.

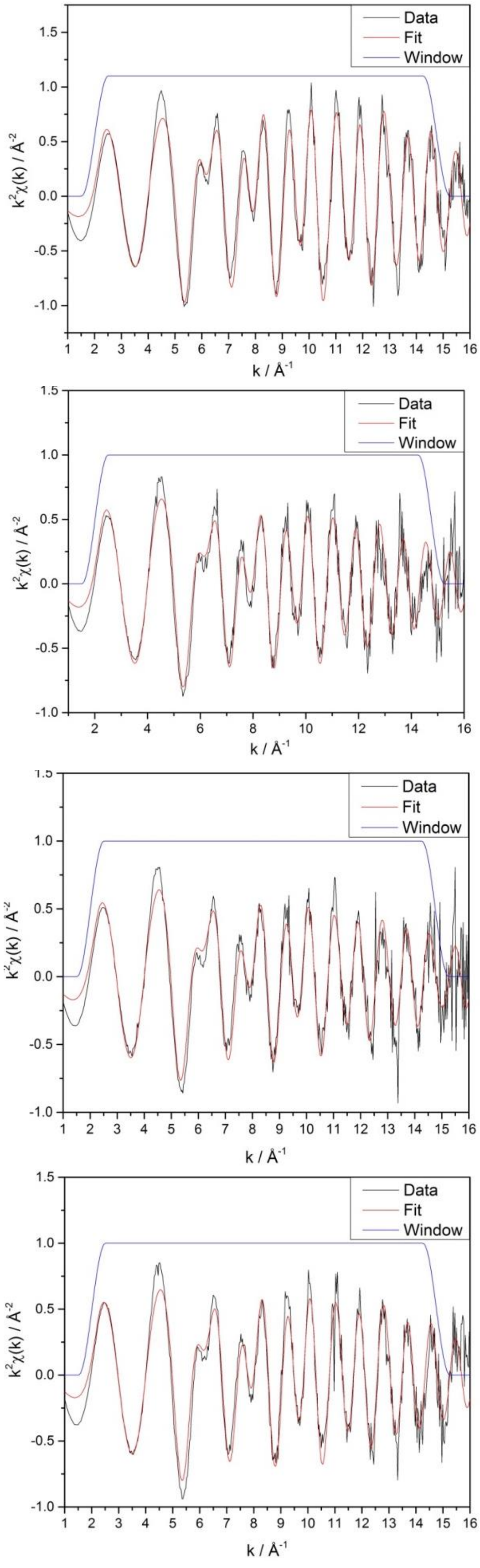

Figure S6: A comparison of the k2χ(k) data and fit: Top Ceria NIST, 2nd HSA Ceria, 3rd Ceria prepared from Ce (III) precursor and bottom Ceria prepared from Ce (IV) precursor.

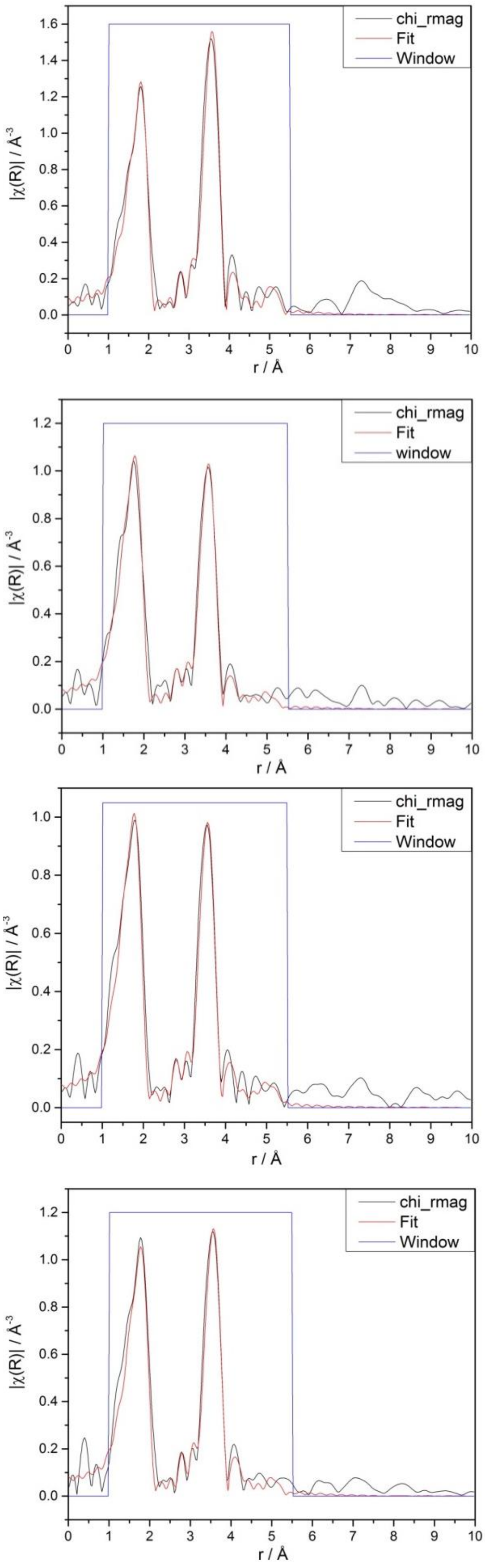

Figure S7: A comparison of the |χ(R)| data and fit: Top Ceria NIST, 2nd HSA Ceria, 3rd Ceria prepared from Ce (III) precursor and bottom Ceria prepared from Ce (IV) precursor.

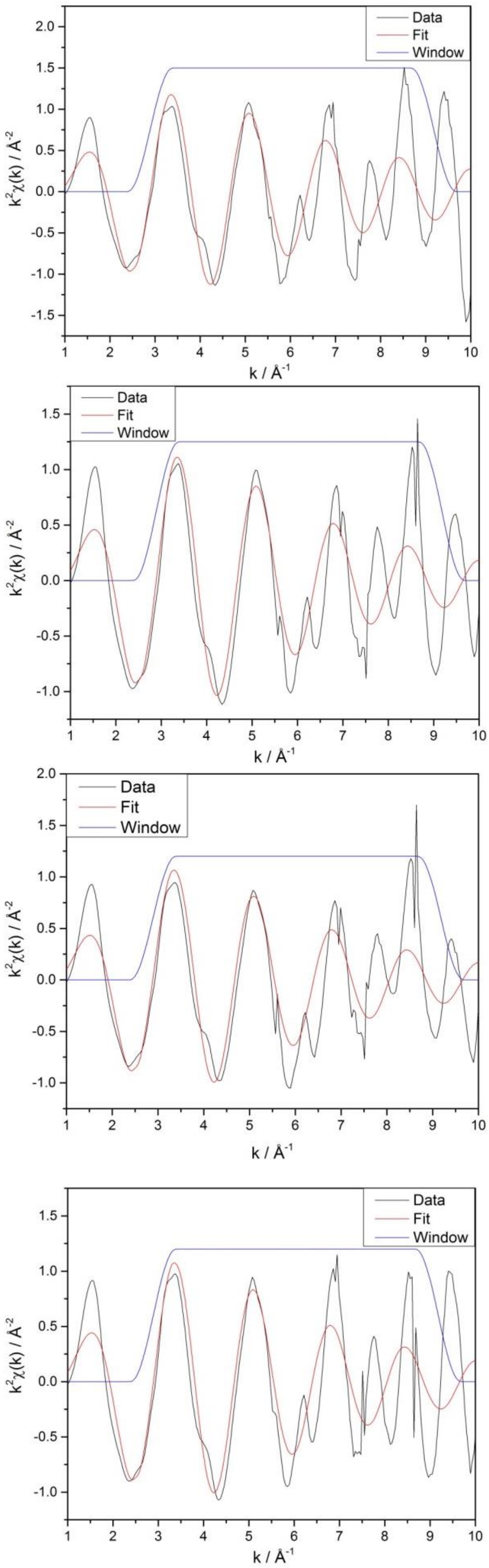

Figure S8: A comparison of the k2χ(k) data and fit: Top Ceria NIST, 2nd HSA Ceria, 3rd Ceria prepared from Ce (III) precursor and bottom Ceria prepared from Ce (IV) precursor.

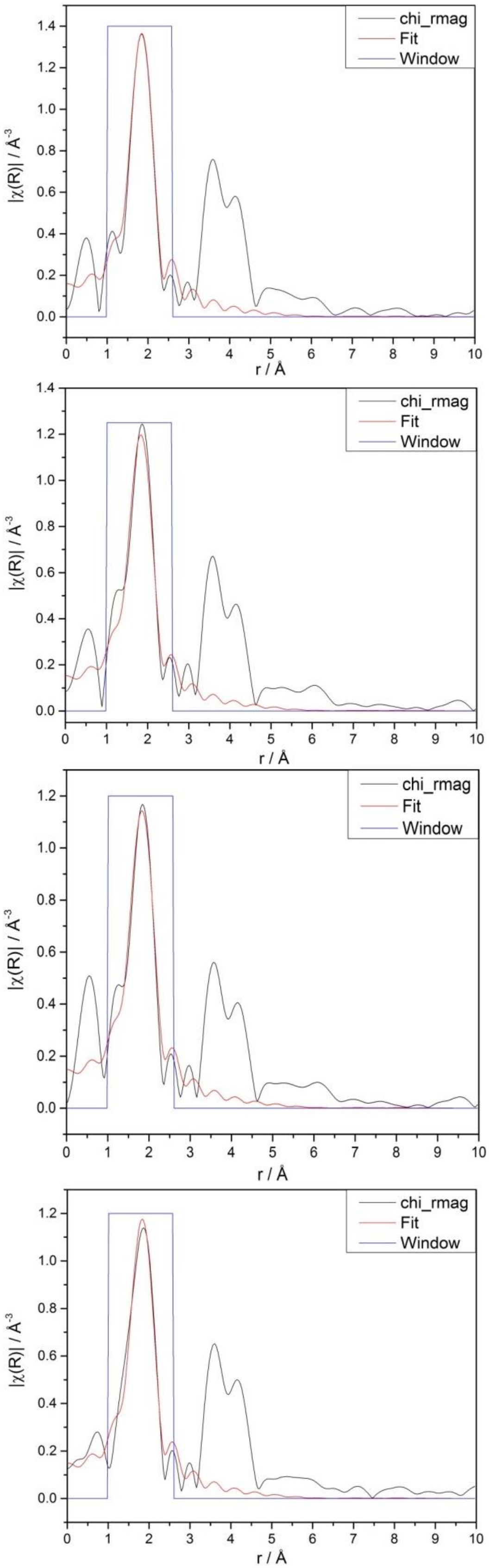

Figure S9: A comparison of the |χ(R)| data and fit: Top Ceria NIST, 2nd HSA Ceria, 3rd Ceria prepared from Ce (III) precursor and bottom Ceria prepared from Ce (IV) precursor.

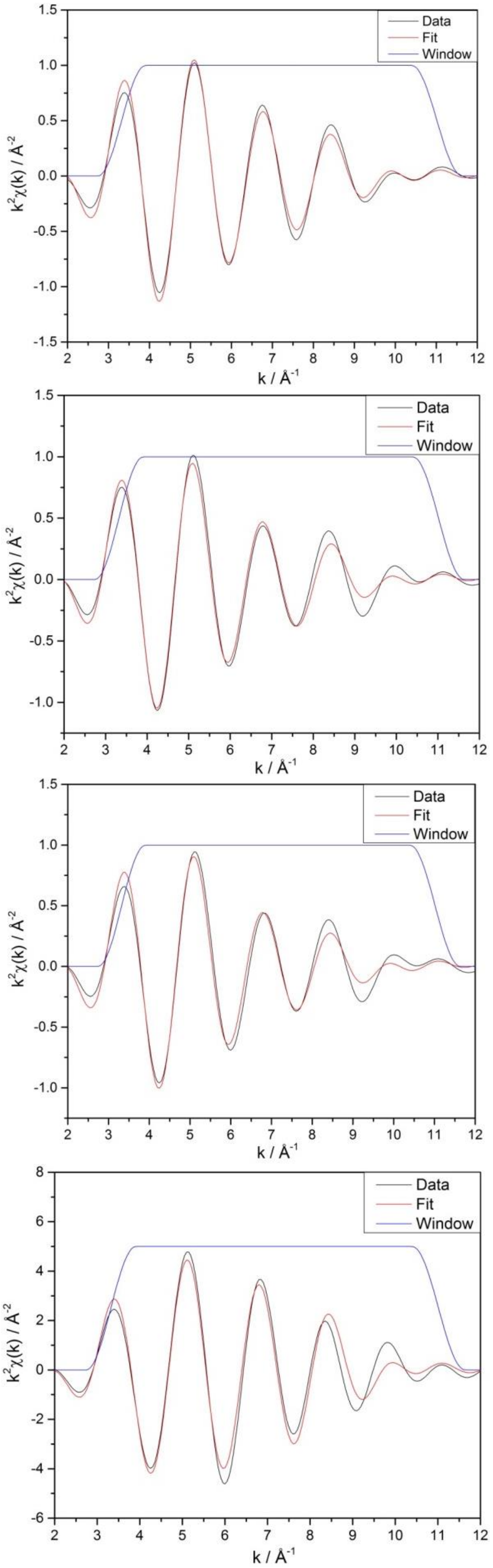

Figure S10: A comparison of the Re[χ(q)] data and fit: Top Ceria NIST, 2nd HSA Ceria, 3rd Ceria prepared from Ce (III) precursor and bottom Ceria prepared from Ce (IV) precursor.

Appendix for Chapter 4

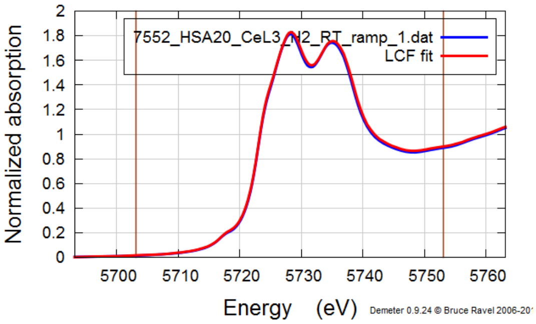

A

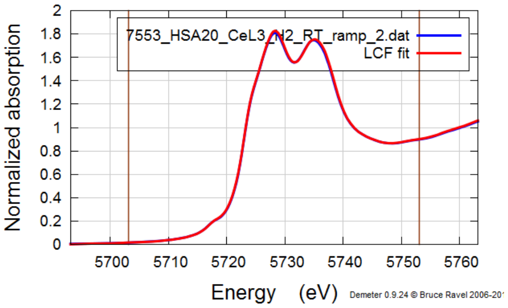

B

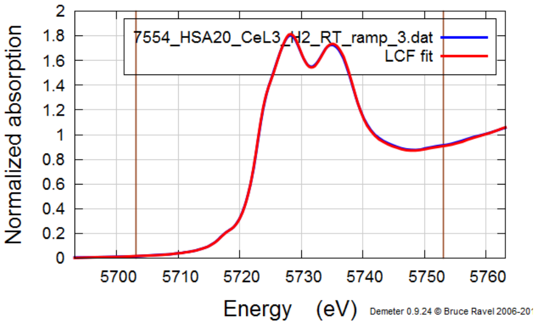

C

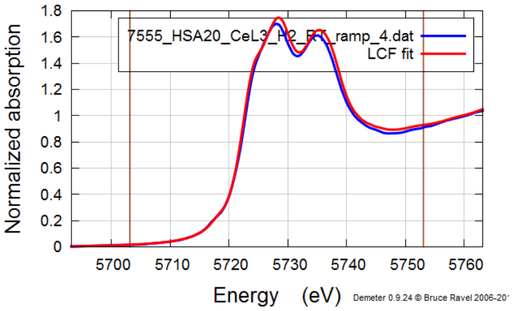

D

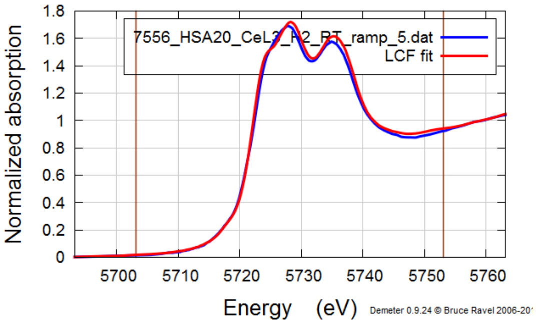

E

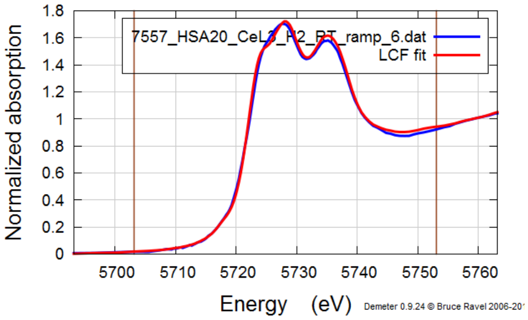

F

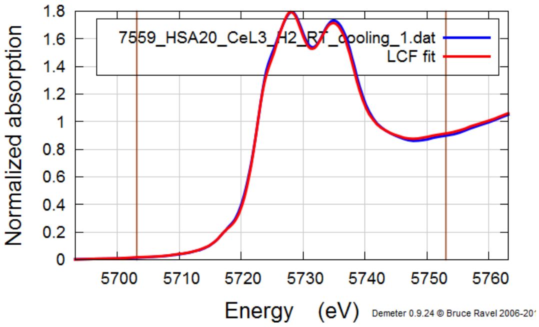

G

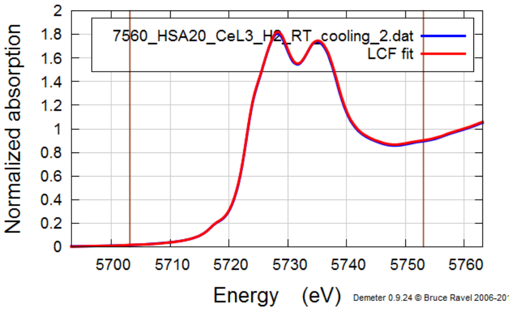

H

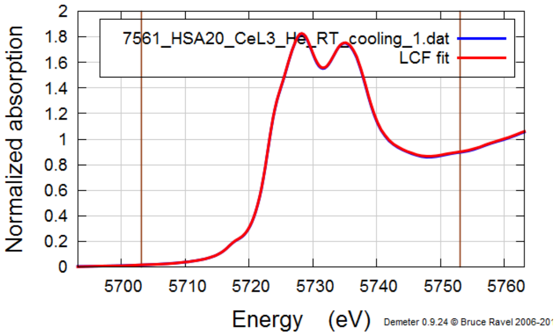

Figure S1a: Comparison of the Observed XANES spectra and Linear Combination Fitting (LCF) for the pure High Surface area support for varying temperatures (for the Ce L3-edge)

- **A. 25°C**
- **B. 118°C**
- **C. 209°C**
- **D. 296°C**
- **E. 387°C**
- **F. 450°C**
- **G. 194°C**
- **H. 100°C**
- **I. 25°C**

I

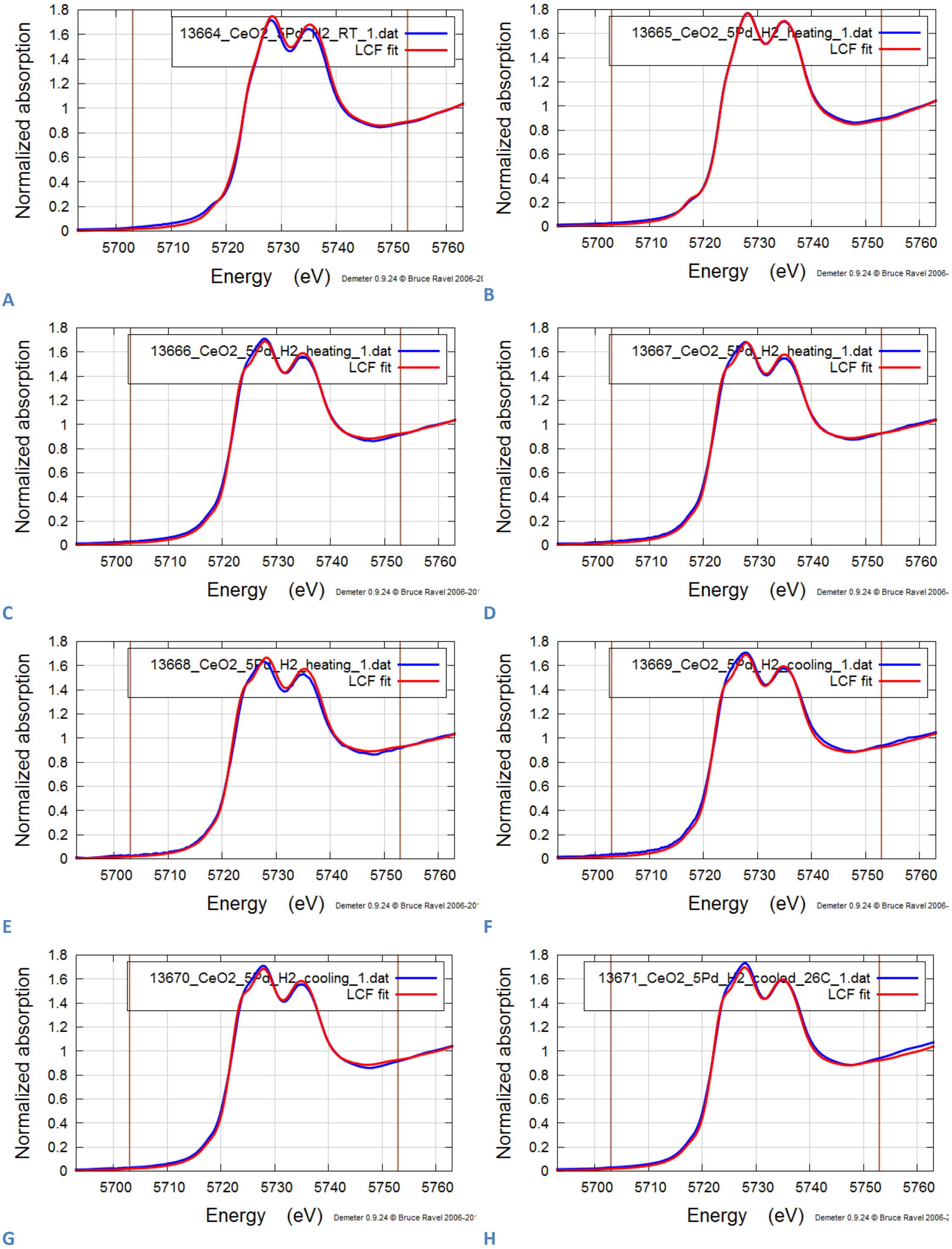

Figure S2a: Comparison of the Observed XANES spectra and LCF for 5 wt% Pd loaded onto a High Surface area support for varying temperatures (for the Ce L3-edge)

- A. 30°C
- B. 43°C
- C. 168°C
- D. 300°C
- E. 409°C
- F. 437°C
- G. 173°C
- H. 26°C

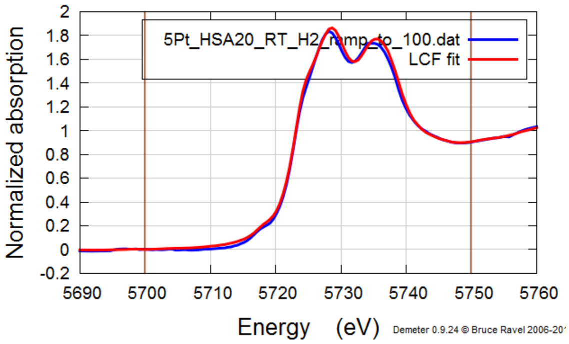
5Pt_HSA20_RT_H2_ramp_to_100.dat
LCF fit
Normalized absorption
Energy (eV)
Demeter 0.9.24 © Bruce Ravel 2006-20
-0.2 0 0.2 0.4 0.6 0.8 1 1.2 1.4 1.6 1.8 2
5690 5700 5710 5720 5730 5740 5750 5760

A

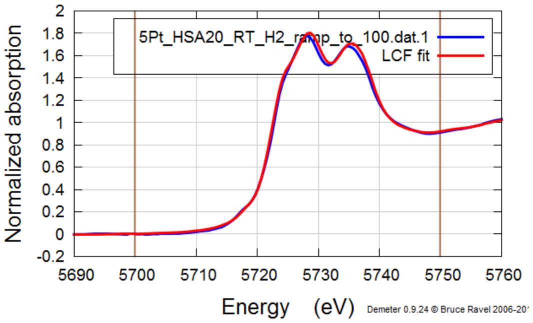
5Pt_HSA20_RT_H2_ramp_to_100.dat.1
LCF fit
Normalized absorption
Energy (eV)
Demeter 0.9.24 © Bruce Ravel 2006-20
-0.2 0 0.2 0.4 0.6 0.8 1 1.2 1.4 1.6 1.8 2
5690 5700 5710 5720 5730 5740 5750 5760

B

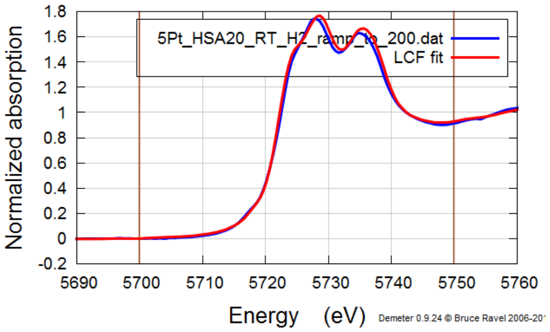
5Pt_HSA20_RT_H2_ramp_to_200.dat
LCF fit
Normalized absorption
Energy (eV)
Demeter 0.9.24 © Bruce Ravel 2006-20
-0.2 0 0.2 0.4 0.6 0.8 1 1.2 1.4 1.6 1.8
5690 5700 5710 5720 5730 5740 5750 5760

C

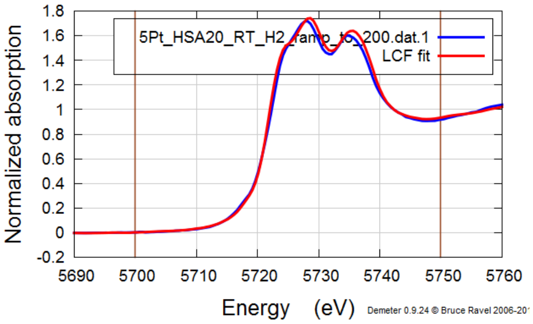
5Pt_HSA20_RT_H2_ramp_to_200.dat.1
LCF fit
Normalized absorption
Energy (eV)
Demeter 0.9.24 © Bruce Ravel 2006-20
-0.2 0 0.2 0.4 0.6 0.8 1 1.2 1.4 1.6 1.8
5690 5700 5710 5720 5730 5740 5750 5760

D

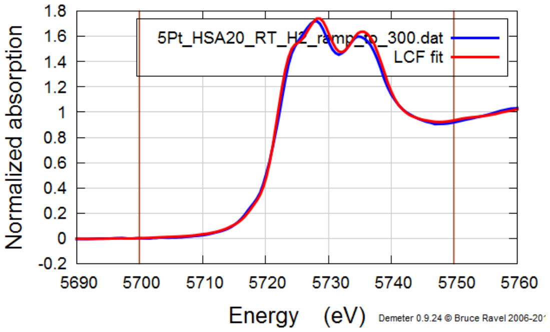
5Pt_HSA20_RT_H2_ramp_to_300.dat
LCF fit
Normalized absorption
Energy (eV)
Demeter 0.9.24 © Bruce Ravel 2006-20
-0.2 0 0.2 0.4 0.6 0.8 1 1.2 1.4 1.6 1.8
5690 5700 5710 5720 5730 5740 5750 5760

E

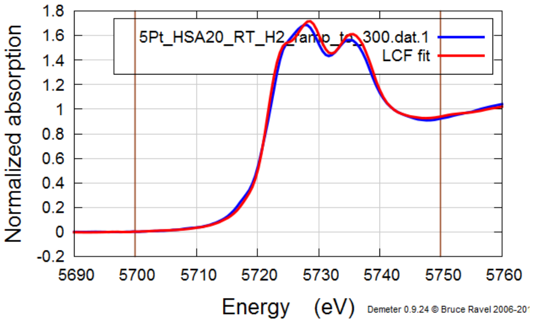
5Pt_HSA20_RT_H2_ramp_to_300.dat.1
LCF fit
Normalized absorption
Energy (eV)
Demeter 0.9.24 © Bruce Ravel 2006-20
-0.2 0 0.2 0.4 0.6 0.8 1 1.2 1.4 1.6 1.8
5690 5700 5710 5720 5730 5740 5750 5760

F

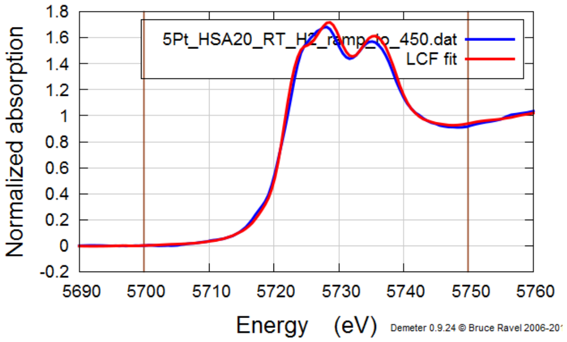
5Pt_HSA20_RT_H2_ramp_to_450.dat
LCF fit
Normalized absorption
Energy (eV)
Demeter 0.9.24 © Bruce Ravel 2006-20
-0.2 0 0.2 0.4 0.6 0.8 1 1.2 1.4 1.6 1.8
5690 5700 5710 5720 5730 5740 5750 5760

G

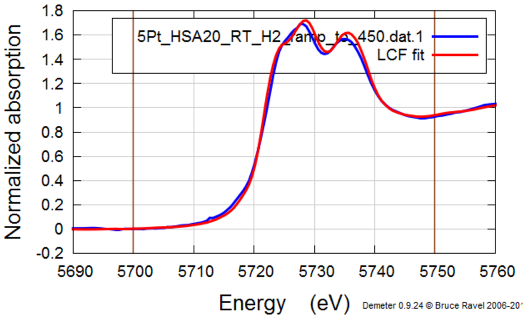
5Pt_HSA20_RT_H2_ramp_to_450.dat.1
LCF fit
Normalized absorption
Energy (eV)
Demeter 0.9.24 © Bruce Ravel 2006-20
-0.2 0 0.2 0.4 0.6 0.8 1 1.2 1.4 1.6 1.8
5690 5700 5710 5720 5730 5740 5750 5760

H

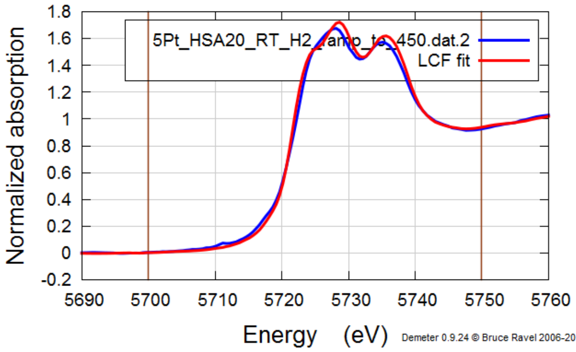
5Pt_HSA20_RT_H2_ramp_to_450.dat.2
LCF fit
Normalized absorption
Energy (eV)
Demeter 0.9.24 © Bruce Ravel 2006-20
-0.2 0 0.2 0.4 0.6 0.8 1 1.2 1.4 1.6 1.8
5690 5700 5710 5720 5730 5740 5750 5760

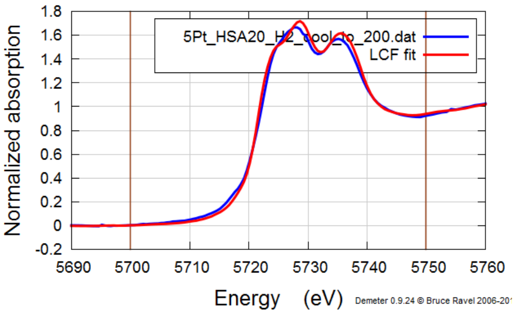
5Pt_HSA20_H2_cool_to_200.dat
LCF fit
Normalized absorption
Energy (eV)
Demeter 0.9.24 © Bruce Ravel 2006-20
-0.2 0 0.2 0.4 0.6 0.8 1 1.2 1.4 1.6 1.8
5690 5700 5710 5720 5730 5740 5750 5760

J

I

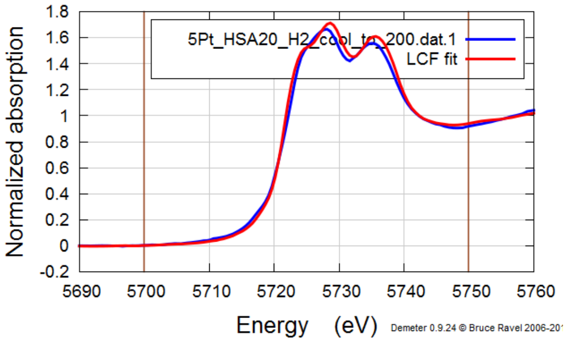

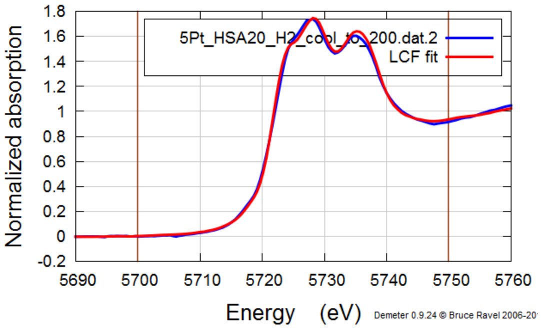

K

L

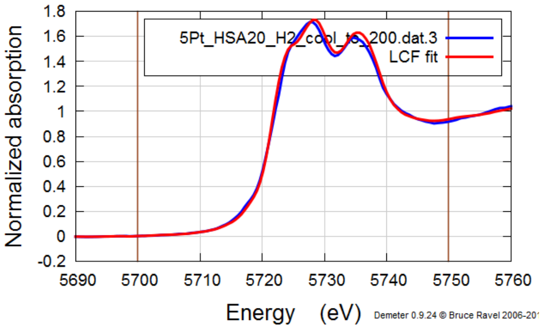

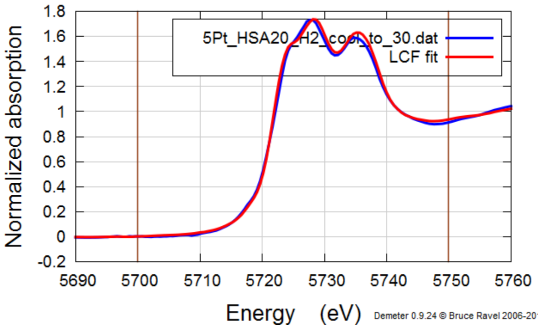

M

N

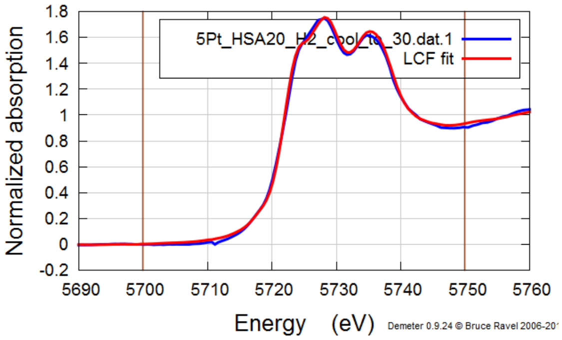

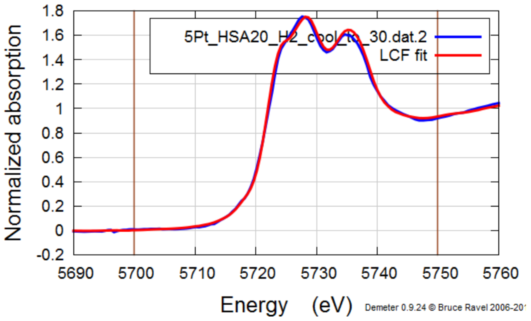

O

P

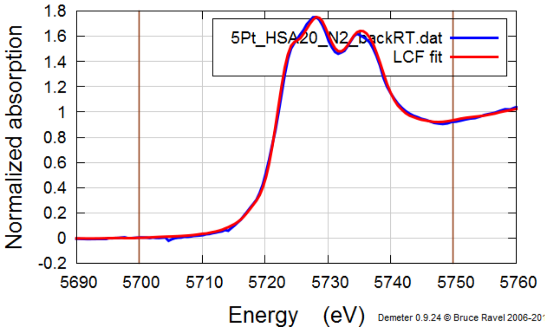

Q

Figure S3a: Comparison of the Observed XANES spectra and LCF for 5 wt% Pt loaded onto a High Surface area support for varying temperatures (for the Ce L3-edge)

- **A.** 35°C
- **B.** 100°C
- **C.** 108°C
- **D.** 200°C
- **E.** 210°C
- **F.** 300°C
- **G.** 305°C
- **H.** 415°C
- **I.** 450°C
- **J.** 438°C
- **K.** 341°C
- **L.** 200°C
- **M.** 200°C
- **N.** 178°C
- **O.** 85°C
- **P.** 30°C
- **Q.** 30°C (Nitrogen)

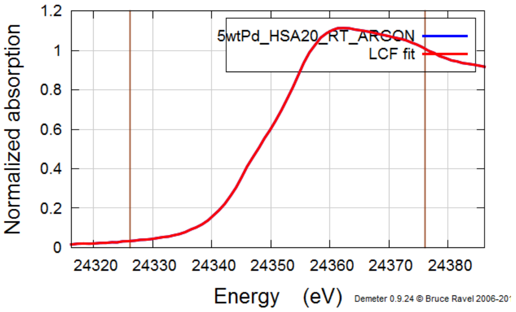

Normalized absorption
0
0.2
0.4
0.6
0.8
1
1.2
24320
24330
24340
24350
24360
24370
24380
Energy (eV)
5wtPd_HSA20_RT_ARGON
LCF fit
Demeter 0.9.24 © Bruce Ravel 2006-20

A

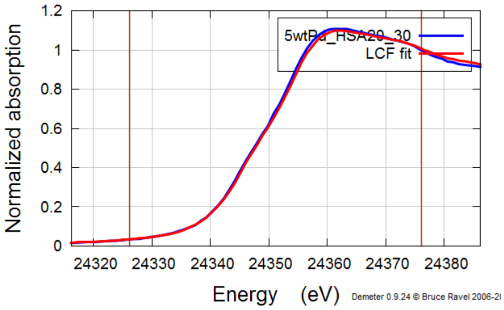

Normalized absorption
0
0.2
0.4
0.6
0.8
1
1.2
24320
24330
24340
24350
24360
24370
24380
Energy (eV)
5wtPd_HSA20_30
LCF fit
Demeter 0.9.24 © Bruce Ravel 2006-20

B

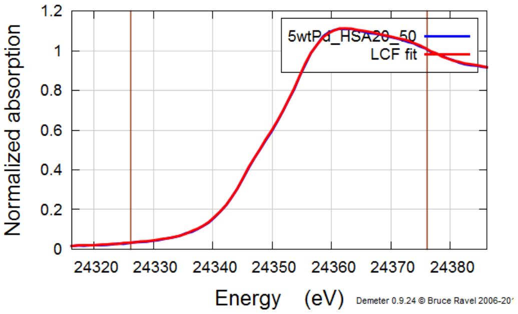

Normalized absorption
0
0.2
0.4
0.6
0.8
1
1.2
24320
24330
24340
24350
24360
24370
24380
Energy (eV)
5wtPd_HSA20_50
LCF fit
Demeter 0.9.24 © Bruce Ravel 2006-20

C

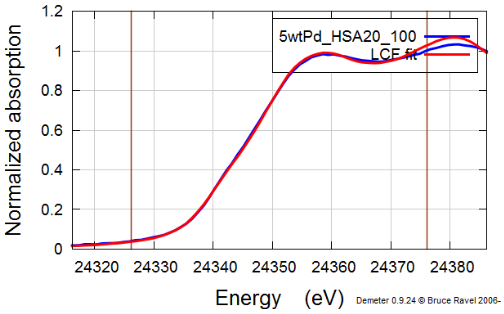

Normalized absorption
0
0.2
0.4
0.6
0.8
1
1.2
24320
24330
24340
24350
24360
24370
24380
Energy (eV)
5wtPd_HSA20_100
LCF fit
Demeter 0.9.24 © Bruce Ravel 2006-

D

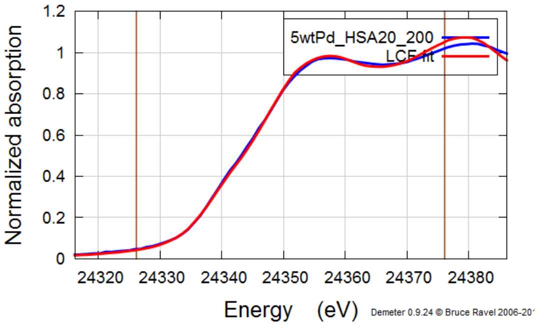

Normalized absorption
0
0.2
0.4
0.6
0.8
1
1.2
24320
24330
24340
24350
24360
24370
24380
Energy (eV)
5wtPd_HSA20_200
LCF fit
Demeter 0.9.24 © Bruce Ravel 2006-20

E

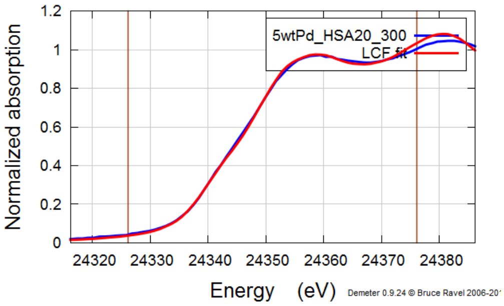

Normalized absorption
0
0.2
0.4
0.6
0.8
1
1.2
24320
24330
24340
24350
24360
24370
24380
Energy (eV)
5wtPd_HSA20_300
LCF fit
Demeter 0.9.24 © Bruce Ravel 2006-20

F

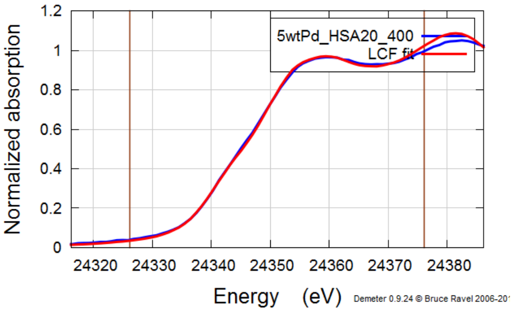

Normalized absorption
0
0.2
0.4
0.6
0.8
1
1.2
24320
24330
24340
24350
24360
24370
24380
Energy (eV)
5wtPd_HSA20_400
LCF fit
Demeter 0.9.24 © Bruce Ravel 2006-20

G

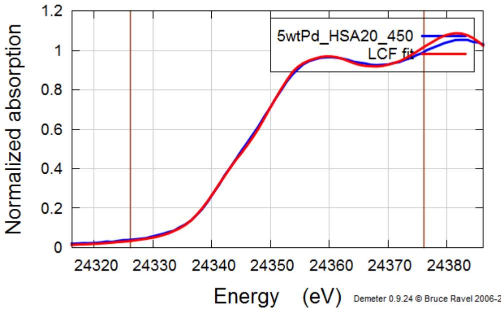

Normalized absorption
0
0.2
0.4
0.6
0.8
1
1.2
24320
24330
24340
24350
24360
24370
24380
Energy (eV)
5wtPd_HSA20_450
LCF fit
Demeter 0.9.24 © Bruce Ravel 2006-2

H

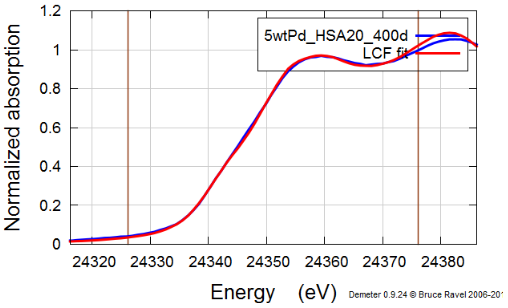

Normalized absorption
0
0.2
0.4
0.6
0.8
1
1.2
24320
24330
24340
24350
24360
24370
24380
Energy (eV)
5wtPd_HSA20_400d
LCF fit
Demeter 0.9.24 © Bruce Ravel 2006-20

I

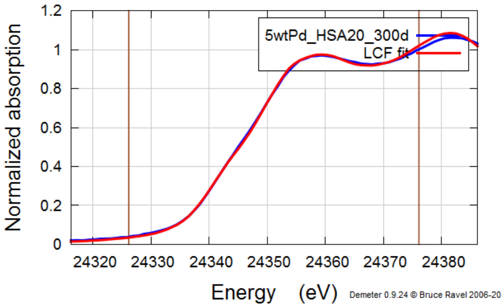

Normalized absorption
0
0.2
0.4
0.6
0.8
1
1.2
24320
24330
24340
24350
24360
24370
24380
Energy (eV)
5wtPd_HSA20_300d
LCF fit
Demeter 0.9.24 © Bruce Ravel 2006-20

J

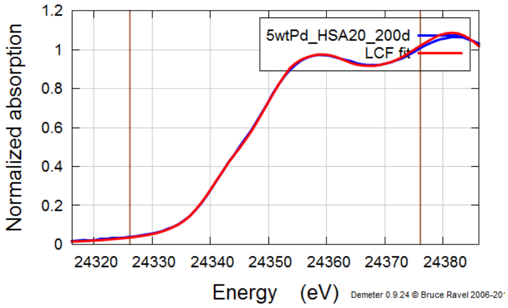

K

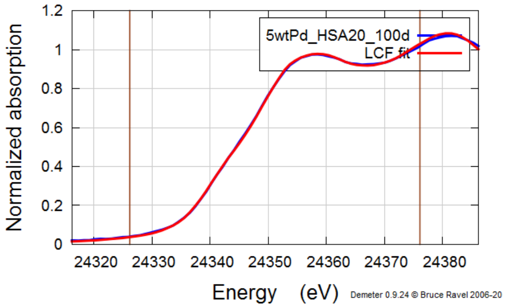

L

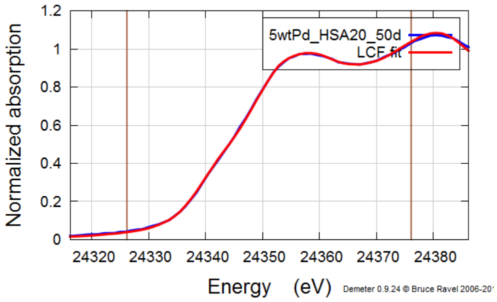

M

Figure S4a: Comparison of the Observed XANES spectra and LCF for 5 wt% Pd loaded onto a High Surface area support for varying temperatures (for the Pd K-edge)

- **A. 30°C (ARGON)**
- **B. 30°C (H_2/N_2)**
- **C. 50°C**
- **D. 100°C**
- **E. 200°C**
- **F. 300°C**
- **G. 400°C**
- **H. 450°C**
- **I. 400°C**
- **J. 300°C**
- **K. 200°C**
- **L. 100°C**
- **M. 50°C**

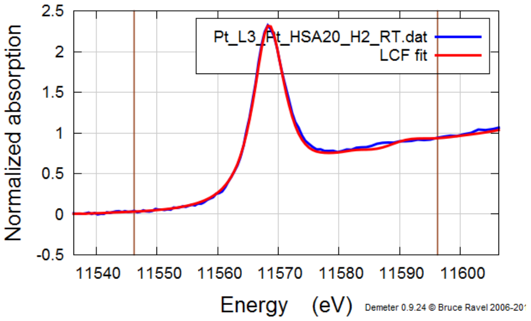

A

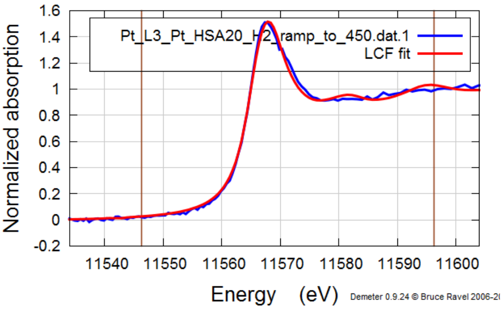

B

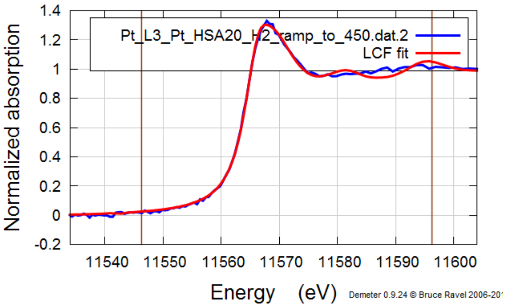

C

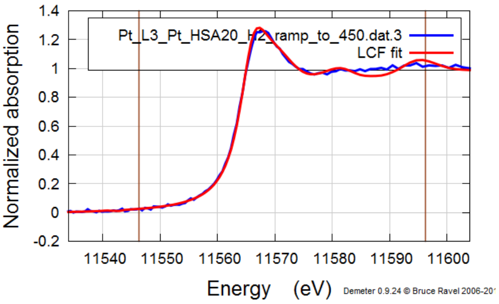

D

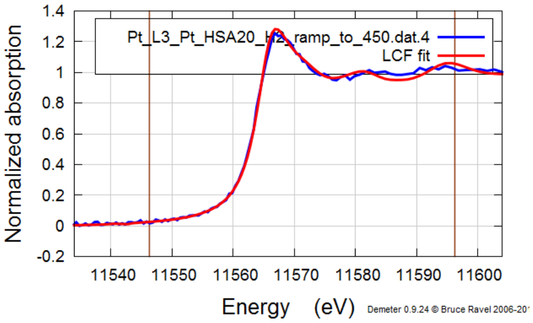

E

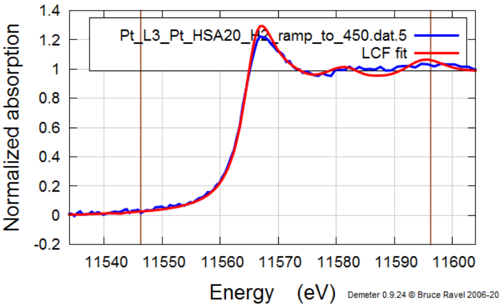

F

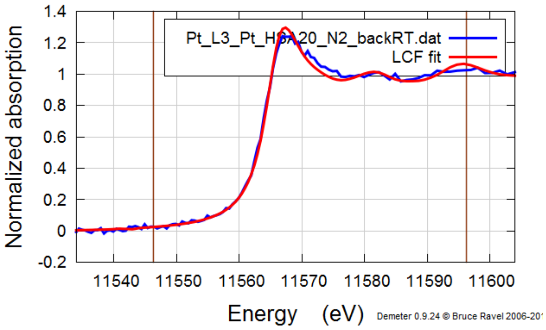

G

Figure S5a: Comparison of the Observed XANES spectra and LCF for 5 wt% Pt loaded onto a High Surface area support for varying temperatures (for the Pt L3-edge)

- **A.** 30°C
- **B.** 140°C
- **C.** 211°C
- **D.** 284°C
- **E.** 356°C
- **F.** 450°C
- **G.** 30°C (N_2)

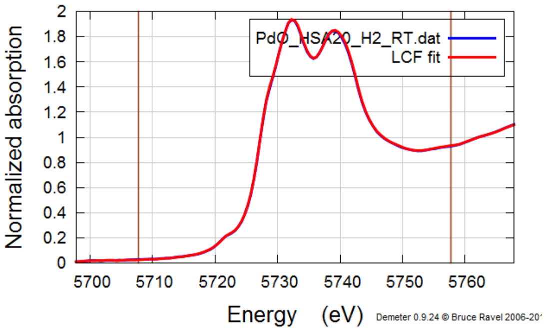
PdO_HSA20_H2_RT.dat
LCF fit
Normalized absorption
0
0.2
0.4
0.6
0.8
1
1.2
1.4
1.6
1.8
2
5700
5710
5720
5730
5740
5750
5760
Energy (eV)
Demeter 0.9.24 © Bruce Ravel 2006-20

A

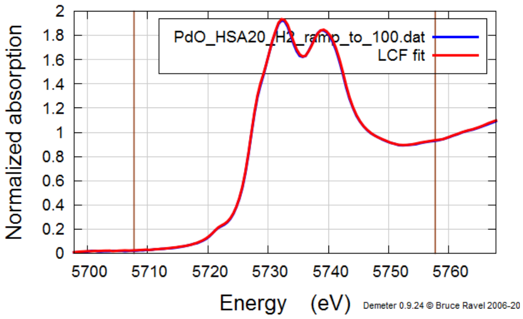
PdO_HSA20_H2_ramp_to_100.dat
LCF fit
Normalized absorption
0
0.2
0.4
0.6
0.8
1
1.2
1.4
1.6
1.8
2
5700
5710
5720
5730
5740
5750
5760
Energy (eV)
Demeter 0.9.24 © Bruce Ravel 2006-20

B

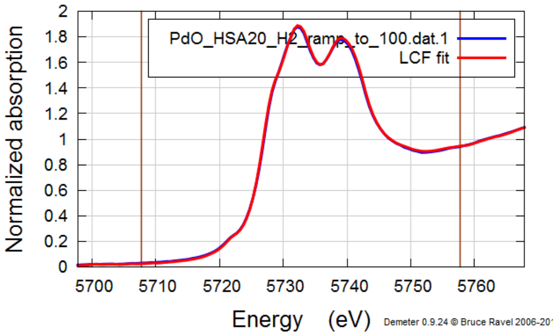
PdO_HSA20_H2_ramp_to_100.dat.1
LCF fit
Normalized absorption
0
0.2
0.4
0.6
0.8
1
1.2
1.4
1.6
1.8
2
5700
5710
5720
5730
5740
5750
5760
Energy (eV)
Demeter 0.9.24 © Bruce Ravel 2006-20

C

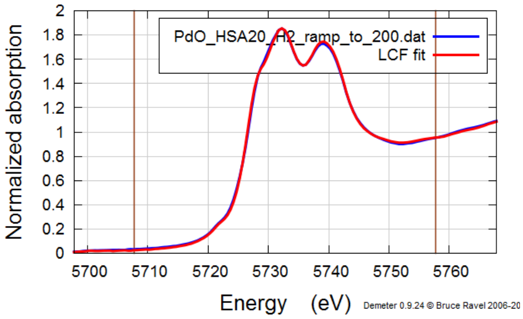
PdO_HSA20_H2_ramp_to_200.dat
LCF fit
Normalized absorption
0
0.2
0.4
0.6
0.8
1
1.2
1.4
1.6
1.8
2
5700
5710
5720
5730
5740
5750
5760
Energy (eV)
Demeter 0.9.24 © Bruce Ravel 2006-20

D

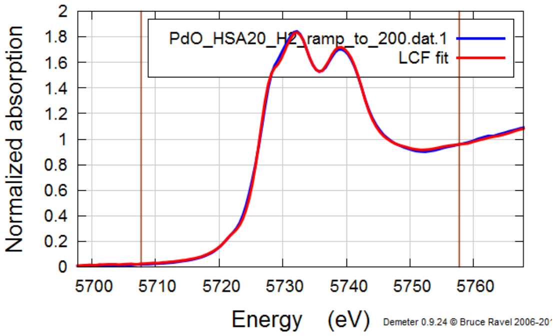
PdO_HSA20_H2_ramp_to_200.dat.1
LCF fit
Normalized absorption
0
0.2
0.4
0.6
0.8
1
1.2
1.4
1.6
1.8
2
5700
5710
5720
5730
5740
5750
5760
Energy (eV)
Demeter 0.9.24 © Bruce Ravel 2006-20

E

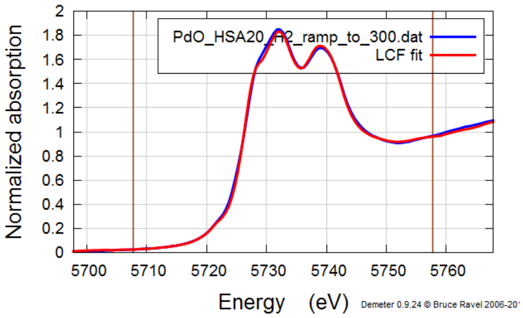
PdO_HSA20_H2_ramp_to_300.dat
LCF fit
Normalized absorption
0
0.2
0.4
0.6
0.8
1
1.2
1.4
1.6
1.8
2
5700
5710
5720
5730
5740
5750
5760
Energy (eV)
Demeter 0.9.24 © Bruce Ravel 2006-20

F

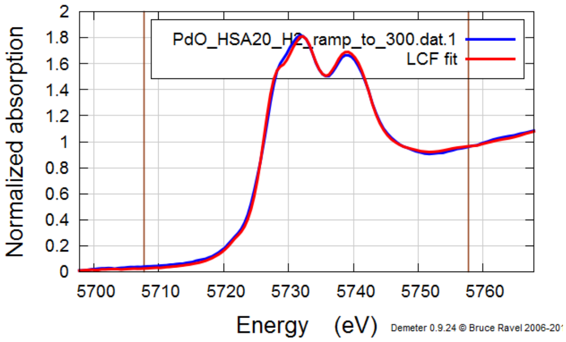
PdO_HSA20_H2_ramp_to_300.dat.1
LCF fit
Normalized absorption
0
0.2
0.4
0.6
0.8
1
1.2
1.4
1.6
1.8
2
5700
5710
5720
5730
5740
5750
5760
Energy (eV)
Demeter 0.9.24 © Bruce Ravel 2006-20

G

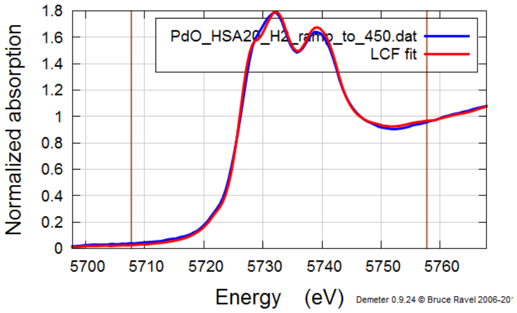
PdO_HSA20_H2_ramp_to_450.dat
LCF fit
Normalized absorption
0
0.2
0.4
0.6
0.8
1
1.2
1.4
1.6
1.8
5700
5710
5720
5730
5740
5750
5760
Energy (eV)
Demeter 0.9.24 © Bruce Ravel 2006-20

H

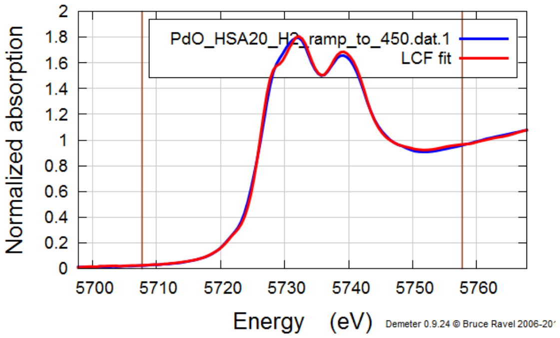
PdO_HSA20_H2_ramp_to_450.dat.1
LCF fit
Normalized absorption
0
0.2
0.4
0.6
0.8
1
1.2
1.4
1.6
1.8
2
5700
5710
5720
5730
5740
5750
5760
Energy (eV)
Demeter 0.9.24 © Bruce Ravel 2006-20

I

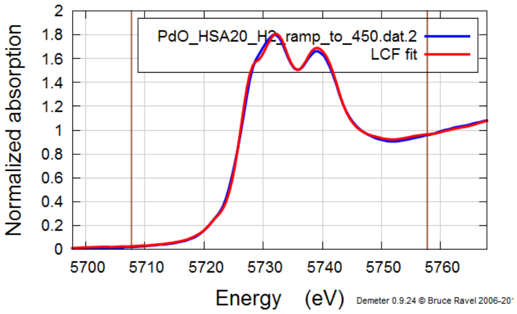
PdO_HSA20_H2_ramp_to_450.dat.2
LCF fit
Normalized absorption
0
0.2
0.4
0.6
0.8
1
1.2
1.4
1.6
1.8
2
5700
5710
5720
5730
5740
5750
5760
Energy (eV)
Demeter 0.9.24 © Bruce Ravel 2006-20

J

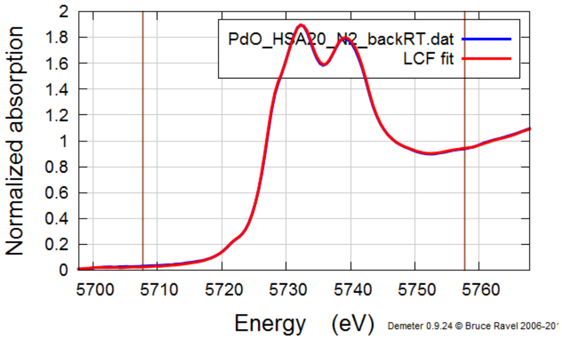

K

Figure S6a: Comparison of the Observed XANES spectra and LCF for the physical mixture of PdO and a High Surface area support for varying temperatures (for the Ce L3-edge)

A. 30
B. 33
C. 100
D. 110
E. 200
F. 205
G. 300
H. 305
I. 410
J. 450
K. 30 (In Nitrogen)

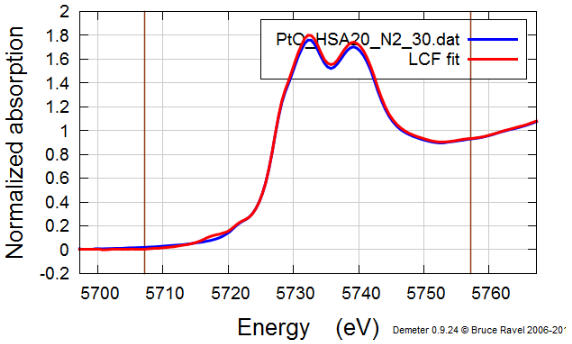
PtO_HSA20_N2_30.dat
LCF fit
Normalized absorption
Energy (eV)
2
1.8
1.6
1.4
1.2
1
0.8
0.6
0.4
0.2
0
-0.2
5700
5710
5720
5730
5740
5750
5760
Demeter 0.9.24 © Bruce Ravel 2006-20

A

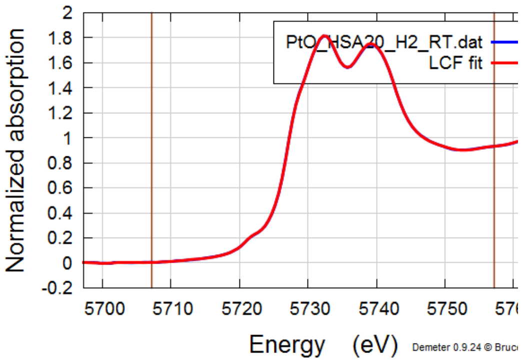
PtO_HSA20_H2_RT.dat
LCF fit
Normalized absorption
Energy (eV)
2
1.8
1.6
1.4
1.2
1
0.8
0.6
0.4
0.2
0
-0.2
5700
5710
5720
5730
5740
5750
57
Demeter 0.9.24 © Bruc

B

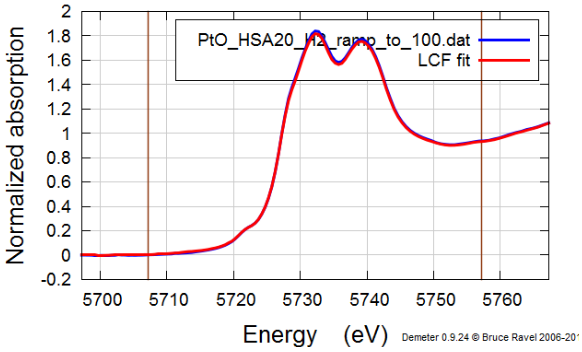
PtO_HSA20_H2_ramp_to_100.dat
LCF fit
Normalized absorption
Energy (eV)
2
1.8
1.6
1.4
1.2
1
0.8
0.6
0.4
0.2
0
-0.2
5700
5710
5720
5730
5740
5750
5760
Demeter 0.9.24 © Bruce Ravel 2006-20

C

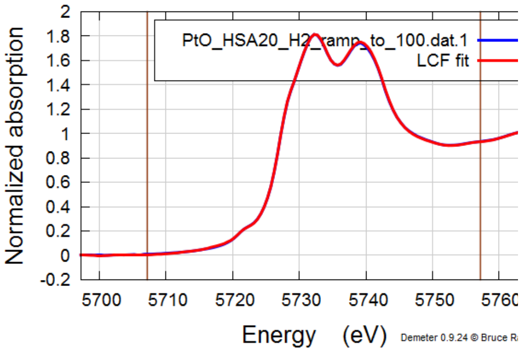
PtO_HSA20_H2_ramp_to_100.dat.1
LCF fit
Normalized absorption
Energy (eV)
2
1.8
1.6
1.4
1.2
1
0.8
0.6
0.4
0.2
0
-0.2
5700
5710
5720
5730
5740
5750
5760
Demeter 0.9.24 © Bruce R

D

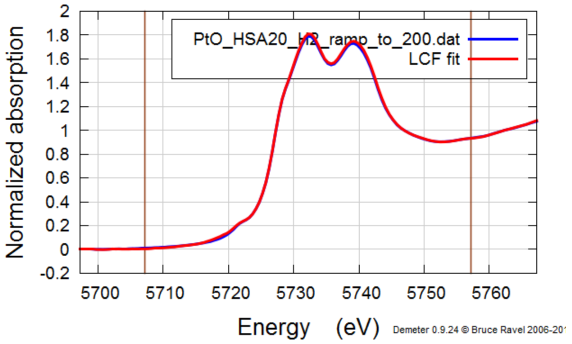
PtO_HSA20_H2_ramp_to_200.dat
LCF fit
Normalized absorption
Energy (eV)
2
1.8
1.6
1.4
1.2
1
0.8
0.6
0.4
0.2
0
-0.2
5700
5710
5720
5730
5740
5750
5760
Demeter 0.9.24 © Bruce Ravel 2006-20

E

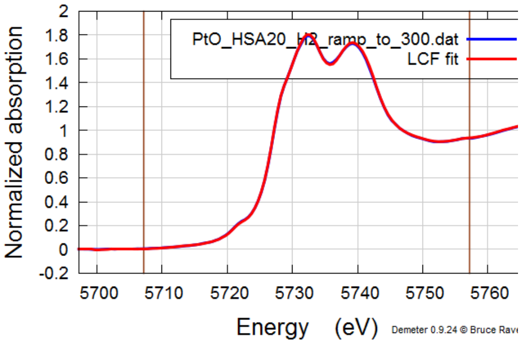
PtO_HSA20_H2_ramp_to_300.dat
LCF fit
Normalized absorption
Energy (eV)
2
1.8
1.6
1.4
1.2
1
0.8
0.6
0.4
0.2
0
-0.2
5700
5710
5720
5730
5740
5750
5760
Demeter 0.9.24 © Bruce Rav

F

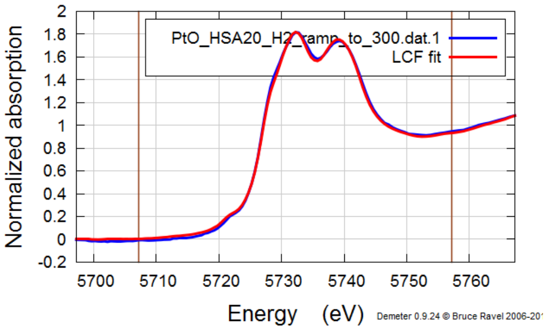
PtO_HSA20_H2_ramp_to_300.dat.1
LCF fit
Normalized absorption
Energy (eV)
2
1.8
1.6
1.4
1.2
1
0.8
0.6
0.4
0.2
0
-0.2
5700
5710
5720
5730
5740
5750
5760
Demeter 0.9.24 © Bruce Ravel 2006-20

G

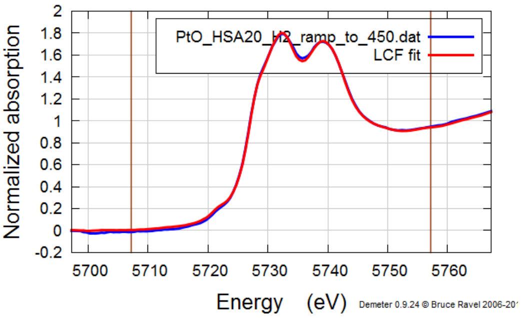
PtO_HSA20_H2_ramp_to_450.dat
LCF fit
Normalized absorption
Energy (eV)
2
1.8
1.6
1.4
1.2
1
0.8
0.6
0.4
0.2
0
-0.2
5700
5710
5720
5730
5740
5750
5760
Demeter 0.9.24 © Bruce Ravel 2006-20

H

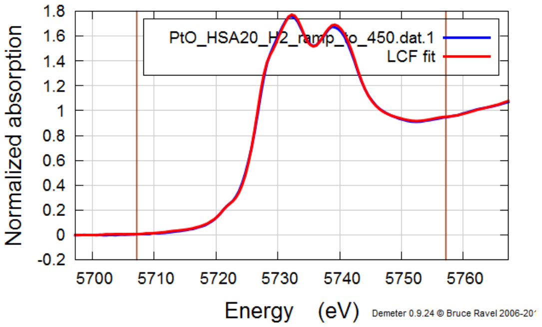
PtO_HSA20_H2_ramp_to_450.dat.1
LCF fit
Normalized absorption
Energy (eV)
1.8
1.6
1.4
1.2
1
0.8
0.6
0.4
0.2
0
-0.2
5700
5710
5720
5730
5740
5750
5760
Demeter 0.9.24 © Bruce Ravel 2006-20

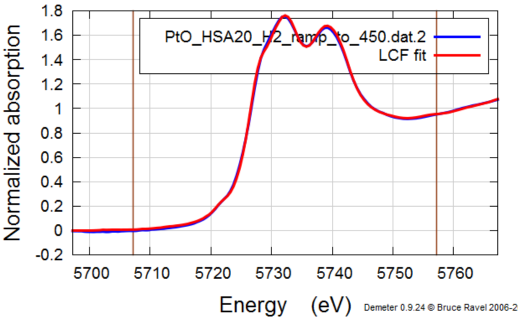
PtO_HSA20_H2_ramp_to_450.dat.2
LCF fit
Normalized absorption
Energy (eV)
1.8
1.6
1.4
1.2
1
0.8
0.6
0.4
0.2
0
-0.2
5700
5710
5720
5730
5740
5750
5760
Demeter 0.9.24 © Bruce Ravel 2006-2

I

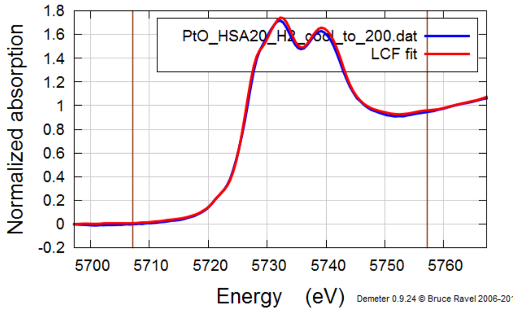

J

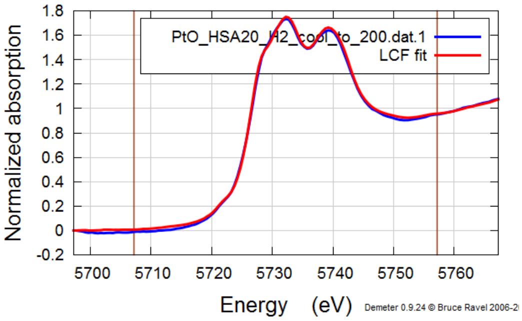

K

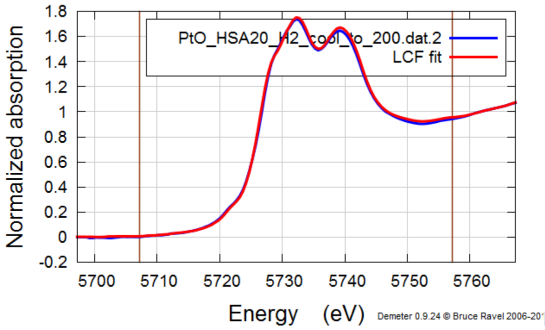

L

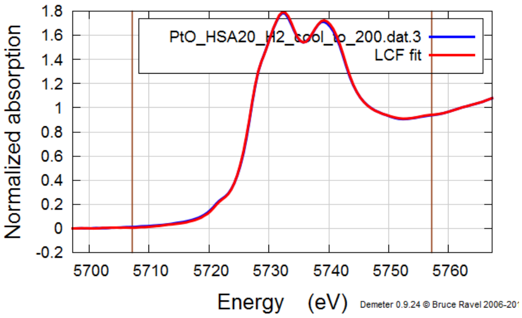

M

N

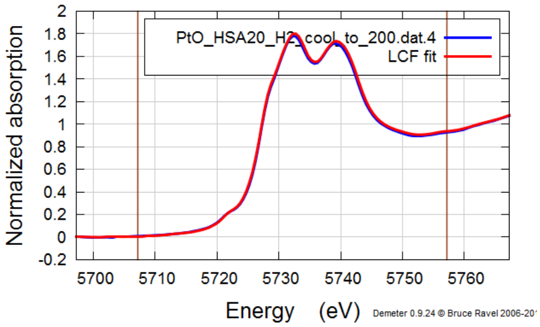

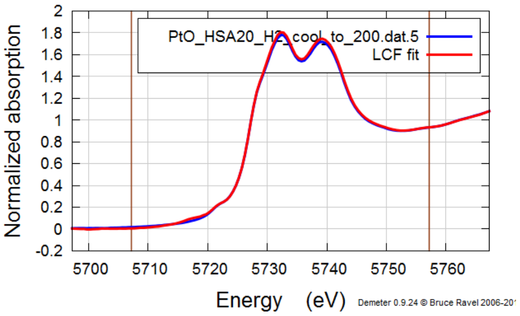

O

P

Figure S7a: Comparison of the Observed XANES spectra and LCF for the physical mixture of PtO_2 and a High Surface area support for varying temperatures (for the Ce L_3-edge)

A. 30
B. 33
C. 100
D. 104
E. 201
F. 205
G. 300
H. 310
I. 386
J. 450
K. 420
L. 318
M. 243
N. 197
O. 75
P. 30 (In Nitrogen)

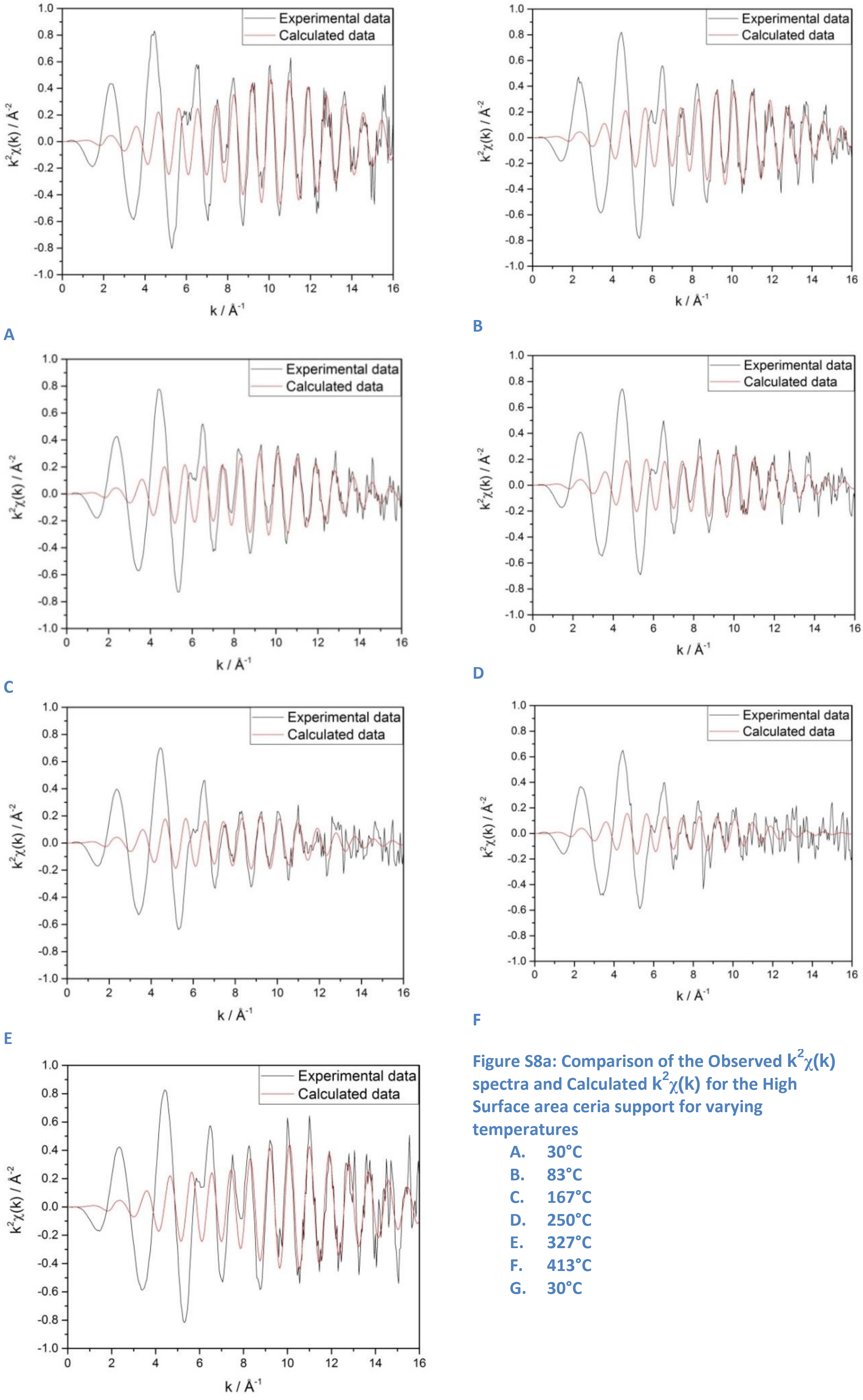

Figure S8a: Comparison of the Observed $k^2\chi(k)$ spectra and Calculated $k^2\chi(k)$ for the High Surface area ceria support for varying temperatures

- **A. 30°C**
- **B. 83°C**
- **C. 167°C**
- **D. 250°C**
- **E. 327°C**
- **F. 413°C**
- **G. 30°C**

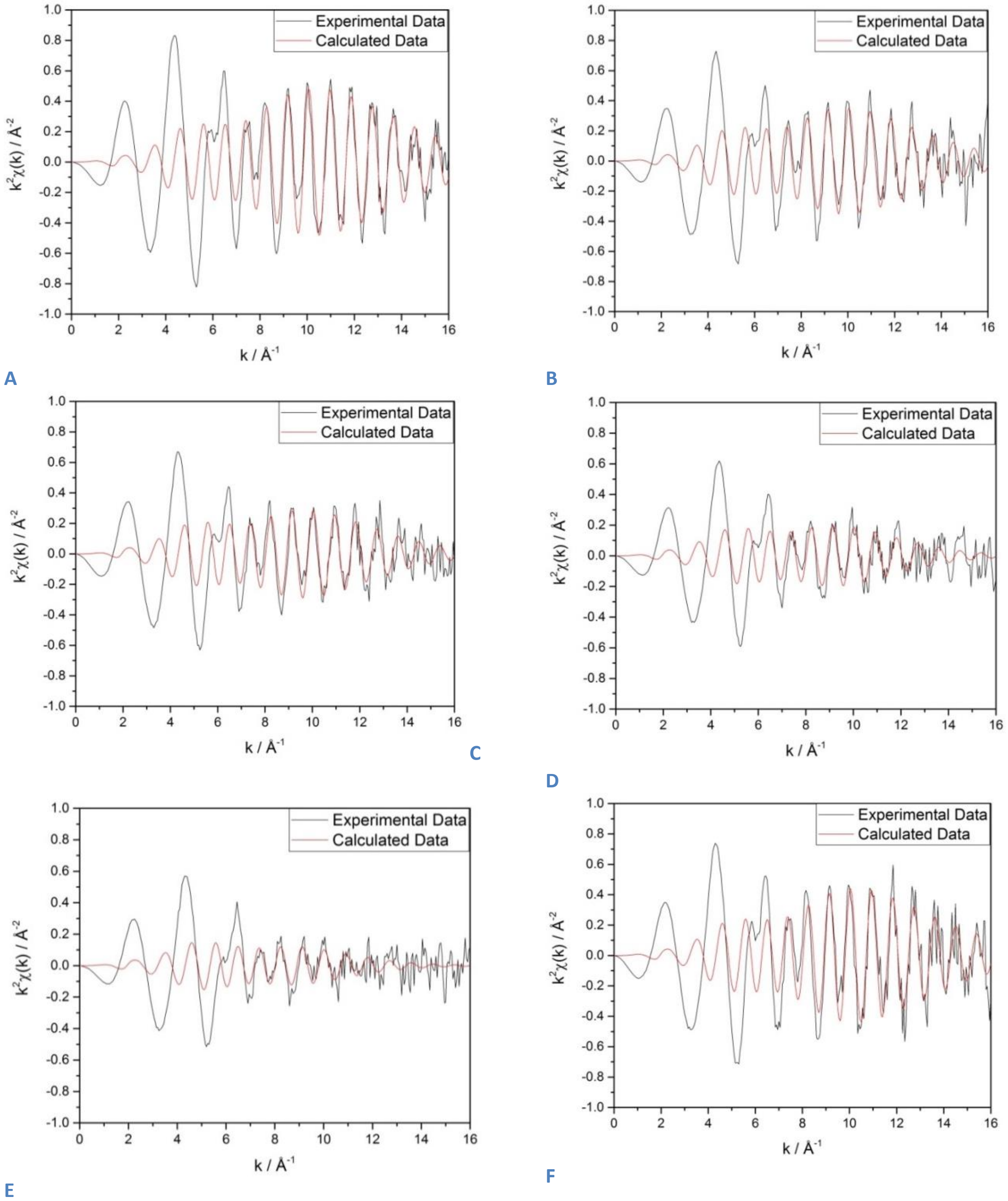

Figure S9a: Comparison of the Observed $k^2\chi(k)$ spectra and Calculated $k^2\chi(k)$ for 5 wt% Pd loaded onto the High Surface area ceria support for varying temperatures

A. 30°C
B. 100°C
C. 200°C
D. 300°C
E. 450°C
F. 30°C

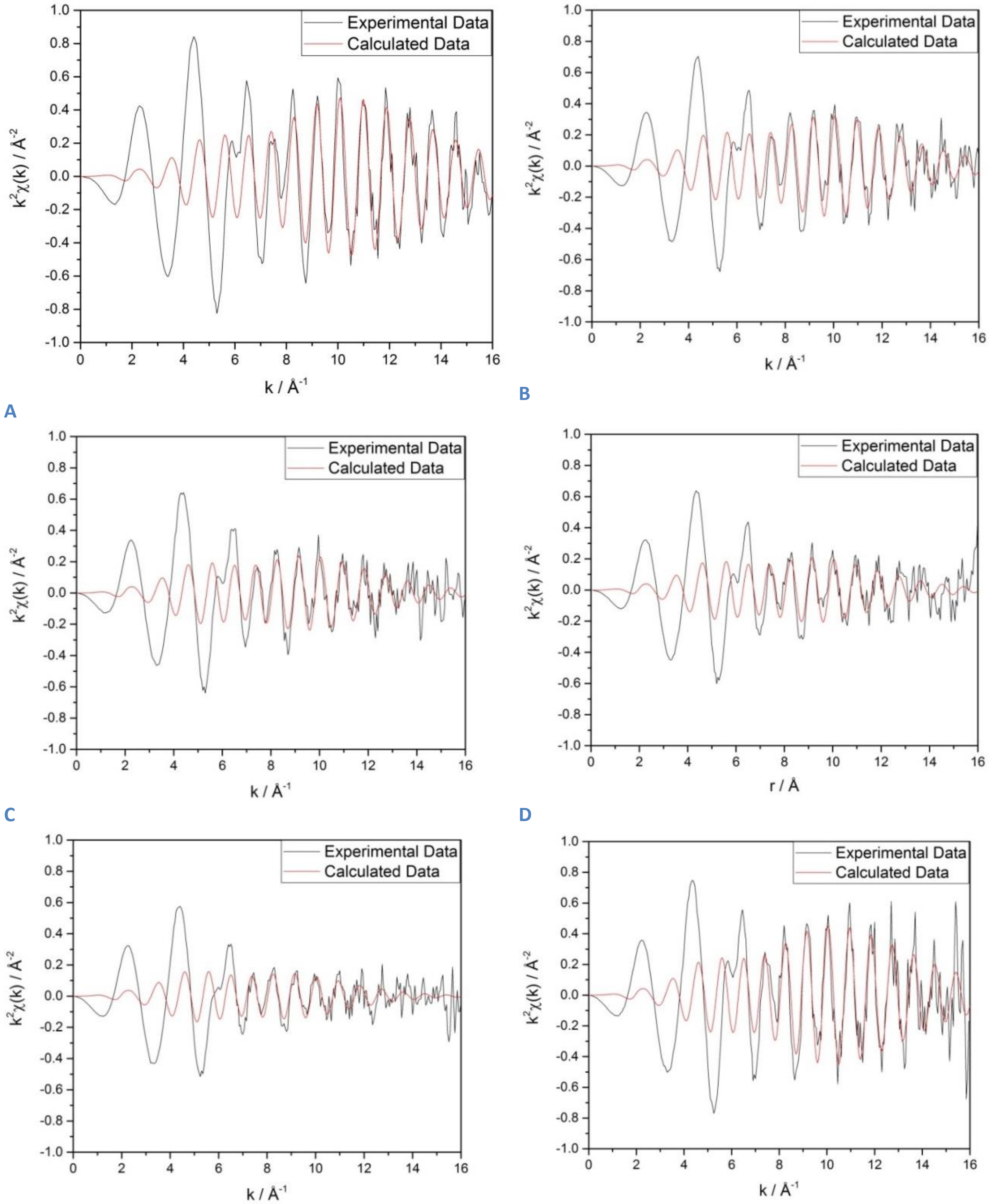

A

B

C

D

E

F

Figure S10a: Comparison of the Observed $k^2\chi(k)$ spectra and Calculated $k^2\chi(k)$ for 5 wt% Pt loaded onto the High Surface area ceria support for varying temperatures

- **A. 30°C**
- **B. 150°C**
- **C. 250°C**
- **D. 350°C**
- **E. 450°C**
- **F. 30°C**

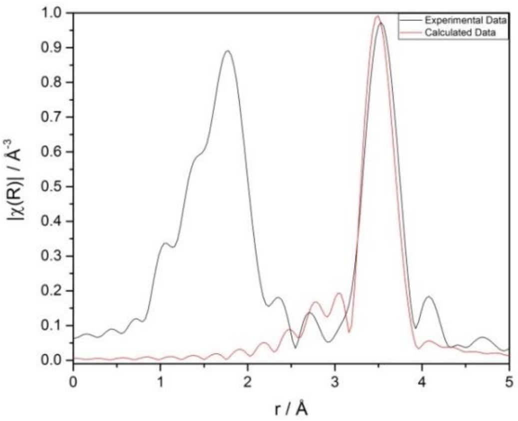

A

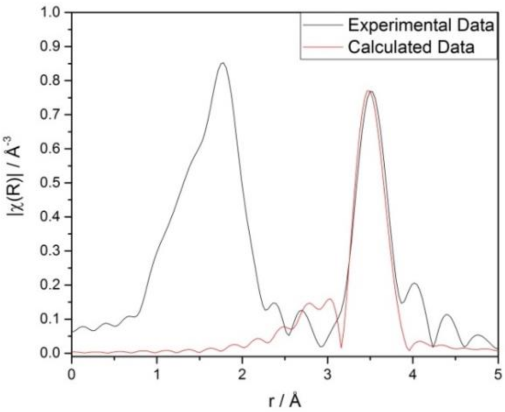

B

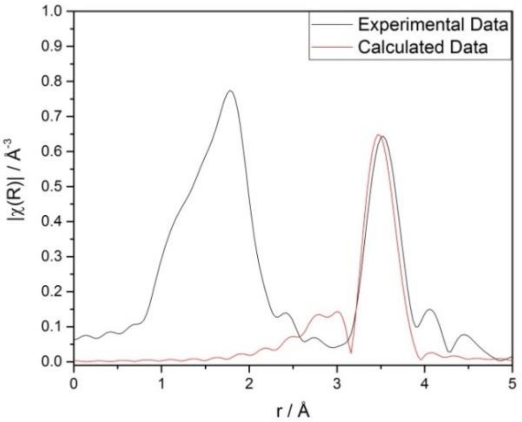

C

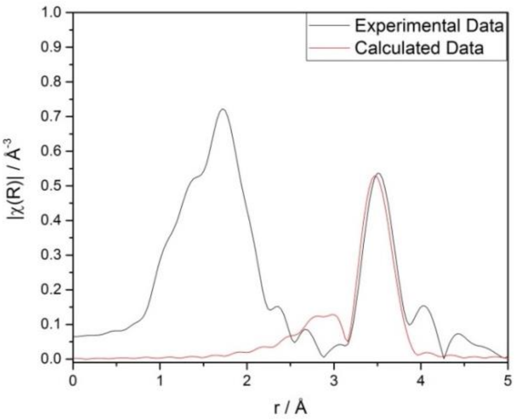

D

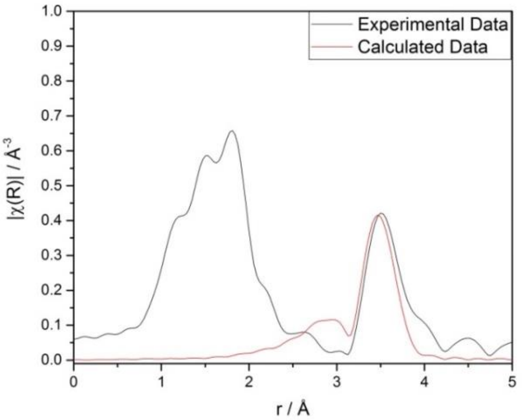

E

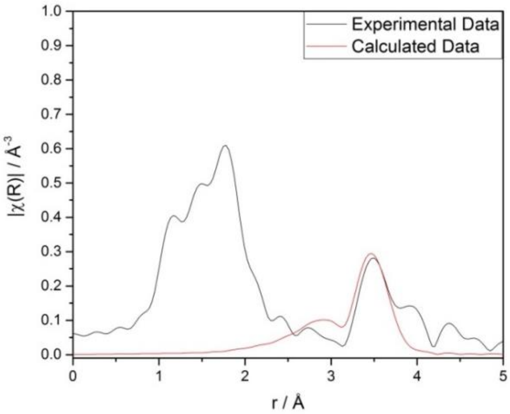

F

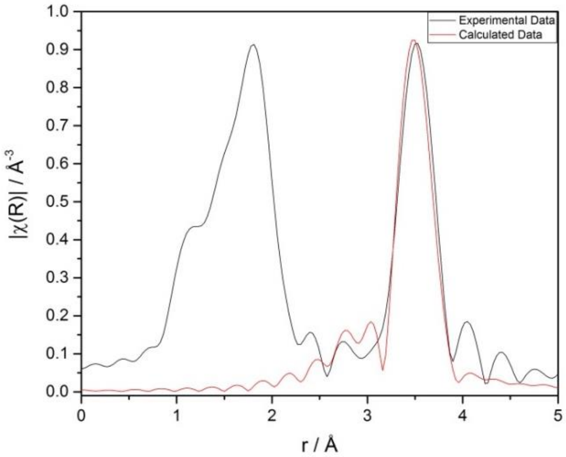

G

Figure S11a: Comparison of the Observed |χ(R)|spectra and Calculated |χ(R)|for the High Surface area ceria support for varying temperatures

A. **30°C**
B. **83°C**
C. **167°C**
D. **250°C**
E. **327°C**
F. **413°C**
G. **30°C**

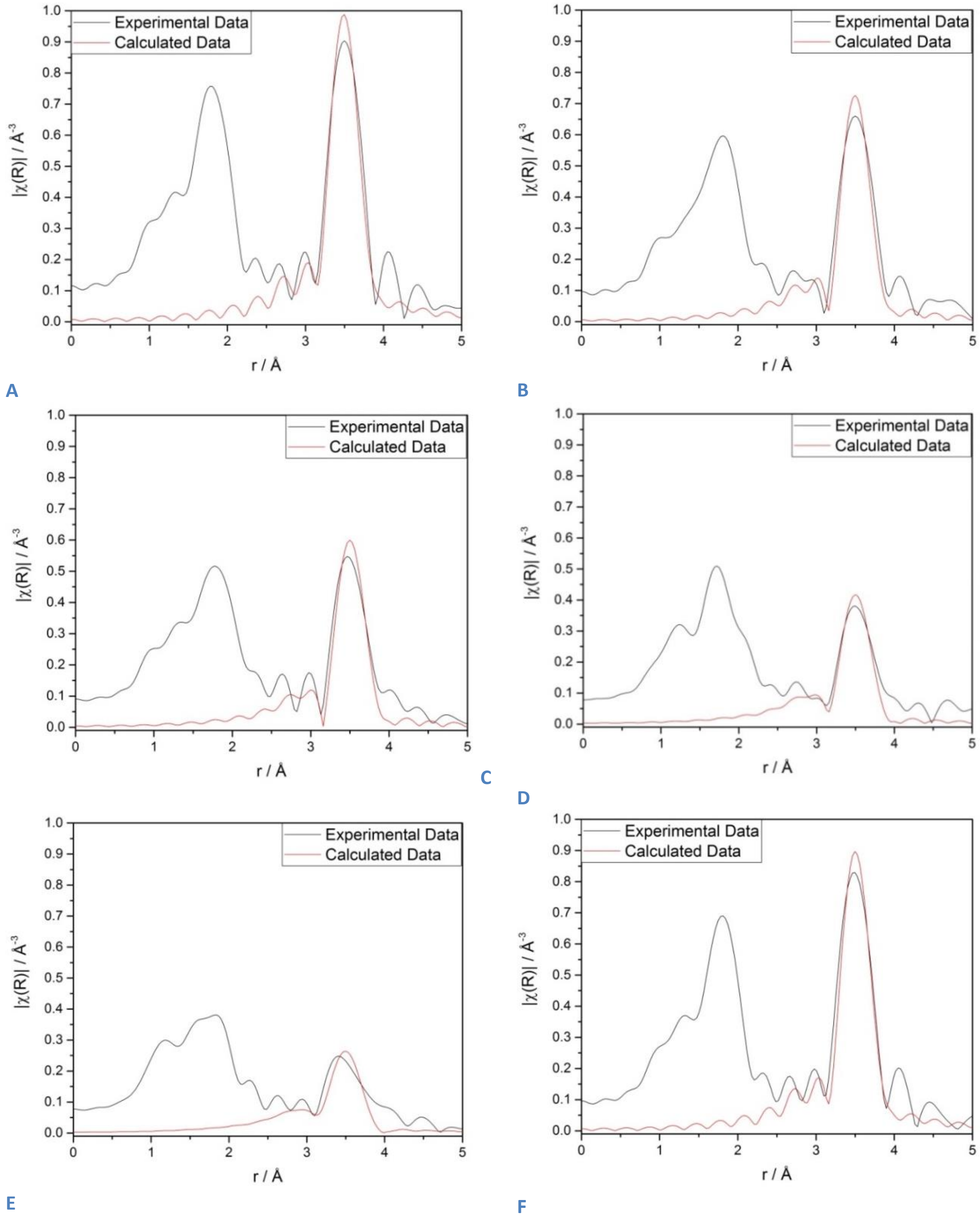

A

B

C

D

E

F

Figure S12a: Comparison of the Observed |χ(R)| spectra and Calculated |χ(R)| for 5 wt% Pd loaded onto the High Surface area ceria support for varying temperatures

- **A. 30°C**
- **B. 100°C**
- **C. 200°C**
- **D. 300°C**
- **E. 450°C**
- **F. 30°C**

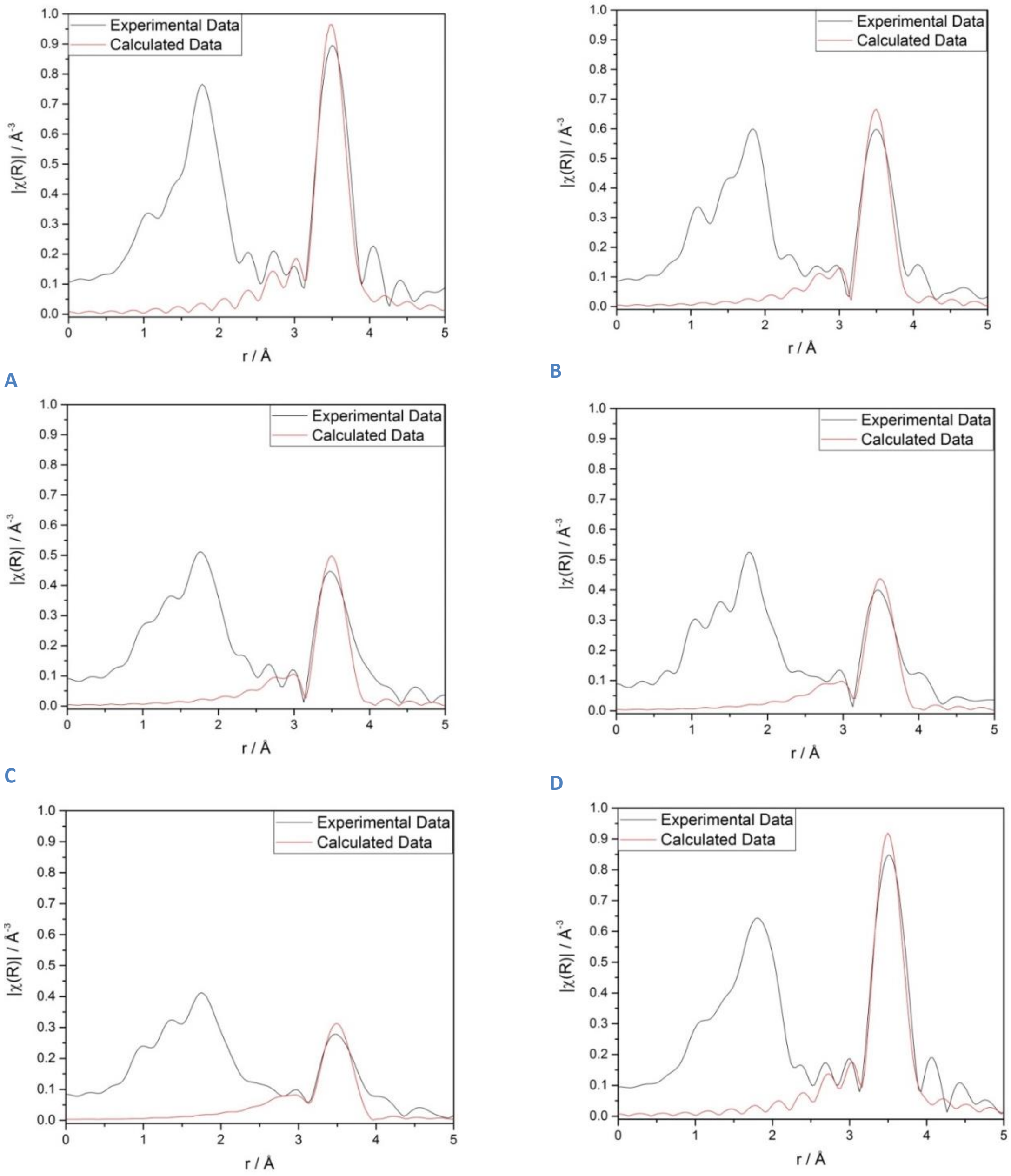

A

B

C

D

E

F

Figure S13a: Comparison of the Observed |χ(R)| spectra and Calculated |χ(R)| for 5 wt% Pt loaded onto the High Surface area ceria support for varying temperatures

- **A. 30°C**
- **B. 150°C**
- **C. 250°C**
- **D. 350°C**
- **E. 450°C**
- **F. 30°C**

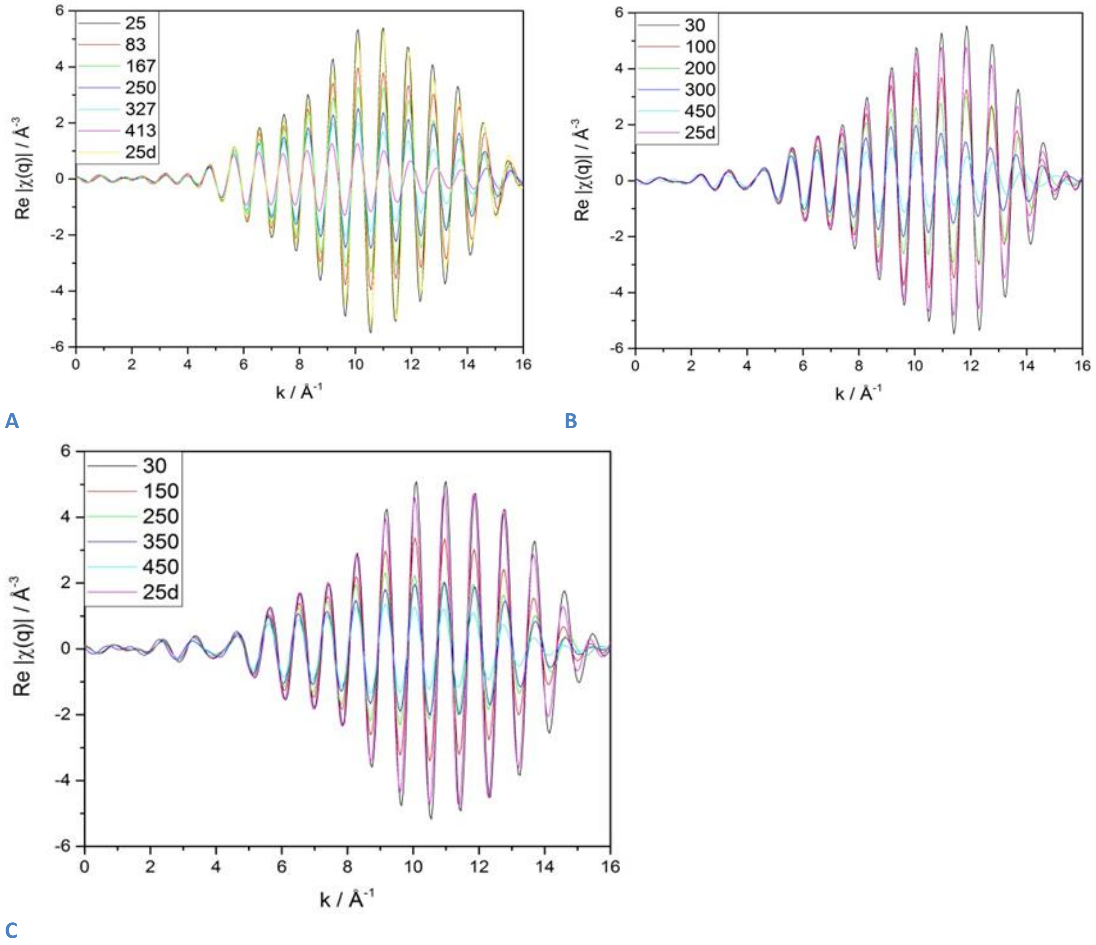

Figure S14a: (A) Comparison of the Re |χ(q)| for the High Surface Area ceria support and the respective 5 wt% Pd and 5 wt% Pt loaded samples (B and C) respectively. These show that under a reducing atmosphere and upon heating there are subtle variations in peak position and intensity.

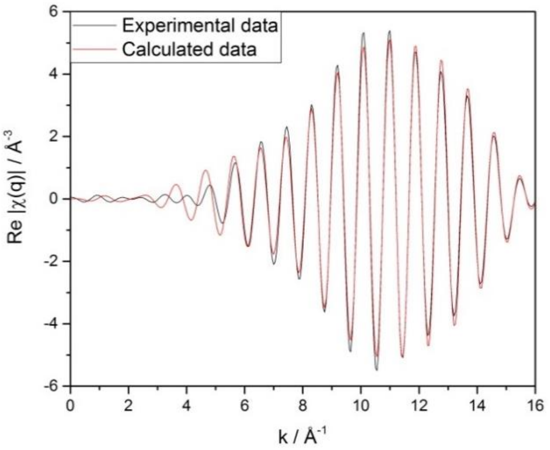
Experimental data
Calculated data
Re |χ(q)| / Å-3
k / Å-1
6
4
2
0
-2
-4
-6
0 2 4 6 8 10 12 14 16

A

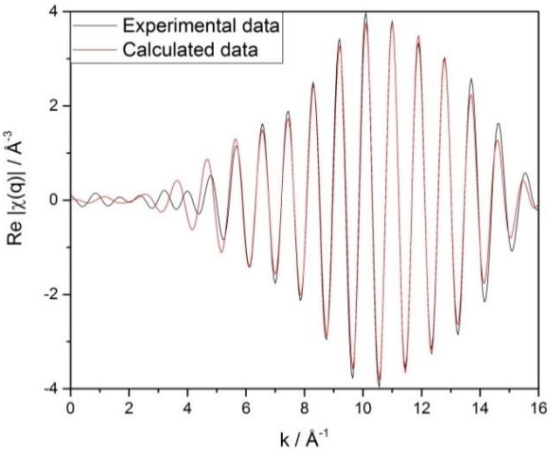
Experimental data
Calculated data
Re |χ(q)| / Å-3
k / Å-1
4
2
0
-2
-4
0 2 4 6 8 10 12 14 16

B

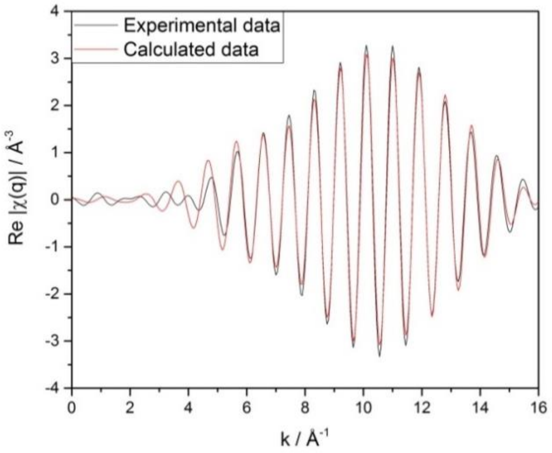
Experimental data
Calculated data
Re |χ(q)| / Å-3
k / Å-1
4
3
2
1
0
-1
-2
-3
-4
0 2 4 6 8 10 12 14 16

C

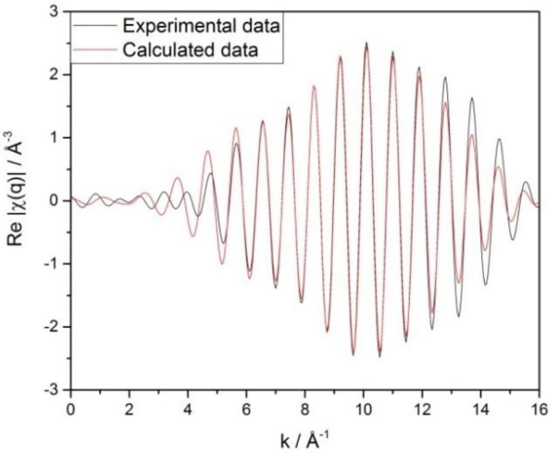
Experimental data
Calculated data
Re |χ(q)| / Å-3
k / Å-1
3
2
1
0
-1
-2
-3
0 2 4 6 8 10 12 14 16

D

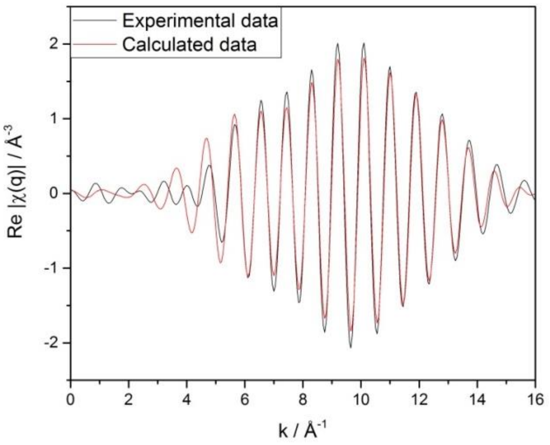
Experimental data
Calculated data
Re |χ(q)| / Å-3
k / Å-1
2
1
0
-1
-2
0 2 4 6 8 10 12 14 16

E

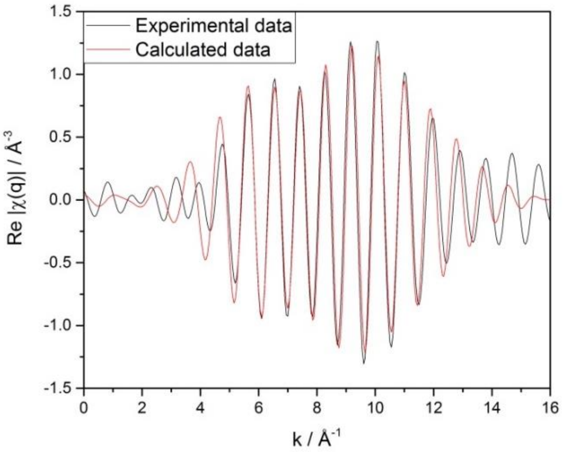
Experimental data
Calculated data
Re |χ(q)| / Å-3
k / Å-1
1.5
1.0
0.5
0.0
-0.5
-1.0
-1.5
0 2 4 6 8 10 12 14 16

F

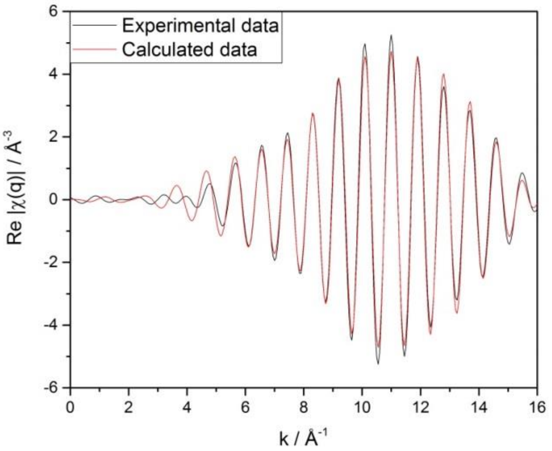

G

Figure S15a: Comparison of the Observed Re |χ(q)| spectra and Calculated |χ(q)| for the High Surface area ceria support for varying temperatures

- **A.** **30°C**
- **B.** **83°C**
- **C.** **167°C**
- **D.** **250°C**
- **E.** **327°C**
- **F.** **413°C**
- **G.** **30°C**

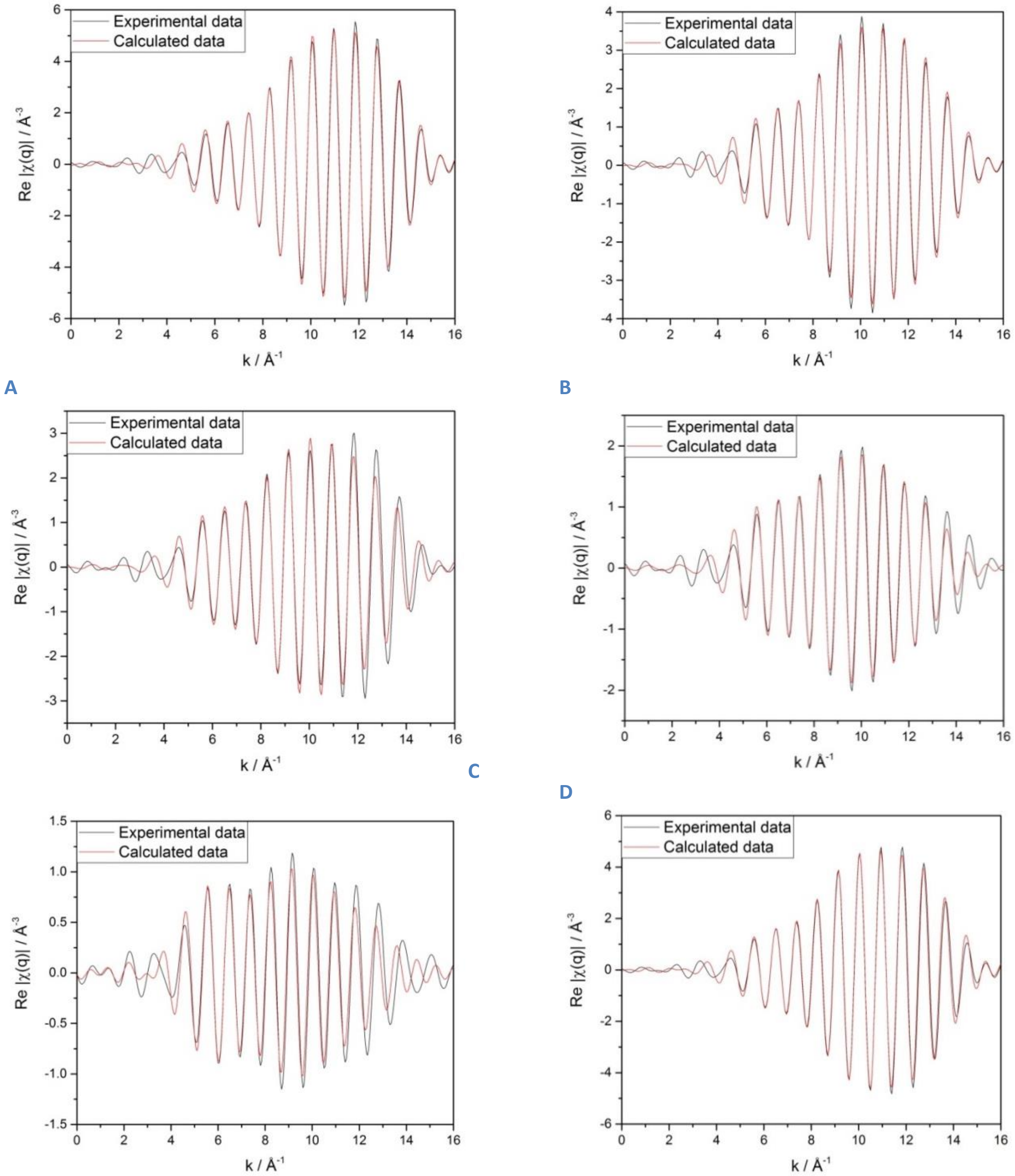

A
B
C
D
E
F

Figure S16a: Comparison of the Observed Re |χ(q)| spectra and Calculated |χ(q)| for 5 wt% Pd loaded onto the High Surface area ceria support for varying temperatures

A. 30°C
B. 100°C
C. 200°C
D. 300°C
E. 450°C
F. 30°C

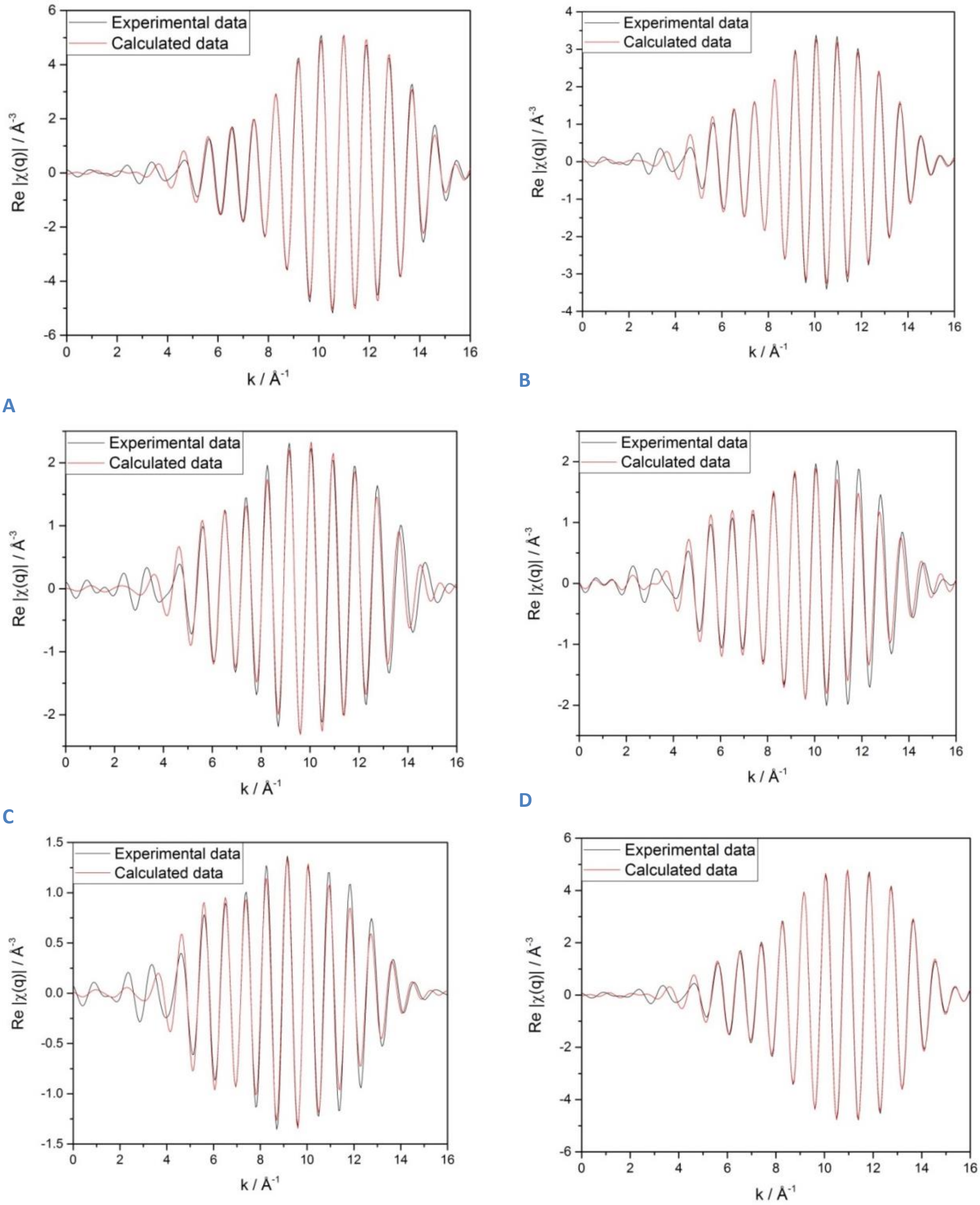

A

B

C

D

E

F

Figure S17a: Comparison of the Observed Re |χ(q)| spectra and Calculated |χ(q)| for 5 wt% Pt loaded onto the High Surface area ceria support for varying temperatures

- A. 30°C
- B. 150°C
- C. 250°C
- D. 350°C
- E. 450°C
- F. 30°C

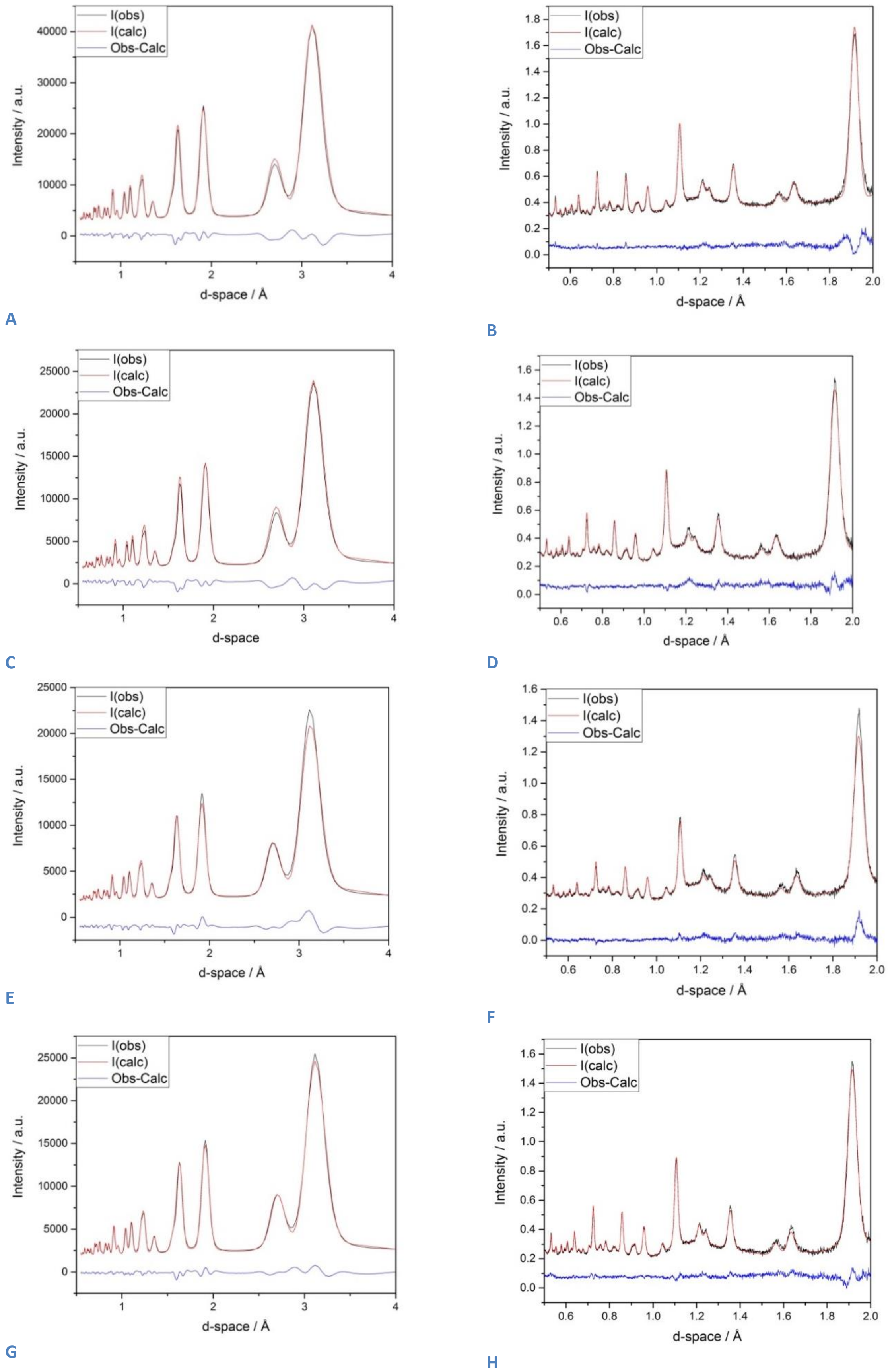

Figure S18a. Comparison of the Observed experimental data and the calculated data for the High Surface Area ceria support using the Rietveld Method.

A. **30°C (X-ray Diffraction (XRD))**
B. **30°C (Neutron Diffraction (ND))**

C. **200°C XRD**
D. **200°C ND**
E. **400°C XRD**
F. **400°C ND**
G. **30°C XRD**
H. **30°C ND**

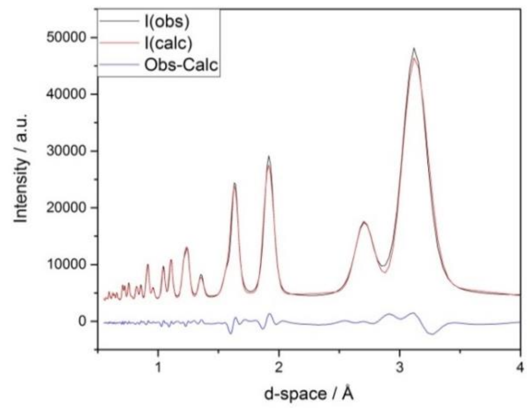
I(obs)
I(calc)
Obs-Calc
Intensity / a.u.
d-space / Å
50000
40000
30000
20000
10000
0
1
2
3
4

A

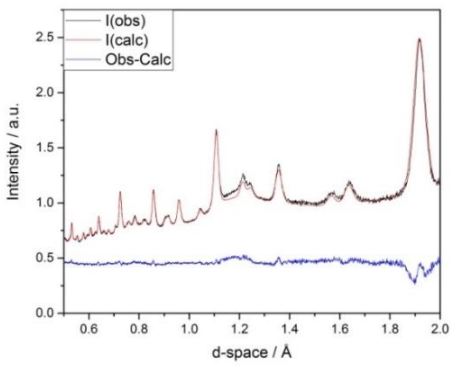
I(obs)
I(calc)
Obs-Calc
Intensity / a.u.
d-space / Å
2.5
2.0
1.5
1.0
0.5
0.0
0.6
0.8
1.0
1.2
1.4
1.6
1.8
2.0

B

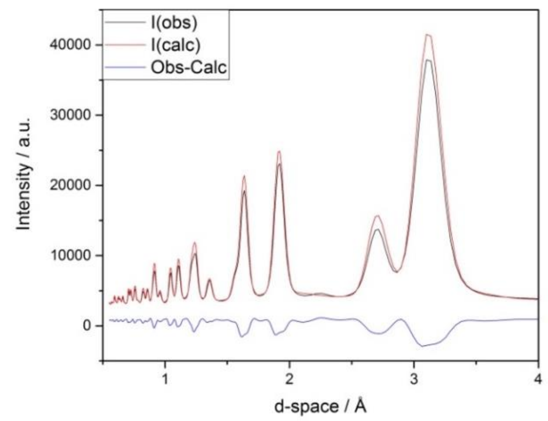
I(obs)
I(calc)
Obs-Calc
Intensity / a.u.
d-space / Å
40000
30000
20000
10000
0
1
2
3
4

C

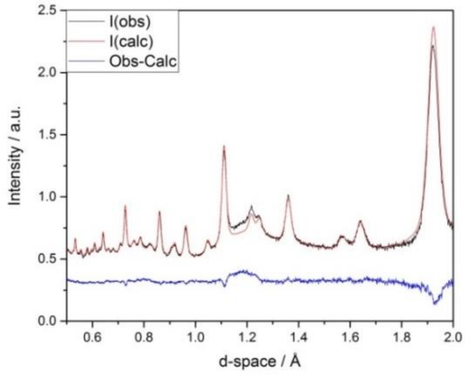
I(obs)
I(calc)
Obs-Calc
Intensity / a.u.
d-space / Å
2.5
2.0
1.5
1.0
0.5
0.0
0.6
0.8
1.0
1.2
1.4
1.6
1.8
2.0

D

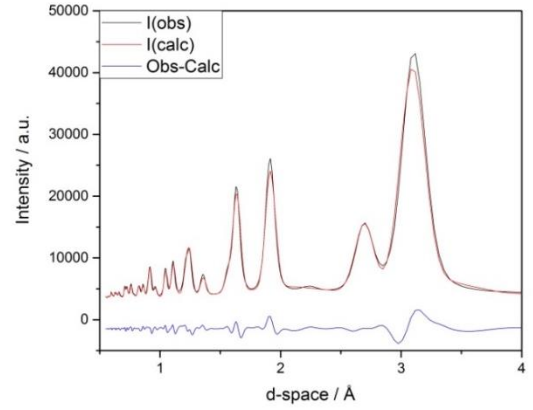
I(obs)
I(calc)
Obs-Calc
Intensity / a.u.
d-space / Å
50000
40000
30000
20000
10000
0
1
2
3
4

E

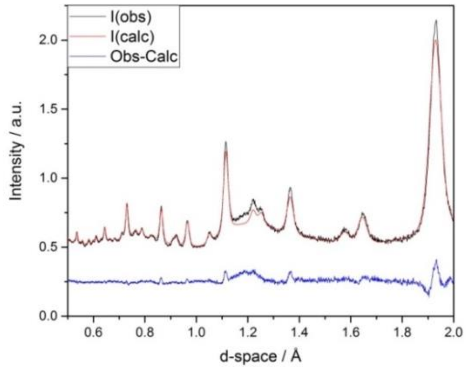
I(obs)
I(calc)
Obs-Calc
Intensity / a.u.
d-space / Å
2.0
1.5
1.0
0.5
0.0
0.6
0.8
1.0
1.2
1.4
1.6
1.8
2.0

F

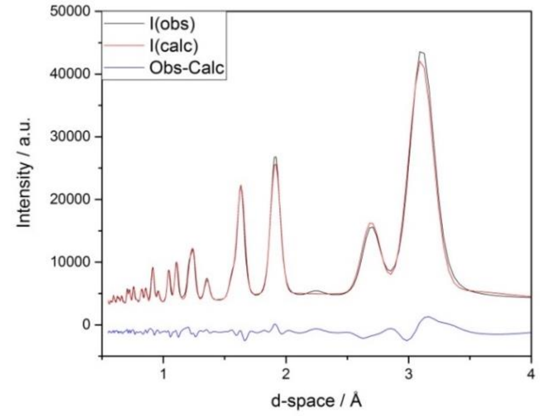
I(obs)
I(calc)
Obs-Calc
Intensity / a.u.
d-space / Å
50000
40000
30000
20000
10000
0
1
2
3
4

G

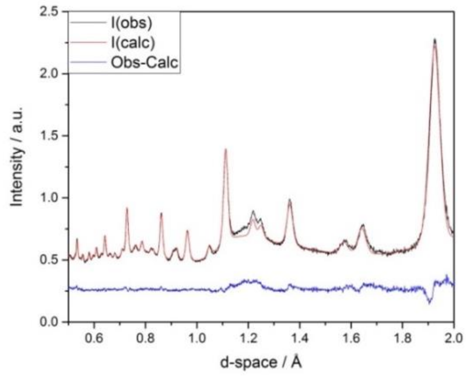
I(obs)
I(calc)
Obs-Calc
Intensity / a.u.
d-space / Å
2.5
2.0
1.5
1.0
0.5
0.0
0.6
0.8
1.0
1.2
1.4
1.6
1.8
2.0

H

Figure S19a. Comparison of the Observed experimental data and the calculated data for 5 wt% Pd on a High Surface Area ceria support using the Rietveld Method.

A. **30°C (X-ray Diffraction (XRD))**
B. **30°C (Neutron Diffraction (ND))**
C. **200°C XRD**
D. **200°C ND**
E. **400°C XRD**
F. **400°C ND**
G. **30°C XRD**
H. **30°C ND**

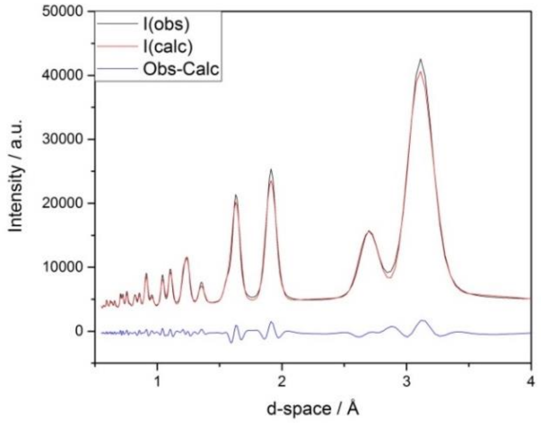
I(obs)
I(calc)
Obs-Calc
Intensity / a.u.
50000
40000
30000
20000
10000
0
1
2
3
4
d-space / Å

A

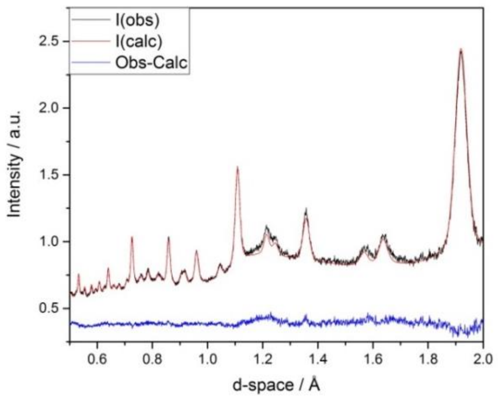
I(obs)
I(calc)
Obs-Calc
Intensity / a.u.
2.5
2.0
1.5
1.0
0.5
0.6
0.8
1.0
1.2
1.4
1.6
1.8
2.0
d-space / Å

B

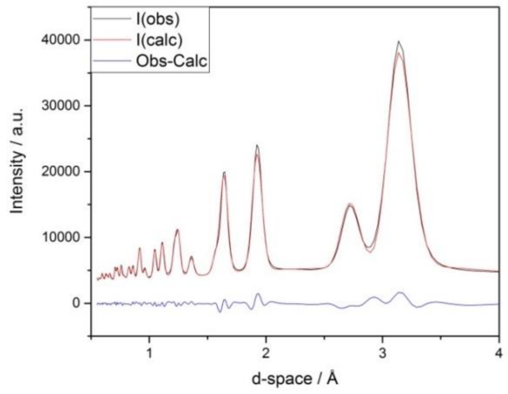
I(obs)
I(calc)
Obs-Calc
Intensity / a.u.
40000
30000
20000
10000
0
1
2
3
4
d-space / Å

C

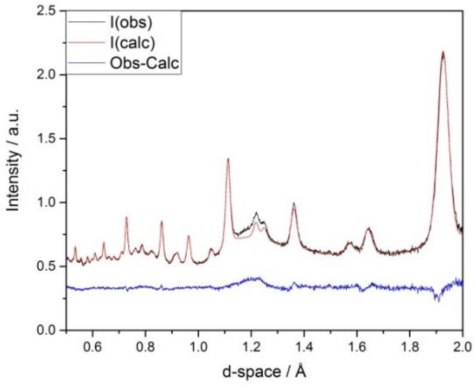
I(obs)
I(calc)
Obs-Calc
Intensity / a.u.
2.5
2.0
1.5
1.0
0.5
0.0
0.6
0.8
1.0
1.2
1.4
1.6
1.8
2.0
d-space / Å

D

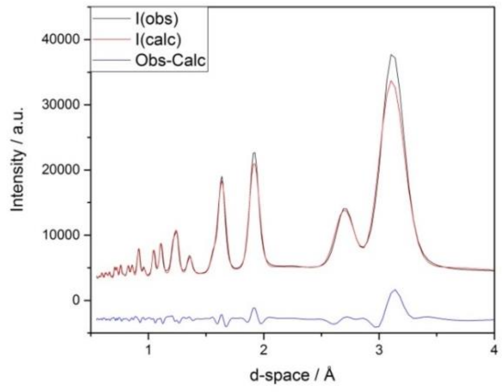
I(obs)
I(calc)
Obs-Calc
Intensity / a.u.
40000
30000
20000
10000
0
1
2
3
4
d-space / Å

E

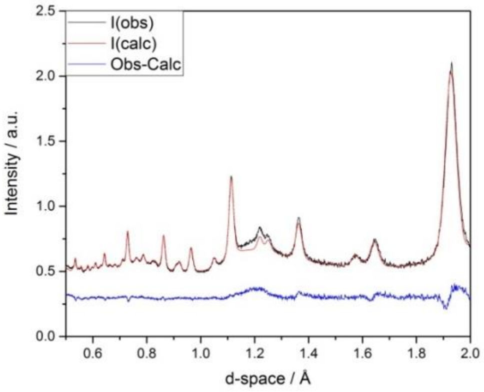
I(obs)
I(calc)
Obs-Calc
Intensity / a.u.
2.5
2.0
1.5
1.0
0.5
0.0
0.6
0.8
1.0
1.2
1.4
1.6
1.8
2.0
d-space / Å

F

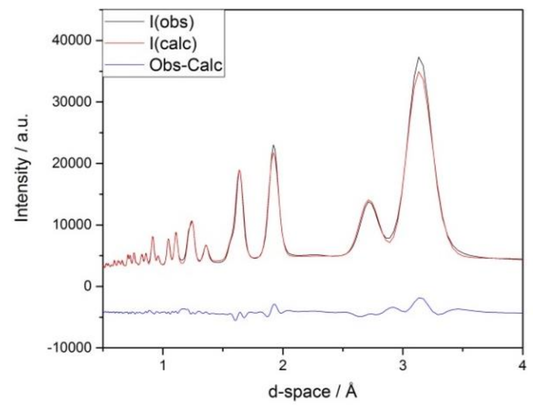
I(obs)
I(calc)
Obs-Calc
Intensity / a.u.
40000
30000
20000
10000
0
-10000
1
2
3
4
d-space / Å

G

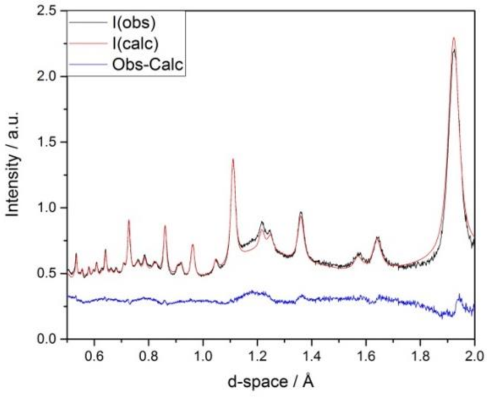
I(obs)
I(calc)
Obs-Calc
Intensity / a.u.
2.5
2.0
1.5
1.0
0.5
0.0
0.6
0.8
1.0
1.2
1.4
1.6
1.8
2.0
d-space / Å

H

Figure S20a. Comparison of the Observed experimental data and the calculated data for 5 wt% Pt on a High Surface Area ceria support using the Rietveld Method.

A. **30°C (X-ray Diffraction (XRD))**
B. **30°C (Neutron Diffraction (ND))**
C. **200°C XRD**
D. **200°C ND**
E. **400°C XRD**
F. **400°C ND**
G. **30°C XRD**
H. **30°C ND**

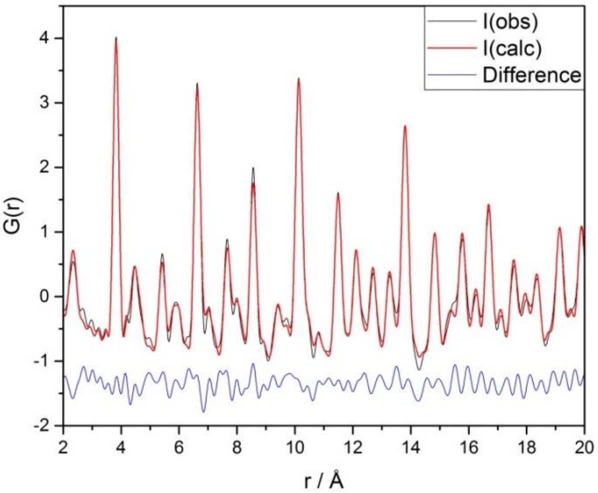

A

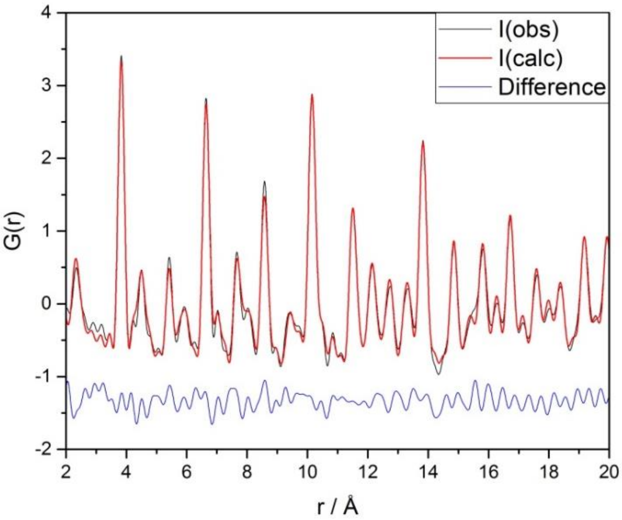

B

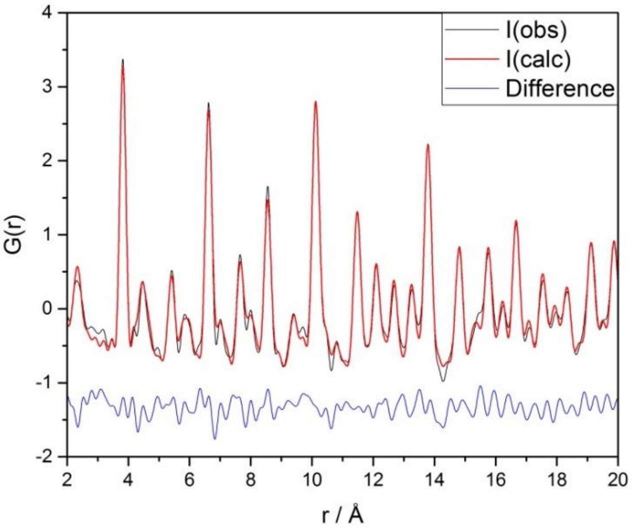

C

Figure S21a. Example of the fits for the PDF analysis, showing a comparison of the Observed Data (I(obs)), Calculated Data (I(calc)) and the difference between these respective data sets.

- **A. High Surface area ceria support**
- **B. 5 wt% Pd on a High Surface area ceria support**
- **C. 5 wt% Pt on a High Surface area ceria support**

Appendix for Chapter 5

Table S1b. Results from Assay showing the amount of Pd present in each sample, showing similar values to those assumed from the synthesis procedures.

Sample	Amount of Pd / %
1 wt% Pd on High surface area ceria support	1.02
2.5 wt% Pd on High surface area ceria support	2.35
5 wt% Pd on High surface area ceria support	4.73

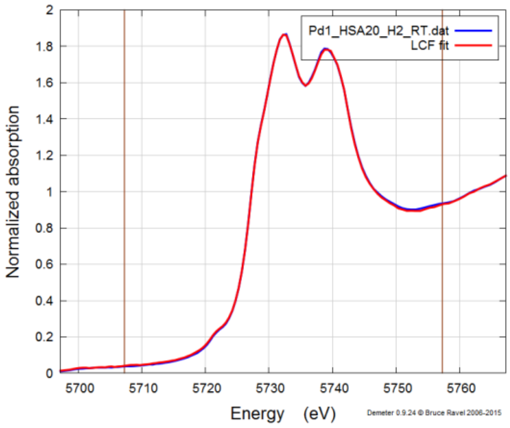

A

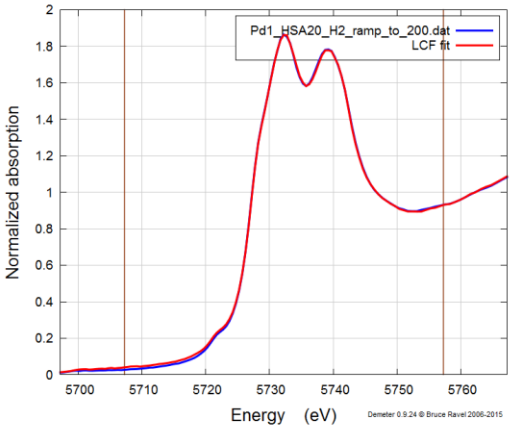

B

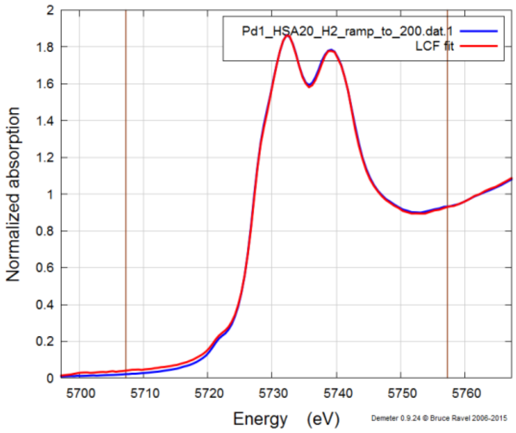

C

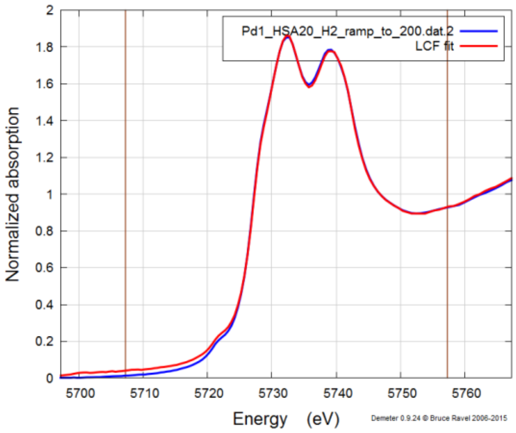

D

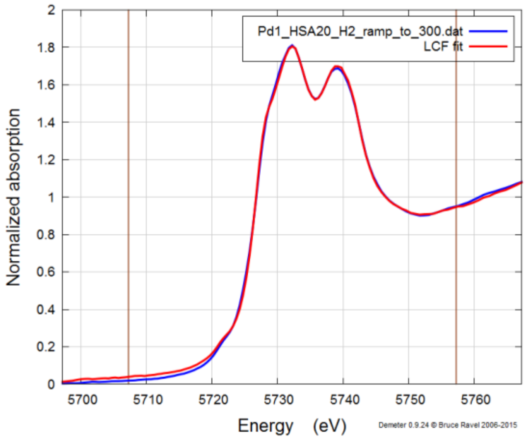

E

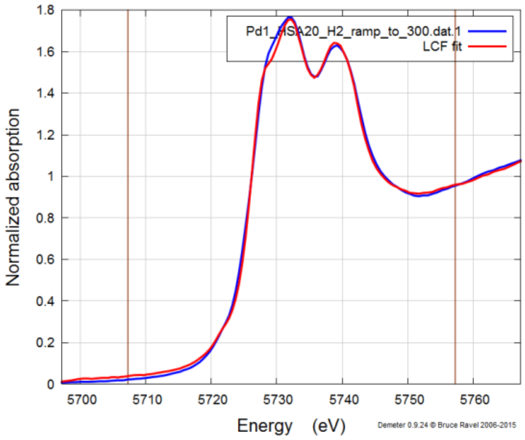

F

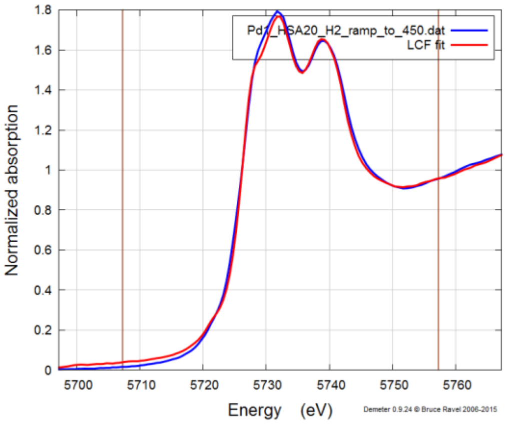
Pd1_HSA20_H2_ramp_to_450.dat
LCF fit
Normalized absorption
0
0.2
0.4
0.6
0.8
1
1.2
1.4
1.6
1.8
5700
5710
5720
5730
5740
5750
5760
Energy (eV)
Demeter 0.9.24 © Bruce Ravel 2006-2015

G

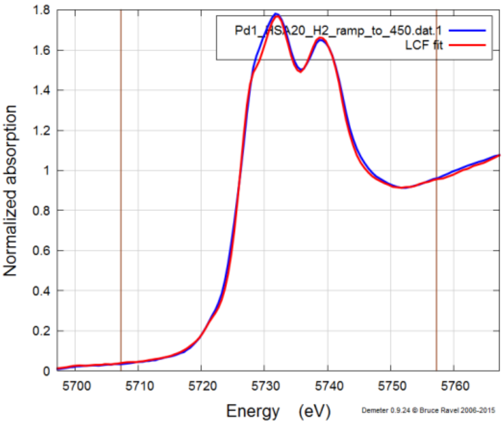
Pd1_HSA20_H2_ramp_to_450.dat.1
LCF fit
Normalized absorption
0
0.2
0.4
0.6
0.8
1
1.2
1.4
1.6
1.8
5700
5710
5720
5730
5740
5750
5760
Energy (eV)
Demeter 0.9.24 © Bruce Ravel 2006-2015

H

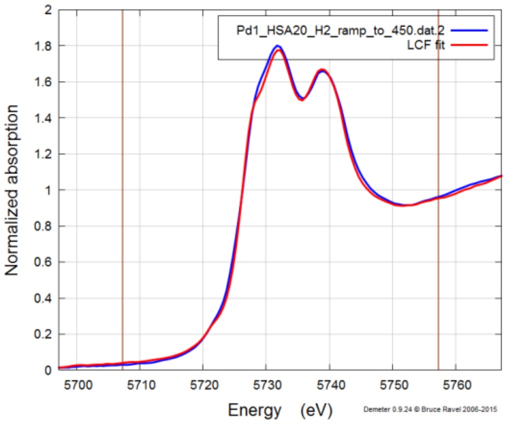
Pd1_HSA20_H2_ramp_to_450.dat.2
LCF fit
Normalized absorption
0
0.2
0.4
0.6
0.8
1
1.2
1.4
1.6
1.8
2
5700
5710
5720
5730
5740
5750
5760
Energy (eV)
Demeter 0.9.24 © Bruce Ravel 2006-2015

I

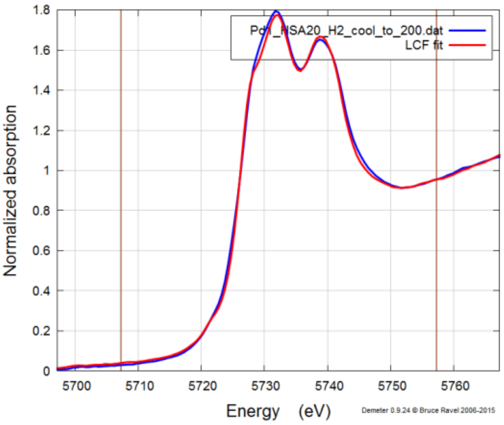
Pd1_HSA20_H2_cool_to_200.dat
LCF fit
Normalized absorption
0
0.2
0.4
0.6
0.8
1
1.2
1.4
1.6
1.8
5700
5710
5720
5730
5740
5750
5760
Energy (eV)
Demeter 0.9.24 © Bruce Ravel 2006-2015

J

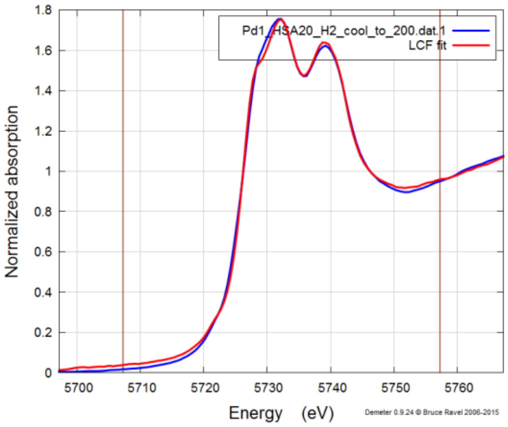
Pd1_HSA20_H2_cool_to_200.dat.1
LCF fit
Normalized absorption
0
0.2
0.4
0.6
0.8
1
1.2
1.4
1.6
1.8
5700
5710
5720
5730
5740
5750
5760
Energy (eV)
Demeter 0.9.24 © Bruce Ravel 2006-2015

K

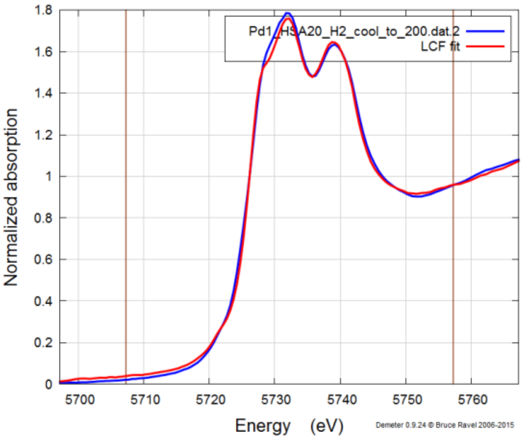
Pd1_HSA20_H2_cool_to_200.dat.2
LCF fit
Normalized absorption
0
0.2
0.4
0.6
0.8
1
1.2
1.4
1.6
1.8
5700
5710
5720
5730
5740
5750
5760
Energy (eV)
Demeter 0.9.24 © Bruce Ravel 2006-2015

L

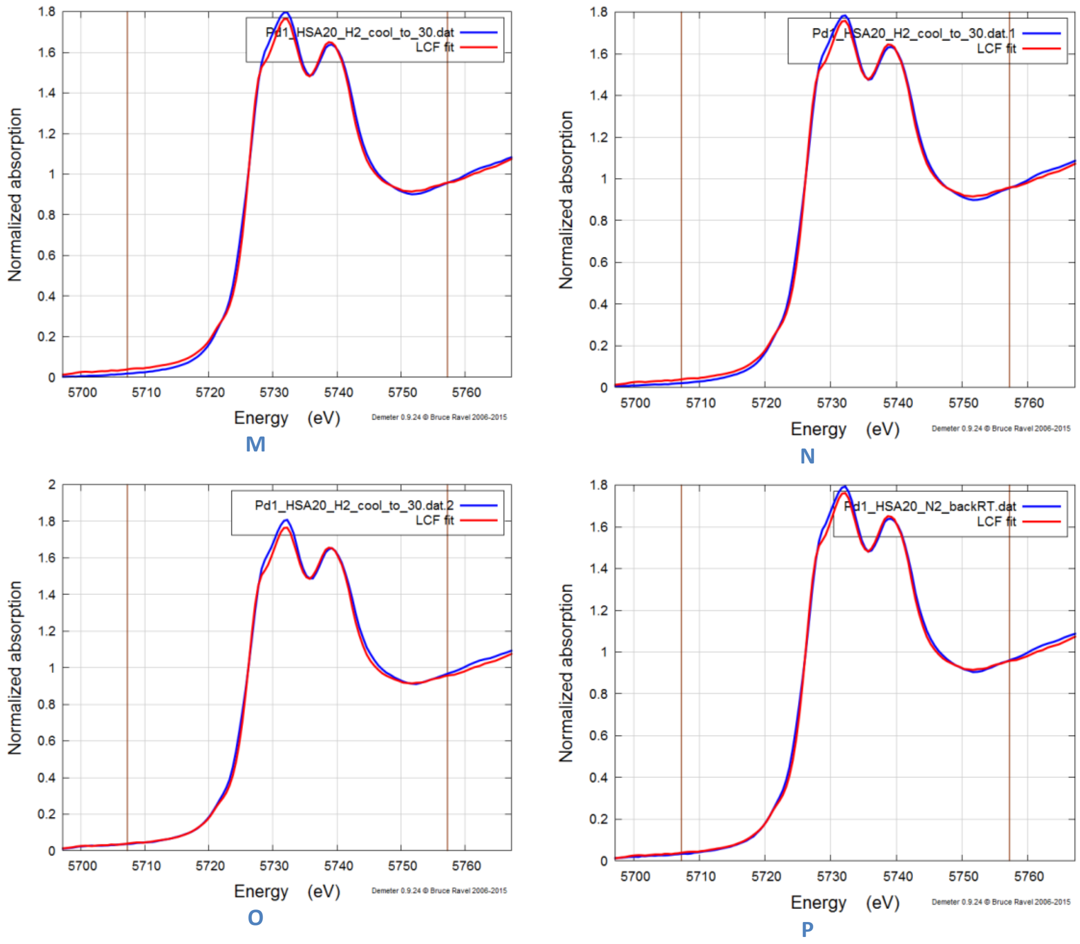

M

N

O

P

Figure S1b. Comparison of the Observed XANES spectra and Linear Combination Fitting (LCF) for the 1 wt% Pd on a High Surface area support for varying temperatures (for the Ce L3-edge)

A. 30
B. 32
C. 146
D. 200
E. 205
F. 300
G. 304
H. 430
I. 450
J. 442
K. 341
L. 220
M. 175
N. 47
O. 30
P. 30 (N_2)

A

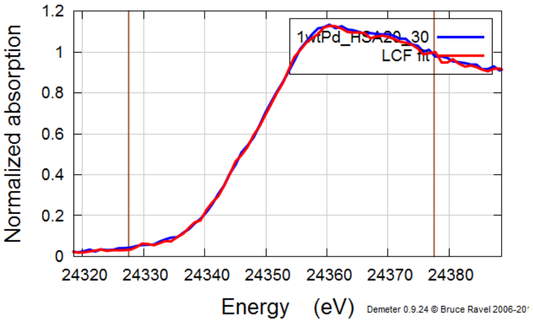
Normalized absorption
0
0.2
0.4
0.6
0.8
1
1.2
24320 24330 24340 24350 24360 24370 24380
Energy (eV)
1wtPd_HSA20_30
LCF fit
Demeter 0.9.24 © Bruce Ravel 2006-20

B

C

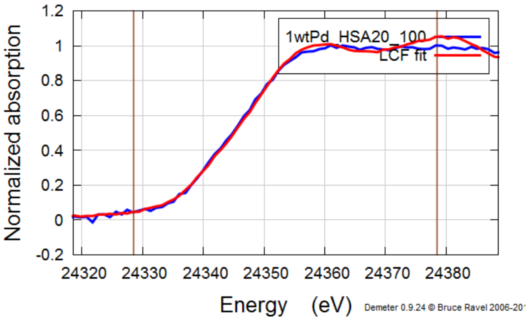
Normalized absorption
-0.2
0
0.2
0.4
0.6
0.8
1
1.2
24320 24330 24340 24350 24360 24370 24380
Energy (eV)
1wtPd_HSA20_100
LCF fit
Demeter 0.9.24 © Bruce Ravel 2006-20

D

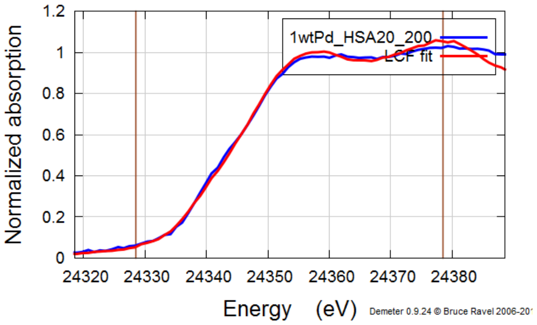
Normalized absorption
0
0.2
0.4
0.6
0.8
1
1.2
24320 24330 24340 24350 24360 24370 24380
Energy (eV)
1wtPd_HSA20_200
LCF fit
Demeter 0.9.24 © Bruce Ravel 2006-20

E

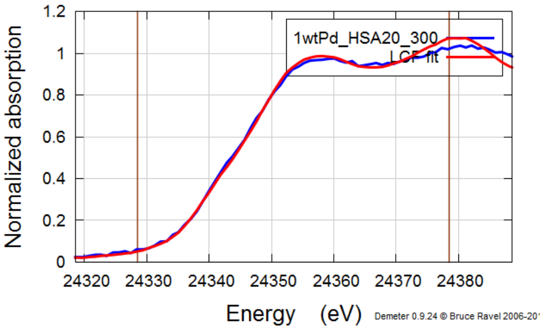
Normalized absorption
0
0.2
0.4
0.6
0.8
1
1.2
24320 24330 24340 24350 24360 24370 24380
Energy (eV)
1wtPd_HSA20_300
LCF fit
Demeter 0.9.24 © Bruce Ravel 2006-20

F

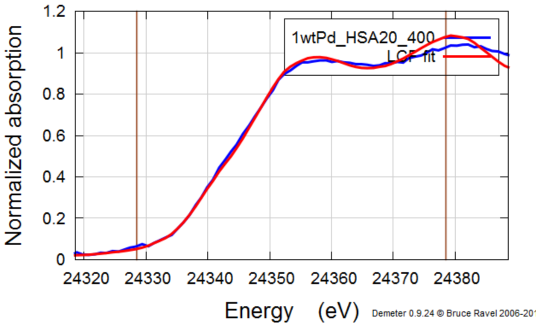
Normalized absorption
0
0.2
0.4
0.6
0.8
1
1.2
24320 24330 24340 24350 24360 24370 24380
Energy (eV)
1wtPd_HSA20_400
LCF fit
Demeter 0.9.24 © Bruce Ravel 2006-20

G

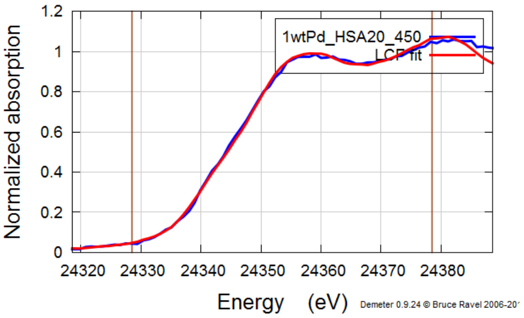
Normalized absorption
0
0.2
0.4
0.6
0.8
1
1.2
24320 24330 24340 24350 24360 24370 24380
Energy (eV)
1wtPd_HSA20_450
LCF fit
Demeter 0.9.24 © Bruce Ravel 2006-20

H

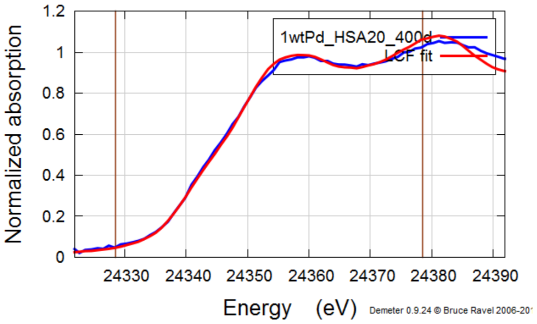
Normalized absorption
0
0.2
0.4
0.6
0.8
1
1.2
24330 24340 24350 24360 24370 24380 24390
Energy (eV)
1wtPd_HSA20_400d
LCF fit
Demeter 0.9.24 © Bruce Ravel 2006-20

I

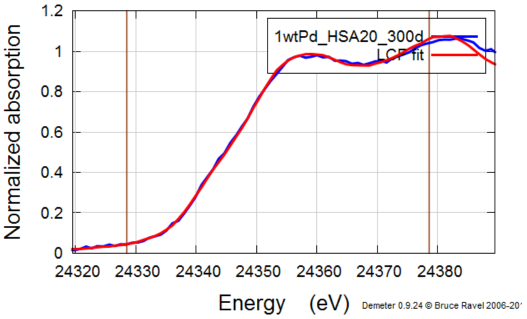
Normalized absorption
0
0.2
0.4
0.6
0.8
1
1.2
24320 24330 24340 24350 24360 24370 24380
Energy (eV)
1wtPd_HSA20_300d
LCF fit
Demeter 0.9.24 © Bruce Ravel 2006-20

J

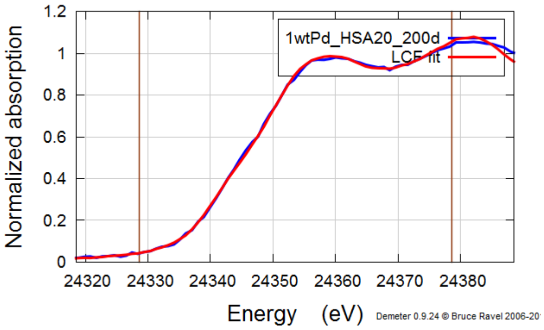

K

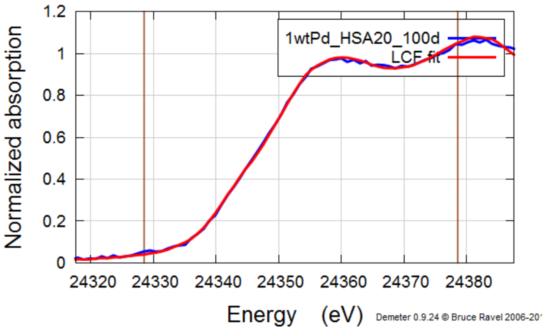

L

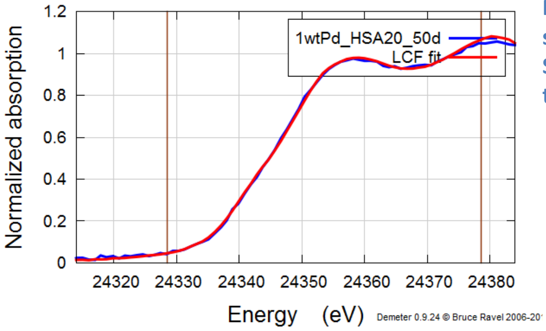

M

Figure S2b. Comparison of the Observed XANES spectra and LCF for 1 wt% Pd loaded onto a High Surface area support for varying temperatures (for the Pd K-edge)

A. 30°C (ARGON)
B. 30°C (H_2:N_2)
C. 50°C
D. 100°C
E. 200°C
F. 300°C
G. 400°C
H. 450°C
I. 400°C
J. 300°C
K. 200°C
L. 100°C
M. 50°C

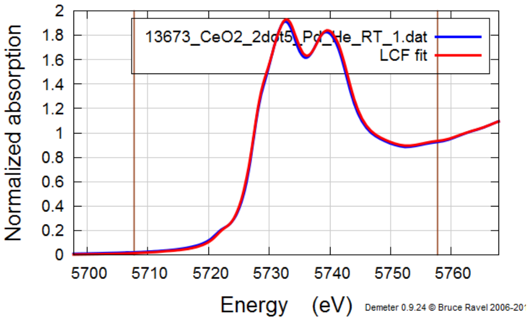

A

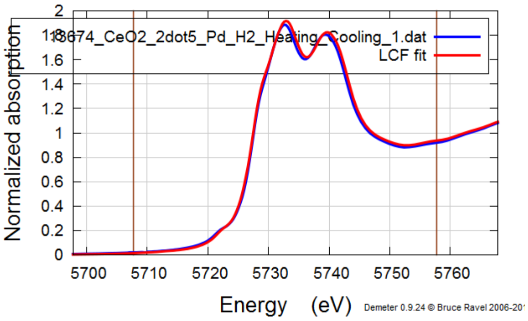

B

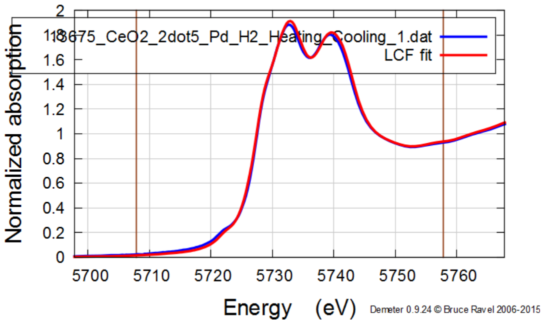

C

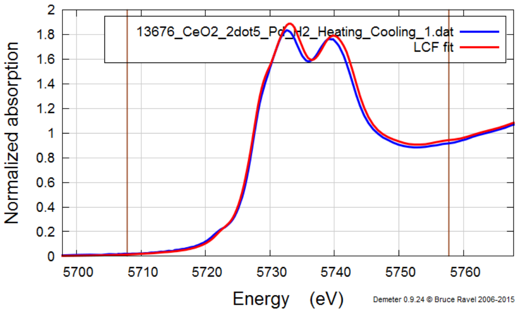

D

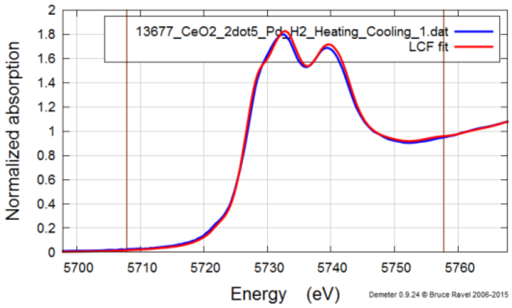

E

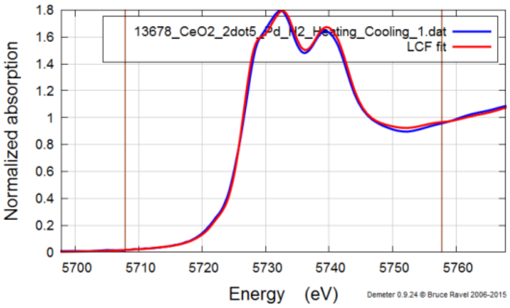

F

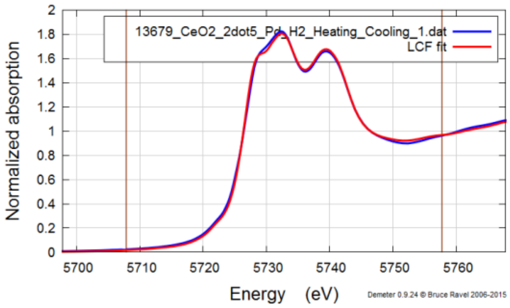

G

Figure S3b. Comparison of the Observed XANES spectra and LCF for 2.5 wt% Pd loaded onto a High Surface area support for varying temperatures (for the Ce L3-edge)

A. 23
B. 93
C. 216
D. 338
E. 450
F. 275
G. 26

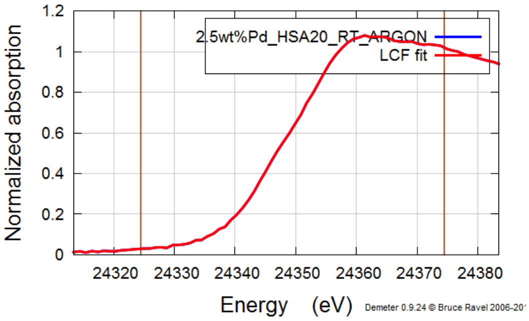
Normalized absorption
1.2
1
0.8
0.6
0.4
0.2
0
24320
24330
24340
24350
24360
24370
24380
Energy (eV)
2.5wt%Pd_HSA20_RT_ARGON
LCF fit
Demeter 0.9.24 © Bruce Ravel 2006-20

A

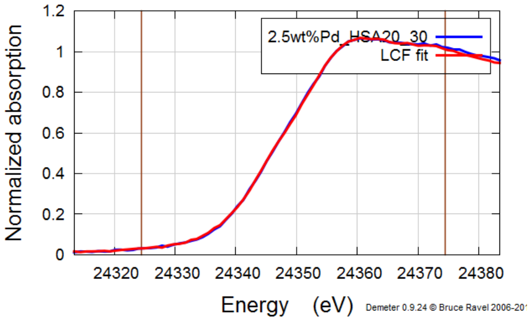
Normalized absorption
1.2
1
0.8
0.6
0.4
0.2
0
24320
24330
24340
24350
24360
24370
24380
Energy (eV)
2.5wt%Pd_HSA20_30
LCF fit
Demeter 0.9.24 © Bruce Ravel 2006-20

B

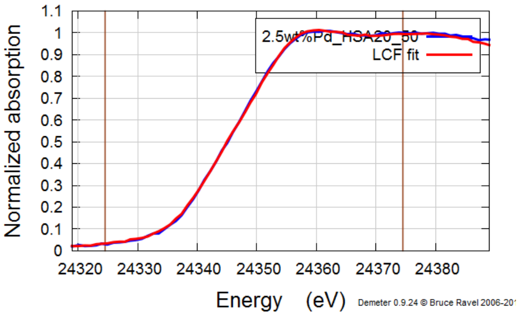
Normalized absorption
1.1
1
0.9
0.8
0.7
0.6
0.5
0.4
0.3
0.2
0.1
0
24320
24330
24340
24350
24360
24370
24380
Energy (eV)
2.5wt%Pd_HSA20_50
LCF fit
Demeter 0.9.24 © Bruce Ravel 2006-20

C

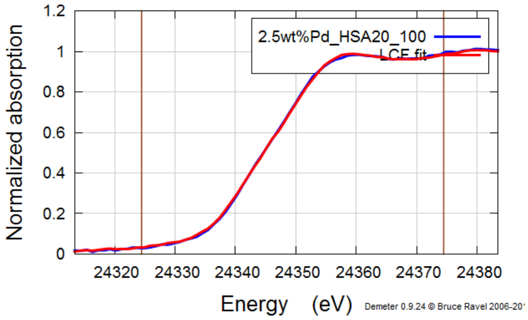
Normalized absorption
1.2
1
0.8
0.6
0.4
0.2
0
24320
24330
24340
24350
24360
24370
24380
Energy (eV)
2.5wt%Pd_HSA20_100
LCF fit
Demeter 0.9.24 © Bruce Ravel 2006-20

D

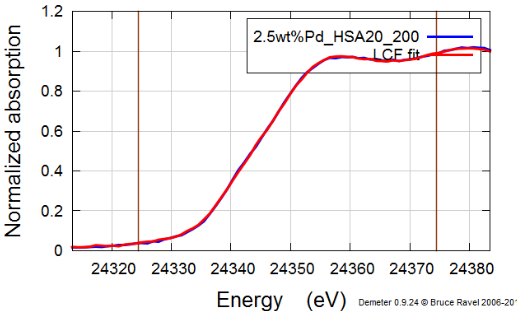
Normalized absorption
1.2
1
0.8
0.6
0.4
0.2
0
24320
24330
24340
24350
24360
24370
24380
Energy (eV)
2.5wt%Pd_HSA20_200
LCF fit
Demeter 0.9.24 © Bruce Ravel 2006-20

E

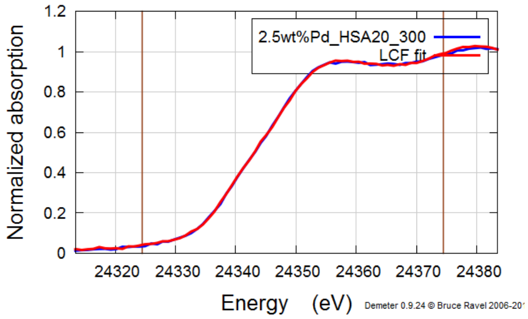
Normalized absorption
1.2
1
0.8
0.6
0.4
0.2
0
24320
24330
24340
24350
24360
24370
24380
Energy (eV)
2.5wt%Pd_HSA20_300
LCF fit
Demeter 0.9.24 © Bruce Ravel 2006-20

F

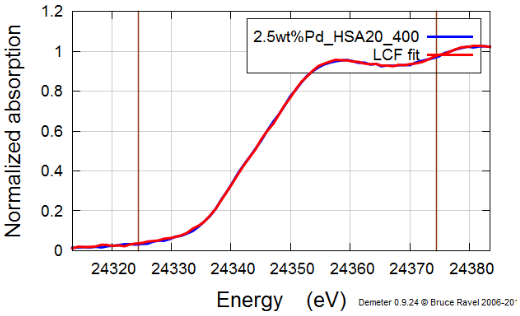
Normalized absorption
1.2
1
0.8
0.6
0.4
0.2
0
24320
24330
24340
24350
24360
24370
24380
Energy (eV)
2.5wt%Pd_HSA20_400
LCF fit
Demeter 0.9.24 © Bruce Ravel 2006-20

G

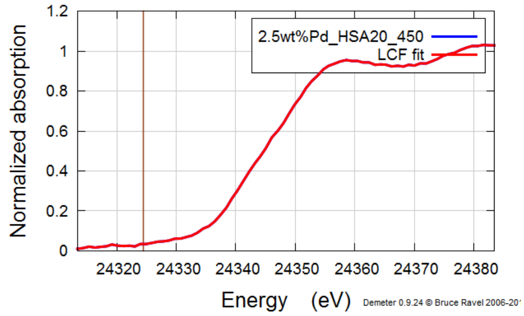
Normalized absorption
1.2
1
0.8
0.6
0.4
0.2
0
24320
24330
24340
24350
24360
24370
24380
Energy (eV)
2.5wt%Pd_HSA20_450
LCF fit
Demeter 0.9.24 © Bruce Ravel 2006-20

H

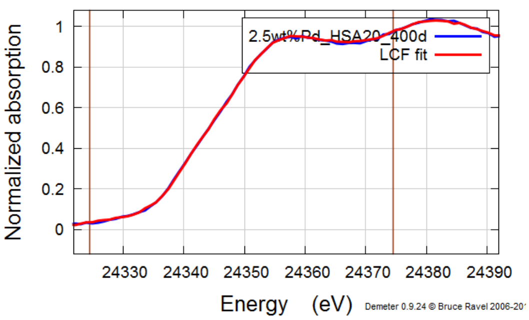
Normalized absorption
1
0.8
0.6
0.4
0.2
0
24330
24340
24350
24360
24370
24380
24390
Energy (eV)
2.5wt%Pd_HSA20_400d
LCF fit
Demeter 0.9.24 © Bruce Ravel 2006-20

I

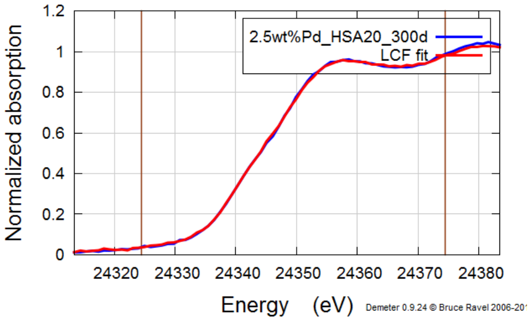
Normalized absorption
1.2
1
0.8
0.6
0.4
0.2
0
24320
24330
24340
24350
24360
24370
24380
Energy (eV)
2.5wt%Pd_HSA20_300d
LCF fit
Demeter 0.9.24 © Bruce Ravel 2006-20

J

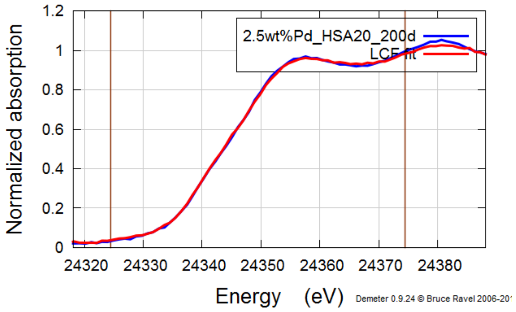

K

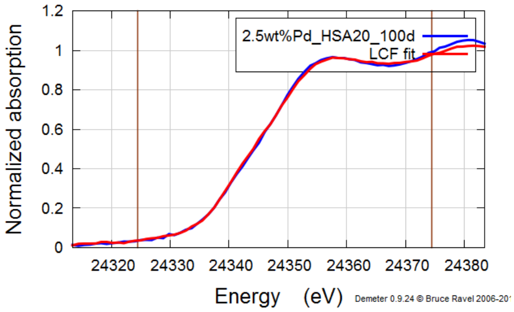

L

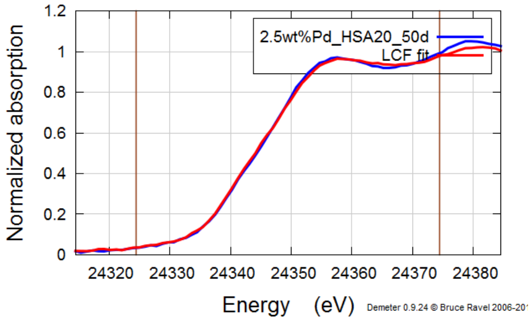

M

Figure S4b. Comparison of the Observed XANES spectra and LCF for 2.5 wt% Pd loaded onto a High Surface area support for varying temperatures (for the Pd K-edge)

A. 30°C (ARGON)
B. 30°C (H2:N2)
C. 50°C
D. 100°C
E. 200°C
F. 300°C
G. 400°C
H. 450°C
I. 400°C
J. 300°C
K. 200°C
L. 100°C
M. 50°C

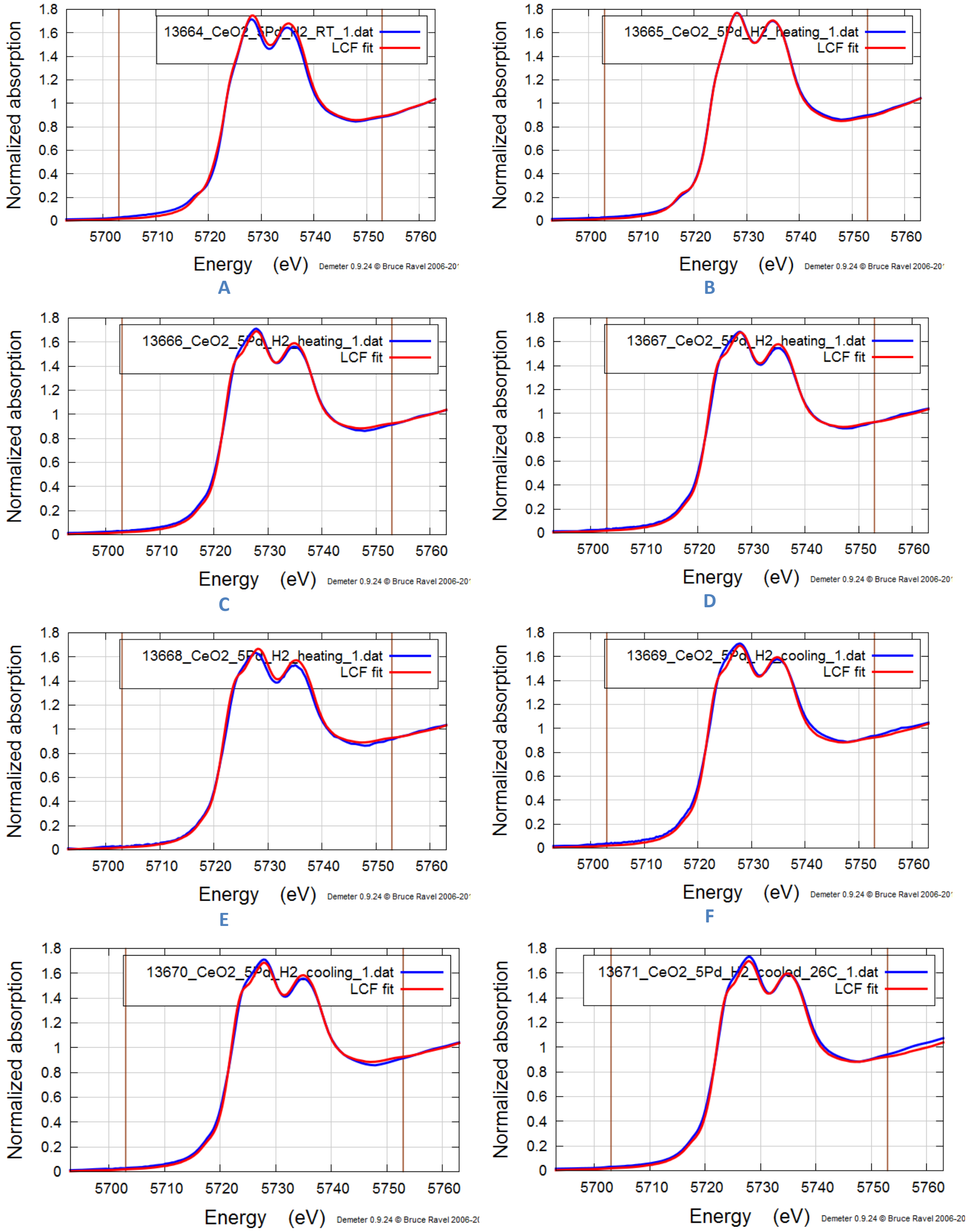

A B C D E F G H

Figure S5b. Comparison of the Observed XANES spectra and LCF for 5 wt% Pd loaded onto a High Surface area support for varying temperatures (for the Ce L3-edge)

- A. 30°C
- B. 43°C
- C. 168°C
- D. 300°C
- E. 409°C
- F. 437°C
- G. 173°C
- H. 26°C

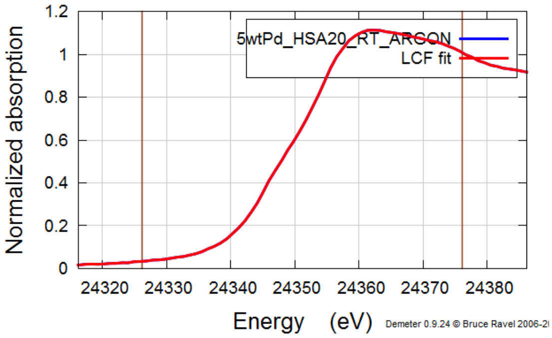
5wtPd_HSA20_RT_ARGON
LCF fit
Normalized absorption
0
0.2
0.4
0.6
0.8
1
1.2
24320
24330
24340
24350
24360
24370
24380
Energy (eV)
Demeter 0.9.24 © Bruce Ravel 2006-2

A

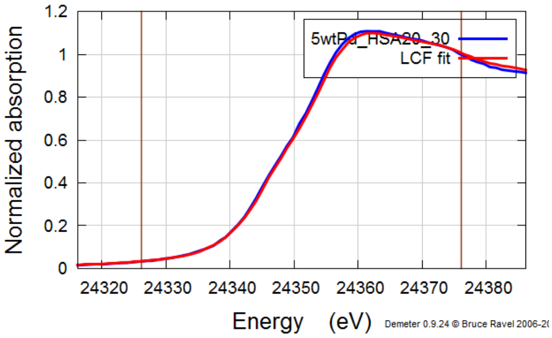
5wtPd_HSA20_30
LCF fit
Normalized absorption
0
0.2
0.4
0.6
0.8
1
1.2
24320
24330
24340
24350
24360
24370
24380
Energy (eV)
Demeter 0.9.24 © Bruce Ravel 2006-2

B

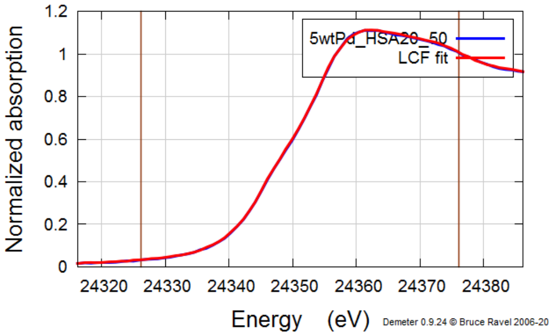
5wtPd_HSA20_50
LCF fit
Normalized absorption
0
0.2
0.4
0.6
0.8
1
1.2
24320
24330
24340
24350
24360
24370
24380
Energy (eV)
Demeter 0.9.24 © Bruce Ravel 2006-20

C

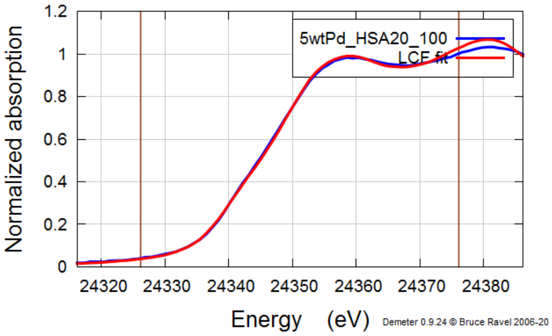
5wtPd_HSA20_100
LCF fit
Normalized absorption
0
0.2
0.4
0.6
0.8
1
1.2
24320
24330
24340
24350
24360
24370
24380
Energy (eV)
Demeter 0.9.24 © Bruce Ravel 2006-20

D

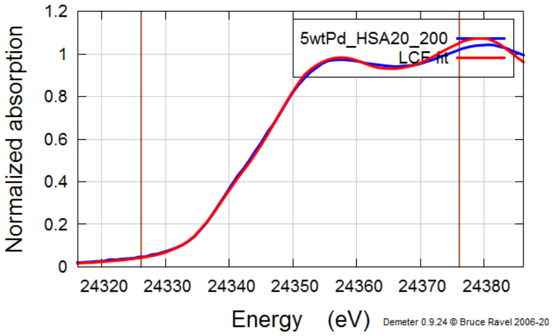
5wtPd_HSA20_200
LCF fit
Normalized absorption
0
0.2
0.4
0.6
0.8
1
1.2
24320
24330
24340
24350
24360
24370
24380
Energy (eV)
Demeter 0.9.24 © Bruce Ravel 2006-20

E

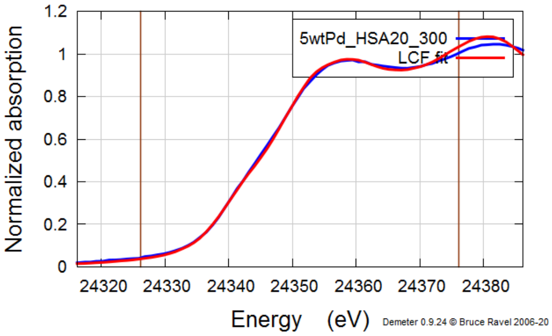
5wtPd_HSA20_300
LCF fit
Normalized absorption
0
0.2
0.4
0.6
0.8
1
1.2
24320
24330
24340
24350
24360
24370
24380
Energy (eV)
Demeter 0.9.24 © Bruce Ravel 2006-20

F

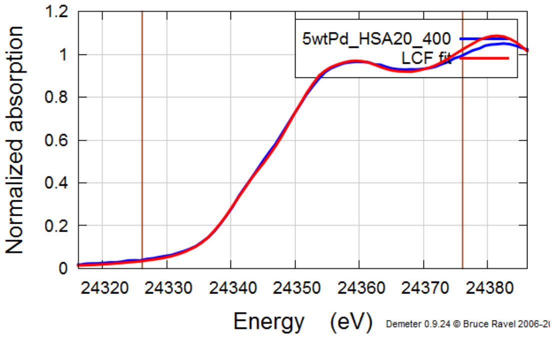
5wtPd_HSA20_400
LCF fit
Normalized absorption
0
0.2
0.4
0.6
0.8
1
1.2
24320
24330
24340
24350
24360
24370
24380
Energy (eV)
Demeter 0.9.24 © Bruce Ravel 2006-2

G

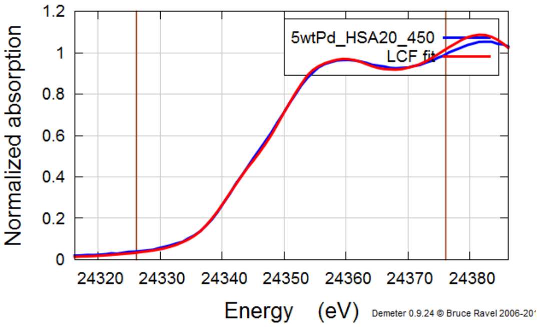
5wtPd_HSA20_450
LCF fit
Normalized absorption
0
0.2
0.4
0.6
0.8
1
1.2
24320
24330
24340
24350
24360
24370
24380
Energy (eV)
Demeter 0.9.24 © Bruce Ravel 2006-20

H

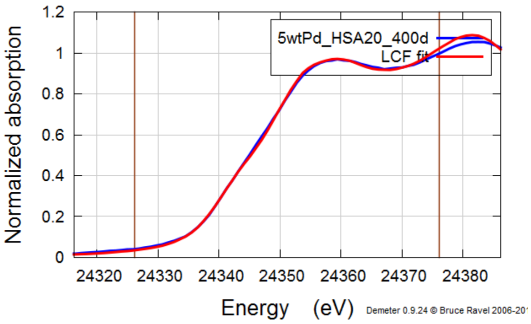
5wtPd_HSA20_400d
LCF fit
Normalized absorption
0
0.2
0.4
0.6
0.8
1
1.2
24320
24330
24340
24350
24360
24370
24380
Energy (eV)
Demeter 0.9.24 © Bruce Ravel 2006-20

I

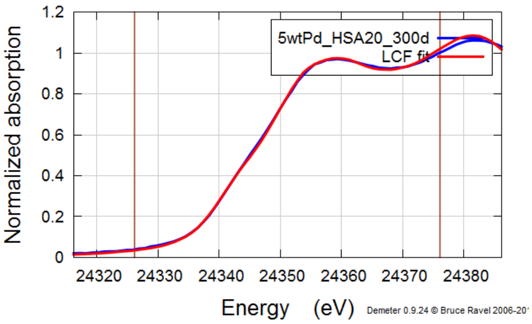
5wtPd_HSA20_300d
LCF fit
Normalized absorption
0
0.2
0.4
0.6
0.8
1
1.2
24320
24330
24340
24350
24360
24370
24380
Energy (eV)
Demeter 0.9.24 © Bruce Ravel 2006-20

J

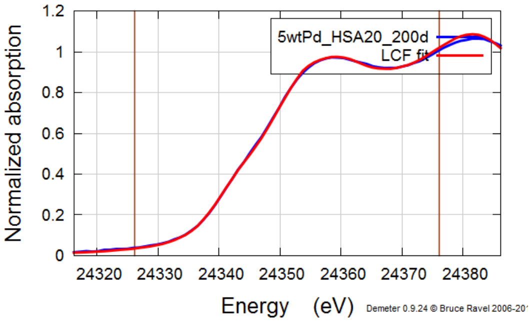

K

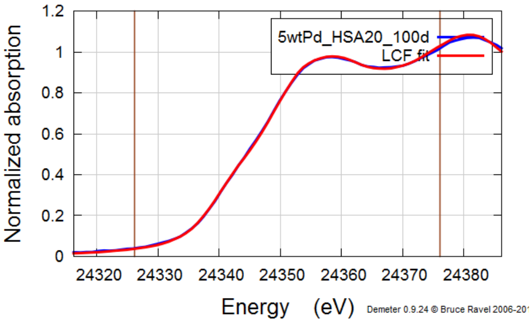

L

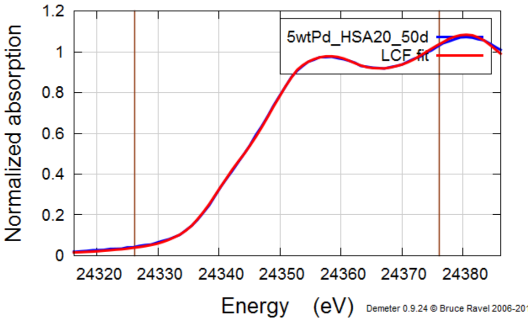

M

Figure S6b. Comparison of the Observed XANES spectra and LCF for 5 wt% Pd loaded onto a High Surface area support for varying temperatures (for the Pd K-edge)

- A. 30°C (ARGON)
- B. 30°C (H2:N2)
- C. 50°C
- D. 100°C
- E. 200°C
- F. 300°C
- G. 400°C
- H. 450°C
- I. 400°C
- J. 300°C
- K. 200°C
- L. 100°C
- M. 50°C

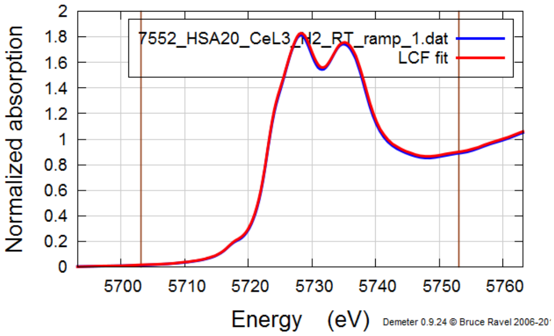

A

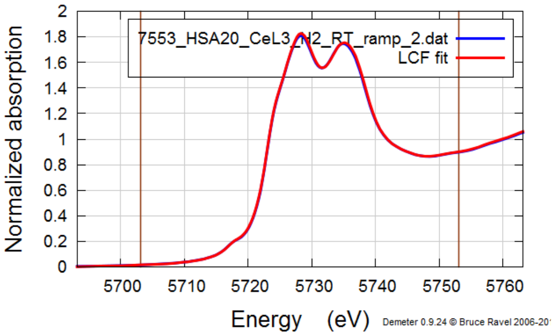

B

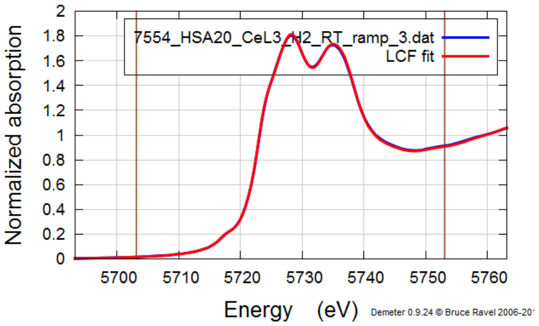

C

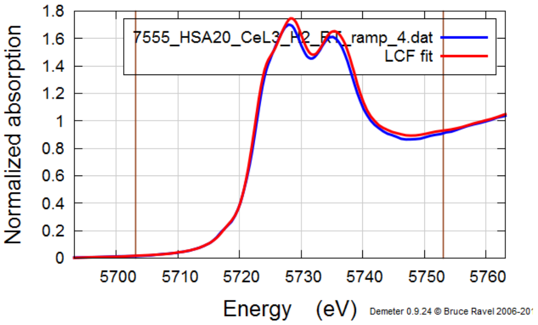

D

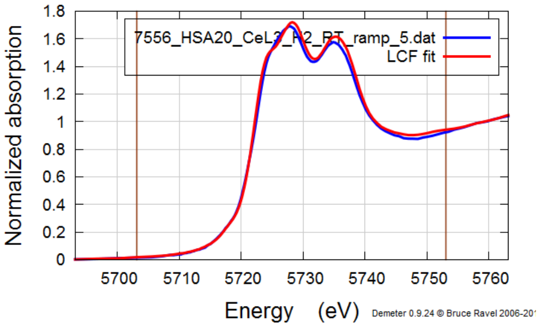

E

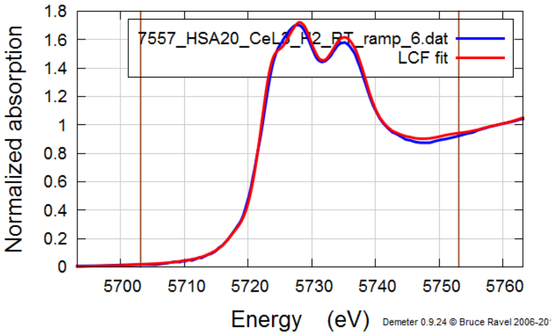

F

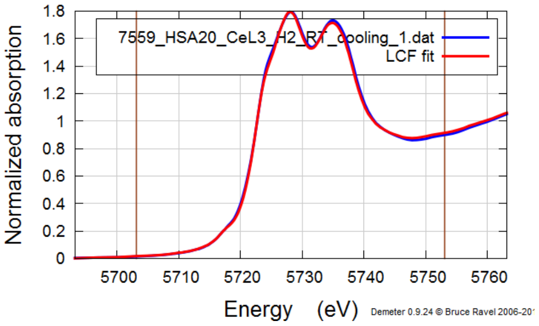

G

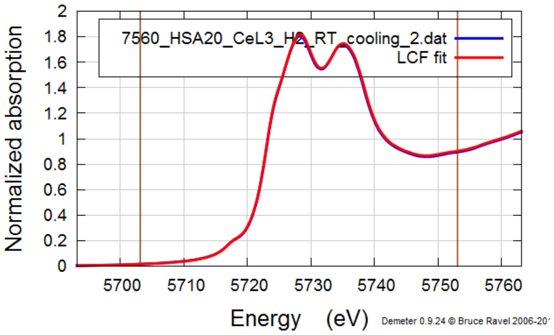

H

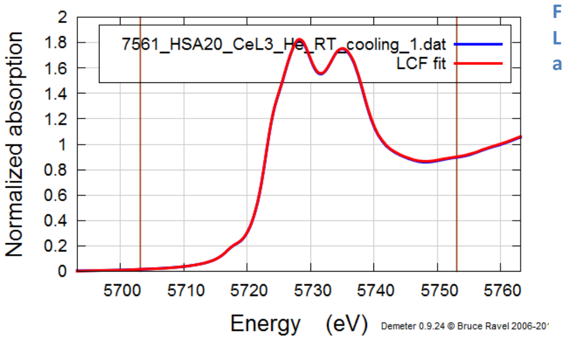

I

Figure S7b. Comparison of the Observed XANES spectra and Linear Combination Fitting (LCF) for the pure High Surface area support for varying temperatures (for the Ce L3-edge)

A. 25°C
B. 118°C
C. 209°C
D. 296°C
E. 387°C
F. 450°C
G. 194°C
H. 100°C
I. 25°C

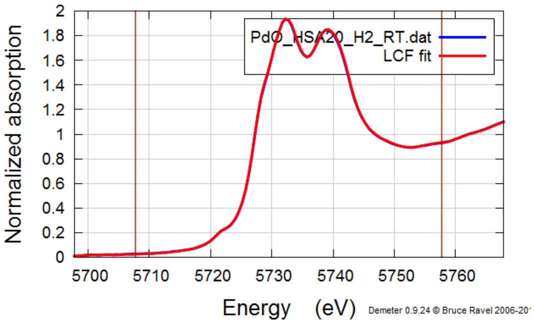
PdO_HSA20_H2_RT.dat
LCF fit
Normalized absorption
Energy (eV)
0
0.2
0.4
0.6
0.8
1
1.2
1.4
1.6
1.8
2
5700
5710
5720
5730
5740
5750
5760
Demeter 0.9.24 © Bruce Ravel 2006-20

A

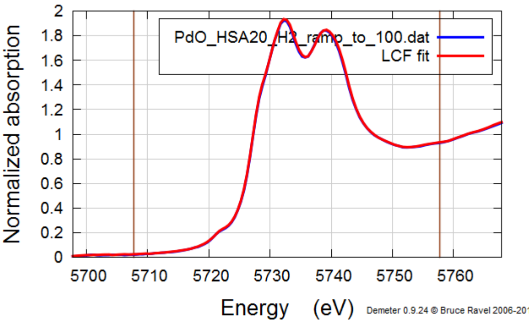
PdO_HSA20_H2_ramp_to_100.dat
LCF fit
Normalized absorption
Energy (eV)
0
0.2
0.4
0.6
0.8
1
1.2
1.4
1.6
1.8
2
5700
5710
5720
5730
5740
5750
5760
Demeter 0.9.24 © Bruce Ravel 2006-20

B

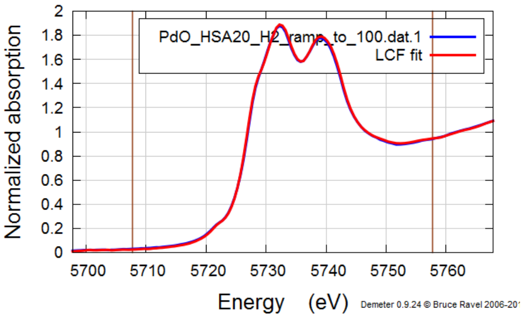
PdO_HSA20_H2_ramp_to_100.dat.1
LCF fit
Normalized absorption
Energy (eV)
0
0.2
0.4
0.6
0.8
1
1.2
1.4
1.6
1.8
2
5700
5710
5720
5730
5740
5750
5760
Demeter 0.9.24 © Bruce Ravel 2006-20

C

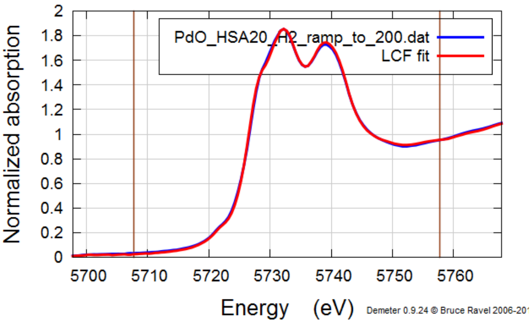
PdO_HSA20_H2_ramp_to_200.dat
LCF fit
Normalized absorption
Energy (eV)
0
0.2
0.4
0.6
0.8
1
1.2
1.4
1.6
1.8
2
5700
5710
5720
5730
5740
5750
5760
Demeter 0.9.24 © Bruce Ravel 2006-20

D

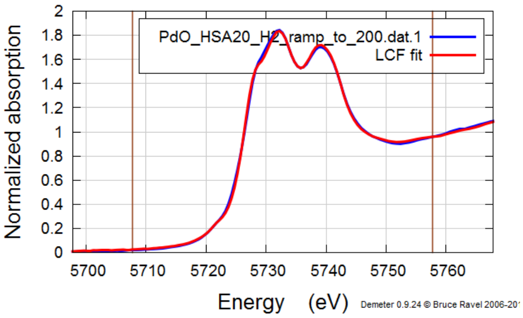
PdO_HSA20_H2_ramp_to_200.dat.1
LCF fit
Normalized absorption
Energy (eV)
0
0.2
0.4
0.6
0.8
1
1.2
1.4
1.6
1.8
2
5700
5710
5720
5730
5740
5750
5760
Demeter 0.9.24 © Bruce Ravel 2006-20

E

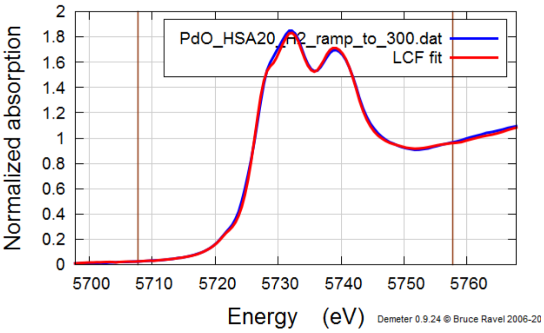
PdO_HSA20_H2_ramp_to_300.dat
LCF fit
Normalized absorption
Energy (eV)
0
0.2
0.4
0.6
0.8
1
1.2
1.4
1.6
1.8
2
5700
5710
5720
5730
5740
5750
5760
Demeter 0.9.24 © Bruce Ravel 2006-20

F

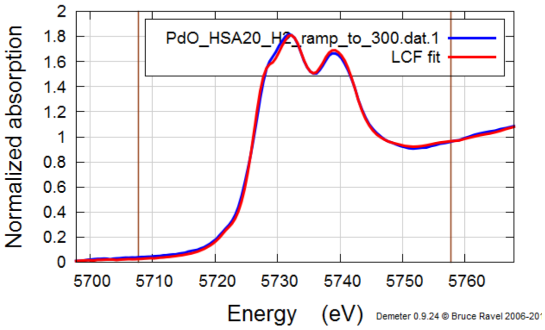
PdO_HSA20_H2_ramp_to_300.dat.1
LCF fit
Normalized absorption
Energy (eV)
0
0.2
0.4
0.6
0.8
1
1.2
1.4
1.6
1.8
2
5700
5710
5720
5730
5740
5750
5760
Demeter 0.9.24 © Bruce Ravel 2006-20

G

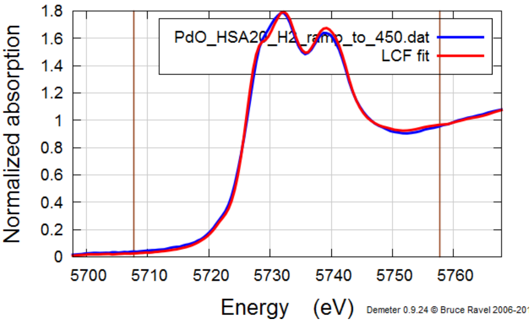
PdO_HSA20_H2_ramp_to_450.dat
LCF fit
Normalized absorption
Energy (eV)
0
0.2
0.4
0.6
0.8
1
1.2
1.4
1.6
1.8
5700
5710
5720
5730
5740
5750
5760
Demeter 0.9.24 © Bruce Ravel 2006-20

H

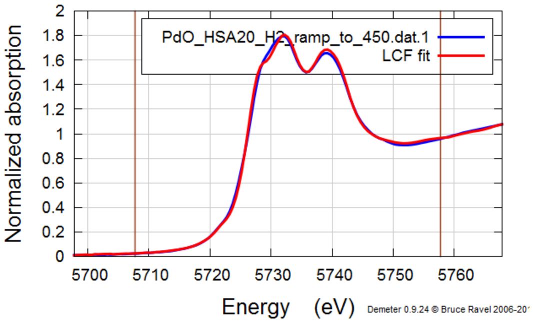
PdO_HSA20_H2_ramp_to_450.dat.1
LCF fit
Normalized absorption
Energy (eV)
0
0.2
0.4
0.6
0.8
1
1.2
1.4
1.6
1.8
2
5700
5710
5720
5730
5740
5750
5760
Demeter 0.9.24 © Bruce Ravel 2006-20

I

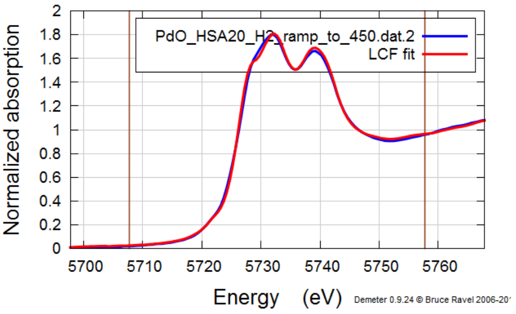
PdO_HSA20_H2_ramp_to_450.dat.2
LCF fit
Normalized absorption
Energy (eV)
0
0.2
0.4
0.6
0.8
1
1.2
1.4
1.6
1.8
2
5700
5710
5720
5730
5740
5750
5760
Demeter 0.9.24 © Bruce Ravel 2006-20

J

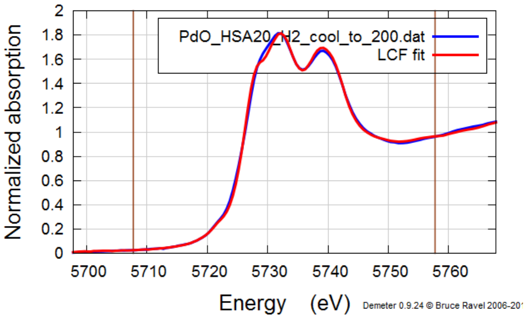

K

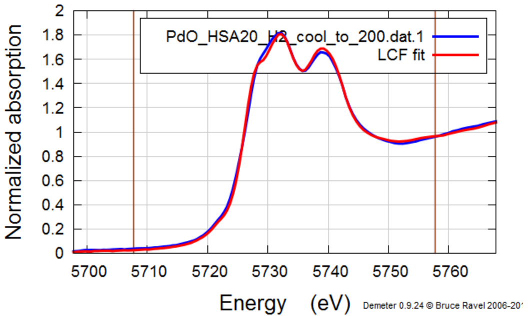

L

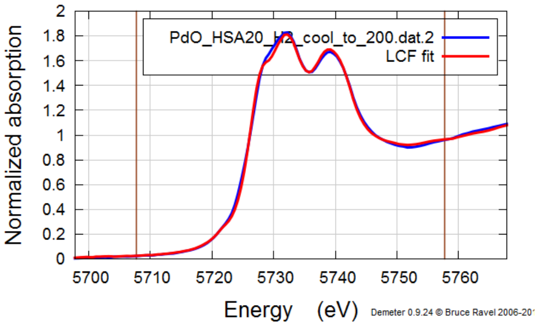

M

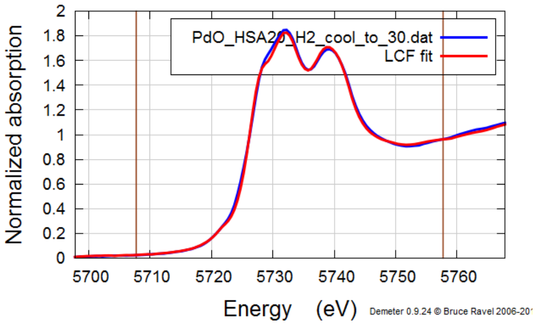

N

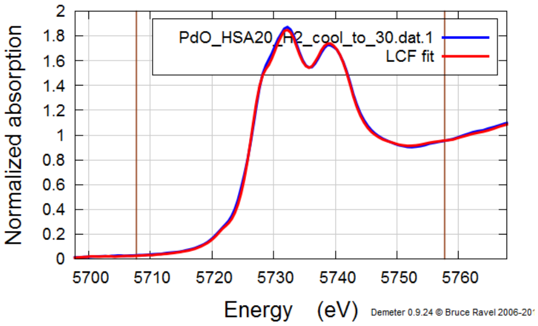

O

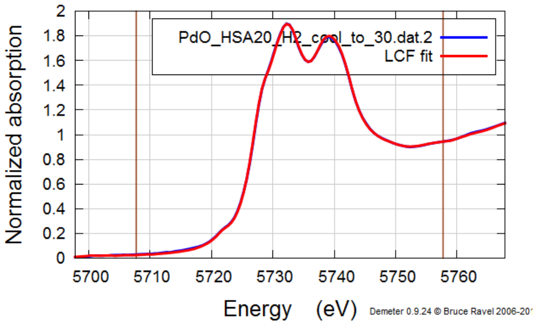

P

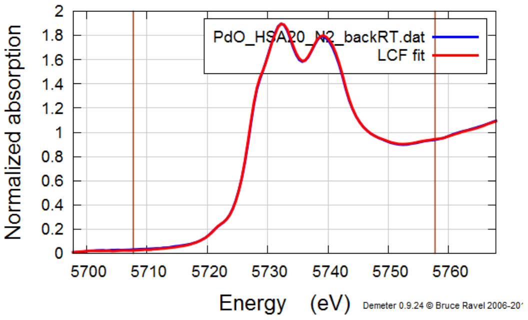

Q

Figure S8b. Comparison of the Observed XANES spectra and Linear Combination Fitting (LCF) for a mixture of PdO and the High Surface area ceria support for varying temperatures (for the Ce L3-edge)

A. 30
B. 33
C. 100
D. 110
E. 200
F. 205
G. 300
H. 305
I. 410
J. 450
K. 440
L. 342
M. 242
N. 192
O. 85
P. 29
Q. 30 (N$_2$)

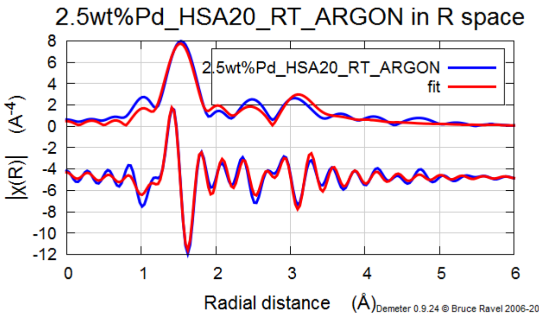
2.5wt%Pd_HSA20_RT_ARGON in R space
2.5wt%Pd_HSA20_RT_ARGON
fit
|χ(R)| (Å-4)
8
6
4
2
0
-2
-4
-6
-8
-10
-12
0
1
2
3
4
5
6
Radial distance (Å)
Demeter 0.9.24 © Bruce Ravel 2006-20

A

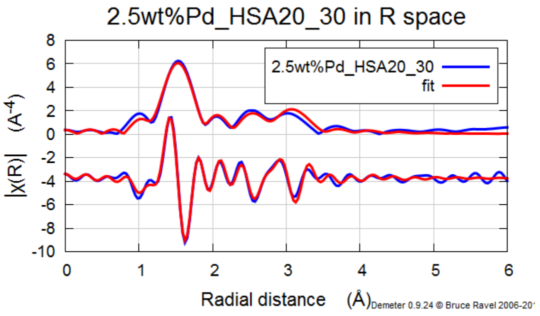
2.5wt%Pd_HSA20_30 in R space
2.5wt%Pd_HSA20_30
fit
|χ(R)| (Å-4)
8
6
4
2
0
-2
-4
-6
-8
-10
0
1
2
3
4
5
6
Radial distance (Å)
Demeter 0.9.24 © Bruce Ravel 2006-20

B

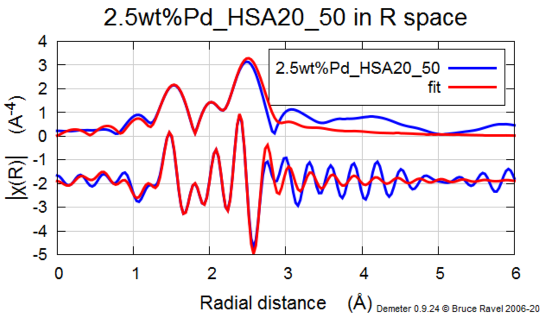
2.5wt%Pd_HSA20_50 in R space
2.5wt%Pd_HSA20_50
fit
|χ(R)| (Å-4)
4
3
2
1
0
-1
-2
-3
-4
-5
0
1
2
3
4
5
6
Radial distance (Å)
Demeter 0.9.24 © Bruce Ravel 2006-20

C

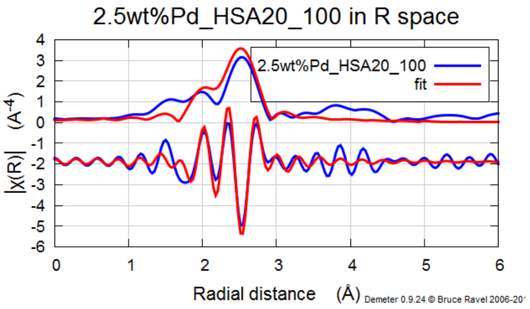
2.5wt%Pd_HSA20_100 in R space
2.5wt%Pd_HSA20_100
fit
|χ(R)| (Å-4)
4
3
2
1
0
-1
-2
-3
-4
-5
-6
0
1
2
3
4
5
6
Radial distance (Å)
Demeter 0.9.24 © Bruce Ravel 2006-20

D

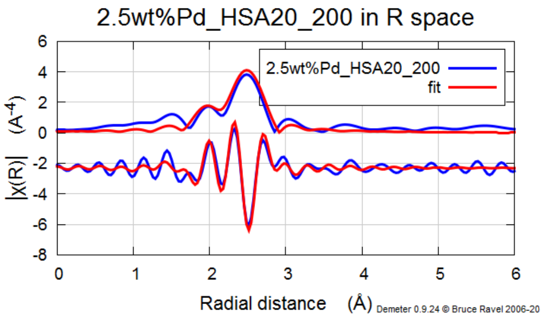
2.5wt%Pd_HSA20_200 in R space
2.5wt%Pd_HSA20_200
fit
|χ(R)| (Å-4)
6
4
2
0
-2
-4
-6
-8
0
1
2
3
4
5
6
Radial distance (Å)
Demeter 0.9.24 © Bruce Ravel 2006-20

E

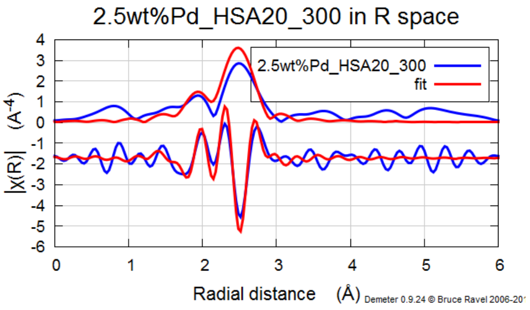
2.5wt%Pd_HSA20_300 in R space
2.5wt%Pd_HSA20_300
fit
|χ(R)| (Å-4)
4
3
2
1
0
-1
-2
-3
-4
-5
-6
0
1
2
3
4
5
6
Radial distance (Å)
Demeter 0.9.24 © Bruce Ravel 2006-20

F

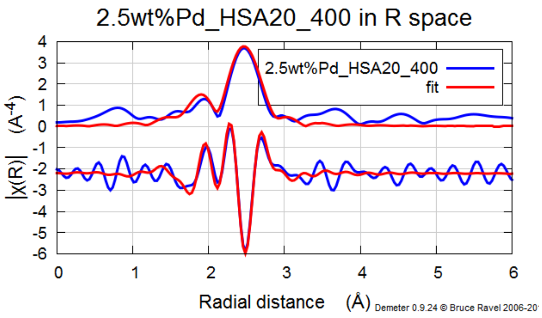
2.5wt%Pd_HSA20_400 in R space
2.5wt%Pd_HSA20_400
fit
|χ(R)| (Å-4)
4
3
2
1
0
-1
-2
-3
-4
-5
-6
0
1
2
3
4
5
6
Radial distance (Å)
Demeter 0.9.24 © Bruce Ravel 2006-20

G

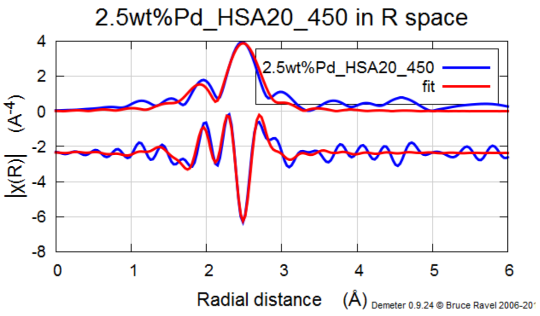
2.5wt%Pd_HSA20_450 in R space
2.5wt%Pd_HSA20_450
fit
|χ(R)| (Å-4)
4
2
0
-2
-4
-6
-8
0
1
2
3
4
5
6
Radial distance (Å)
Demeter 0.9.24 © Bruce Ravel 2006-20

H

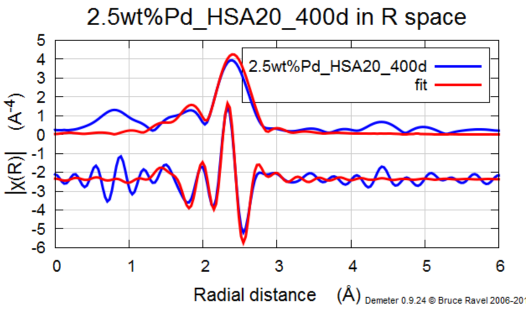
2.5wt%Pd_HSA20_400d in R space
2.5wt%Pd_HSA20_400d
fit
|χ(R)| (Å-4)
5
4
3
2
1
0
-1
-2
-3
-4
-5
-6
0
1
2
3
4
5
6
Radial distance (Å)
Demeter 0.9.24 © Bruce Ravel 2006-20

I

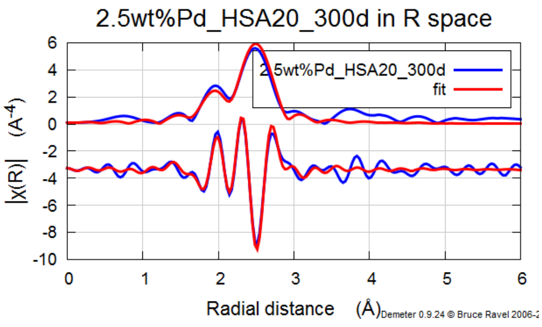
2.5wt%Pd_HSA20_300d in R space
2.5wt%Pd_HSA20_300d
fit
|χ(R)| (Å-4)
6
4
2
0
-2
-4
-6
-8
-10
0
1
2
3
4
5
6
Radial distance (Å)
Demeter 0.9.24 © Bruce Ravel 2006-2

J

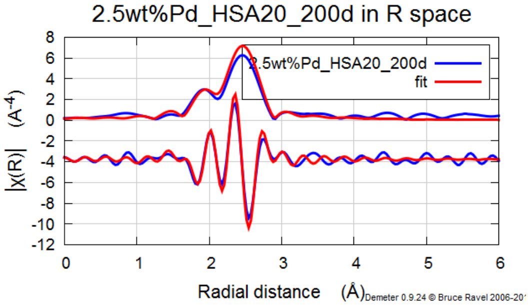

K

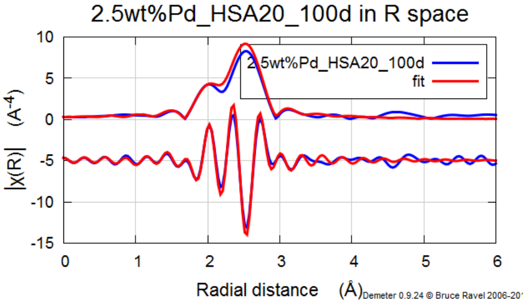

L

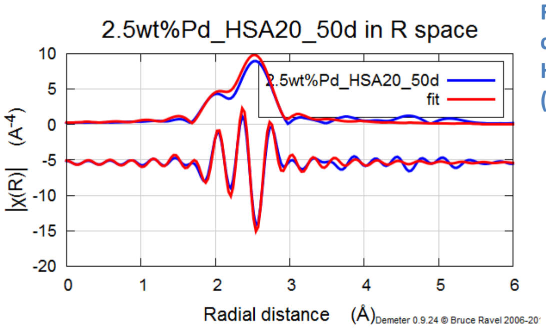

M

Figure S9b. Comparison of the Observed and calculated EXAFS data for 2.5 wt% Pd loaded onto a High Surface area support for varying temperatures (for the Pd K-edge)

- **A.** **30°C (ARGON)**
- **B.** **30°C (H2:N2)**
- **C.** **50°C**
- **D.** **100°C**
- **E.** **200°C**
- **F.** **300°C**
- **G.** **400°C**
- **H.** **450°C**
- **I.** **400°C**
- **J.** **300°C**
- **K.** **200°C**
- **L.** **100°C**
- **M.** **50°C**

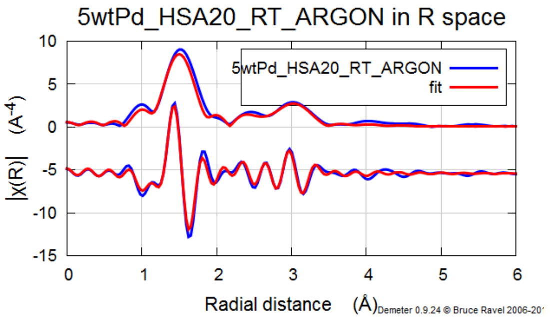
5wtPd_HSA20_RT_ARGON in R space
5wtPd_HSA20_RT_ARGON
fit
10
5
0
-5
-10
-15
|χ(R)| (Å^{-4})
0
1
2
3
4
5
6
Radial distance   (Å)
Demeter 0.9.24 © Bruce Ravel 2006-20

A

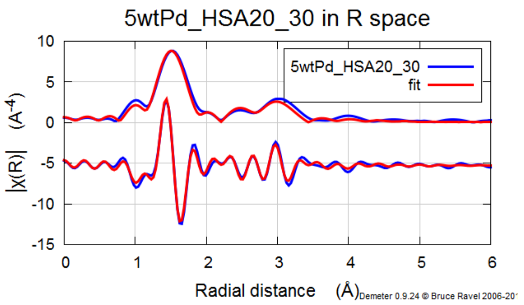
5wtPd_HSA20_30 in R space
5wtPd_HSA20_30
fit
10
5
0
-5
-10
-15
|χ(R)| (Å^{-4})
0
1
2
3
4
5
6
Radial distance   (Å)
Demeter 0.9.24 © Bruce Ravel 2006-20

B

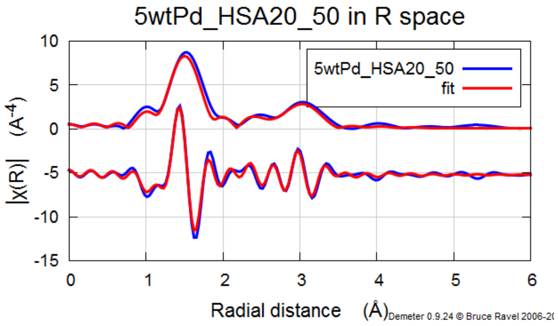
5wtPd_HSA20_50 in R space
5wtPd_HSA20_50
fit
10
5
0
-5
-10
-15
|χ(R)| (Å^{-4})
0
1
2
3
4
5
6
Radial distance   (Å)
Demeter 0.9.24 © Bruce Ravel 2006-2

C

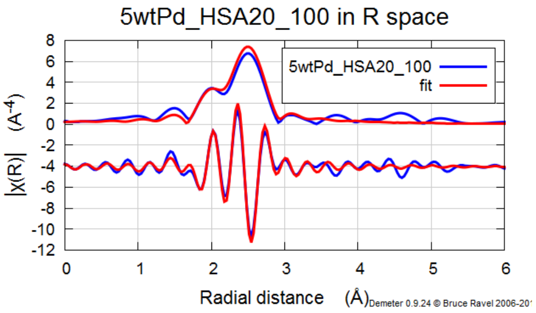
5wtPd_HSA20_100 in R space
5wtPd_HSA20_100
fit
8
6
4
2
0
-2
-4
-6
-8
-10
-12
|χ(R)| (Å^{-4})
0
1
2
3
4
5
6
Radial distance   (Å)
Demeter 0.9.24 © Bruce Ravel 2006-20

D

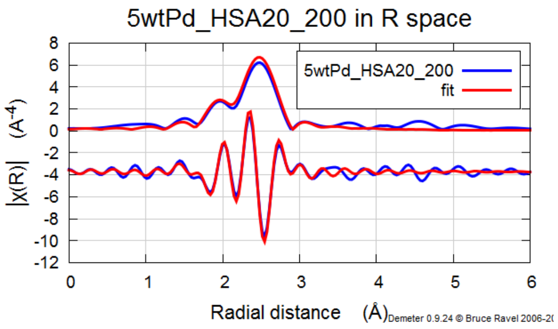
5wtPd_HSA20_200 in R space
5wtPd_HSA20_200
fit
8
6
4
2
0
-2
-4
-6
-8
-10
-12
|χ(R)| (Å^{-4})
0
1
2
3
4
5
6
Radial distance   (Å)
Demeter 0.9.24 © Bruce Ravel 2006-2

E

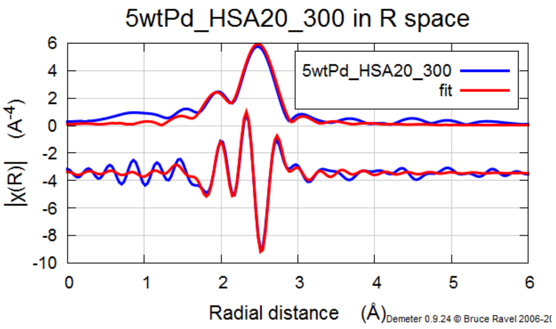
5wtPd_HSA20_300 in R space
5wtPd_HSA20_300
fit
6
4
2
0
-2
-4
-6
-8
-10
|χ(R)| (Å^{-4})
0
1
2
3
4
5
6
Radial distance   (Å)
Demeter 0.9.24 © Bruce Ravel 2006-2

F

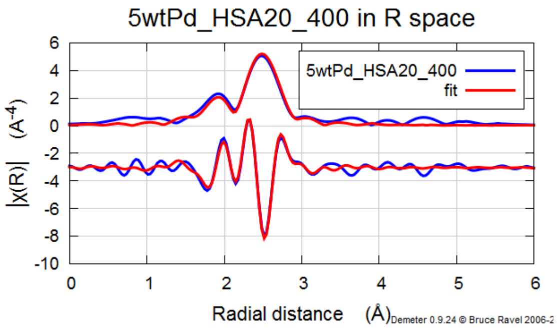
5wtPd_HSA20_400 in R space
5wtPd_HSA20_400
fit
6
4
2
0
-2
-4
-6
-8
-10
|χ(R)| (Å^{-4})
0
1
2
3
4
5
6
Radial distance   (Å)
Demeter 0.9.24 © Bruce Ravel 2006-2

G

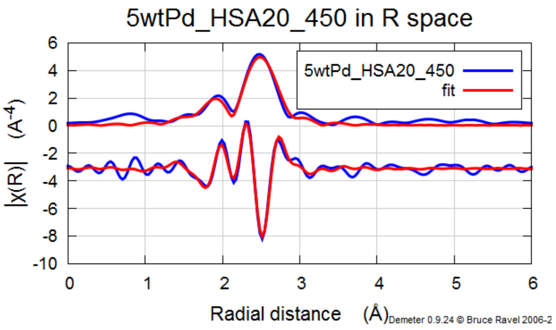
5wtPd_HSA20_450 in R space
5wtPd_HSA20_450
fit
6
4
2
0
-2
-4
-6
-8
-10
|χ(R)| (Å^{-4})
0
1
2
3
4
5
6
Radial distance   (Å)
Demeter 0.9.24 © Bruce Ravel 2006-2

H

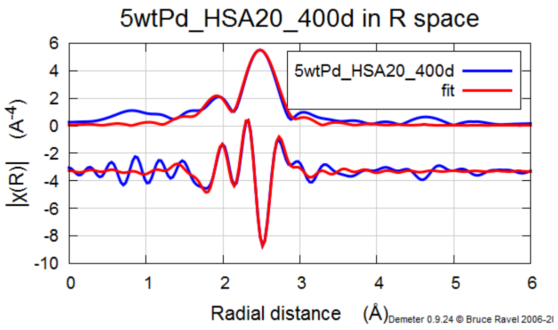
5wtPd_HSA20_400d in R space
5wtPd_HSA20_400d
fit
6
4
2
0
-2
-4
-6
-8
-10
|χ(R)| (Å^{-4})
0
1
2
3
4
5
6
Radial distance   (Å)
Demeter 0.9.24 © Bruce Ravel 2006-2

I

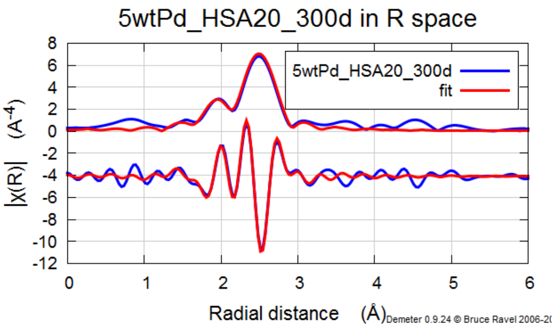
5wtPd_HSA20_300d in R space
5wtPd_HSA20_300d
fit
8
6
4
2
0
-2
-4
-6
-8
-10
-12
|χ(R)| (Å^{-4})
0
1
2
3
4
5
6
Radial distance   (Å)
Demeter 0.9.24 © Bruce Ravel 2006-2

J

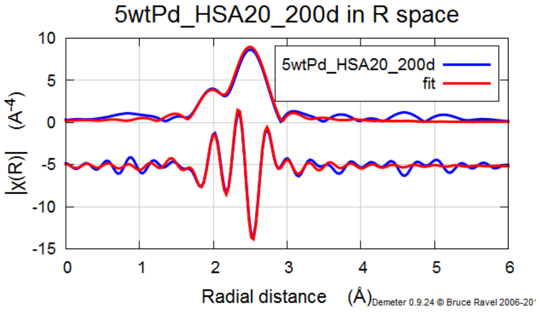

K

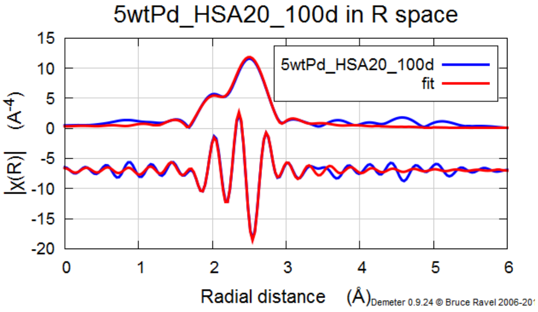

L

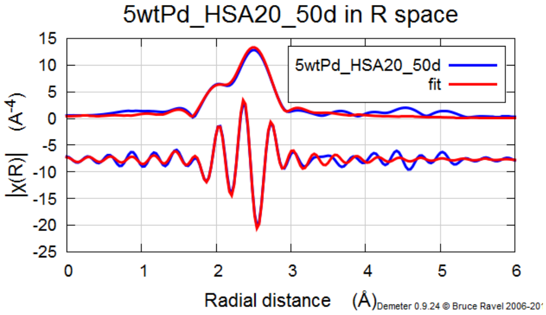

M

Figure S10b. Comparison of the Observed and calculated EXAFS data for 5 wt% Pd loaded onto a High Surface area support for varying temperatures (for the Pd K-edge)

- **A. 30°C (ARGON)**
- **B. 30°C (H2:N2)**
- **C. 50°C**
- **D. 100°C**
- **E. 200°C**
- **F. 300°C**
- **G. 400°C**
- **H. 450°C**
- **I. 400°C**
- **J. 300°C**
- **K. 200°C**
- **L. 100°C**
- **M. 50°C**

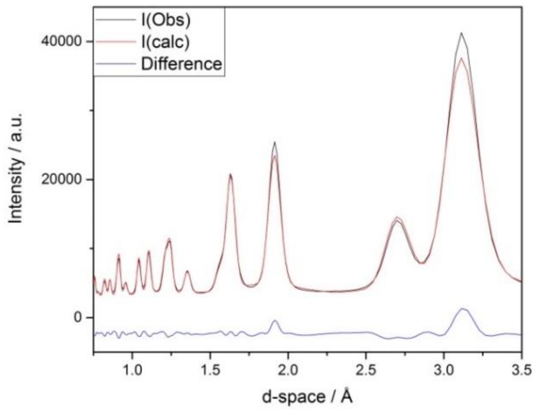
I(Obs)
I(calc)
Difference
Intensity / a.u.
40000
20000
0
1.0
1.5
2.0
2.5
3.0
3.5
d-space / Å

A

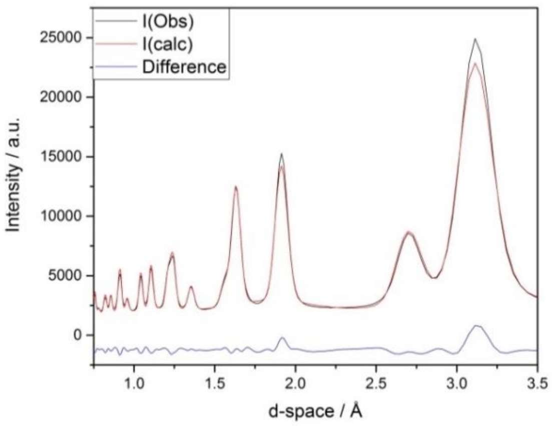
I(Obs)
I(calc)
Difference
Intensity / a.u.
25000
20000
15000
10000
5000
0
1.0
1.5
2.0
2.5
3.0
3.5
d-space / Å

B

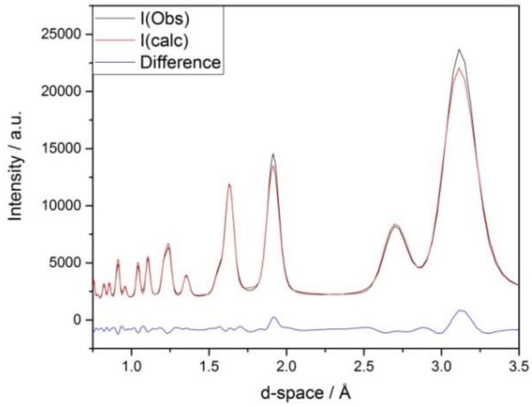
I(Obs)
I(calc)
Difference
Intensity / a.u.
25000
20000
15000
10000
5000
0
1.0
1.5
2.0
2.5
3.0
3.5
d-space / Å

C

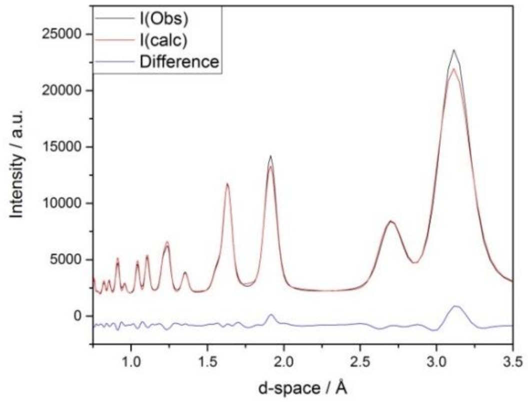
I(Obs)
I(calc)
Difference
Intensity / a.u.
25000
20000
15000
10000
5000
0
1.0
1.5
2.0
2.5
3.0
3.5
d-space / Å

D

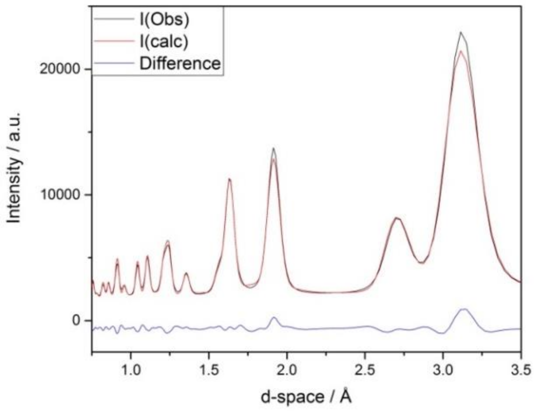
I(Obs)
I(calc)
Difference
Intensity / a.u.
20000
10000
0
1.0
1.5
2.0
2.5
3.0
3.5
d-space / Å

E

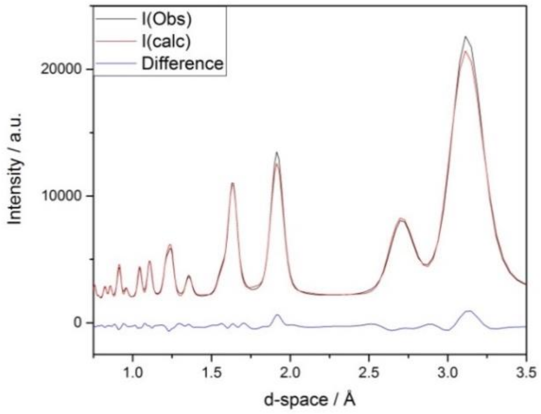
I(Obs)
I(calc)
Difference
Intensity / a.u.
20000
10000
0
1.0
1.5
2.0
2.5
3.0
3.5
d-space / Å

F

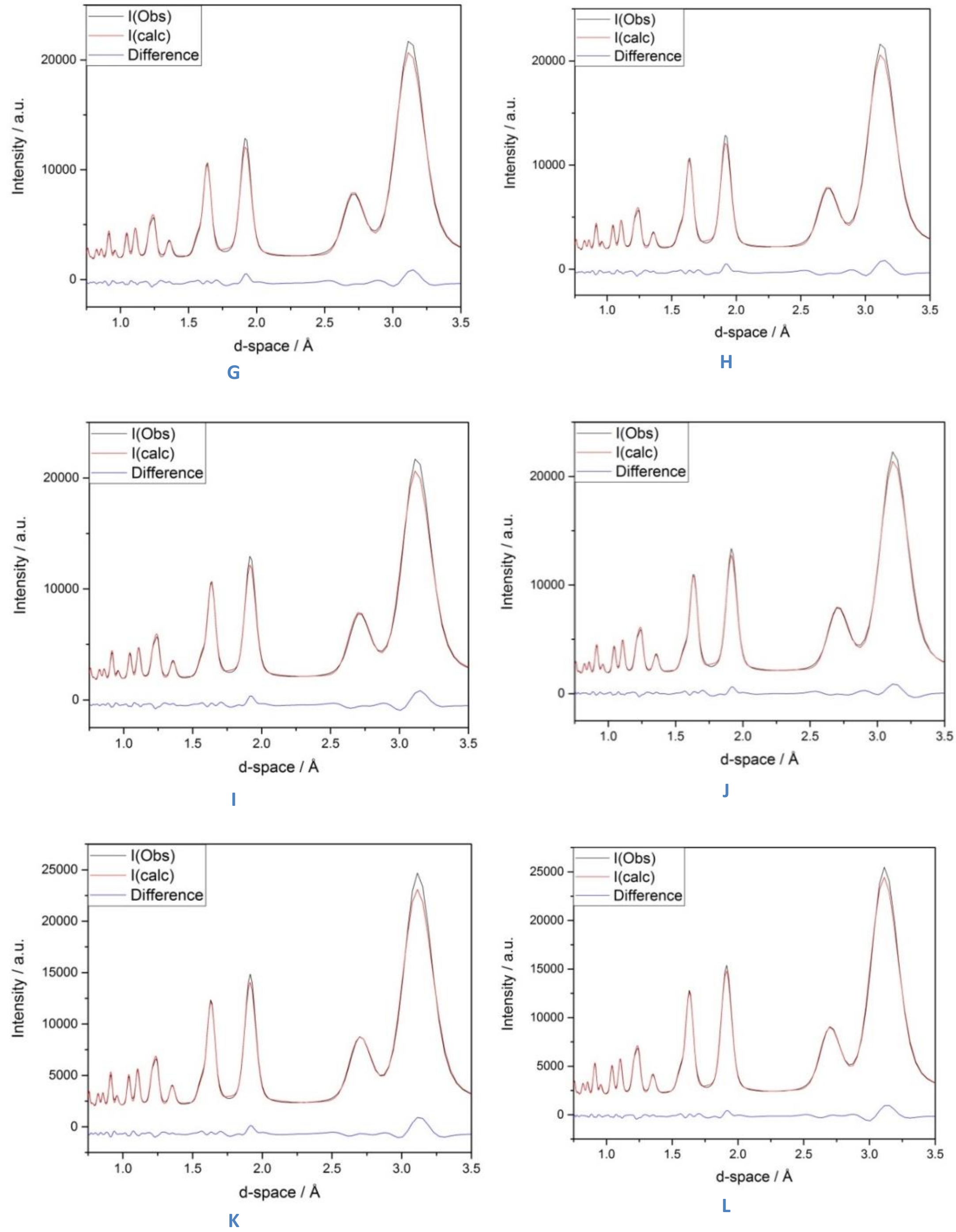

Figure S11b. Comparison of the Observed and calculated XRD data for the pure High Surface Ceria area support for varying temperatures

- **A.** **30°C**
- **B.** **50°C**
- **C.** **100°C**
- **D.** **200°C**
- **E.** **300°C**
- **F.** **400°C**
- **G.** **450°C**
- **H.** **400°C**
- **I.** **300°C**
- **J.** **200°C**
- **K.** **100°C**
- **L.** **50°C**

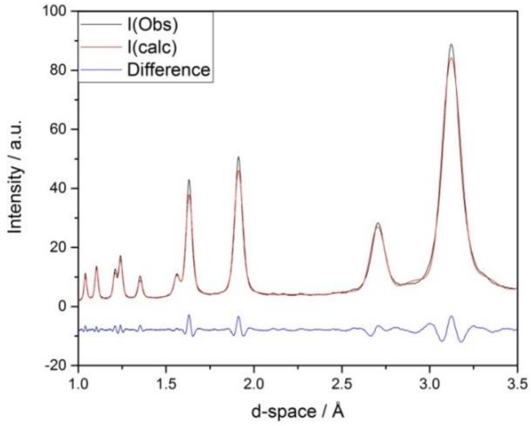
I(Obs)
I(calc)
Difference
Intensity / a.u.
d-space / Å
100
80
60
40
20
0
-20
1.0
1.5
2.0
2.5
3.0
3.5

A

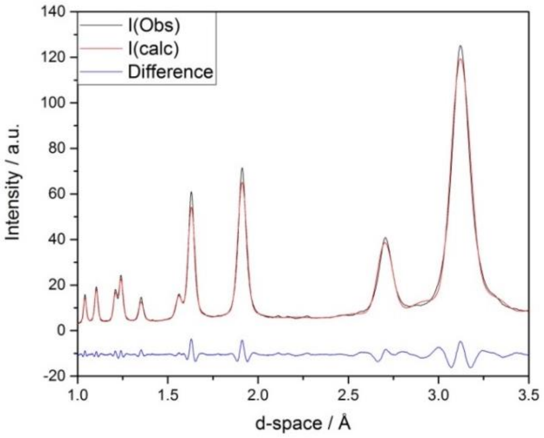
I(Obs)
I(calc)
Difference
Intensity / a.u.
d-space / Å
140
120
100
80
60
40
20
0
-20
1.0
1.5
2.0
2.5
3.0
3.5

B

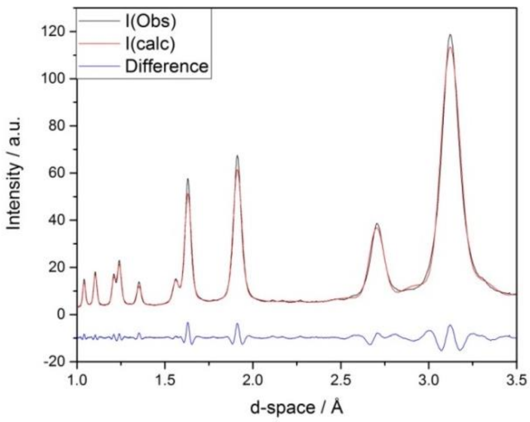
I(Obs)
I(calc)
Difference
Intensity / a.u.
d-space / Å
120
100
80
60
40
20
0
-20
1.0
1.5
2.0
2.5
3.0
3.5

C

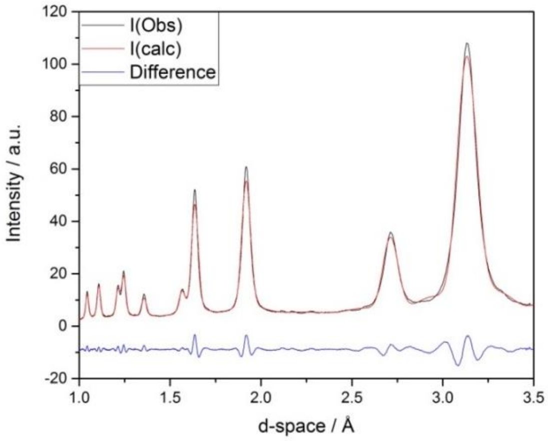
I(Obs)
I(calc)
Difference
Intensity / a.u.
d-space / Å
120
100
80
60
40
20
0
-20
1.0
1.5
2.0
2.5
3.0
3.5

D

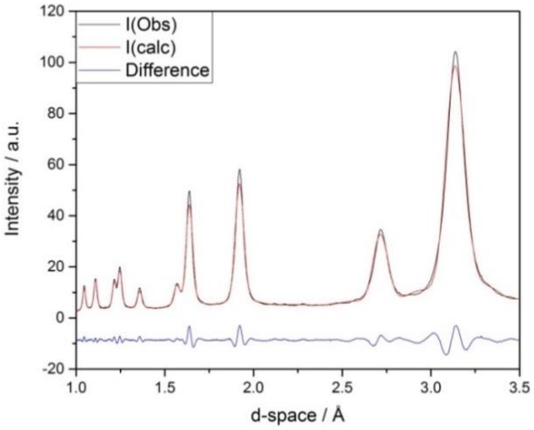
I(Obs)
I(calc)
Difference
Intensity / a.u.
d-space / Å
120
100
80
60
40
20
0
-20
1.0
1.5
2.0
2.5
3.0
3.5

E

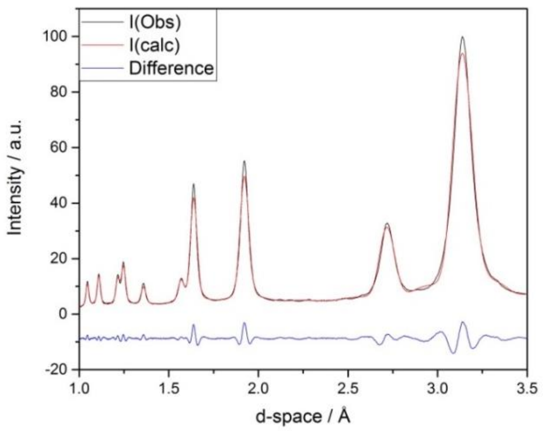
I(Obs)
I(calc)
Difference
Intensity / a.u.
d-space / Å
100
80
60
40
20
0
-20
1.0
1.5
2.0
2.5
3.0
3.5

F

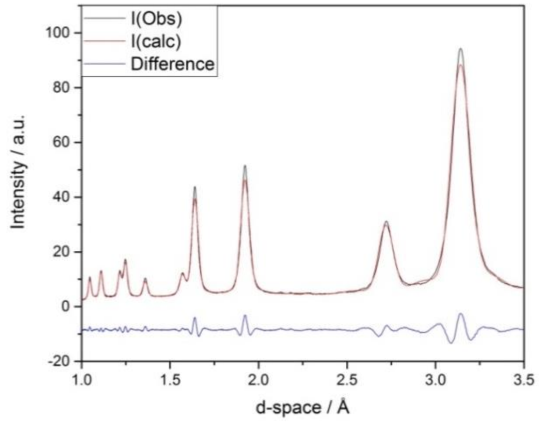
I(Obs)
I(calc)
Difference
Intensity / a.u.
-20
0
20
40
60
80
100
d-space / Å
1.0
1.5
2.0
2.5
3.0
3.5

G

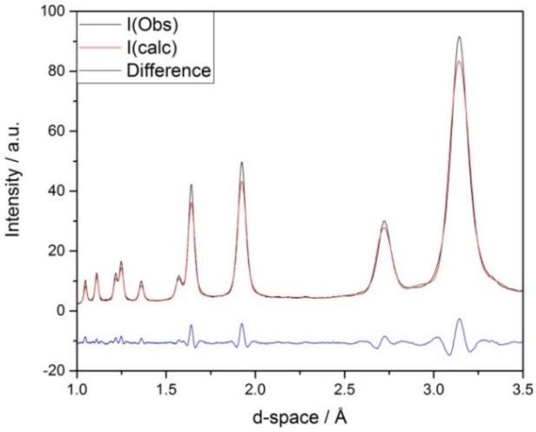
I(Obs)
I(calc)
Difference
Intensity / a.u.
-20
0
20
40
60
80
100
d-space / Å
1.0
1.5
2.0
2.5
3.0
3.5

H

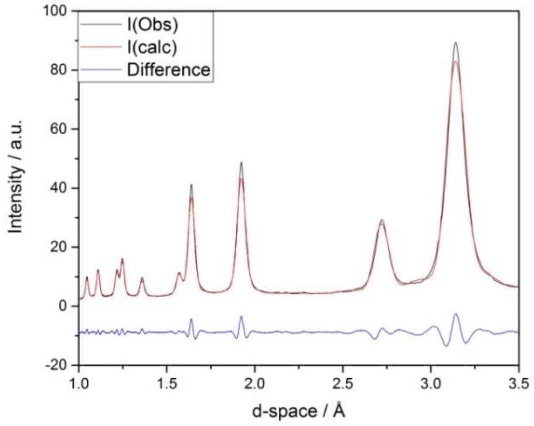
I(Obs)
I(calc)
Difference
Intensity / a.u.
-20
0
20
40
60
80
100
d-space / Å
1.0
1.5
2.0
2.5
3.0
3.5

I

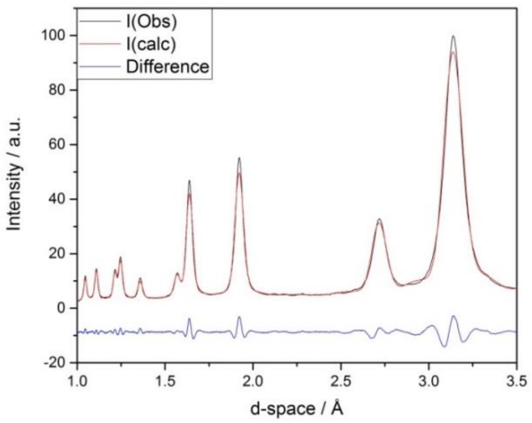
I(Obs)
I(calc)
Difference
Intensity / a.u.
-20
0
20
40
60
80
100
d-space / Å
1.0
1.5
2.0
2.5
3.0
3.5

J

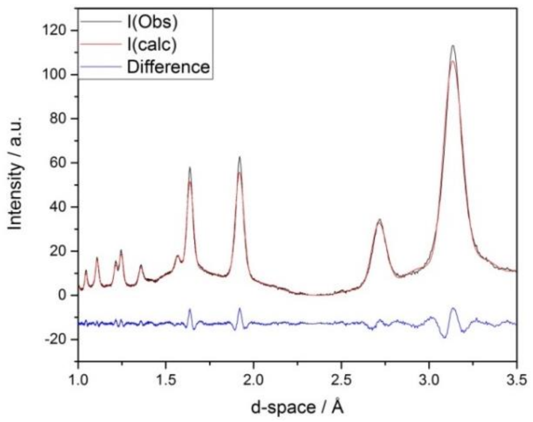
I(Obs)
I(calc)
Difference
Intensity / a.u.
-20
0
20
40
60
80
100
120
d-space / Å
1.0
1.5
2.0
2.5
3.0
3.5

K

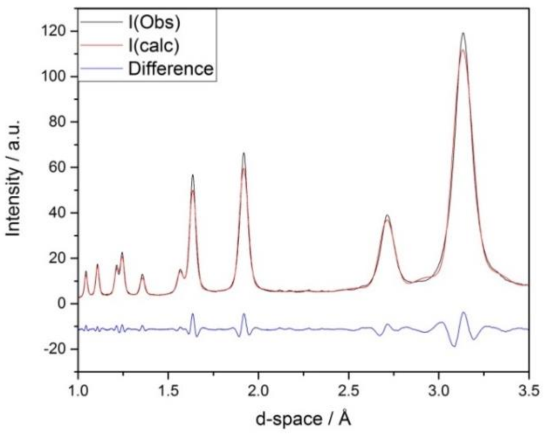
I(Obs)
I(calc)
Difference
Intensity / a.u.
-20
0
20
40
60
80
100
120
d-space / Å
1.0
1.5
2.0
2.5
3.0
3.5

L

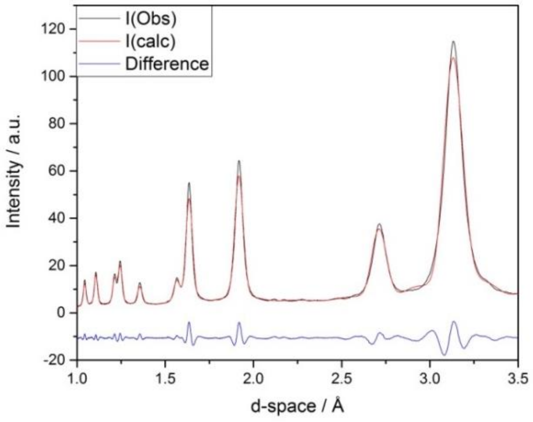

M

Figure S12b. Comparison of the Observed and calculated XRD data for 1 wt% Pd loaded onto a High Surface area support for varying temperatures

- **A. 30°C (ARGON)**
- **B. 30°C (H2:N2)**
- **C. 50°C**
- **D. 100°C**
- **E. 200°C**
- **F. 300°C**
- **G. 400°C**
- **H. 450°C**
- **I. 400°C**
- **J. 300°C**
- **K. 200°C**
- **L. 100°C**
- **M. 50°C**

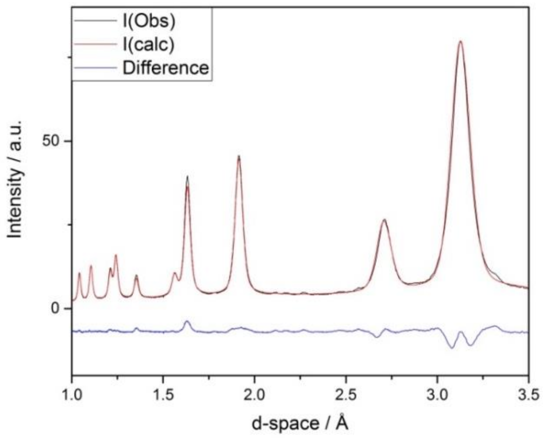
I(Obs)
I(calc)
Difference
Intensity / a.u.
50
0
1.0
1.5
2.0
2.5
3.0
3.5
d-space / Å

A

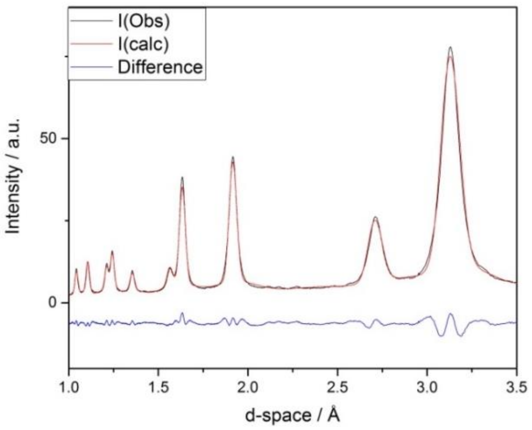
I(Obs)
I(calc)
Difference
Intensity / a.u.
50
0
1.0
1.5
2.0
2.5
3.0
3.5
d-space / Å

B

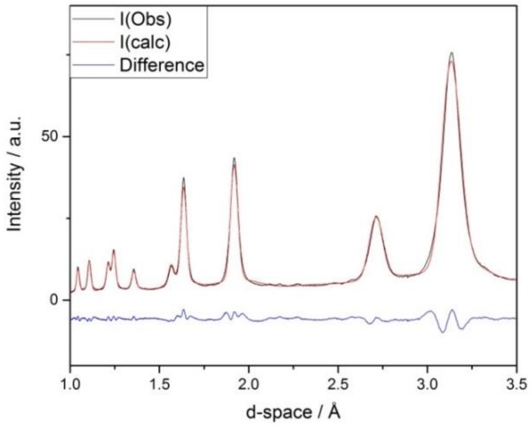
I(Obs)
I(calc)
Difference
Intensity / a.u.
50
0
1.0
1.5
2.0
2.5
3.0
3.5
d-space / Å

C

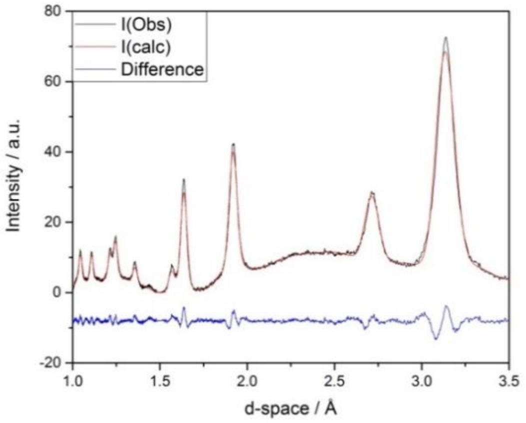
80
60
40
20
0
-20
I(Obs)
I(calc)
Difference
Intensity / a.u.
1.0
1.5
2.0
2.5
3.0
3.5
d-space / Å

D

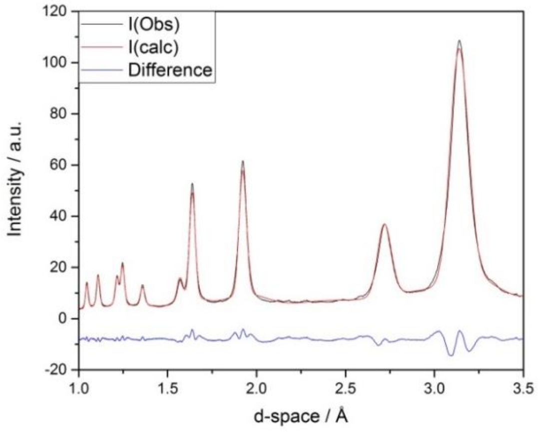
120
100
80
60
40
20
0
-20
I(Obs)
I(calc)
Difference
Intensity / a.u.
1.0
1.5
2.0
2.5
3.0
3.5
d-space / Å

E

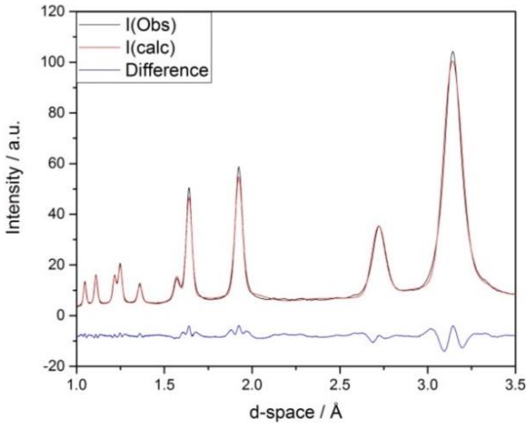
120
100
80
60
40
20
0
-20
I(Obs)
I(calc)
Difference
Intensity / a.u.
1.0
1.5
2.0
2.5
3.0
3.5
d-space / Å

F

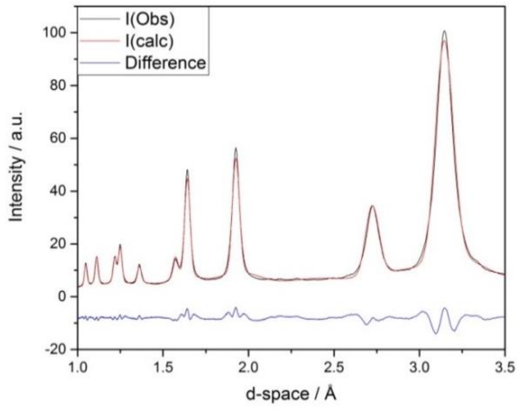
100
80
60
40
20
0
-20
I(Obs)
I(calc)
Difference
Intensity / a.u.
1.0
1.5
2.0
2.5
3.0
3.5
d-space / Å

G

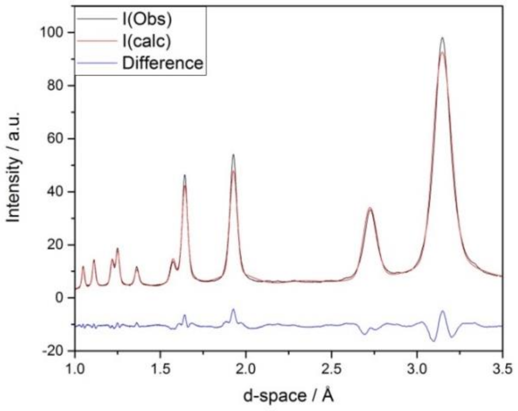
100
80
60
40
20
0
-20
I(Obs)
I(calc)
Difference
Intensity / a.u.
1.0
1.5
2.0
2.5
3.0
3.5
d-space / Å

H

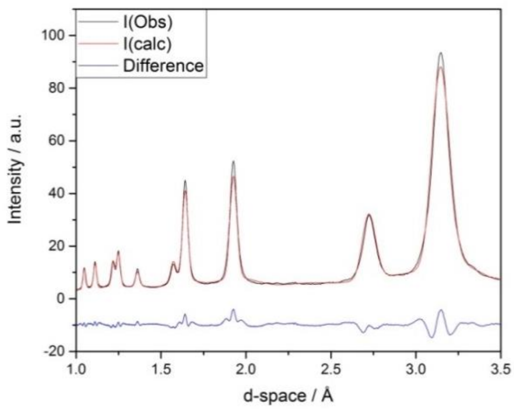

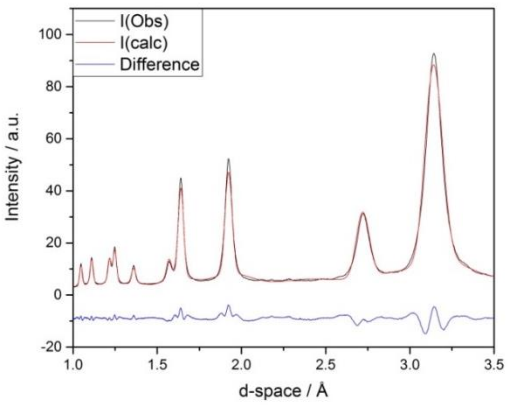

I

J

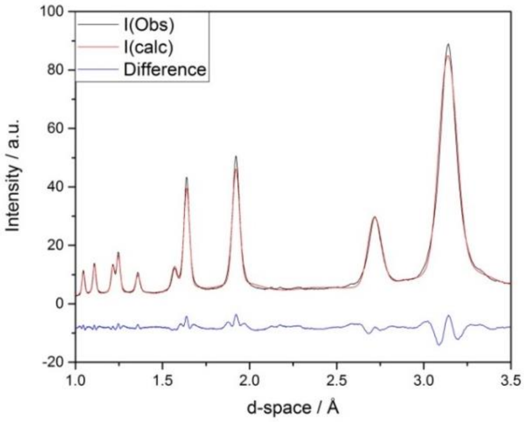

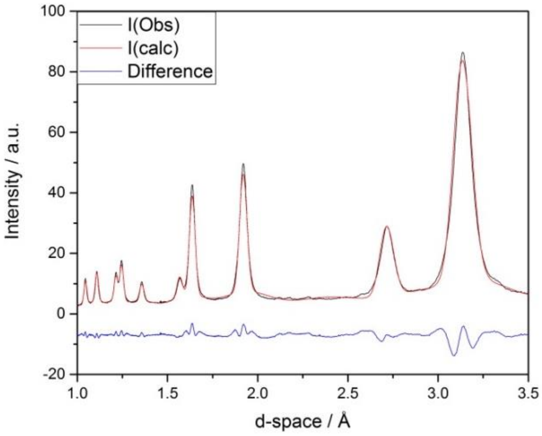

K

L

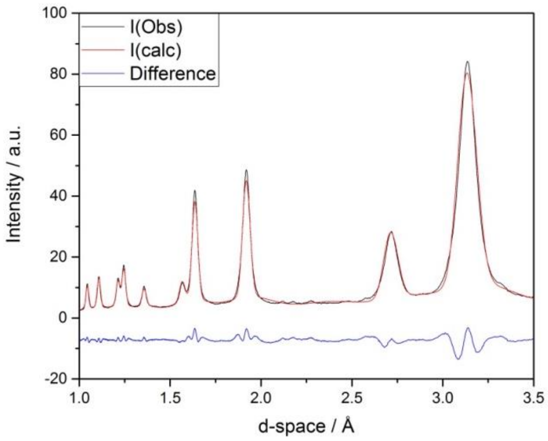

M

Figure S13b. Comparison of the Observed and calculated XRD data for 2.5 wt% Pd loaded onto a High Surface area support for varying temperatures

A. 30°C (ARGON)
B. 30°C (H2:N2)
C. 50°C
D. 100°C
E. 200°C
F. 300°C
G. 400°C
H. 450°C
I. 400°C
J. 300°C
K. 200°C
L. 100°C
M. 50°C

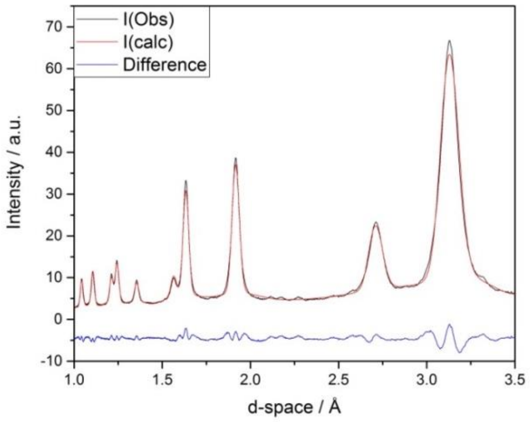
I(Obs)
I(calc)
Difference
Intensity / a.u.
d-space / Å
-10
0
10
20
30
40
50
60
70
1.0
1.5
2.0
2.5
3.0
3.5

A

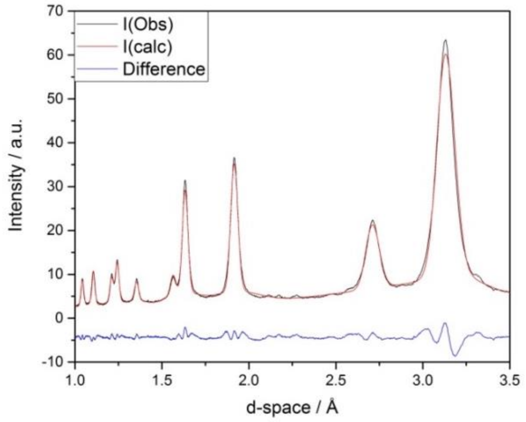
I(Obs)
I(calc)
Difference
Intensity / a.u.
d-space / Å
-10
0
10
20
30
40
50
60
70
1.0
1.5
2.0
2.5
3.0
3.5

B

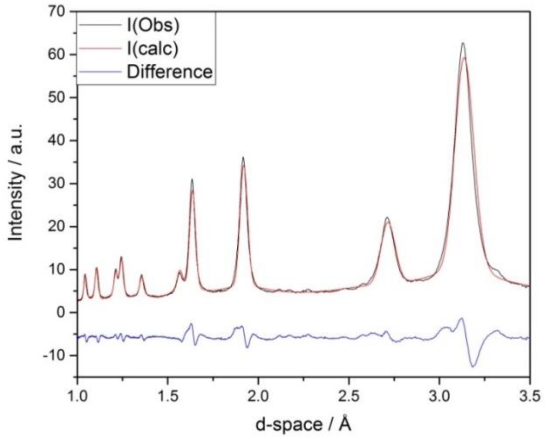
I(Obs)
I(calc)
Difference
Intensity / a.u.
d-space / Å
-10
0
10
20
30
40
50
60
70
1.0
1.5
2.0
2.5
3.0
3.5

C

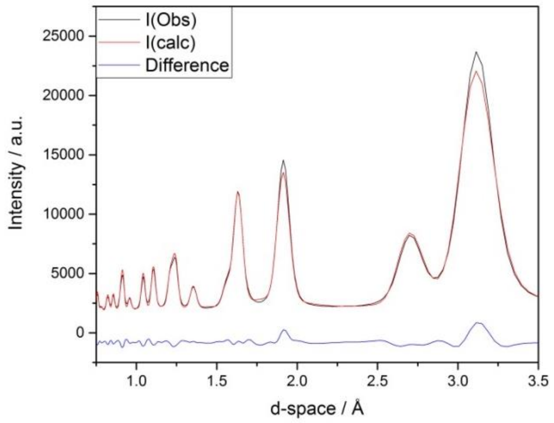
I(Obs)
I(calc)
Difference
Intensity / a.u.
d-space / Å
0
5000
10000
15000
20000
25000
1.0
1.5
2.0
2.5
3.0
3.5

D

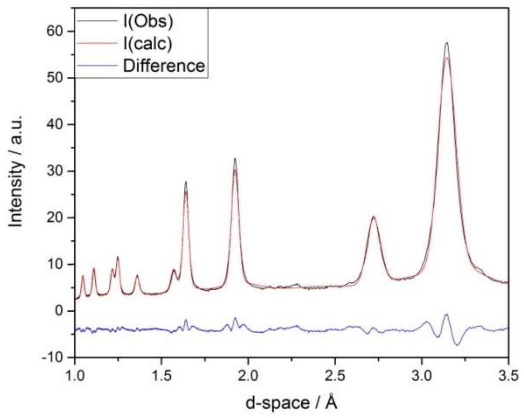
I(Obs)
I(calc)
Difference
Intensity / a.u.
d-space / Å
-10
0
10
20
30
40
50
60
1.0
1.5
2.0
2.5
3.0
3.5

E

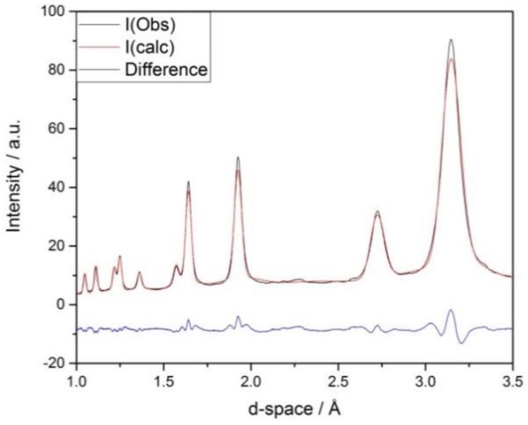
I(Obs)
I(calc)
Difference
Intensity / a.u.
d-space / Å
-20
0
20
40
60
80
100
1.0
1.5
2.0
2.5
3.0
3.5

F

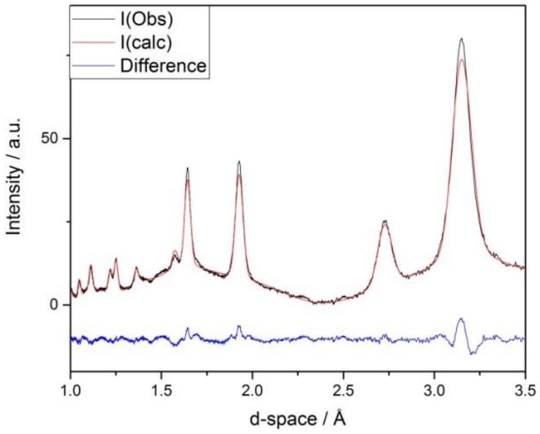
I(Obs)
I(calc)
Difference
Intensity / a.u.
50
0
1.0
1.5
2.0
2.5
3.0
3.5
d-space / Å

G

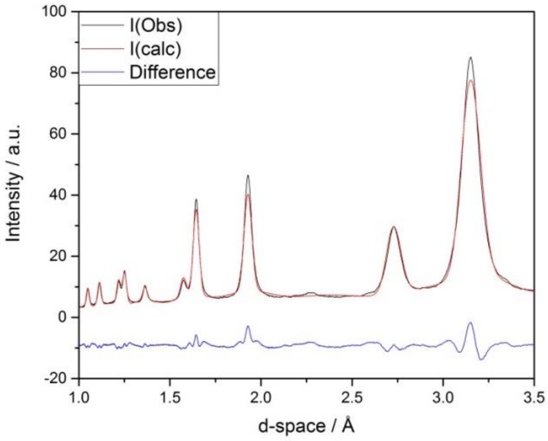
I(Obs)
I(calc)
Difference
Intensity / a.u.
100
80
60
40
20
0
-20
1.0
1.5
2.0
2.5
3.0
3.5
d-space / Å

H

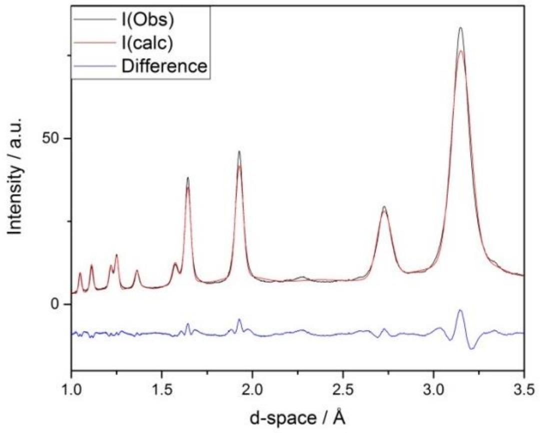
I(Obs)
I(calc)
Difference
Intensity / a.u.
50
0
1.0
1.5
2.0
2.5
3.0
3.5
d-space / Å

I

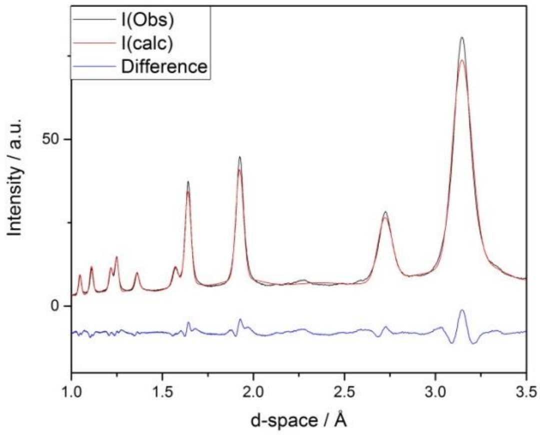
I(Obs)
I(calc)
Difference
Intensity / a.u.
50
0
1.0
1.5
2.0
2.5
3.0
3.5
d-space / Å

J

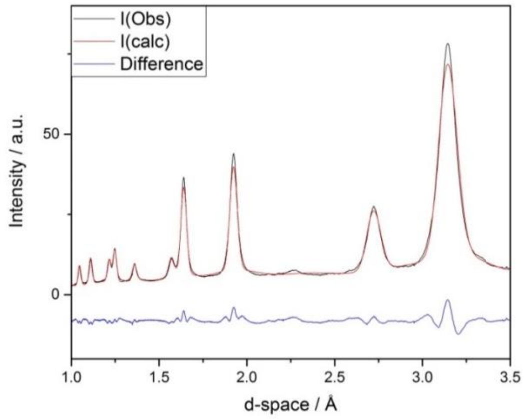
I(Obs)
I(calc)
Difference
Intensity / a.u.
50
0
1.0
1.5
2.0
2.5
3.0
3.5
d-space / Å

K

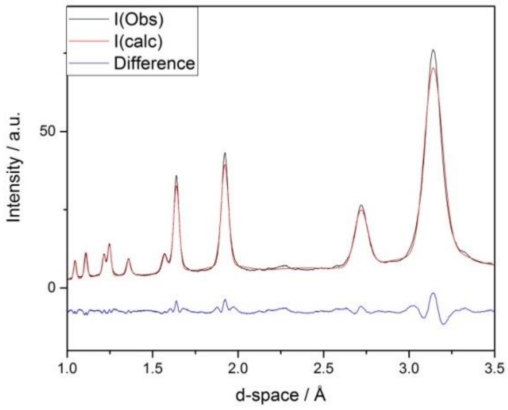
I(Obs)
I(calc)
Difference
Intensity / a.u.
50
0
1.0
1.5
2.0
2.5
3.0
3.5
d-space / Å

L

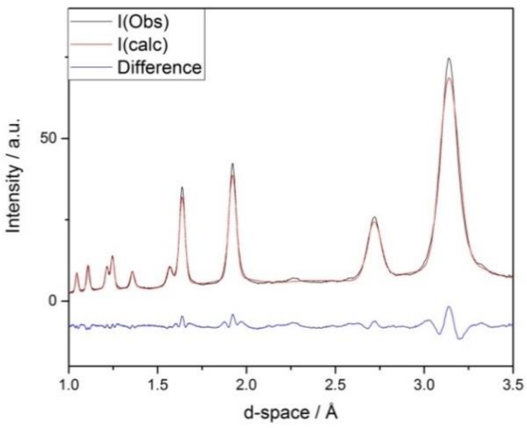

M

Figure S14b. Comparison of the Observed and calculated XRD data for 5 wt% Pd loaded onto a High Surface area support for varying temperatures

A. 30°C (ARGON)
B. 30°C (H2:N2)
C. 50°C
D. 100°C
E. 200°C
F. 300°C
G. 400°C
H. 450°C
I. 400°C
J. 300°C
K. 200°C
L. 100°C
M. 50°C

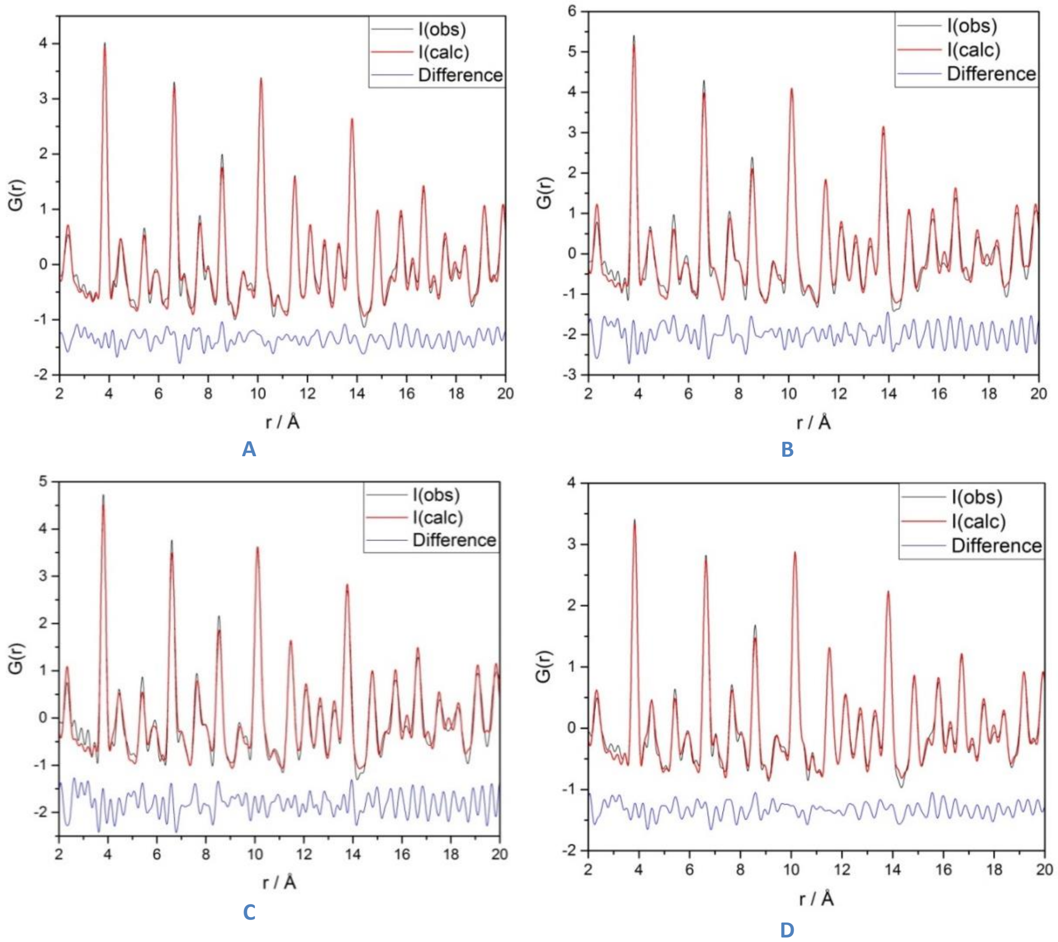

A

B

C

D

Figure S15b. Example of the fits for the PDF analysis, showing a comparison of the Observed Data (I(obs)), Calculated Data (I(calc)) and the difference between these respective data sets.

A. High Surface area ceria support
B. 1 wt% Pd on a High Surface area ceria support
C. 2.5 wt% Pd on a High Surface area ceria support
D. 5 wt% Pd on a High Surface area ceria support

Appendix for Chapter 6

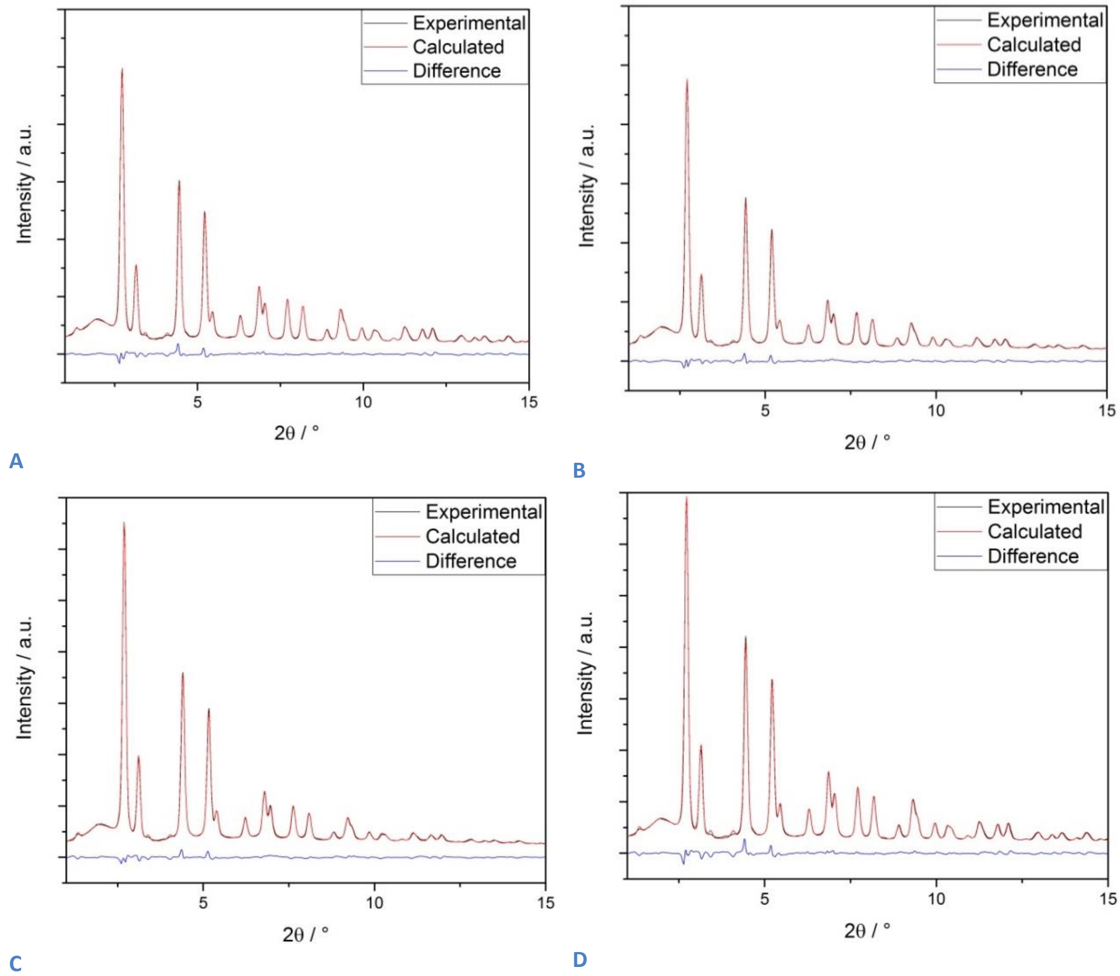

Figure S1c:

(A) Comparison of the fit between the experimental and calculated data for the κ-$Ce_{0.5}Zr_{0.5}O_2$ at 30°C under air

(B) Comparison of the fit between the experimental and calculated data for the κ-$Ce_{0.5}Zr_{0.5}O_2$ at 500°C under air

(C) Comparison of the fit between the experimental and calculated data for the κ-$Ce_{0.5}Zr_{0.5}O_2$ at 900°C under air

(D) Comparison of the fit between the experimental and calculated data for the κ-$Ce_{0.5}Zr_{0.5}O_2$ back at 30°C under air

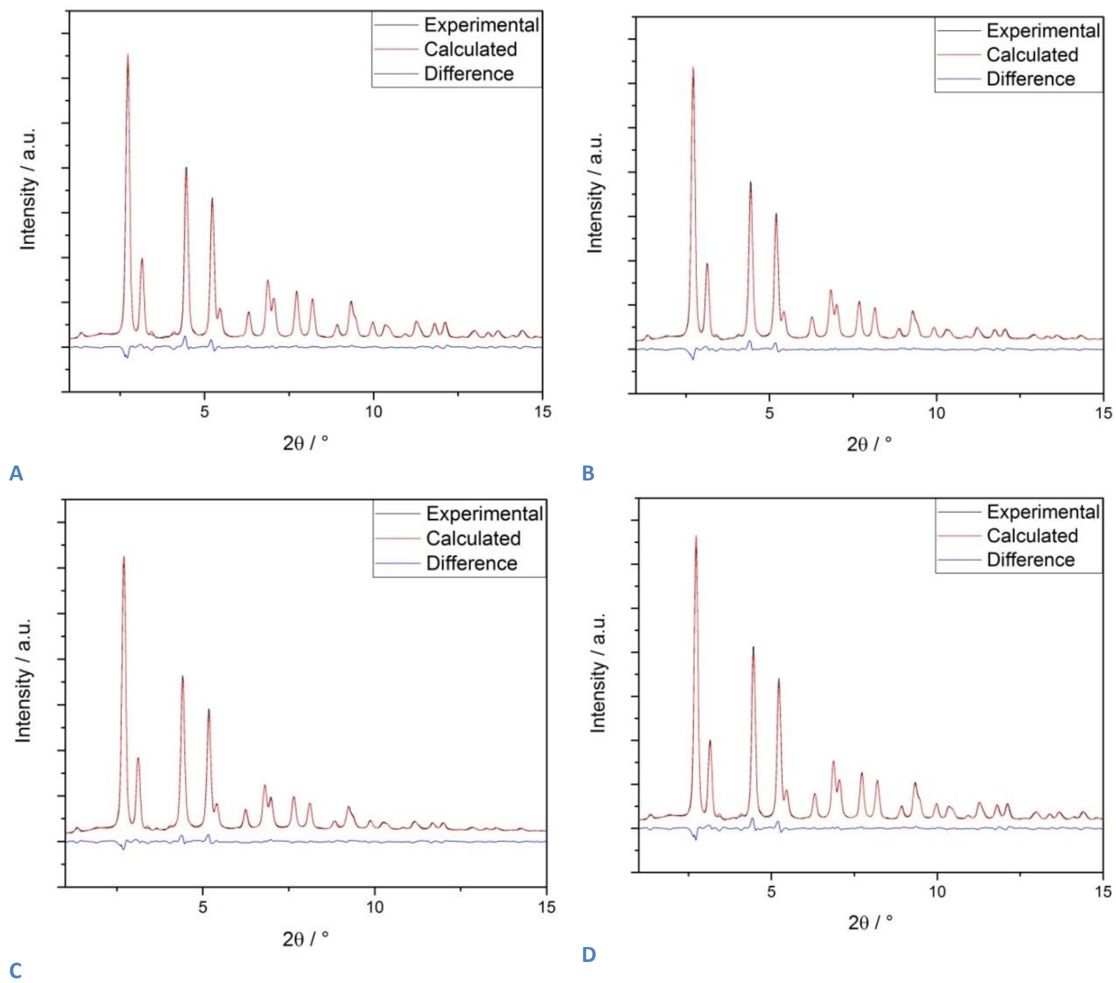

Figure S2c:

(A) Comparison of the fit between the experimental and calculated data for the 1Pd/κ-$Ce_{0.5}Zr_{0.5}O_2$ at 30°C under air

(B) Comparison of the fit between the experimental and calculated data for the 1Pd/κ-$Ce_{0.5}Zr_{0.5}O_2$ at 500°C under air

(C) Comparison of the fit between the experimental and calculated data for the 1Pd/κ-$Ce_{0.5}Zr_{0.5}O_2$ at 900°C under air

(D) Comparison of the fit between the experimental and calculated data for the 1Pd/κ-$Ce_{0.5}Zr_{0.5}O_2$ back at 30°C under air

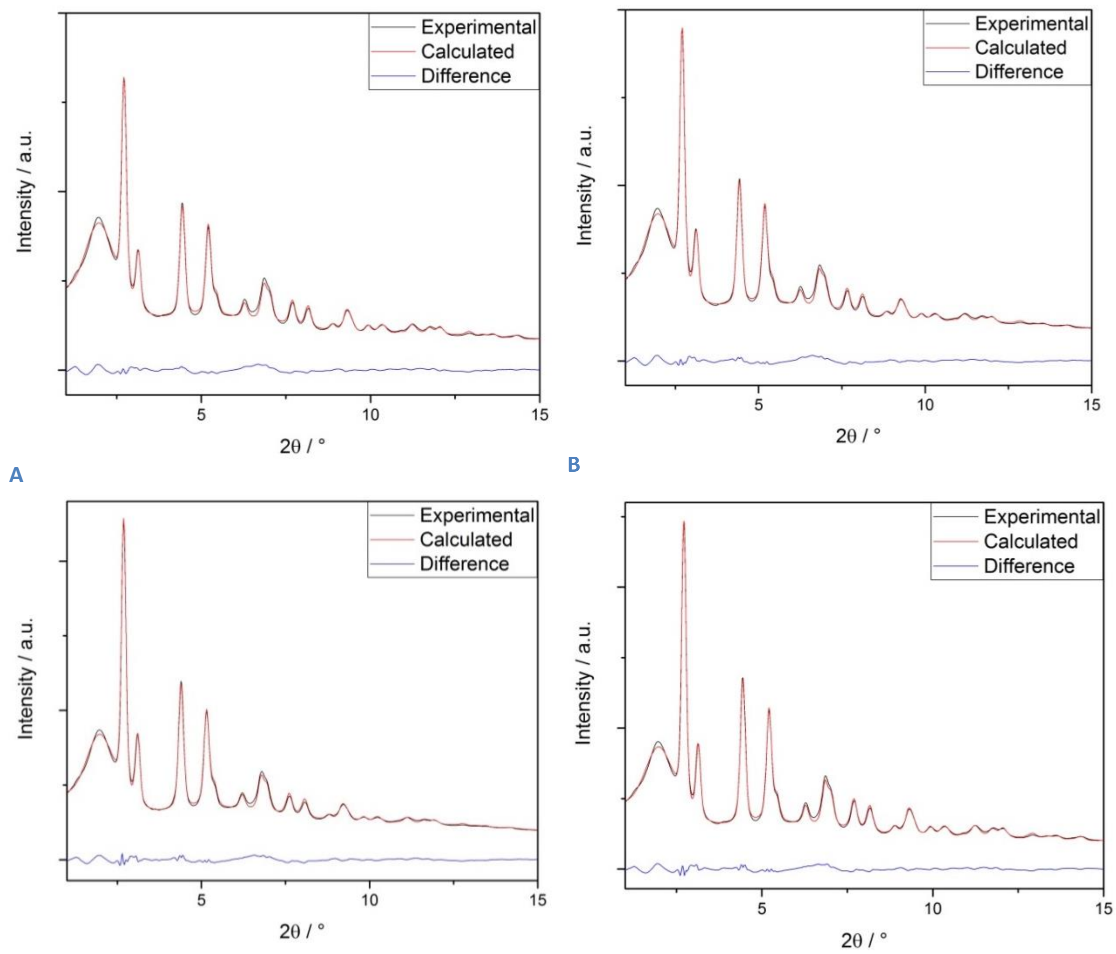

A

B

C

D

Figure S3c:
(A) Comparison of the fit between the experimental and calculated data for the 1Pd/$Ce_{0.5}Zr_{0.5}O_2$ at 30°C under air
(B) Comparison of the fit between the experimental and calculated data for the 1Pd/$Ce_{0.5}Zr_{0.5}O_2$ at 500°C under air
(C) Comparison of the fit between the experimental and calculated data for the 1Pd/$Ce_{0.5}Zr_{0.5}O_2$ at 900°C under air
(D) Comparison of the fit between the experimental and calculated data for the 1Pd/$Ce_{0.5}Zr_{0.5}O_2$ back at 30°C under air

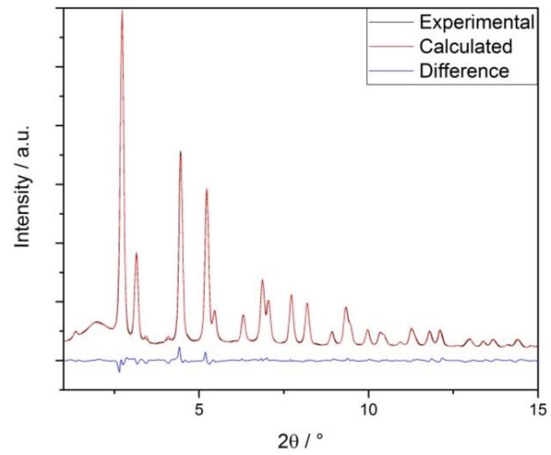
Experimental
Calculated
Difference
Intensity / a.u.
5
10
15
2θ / °

A

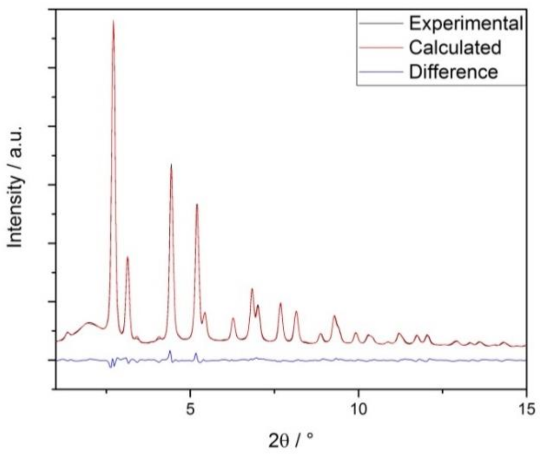
Experimental
Calculated
Difference
Intensity / a.u.
5
10
15
2θ / °

B

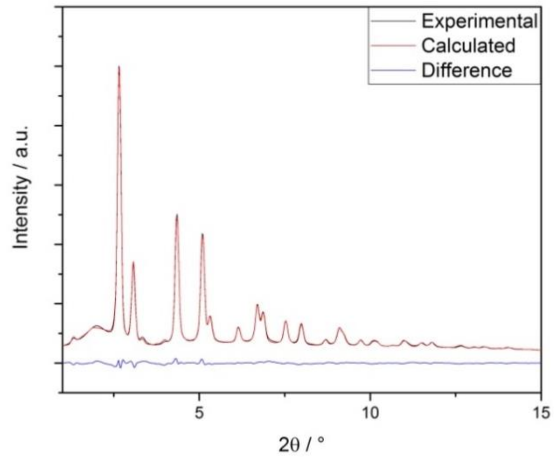
Experimental
Calculated
Difference
Intensity / a.u.
5
10
15
2θ / °

C

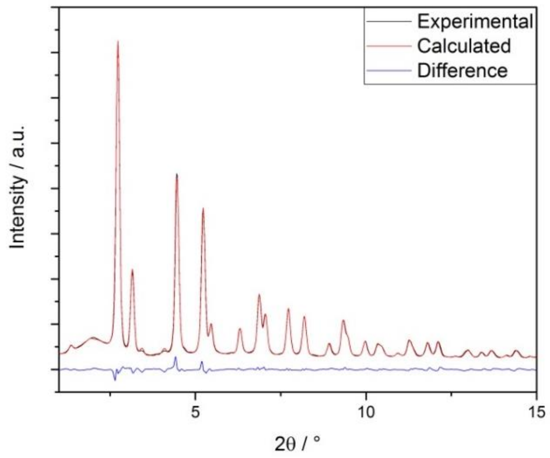
Experimental
Calculated
Difference
Intensity / a.u.
5
10
15
2θ / °

D

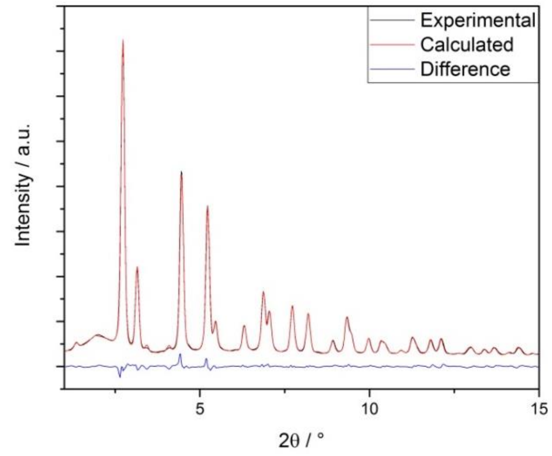
Experimental
Calculated
Difference
Intensity / a.u.
5
10
15
2θ / °

E

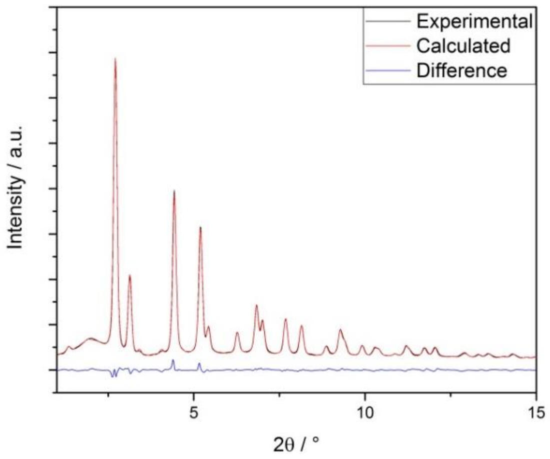
Experimental
Calculated
Difference
Intensity / a.u.
5
10
15
2θ / °

F

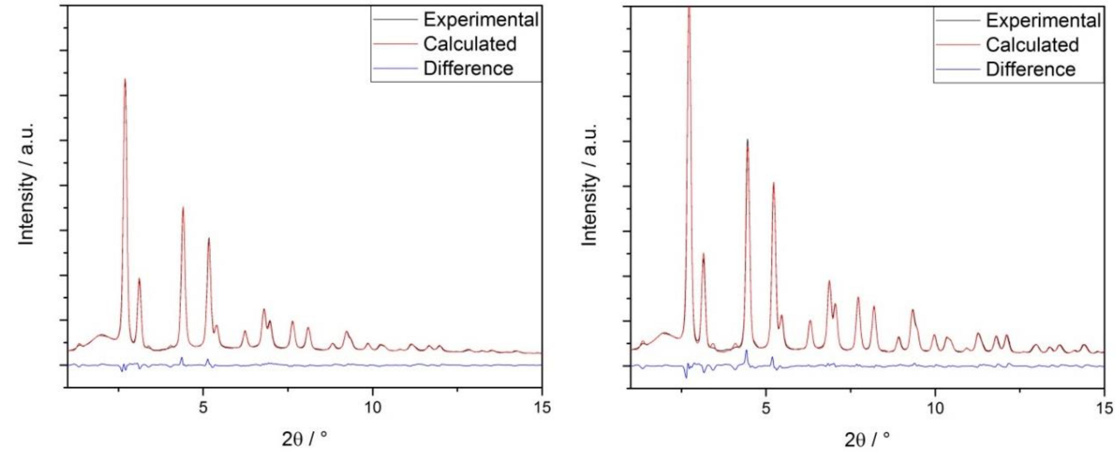

G **H**

Figure S4c:

(A) Comparison of the fit between the experimental and calculated data for the κ-$Ce_{0.5}Zr_{0.5}O_2$ at 30°C under H2:N2

(B) Comparison of the fit between the experimental and calculated data for the κ-$Ce_{0.5}Zr_{0.5}O_2$ at 500°C under H2:N2

(C) Comparison of the fit between the experimental and calculated data for the κ-$Ce_{0.5}Zr_{0.5}O_2$ at 900°C under H2:N2

(D) Comparison of the fit between the experimental and calculated data for the κ-$Ce_{0.5}Zr_{0.5}O_2$ back at 30°C under H2:N2

(E) Comparison of the fit between the experimental and calculated data for the κ-$Ce_{0.5}Zr_{0.5}O_2$ at 30°C under air

(F) Comparison of the fit between the experimental and calculated data for the κ-$Ce_{0.5}Zr_{0.5}O_2$ at 500°C under air

(G) Comparison of the fit between the experimental and calculated data for the κ-$Ce_{0.5}Zr_{0.5}O_2$ at 900°C under air

(H) Comparison of the fit between the experimental and calculated data for the κ-$Ce_{0.5}Zr_{0.5}O_2$ back at 30°C under air

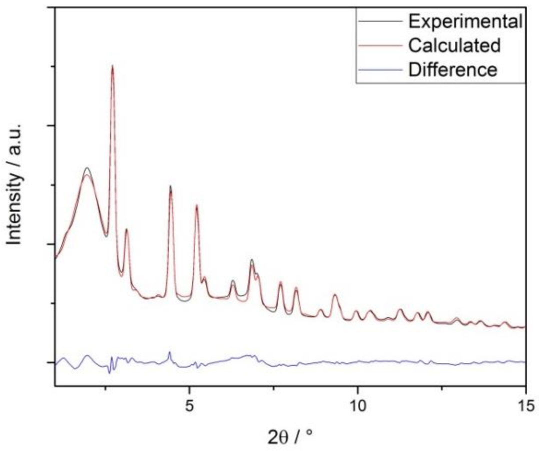
Experimental
Calculated
Difference
Intensity / a.u.
5
10
15
2θ / °

A

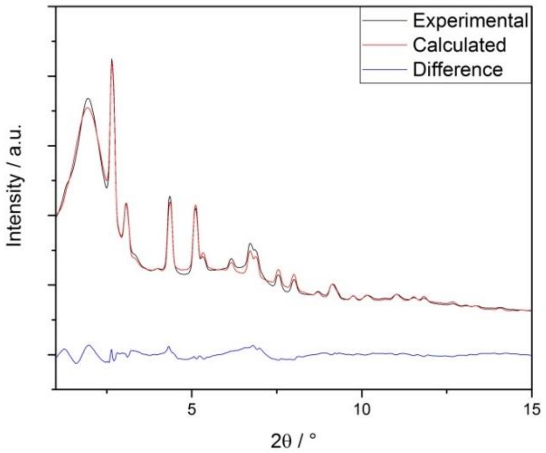
Experimental
Calculated
Difference
Intensity / a.u.
5
10
15
2θ / °

B

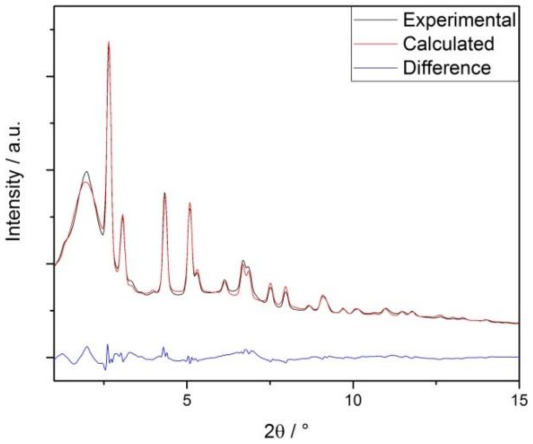
Experimental
Calculated
Difference
Intensity / a.u.
5
10
15
2θ / °

C

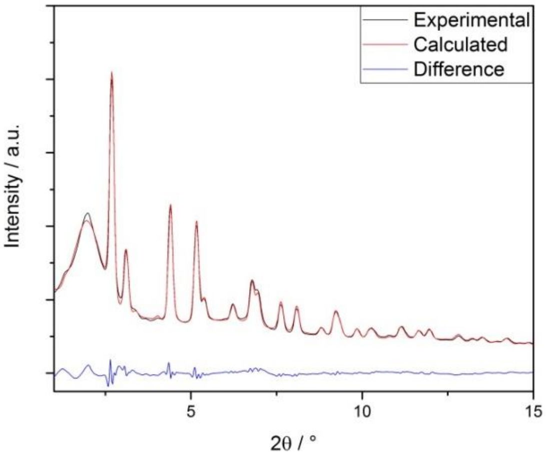
Experimental
Calculated
Difference
Intensity / a.u.
5
10
15
2θ / °

D

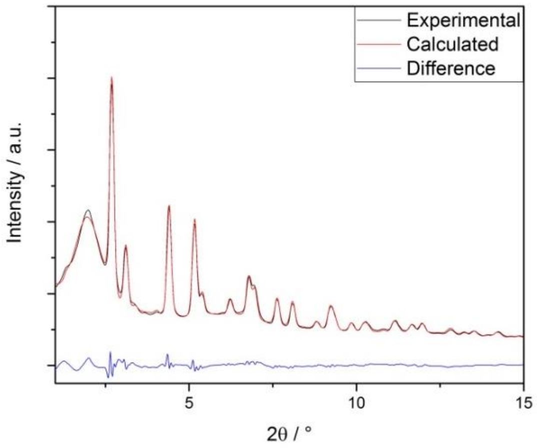
Experimental
Calculated
Difference
Intensity / a.u.
5
10
15
2θ / °

E

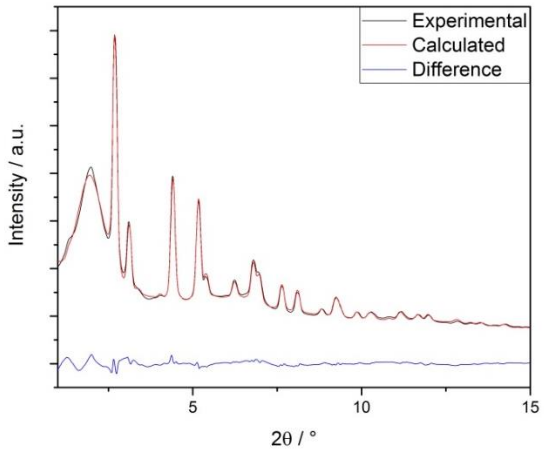
Experimental
Calculated
Difference
Intensity / a.u.
5
10
15
2θ / °

F

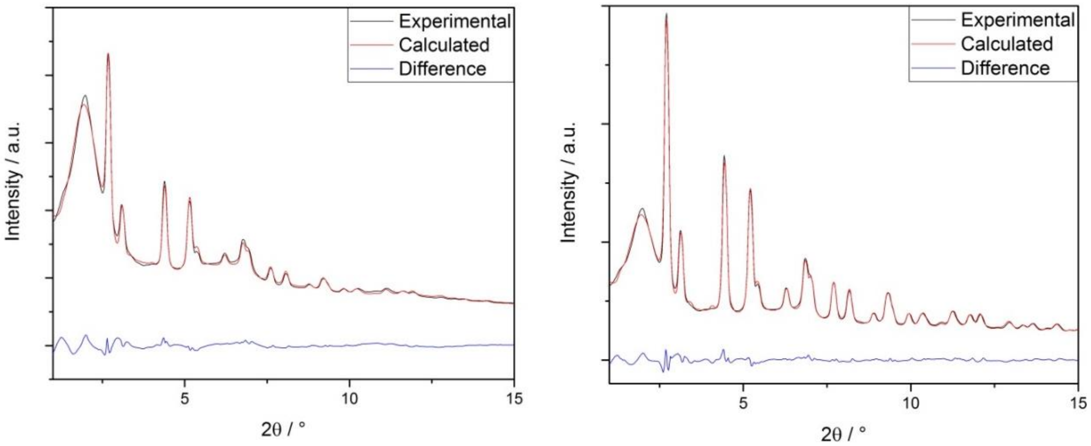

G

H

Figure S5c:

(A) Comparison of the fit between the experimental and calculated data for the 1Pd/κ-$Ce_{0.5}Zr_{0.5}O_2$ at 30°C under H2:N2

(B) Comparison of the fit between the experimental and calculated data for the 1Pd/κ-$Ce_{0.5}Zr_{0.5}O_2$ at 500°C under H2:N2

(C) Comparison of the fit between the experimental and calculated data for the 1Pd/κ-$Ce_{0.5}Zr_{0.5}O_2$ at 900°C under H2:N2

(D) Comparison of the fit between the experimental and calculated data for the 1Pd/κ-$Ce_{0.5}Zr_{0.5}O_2$ back at 30°C under H2:N2

(E) Comparison of the fit between the experimental and calculated data for the 1Pd/κ-$Ce_{0.5}Zr_{0.5}O_2$ at 30°C under air

(F) Comparison of the fit between the experimental and calculated data for the 1Pd/κ-$Ce_{0.5}Zr_{0.5}O_2$ at 500°C under air

(G) Comparison of the fit between the experimental and calculated data for the 1Pd/κ-$Ce_{0.5}Zr_{0.5}O_2$ at 900°C under air

(H) Comparison of the fit between the experimental and calculated data for the 1Pd/κ-$Ce_{0.5}Zr_{0.5}O_2$ back at 30°C under air

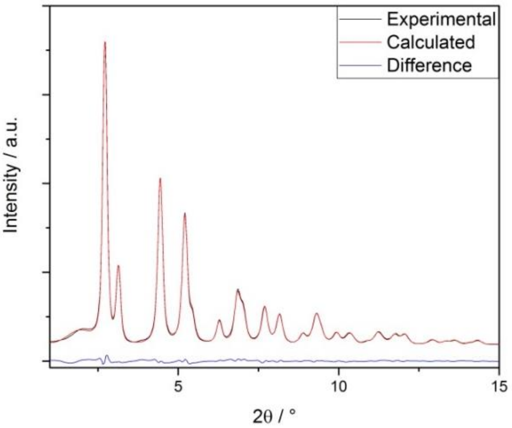
Experimental
Calculated
Difference
Intensity / a.u.
2θ / °
5
10
15

A

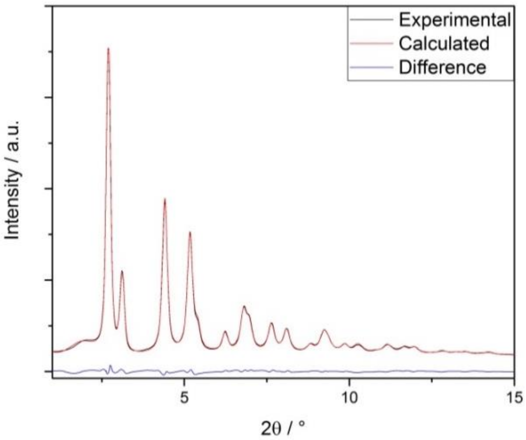
Experimental
Calculated
Difference
Intensity / a.u.
2θ / °
5
10
15

B

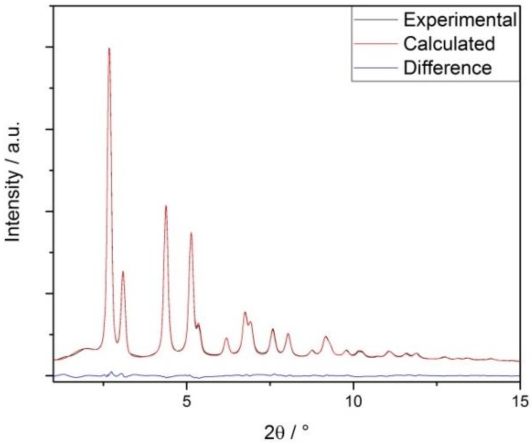
Experimental
Calculated
Difference
Intensity / a.u.
2θ / °
5
10
15

C

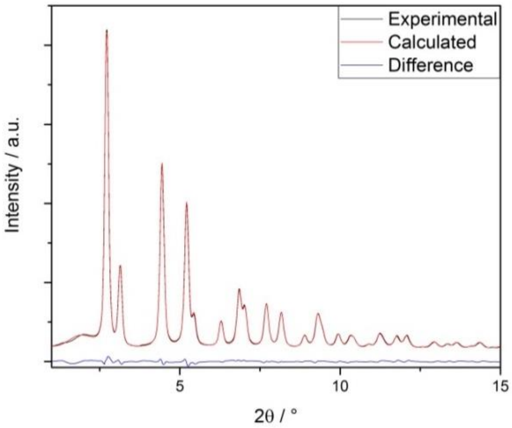
Experimental
Calculated
Difference
Intensity / a.u.
2θ / °
5
10
15

D

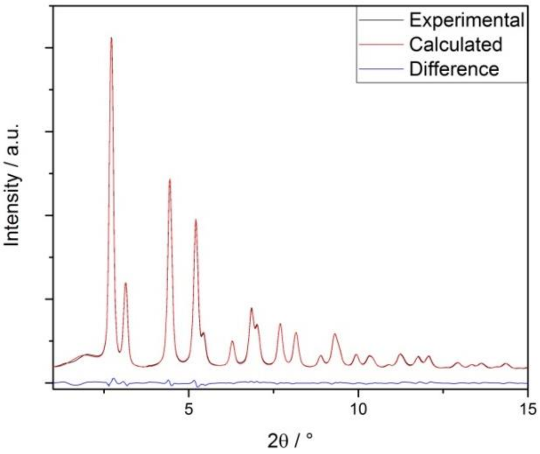
Experimental
Calculated
Difference
Intensity / a.u.
2θ / °
5
10
15

E

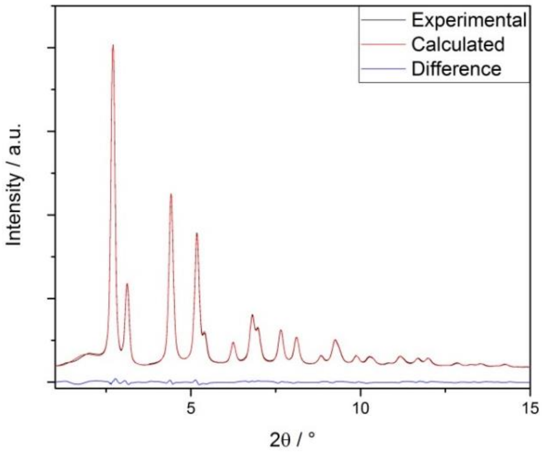
Experimental
Calculated
Difference
Intensity / a.u.
2θ / °
5
10
15

F

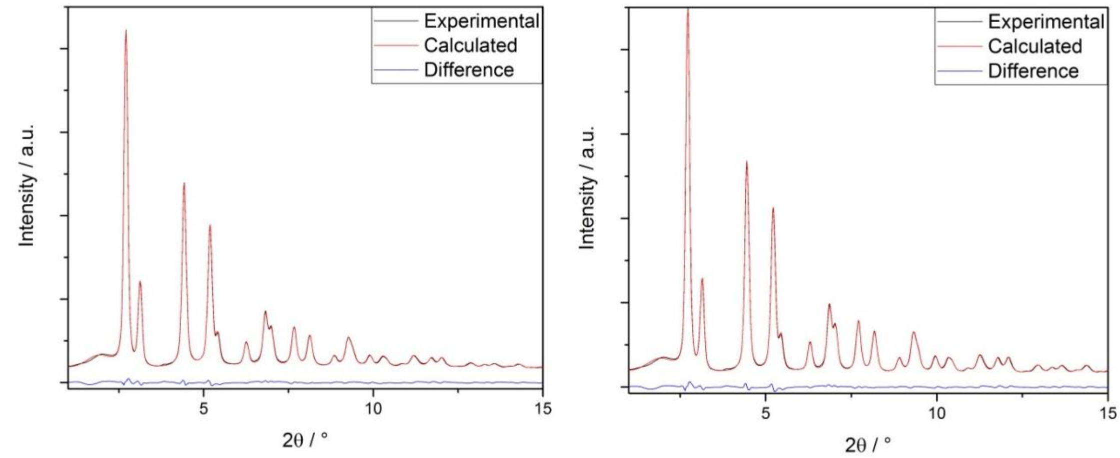

G **H**

Figure S6c:

(A) Comparison of the fit between the experimental and calculated data for the $Ce_{0.5}Zr_{0.5}O_2$ at 30°C under H2:N2

(B) Comparison of the fit between the experimental and calculated data for the $Ce_{0.5}Zr_{0.5}O_2$ at 500°C under H2:N2

(C) Comparison of the fit between the experimental and calculated data for the $Ce_{0.5}Zr_{0.5}O_2$ at 900°C under H2:N2

(D) Comparison of the fit between the experimental and calculated data for the $Ce_{0.5}Zr_{0.5}O_2$ back at 30°C under H2:N2

(E) Comparison of the fit between the experimental and calculated data for the $Ce_{0.5}Zr_{0.5}O_2$ at 30°C under air

(F) Comparison of the fit between the experimental and calculated data for the $Ce_{0.5}Zr_{0.5}O_2$ at 500°C under air

(G) Comparison of the fit between the experimental and calculated data for the $Ce_{0.5}Zr_{0.5}O_2$ at 900°C under air

(H) Comparison of the fit between the experimental and calculated data for the $Ce_{0.5}Zr_{0.5}O_2$ back at 30°C under air

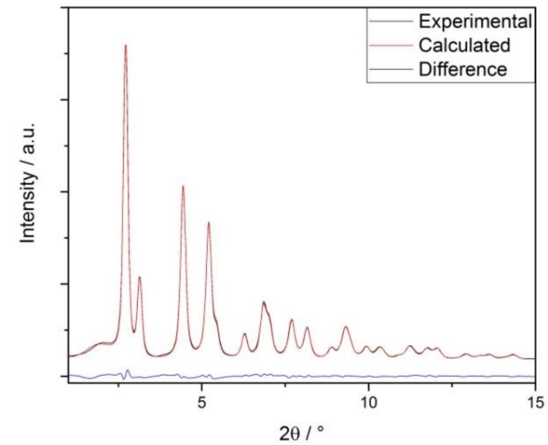
Experimental
Calculated
Difference
Intensity / a.u.
5
10
15
2θ / °

A

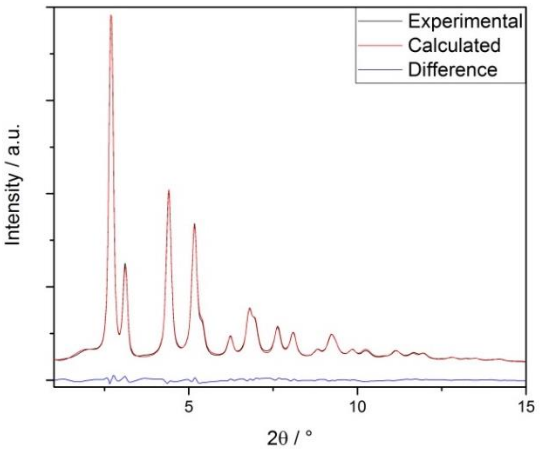
Experimental
Calculated
Difference
Intensity / a.u.
5
10
15
2θ / °

B

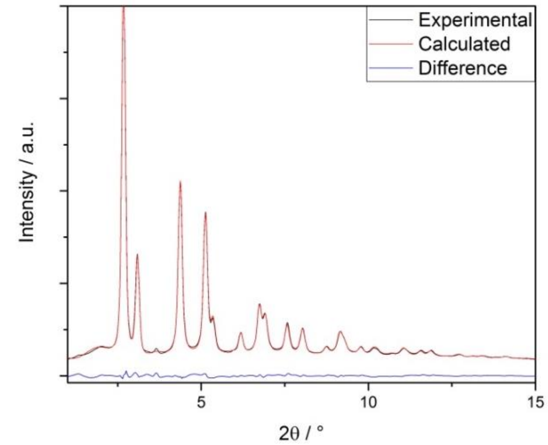
Experimental
Calculated
Difference
Intensity / a.u.
5
10
15
2θ / °

C

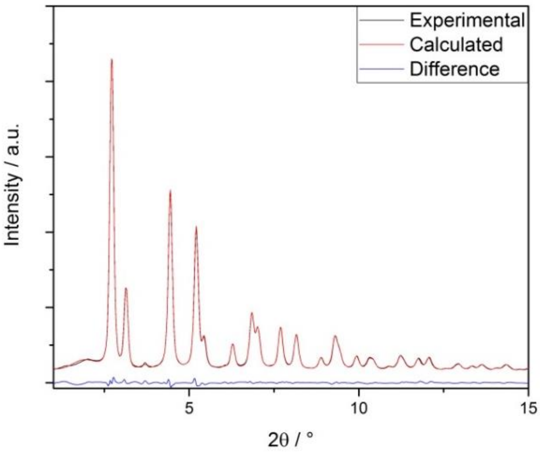
Experimental
Calculated
Difference
Intensity / a.u.
5
10
15
2θ / °

D

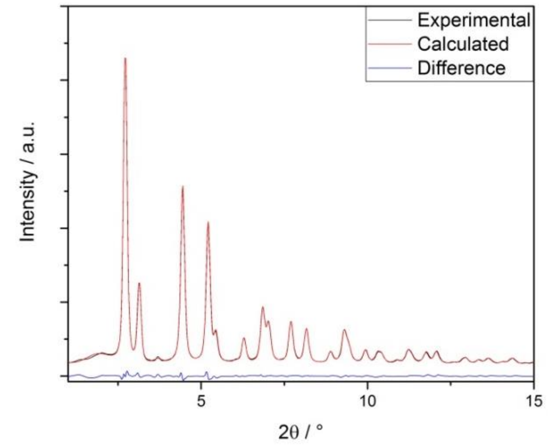
Experimental
Calculated
Difference
Intensity / a.u.
5
10
15
2θ / °

E

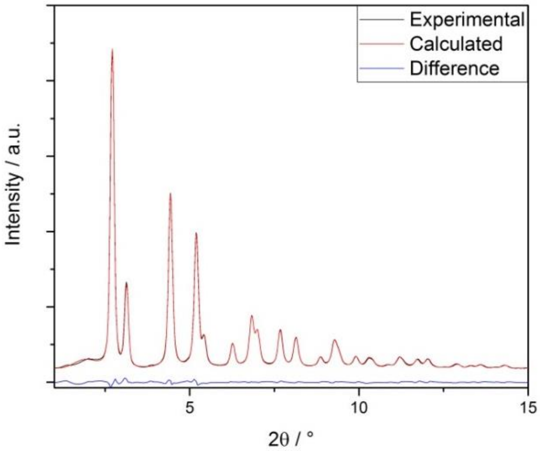
Experimental
Calculated
Difference
Intensity / a.u.
5
10
15
2θ / °

F

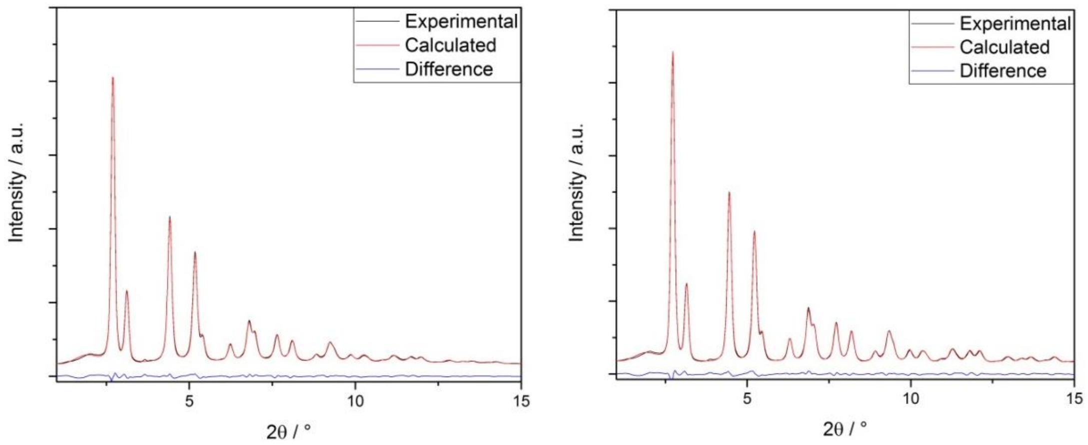

G **H**

Figure S7c:

(A) Comparison of the fit between the experimental and calculated data for the 1Pd/$Ce_{0.5}Zr_{0.5}O_2$ at 30°C under H2:N2

(B) Comparison of the fit between the experimental and calculated data for the 1Pd/$Ce_{0.5}Zr_{0.5}O_2$ at 500°C under H2:N2

(C) Comparison of the fit between the experimental and calculated data for the 1Pd/$Ce_{0.5}Zr_{0.5}O_2$ at 900°C under H2:N2

(D) Comparison of the fit between the experimental and calculated data for the 1Pd/$Ce_{0.5}Zr_{0.5}O_2$ back at 30°C under H2:N2

(E) Comparison of the fit between the experimental and calculated data for the 1Pd/$Ce_{0.5}Zr_{0.5}O_2$ at 30°C under air

(F) Comparison of the fit between the experimental and calculated data for the 1Pd/$Ce_{0.5}Zr_{0.5}O_2$ at 500°C under air

(G) Comparison of the fit between the experimental and calculated data for the 1Pd/$Ce_{0.5}Zr_{0.5}O_2$ at 900°C under air

(H) Comparison of the fit between the experimental and calculated data for the 1Pd/$Ce_{0.5}Zr_{0.5}O_2$ back at 30°C under air